PELDOR IN MULTI-SPIN SYSTEMS – FROM MODEL SYSTEMS SYNTHESIS TO BIOLOGICAL APPLICATIONS

Silvia Valera

A Thesis Submitted for the Degree of PhD
at the
University of St Andrews

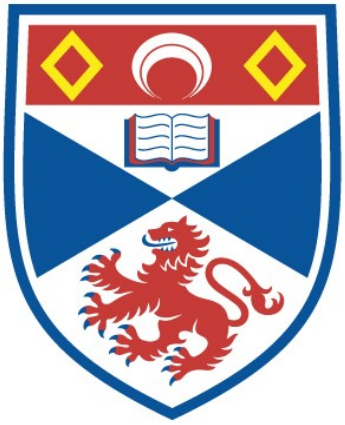

2016

PELDOR in multi-spin systems – from model systems synthesis to biological applications

Silvia Valera

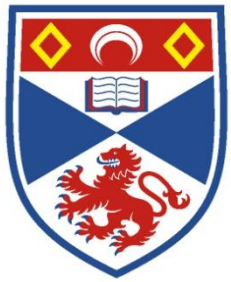

University of
St Andrews

This thesis is submitted in partial fulfilment for the degree of PhD
at the
University of St Andrews

10th June 2016

1. Candidate's declarations:

I, Silvia Valera, hereby certify that this thesis, which is approximately 39,700 words in length, has been written by me, and that it is the record of work carried out by me, or principally by myself in collaboration with others as acknowledged, and that it has not been submitted in any previous application for a higher degree.

I was admitted as a research student in September 2012 and as a candidate for the PhD in September 2013; the higher study for which this is a record was carried out in the University of St Andrews between 2012 and 2016.

Date: 10/06/2016 Signature of candidate …….....

2. Supervisor's declaration:

I hereby certify that the candidate has fulfilled the conditions of the Resolution and Regulations appropriate for the degree of Chemistry in the University of St Andrews and that the candidate is qualified to submit this thesis in application for that degree.

Date: 10/06/2016 Signature of supervisor …….....

3. Permission for publication:

In submitting this thesis to the University of St Andrews I understand that I am giving permission for it to be made available for use in accordance with the regulations of the University Library for the time being in force, subject to any copyright vested in the work not being affected thereby. I also understand that the title and the abstract will be published, and that a copy of the work may be made and supplied to any bona fide library or research worker, that my thesis will be electronically accessible for personal or research use unless exempt by award of an embargo as requested below, and that the library has the right to migrate my thesis into new electronic forms as required to ensure continued access to the thesis. I have obtained any third-party copyright permissions that may be required in order to allow such access and migration, or have requested the appropriate embargo below.

The following is an agreed request by candidate and supervisor regarding the publication of this thesis:

PRINTED COPY

Embargo on all or part of print copy for a period of two years on the following ground: publication would preclude future publication

ELECTRONIC COPY

Embargo on all or part of electronic copy for a period of two years on the following ground: publication would preclude future publication

Date: 10/06/2016

Signature of candidate …….....

Signature of supervisor …….....

Acknowledgments

I thank my supervisor for giving me the opportunity to work with him, and providing training, expertise, guidance and support throughout the duration of my studies.

I thank the rest of our research group, comprising Dr. Katrin Ackermann, Angeliki Giannoulis and Sonia Chabbra, for providing support, constructive discussions, guidance, and a good working atmosphere.

I am grateful to all my collaborators, Dr. James E. Taylor, Dr. David S. S. B. Daniels, Dr. Daniel Dawson, Dr. Kasun S. Athukorala Arachchige, Dr. Christos Pliotas, Dr. Hexian Huang, Dr. Nitin Kunjir together with Prof. James H. Naismith, Prof. Snorri Sigurdsson, Prof. Sharon E. Ashbrook and Prof. Alexandra M. Z. Slawin for contributing to the projects with samples, analyses and expert knowledge. I thank the following for providing excellent scientific service and expertise: Dr. Thomas Lebl and Melanja Smith for solution state NMR, the EPSRC Mass Spectrometry Service offered by the team based at the University of Swansea, Dr. Catherine Booting and Dr. Sally Shiran part of the School of Biology Mass Spectrometry Service, and finally Dr. Stephen Boyer from the Metropolitan University London providing Elemental Analysis.

Thanks to my friends and colleagues Paula Sanz Camacho, Diego Barrios Antunez, Sonia Chabbra, Dr. Ricardo Callejo, Dr. Emily Robinson, Dr. Pei-Pei Yeh, Dr. Damiano Bonaccorso, Dr. Orlando Santoro, Dr. Brunello Nardone and Sucharita Mandal, together with present and past members of the Smith group, for their encouragement. I would like also to thank Dr. Brian O' Rourke for his encouragement, guidance and support that allowed me to start my post graduate experience.

A final honourable thank you goes to my partner, my wonderful mother and brother for always helping and believing in me, and extended Irish family and friends for their guidance and invaluable moral support provided throughout this constructive experience.

To those who make my rock rose

The scientific man does not aim at an immediate result. He does not expect that his advanced ideas will be readily taken up. His work is like that of the planter - for the future. His duty is to lay the foundation for those who are to come, and point the way. *Nikola Tesla*

Abstract

Pulsed electron-electron double resonance (PELDOR) is an emerging technique for nanometre distance measurements in nano-sized assemblies and between specific sites of molecules. Most commonly nitroxide radicals are used as probes for EPR distance measurements because they are easy to introduce in biological systems such as soluble and membrane proteins or nucleic acids.

PELDOR distance measurements currently rely on data processing software which has been proven to accurately extract inter-spin distances from the dipolar coupling between two paramagnetic centres. However, when the dipolar coupling is affected by contributions from other close-by unpaired electrons inaccuracies as broadening effects and artefacts are introduced in the distance distributions derived. This challenge, commonly referred as multi-spin effects, has been affecting the extraction of accurate distance information from PELDOR measurements in chemical and biological systems with multiple spin labels.

The aim of this project is to approach, identify and suppress inaccuracies introduced in PELDOR-based distance distributions by multi-spin effects. This is achieved through the synthesis of multiply labelled model systems which would allow for assessment of the impact of multi-spin effects on distance measurements of simple geometries whose behaviour can be easily predicted and modelled. In this work existing methods for suppression of multi-spin effects are tested, together with their efficiency and limitations. The results are used to devise better sets of parameters including alternative settings for extraction of accurate distances from multi-spin systems and to explore their efficiency and limitations. Additional effects influencing distance measurements by pulsed EPR are also examined; in particular the effects of orientation selection and their interplay with multi-spin effects is studied in depth.

Studies on rigid symmetric and asymmetric chemical model systems together with heptameric channel membrane proteins allow for outlining of recommendations for PELDOR distance measurements settings on systems presenting similar structural features, including symmetries and inter-spin distances.

Chapter 1 - Introduction 1

1.1 Preamble 1

1.2 Distance measurements by pulsed EPR 3

1.3 Extraction of distance distributions: DeerAnalysis and Tikhonov regularization 9

1.4 Model systems: calibration tools for extraction of nanometre distances 13

1.4.1 Spin Labels 14

1.5 Model systems 15

1.5.1 Biradicals 16

1.5.1.1 Nitroxide-Based Biradicals 17

1.5.1.2 Trityl-Based Biradicals 26

1.5.2 Polyradicals 29

1.5.3 Metal Ions 31

1.6 PELDOR measurements in multi-spin systems 38

1.6.1 Spin-counting 40

1.6.2 Methods for suppression of multi-spin effects to-date 42

1.6.2.1 Suppression by experimental methods 43

1.6.2.2 Suppression by post-processing methods 43

1.6.2.3 Suppression by sample sparse labelling 45

1.7 Project aims 46

Chapter 2 - Synthesis of polyradical model systems 47

2.1 Project Background 47

2.2 Project aims 48

2.3 Results and discussion 49

2.3.1 Optimisation of esterification conditions 49

2.3.2 Synthesis of polyradicals 52

2.4 Conclusion 60

Chapter 3 - Novel experimental approach for suppression of multi-spin effects 61

3.1 Project background 61

3.2 Project Aims 62

3.3 Results and Discussion 63
3.3.1 Multi-spin effects suppression by λ reduction 63
3.3.2 Multi-spin effects suppression by power-scaling 71
3.3.3 Multi-spin effects suppression by frequency interchange 80
3.3.4 Comparison of frequency-interchanged and λ reduction experiments 87
3.4 Conclusion 95
Chapter 4 - Sparse labelling as method for suppression of multi-spin effects 96
4.1 Project background 96
4.2 Project Aims 98
4.3 Results and Discussion 99
4.3.1 Simulations 99
4.3.2 PELDOR experiments 99
4.3.2.1 Sparse labelling: extraction of inter-spin distances 99
4.3.2.2 Sparse labelling: effects on measurements sensitivity 105
4.3.3 Frequency-interchanged PELDOR experiments: 108
4.3.3.1 Sparse labelling and frequency-interchange: effects on distance distributions 108
4.3.3.2 Sparse labelling and frequency-interchange: effects on sensitivity 121
4.3.4 Combination of lambda reduction and sparse labelling 125
4.3.5 Comparison between frequency-interchanged and sparse labelling 128
4.4 Conclusion 130
Chapter 5 - Orientation selection and multi-spin effects in PELDOR distance measurements 131
5.1 Introduction 131
5.2 Project aims 135
5.3 Results and Discussion 136
5.3.1 Solvent effect 136
5.3.2 Orientation selection and multi-spin effects 138
5.3.3 Orientation averaging 145
5.4 Conclusion 150
Conclusions and Outlook 151

Materials and Methods *153*

References *171*

List of figures *181*

Abbreviations

ASAP	Atmospheric solid analysis probe
ATR	Attenuated total reflectance
BAMBI	Based on minor broad inversion
BOP	(Benzotriazol-1-yloxy)tris(dimethylamino)phosphonium hexafluorophosphate
CW	Continuous wave
d	Doublet
δ	Chemical shift
DCC	Dicyclohexylcarbodiimide
DEER	Double electron-electron resonance
DFT	Density functional theory
DMAP	4-(Dimethylamino)pyridine
DMF	*N*, *N*-Dimethylformamide
DMSO	Dimethylsulfoxide
DNA	2'-Deoxyribonucleic acid
DNP	Dynamic nuclear polarisation
DQC	Double quantum coherence
E. coli	Escherichia coli
EDCI	1-Ethyl-3-(3-dimethylaminopropyl)carbodiimide
ELDOR	Electron-electron double resonance
EPR	Electron paramagnetic resonance
ES	Electronspray ionisation
EtOAc	Ethyl acetate
ESEEM	Electron spin echo envelope modulation
FRET	Fluorescence resonance energy transfer
FTIR	Fourier transform infrared
HOBT	Hydroxybenzotriazole
HPLC	High performance liquid chormatography
HRMS	High resolution mass spectroscopy
ID	Instantaneous diffusion
J	Coupling constant – electron exchange coupling
m	Multiplet
m-CPBA	*meta*-chloroperoxybenzoic acid
MALDI	Matrix-assisted laser desorption ionisation

MAS	Magic angle spinning
MeOH	Methanol
mp	Melting point
MS	Mass spectrometry
MscS	Mechanosensitive channel of small conductance
MTSSL	(1-Oxyl-2,2,5,5-tetramethylpyrroline-3-methyl)methanethiosulfonate
NMR	Nuclear magnetic resonance
NSI	Nanospray ionisation
o	Ortho
PELDOR	Pulsed electron-electron double resonance
R*f*	Retention factor
RIDME	Relaxation induced dipolar modulation enhancement
RNA	Ribonucleic acid
s	Singlet
SDSL	Site-directed spin labelling
SIFTER	Single frequency technique for refocusing
SPS	Solvent purification system
TBDMS	Tert-butyldimethylsilyl
TFA	Trifluoroacetic acid
THF	Tetrahydrofuran
THP	Tetrahydropyranyl
TMEDA	N,N,N',N'-tetramethylethylenediamine
TMS	Trimethylsilyl
TOF	Time of flight
TPA	2,2,5,5-tetramethyl-pyrrolin-1-oxyl-3-acetylene
TPC	1-oxyl-2,2,5,5-tetramethylpyrroline-3-carboxylic acid

Chapter 1 - Introduction

1.1 Preamble

Measurement of inter atomic distances is a key element towards elucidation of structural features of biological systems, such as membrane and channel proteins, and the understanding of their conformational and oligomerisation dynamics. Several techniques such as X-ray crystallography,[1] fluorescence resonance energy transfer (FRET)[2] and nuclear magnetic resonance (NMR)[3] give access to accurate measurement of distances on atomic and molecular scales. In this respect, X-ray crystallography is the most extensively used technique because of its high levels of accuracy achievable and its accessibility; however it requires crystalline samples with a diffraction pattern suitable for structure resolution. Often only specific protein conformations can be crystallised, thus limiting the information accessible through this technique.[4] FRET is another commonly used technique for measurement of intermolecular distances in biological systems.[5] It can be applied in solution at room temperature and reach single molecule sensitivity levels giving real-time resolution of molecular dynamics. However, it requires the introduction of two large, chemically different and complementary chromophores, a donor and an acceptor, within the system taken under study, which can be challenging and often gives access to information with low accuracy levels.[6] To overcome some of these limitations, NMR and electron paramagnetic resonance (EPR) spectroscopic techniques have been introduced as complementary methods for structural elucidation of biological systems. These have been found to give access to accurate distance information, by measurement of dipolar couplings, and under experimental conditions resembling the native biological environments. NMR has been used as a powerful tool for elucidation of structural properties of biological systems, measuring distances in the short range, with the higher limits varying between 3.5 and 10 Å depending on the isotopes chosen and signal-to-noise levels.[7] This method often faces challenges when extracting information from complex systems, commonly caused by the presence of overlapping signals limiting structural assignment. These limitations lead to the requirement of additional measurements and in-depth modelling. Additionally, NMR measurements require highly concentrated samples for gaining the required sensitivity for extraction of inter-atomic and inter-molecular distances; this limitation has been recently partially addressed by the combining solid state NMR measurements with dynamic nuclear polarisation (DNP) techniques.[8]

Pulsed and continuous-wave (CW) EPR methods have been previously introduced as complementary tools for accurate extraction of inter-spin distances on the nanometre scale.[2b, 9] EPR-based measurements give access to exclusive detection of endogenous paramagnetic centres, as metal centres or cofactor radicals, or chemically introduced spin labels. Specifically, spin labels are organic molecules bearing paramagnetic centres, commonly stable organic radicals or metal ions, which are frequently introduced in specific sites of biological systems by site-directed spin labelling (SDSL).[10] The combination of SDSL and pulsed EPR techniques, such as pulsed electron-electron double resonance (PELDOR or DEER)[11] and double quantum coherence (DQC)[12] methods, has allowed measurement of inter-spin distances up to 10 nm.[13] Pulsed EPR distance measurements have been extensively used for determination of structural features and conformational distributions of complex biological systems.[2b, 9b] EPR measurements require a limited sample concentration, with the optimum spin concentration being around 100 μM.[9b] EPR measurements of spin labelled systems or bearing native paramagnetic centres give access to distances in the nanometre range, typically between 0.8 and 2.5 nm with CW methods[4] and 1.5 to 8 nm[14] when using pulsed technique. Recently, distances of up to 10 nm have been reported in fully deuterated proteins.[9b] Distance measurements can be performed under experimental conditions shown to allow the observation of native structures and conformations: within membranes, bicelles or aqueous buffer. However, they often require cryogenic temperatures to minimise the residual motion of the label and allow accurate extraction of the exchange and dipolar interactions.[15,16] Pulsed EPR distance measurements not only give information on inter-spin distances, but also provide powerful geometric constraints for structure determination of biomolecules such as angular correlations,[17] structural flexibility[18] and the number of interacting spins[19], in the presence or absence of electron-electron exchange couplings (*J*).[20] Specifically, counting the number of coupled spins from the echo amplitude[19d, 21] allows determination of the aggregation states of small peptides.[22] Thus, pulsed EPR measurements are able to provide information beyond distances on the system under study. EPR distance measurements, however, can be challenging to quantify and interpret, for example when performing distance measurements on systems bearing metal centres or multiple paramagnetic centres,[2b] possibly leading to data misinterpretation.[23]

1.2 Distance measurements by pulsed EPR

Magnetic resonance methods give access to distance measurements between spins based on the extraction and quantification of the magnetic dipole-dipole coupling between the spins. The interaction energy E of the magnetic dipole-dipole coupling between one spin with magnetic moment $\boldsymbol{\mu_1}$ with a neighbouring spin(s) with magnetic moment $\boldsymbol{\mu_2}$ in the presence of an external magnetic field B_0 is expressed by Equation 1.1 and shown in Figure 1.1:

$$E = \frac{\mu_0}{4\pi}\left[\frac{\boldsymbol{\mu_1}\cdot\boldsymbol{\mu_2}}{r^3} - \frac{3(\boldsymbol{\mu_1}\cdot\mathbf{r})(\boldsymbol{\mu_2}\cdot\mathbf{r})}{r^5}\right] \quad (1.1)$$

where $\mathbf{r}$ is the distance vector interconnecting $\boldsymbol{\mu_1}$ and $\boldsymbol{\mu_2}$, and μ_0 is the vacuum permeability. This through space interaction depends on the relative orientation of the distance r between the two dipoles with respect to the external magnetic field B_0, represented by the angle θ.[15] Consequently, the coupling frequency can be described, when following the secular and point dipole approximations, by Equation 1.2: [21, 24]

$$\nu_{dd} = \frac{\mu_0\mu_B^2}{8\pi^2\hbar}\frac{g_A g_B}{r_{AB}^3}(1 - 3cos^2\theta_{AB}) \quad (1.2)$$

where ν_{dd} is the dipole-dipole splitting in frequency units, μ_B is the Bohr magneton, g_A and g_B are the g-factors of the electron spins, A and B, $\hbar$ is the reduced Plank's constant, r_{AB} is the distance between two spins and θ is the angle between the distance vector connecting the two spins and the external magnetic field, B_0.

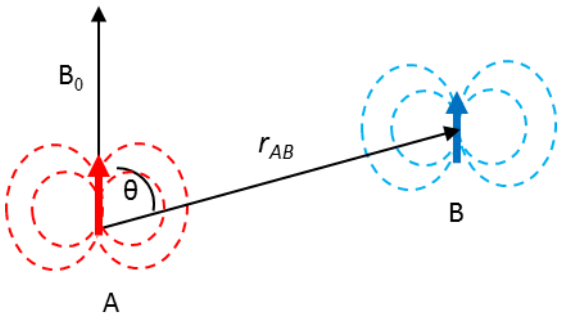

Figure 1.1: Interaction between two paramagnetic centres A and B, at a distance r_{AB} and with an angle θ relative to the external magnetic field B_0.

For the interaction between two organic radicals ($g_A = g_B = 2.005$) this can be simplified to Equation 1.3 showing the direct relationship between the coupling frequency and inter-spin distance: [25]

$$r_{AB}[nm] = \sqrt[3]{\frac{52.18[MHz]}{\nu_{dd}}}(1 - 3cos^2\theta_{AB}) \tag{1.3}$$

with ν_{dd} being the dipolar frequency expressed in MHz.

In CW EPR distances between 0.8 and 2.5 nm can be estimated by analysis of the spectral broadening that is caused by the presence of strong dipolar frequencies, corresponding to short distances. Thus, the effect of the dipolar coupling on the line broadening must be sufficiently strong to shadow other effects affecting the line shape. CW EPR experiments consist of a continuous microwave radiation of a sample at a fixed frequency while the magnetic field intensity is swept. The first derivative of absorption peaks are recorded when the resonance conditions are met to allow transitions between the energy levels of the system. Spectral features, such as the number of splittings and line broadenings, can be induced by several factors such as the electronic structure of the compound, which underpins the g value and varies hyperfine couplings. Hyperfine couplings, in particular, describe the interaction between the electron spin magnetic moment of the unpaired electron and nuclear magnetic moment of coupled nuclei. These are important elements for identification of unknown species as each nuclear spin and resulting hyperfine coupling constants will give different splitting patterns. If these are unresolved they can introduce additional broadening to the line shape of the signal, thus affecting or impeding extraction of inter-spin distances. Relaxation phenomena, caused by dynamics of the molecule or its environment, together with *g* anisotropies, may further contribute to line broadening and challenge distance measurements.[4, 22] In particular, *g* anisotropies introduce broadenings due to the orientation dependence of the electron Zeeman splitting.

For nitroxides it is commonly found that only dipolar couplings corresponding to distances below 2 nm can be extracted as the broadening of X-band CW EPR line shape generally becomes negligible for distances between 1.5 and 2 nm. The lower limit of 0.8 nm is imposed by the presence of exchange couplings which can be larger than, or comparable to, the dipolar coupling term.[15]

Separation of the dipolar couplings for extraction of longer distances by refocusing all inhomogeneous broadenings caused by contributions from electron nuclear couplings and different resonance frequencies can be achieved by pulsed dipolar spectroscopy.[9a, 15] The use of different pulsed EPR methods becomes necessary as the weak dipolar couplings, corresponding to large distances, can be easily hidden by the inhomogeneous broadening of the EPR spectrum and other interactions.[26] Signal contributions from distances shorter than 1.5 nm induce couplings that are beyond the excitation bandwidth of standard experiments, making their detection inaccessible by PELDOR methods.[15] The limit for the maximum distance to be resolved by pulsed methods is set by the lifetime of the transversal relaxation of the system. This depends on the nature of the paramagnetic centre and on the measuring temperature.[15] When performing pulsed EPR measurements an appropriate measurement time window has to be chosen to exclude cut-off artefacts, and to accurately extract the expected distance. The longer the inter-spin distances, the smaller the dipolar frequency, the longer the measuring time windows required for accurate resolution of distances.[27]

The first PELDOR experiment consisted of the combination of a two-pulse Hahn echo sequence with a fixed interval, τ, applied at a frequency (ν_A), to selectively excite spins A of the A-B spin pair, and an additional pump or inversion pulse at a second frequency (ν_B) in resonance with spins B (Figure 1.2).[11]

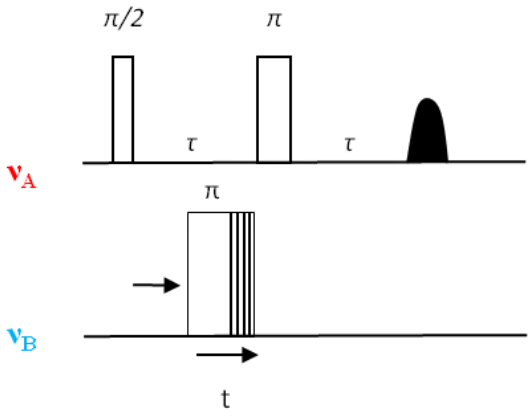

Figure 1.2: Three pulse PELDOR experiment pulse sequence.

The frequency ν_A, also called the observer or detection frequency, refocuses all inhomogeneities and eliminates the differences in the Larmor resonance frequency of the excited A spins arising from *g* anisotropies and hyperfine couplings at the time of the echo formation.[28] Refocusing of all interactions leads to the formation of a constant echo,

commonly referred to as Hahn echo. The pulse sequence also refocuses the dipolar interaction to the B spins; selective introduction of the dipolar frequency at a specific time is achieved by an inversion pump pulse at a second microwave frequency ν_B. The pulse applied at the second frequency ν_B, also known as the pump or inversion frequency, introduced at a variable time *t* within the time interval between the two echo-forming pulses, inverts the magnetic dipole of all resonant B spins. Flipping the B spins changes the local magnetic field of coupled A spins by electron-electron coupling ω_{dd}. The extent of the change in the Larmor frequency of spins A is related to the magnetic dipolar interaction between A and B spins, which is proportional to the inverse cube of the distance r_{AB} between the two spins (Equation 1.2). This leads to a change in the Larmor frequency of A spins at time *t* by $\pm\omega_{dd}$ and the resulting echo amplitude to modulate with $\cos(\omega_{dd}t)$.[15] The integral of the intensity of the refocused echo is measured against *t*,[6] thus allowing ω_{dd} to be determined.[26]

Modulation of the PELDOR signal, *V*(*t*), with time *t* follows the relationship expressed in Equation 1.4:

$$V(t) = \langle V_o \cos(\omega_{dd} t) \rangle \tag{1.4}$$

with V_0 being the echo intensity at t = 0, in the absence of a pump pulse, and ω_{dd} as the dipolar frequency between two spins expressed in radians, <…> indicates averaging of all orientations. This is valid in an ideal case assuming full inversion of the echo and excitation of all orientations. In most applications the resonance frequencies of spins A and B overlap and the bandwidth of the two pulses only allows for partial excitation of the EPR spectrum. This induces the excitation of subensembles of A and B spins with specific orientations with respect to B_0, leading to a reduction of the PELDOR signal intensity and modulation depth. The signal also shows an exponential decay due to the presence of inter-molecular interactions.[7a]

The three-pulse version of the PELDOR experiment has one important limitation: an inherent dead time. As reported in Figure 1.2 the first $\pi/2$ pulse applied at the detection frequency and the π pulse applied at the pump frequency will need to be applied at the same time to achieve the zero-time of the dipolar evolution. This overlap in the amplifier causes a decrease in the output power of each pulse, as it cannot take the power of two overlapping microwave pulses. This results in the two pulses having reduced flip angles and in the introduction of experimental artefacts. Thus, overlapping pulses prevent to accurately

record, within the first nanoseconds of the signal amplitude around $t = 0$. [26] This results in introduction of challenges for extraction of short distances, up to 2.5 nm and diminishes the overall experiment sensitivity.[15] The 4-pulse version of the same experiment, reported in Figure 1.3, was later introduced . This new experiment is now dead-time free.[14]

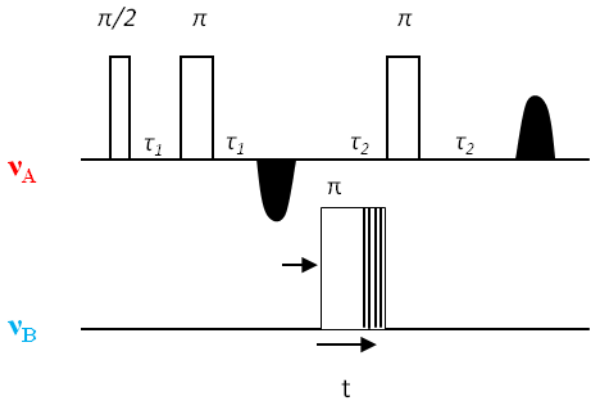

Figure 1.3: Four pulse PELDOR pulse sequence.

Here, the problem is overcome by refocusing the primary two-pulse Hahn echo with an additional π pulse at the frequency ν_A. The primary Hahn echo forms at time $2\tau_1$ and the refocusing pulse at time τ after the Hahn echo leads to the formation of a refocused echo at $2(\tau_1 + \tau_2)$ after the first pulse. The pump pulse is now stepped in the time interval between the second and the third detection pulses. Refocusing of spin A magnetization allows avoiding interference between microwave pulses and the maximum of the dipolar evolution to be detected ($t = 2\tau_1$). [7a, 15] The sequence allows for observation of the whole powder pattern, giving access to reliable measurement of electron-electron coupling distributions.[14-15, 29] The major disadvantage of this dead-time free PELDOR experiment is that the detection sequence is at least twice as long as the three-pulse version, depending on the choice of τ_1 and τ_2. This leads to losses in signal intensity due to the effects of transverse relaxation and incomplete refocusing. To partially relieve the effects introduced by transverse relaxation the original sequence reported in Figure 1.3 was modified by increasing the evolution period τ_2 prior the refocusing pulse. This allows measuring longer dipolar evolution times with similar overall sequence lengths and to detect different species present within the same system with slightly differing relaxation times.[7a] Usually, a two-step phase cycling of the π/2 pulse at the detection frequency is introduced to eliminate receiver offsets, which may hamper deconvolution of the intramolecular contributions from

the intermolecular ones from the echo decay, thus affecting subtraction of the background function and consequently accurate extraction of distance distributions. The phase cycle uses the repetition of the detection $\pi/2$ pulse with opposite phases; subtraction of the signals obtained from the two experiments isolates the PELDOR signal from instrumental artefacts.[26]

Once the PELDOR signal *V(t)* has been isolated, using the dead-time free pulse sequence, its Fourier transformation gives a spectrum, in the case of a glass powder and with spins randomly oriented, also referred to as Pake pattern (Figure 1.4). This transformation, exploiting the unique correspondence between time and frequency domains, allows for extraction of the dipolar coupling frequency ω_{AB} contributing to the signal achieved by observing the separation of the two singularities. Specifically, the edge-to-edge distance corresponds to the dipolar splitting of molecules with an angle $\theta = 0°$ between the distance vector and the external magnetic field and the peak-to-peak distance corresponds to the dipolar splitting for molecules with $\theta = 90°$.[2b] The shape of the Fourier transform suggests the distribution of the spin populations with specific orientations within the sample. In a randomly distributed sample the most probable angle between the dipolar vector **r** and B_0 is 90°, as evident from the intensity of the two singularities (Figure 1.4).[26]

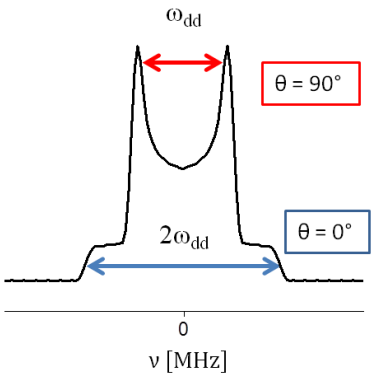

Figure 1.4: Pake pattern from the Fourier transformation of a PELDOR simulation of a rigid biradical.

In this regard, it is important to stress that accurate extraction of inter-spin distances from PELDOR data requires excitation of the entire Pake pattern. Full excitation is not always achievable with the three-pulse sequence, where the most pronounced components are the two singularities corresponding to spins with dipolar angle θ of 90°. Excitation of all components can be more easily achieved using the four-pulse sequence especially as it gives access to the zero-frequency component of the dipolar coupling.[15, 26]

The shape of the Fourier transformed spectrum is affected by three major factors: inter-spin distance, presence or absence of through bond exchange couplings *J* and orientation selection effects. Orientation selection effects, specifically, are induced by the excitation of subensembles of spins with specific molecule orientations in respect to B_0. This is usually favoured by the presence of angular correlations that create a dependence of the PELDOR signal on both distance and orientation of the spin probes with respect to the external magnetic field.[2b] This dependence affects the shape of the Fourier transformed spectrum revealing the distribution of orientations of spin labels and dipolar vectors with respect to B_0. Selection of specific orientations makes extraction of inter-spin distances more challenging than in flexible systems exhibiting a random distribution of orientations.[18b]

1.3 Extraction of distance distributions: DeerAnalysis and Tikhonov regularization

Recently the software DeerAnalysis[30] has been implemented in MATLAB® to give access to distance distributions using alternative methods to Fourier transformation. It is the most commonly used software for processing PELDOR data, as it provides a combination of algorithms for background deconvolution, phase correction and determination of zero-time for processing of time domain data together with Tikhonov regularization, which facilitates extraction of inter-spin distance distributions, as shown in Figure 1.5.

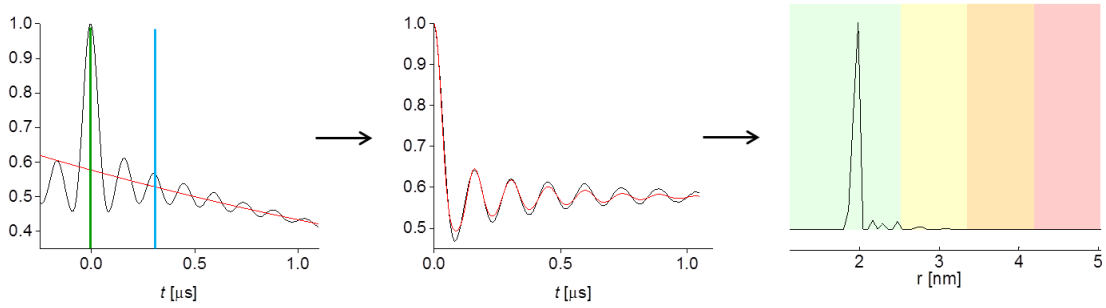

Figure 1.5: Processing of dipolar frequency data for extraction of inter-spin distances by DeerAnalysis 2013. In the first panel the green line indicates the zero time of the dipolar time trace and the blue line indicates the starting point for fitting the slope for subtraction of the background signal V_{inter}. The second figure shows the background corrected experimental data (black) V_{intra} and the simulated dipolar trace (red) generate by DeerAnalysis. The third figure shows the distance distribution obtained from the dipolar signal with colour bars indicating the reliability of the distance distribution defined by the length of the measuring time window of choice.

DeerAnalysis allows to perform background correction of the PELDOR trace by fitting a decaying background function and separating the signal from interactions of spins within the same nano-object (V_{intra}) from the background contributions due to interactions of spins in neighbouring nano-objects (V_{inter}). Elimination of the background function from the raw PELDOR signal gives the so called background-corrected trace. DeerAnalysis also offers tools to evaluate the level of accuracy for extraction of inter-spin distances from the background corrected trace (Figure 1.5). Extraction of accurate inter-spin distances relies not only on the signal-to-noise ratio, but also on the length of the measuring time window. Extraction of long distances, which correspond to weak dipolar couplings, require long time windows to reliably extract the mean distance(s).[27, 31] DeerAnalysis, as shown in Figure 1.5, provides green, yellow and orange coloured bars as guideline indicating whether the distance distribution is reliable with respect to shape, mean and width, or mean only, respectively. If the distance distribution lies in the red bar care should be taken when interpreting the distance data as it should only be considered an indication of the presence of longer distances. The measuring time window is not long enough for accurate extraction of the suggested distance peak(s).

The process for extraction of distance distributions from PELDOR background-corrected data is an ill-posed problem, suggesting that significantly different distance distributions may correspond to very similar dipolar evolution functions. This ill-posedness must be dealt with during data analysis. Usually, this is achieved by trying to find a solution in the distance domain to which the experimental data can be stably fitted without introducing artefacts in the distance distribution.[30] Tikhonov regularisation has been recently introduced as a reliable method for extraction of accurate distance distributions, as it allows for constraining the smoothness of the distance distributions as well as the introduction of the constraint for positive distance distributions, important element for the stability of the solution.[30] It generates a simulated signal described by means of a kernel function $K(t,r)$ and a distance distribution function $P(r)$, with r being the inter-spin distance. The solution to the ill-posed problem is obtained by minimising the square deviation between simulated $S(t)$ and experimental data while compromising for the smoothness of the distance distribution, as shown in Equation 1.5. This is done by optimisation of the regularisation parameter α, representing the level of compromise between the smoothness of distance distribution ($\log \eta$) and quality of fit ($\log \rho$).The relationship between the weighting parameter α, smoothness ρ and fit η is shown in Equation 1.5:

$$G_\alpha(P) = \|S\,(t) - D\,(t)\|^2 + \alpha \left\| \frac{d}{dr^2} P(r) \right\|^2 \tag{1.5}$$

with

$$\rho\,(\alpha) = \|S\,(t) - D\,(t)\|_\alpha^2$$

$$\eta\,(\alpha) = \left\| \frac{d}{dr^2} P(r) \right\|_\alpha^2$$

As guideline for estimating the optimum compromise between these parameters, thus the optimum α value, DeerAnalysis generates an L-curve,[32] as shown in Figure 1.6. The L-curve reports a number of points corresponding to different α values; by choosing different points of this curve one of the two parameters is favoured over the other. Specifically, by choosing a higher α value from the L-curve the smoothness of the distance distribution is increased, while the quality of fit is weighed lower (see blue point with α = 1000 in Figure 1.6).

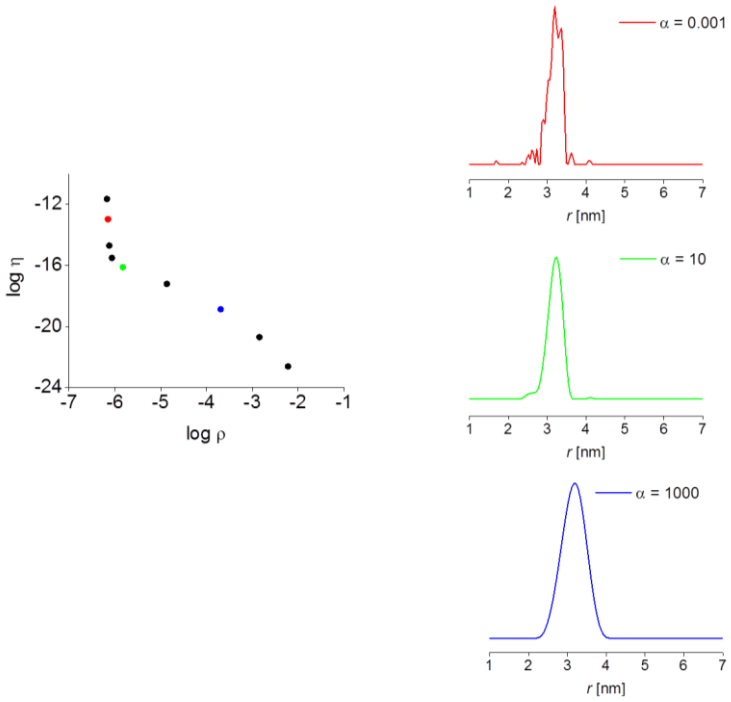

Figure 1.6: L-curve obtained from processing of PELDOR data by DeerAnalysis. The effects of choice of regularization parameter α on distance distributions, obtained from distance measurements on a chemical biradical model system, are reported in the three distance distributions in corresponding colours: 0.001 (red – under smoothed), 10 (green – most appropriate) and 1000 (blue – over smoothed).

This can result in over smoothing the distance distribution and in a compromised quality of fit of the simulated trace to the experimental one. When choosing a small α, instead, the opposite effects can occur: an unphysical under smoothed distance distribution and over-fitted trace. The compromise between the two parameters is usually met at the kink of the L-curve (here, green dot with $\alpha = 10$ in Figure 1.6), at which a smooth distance distribution is obtained together with a good match between simulated and experimental data.

From here under-smoothing leads to a strong decline of smoothness with a minor increase of the quality fit, while over smoothing leads to a moderate increase in smoothness with a substantial decrease in quality of fit. Thus, choice of appropriate α from the L-curve (Figure 1.6) identifies the optimum regularisation parameter for computation of the most appropriate distance distributions using methods based on Tikhonov regularisation.DeerAnalysis is a very convenient tool for extraction of inter-spin distance distributions from PELDOR signal; however care has to be taken when looking at systems with particular properties. Specifically, DeerAnalysis is designed for extraction of distance distributions from a distribution of pairs of interacting spins in the absence of orientation selection, multi-spin effects and *J* couplings. Thus, when interpreting PELDOR data from systems containing contributions from these additional effects they formally cannot be appropriately processed by the software. In these cases the use of DeerAnalysis would have to be validated to be justified. Extraction of distances by DeerAnalysis from systems bearing more than two spin centres and presenting orientation selection effects will be discussed in Chapter 3 and 5 respectively.

1.4 Model systems: calibration tools for extraction of nanometre distances

The discussion underlying Section 1.4 has been published in similar form in *Molecules*, **2014**, *19(12)*, 20227 under the title "Strategies for the synthesis of yardsticks and abaci for nanometre distance measurements by pulsed EPR".[23] The author performed the literature research and wrote the manuscript jointly with Dr. Bela Bode.

Pulsed EPR measurements are frequently used as complementary tools to NMR, X-ray crystallography and FRET for the elucidation of the structure of complex biological systems.[2b, 9b] The main structural features of such systems or their components can be often gained from crystal structures, when possible, or by NMR or electron microscopy. However, the studies of structural transitions and dynamics, such as conformational changes, cannot always be resolved by using these techniques, but potentially by EPR distance measurements. Interpretation of pulsed EPR distance measurements data on these complex systems may become difficult to interpret and quantify and could lead to possible ambiguous interpretation. To study the effects of the parameters affecting pulsed EPR data, chemical model systems, such as simple spin labelled aromatic or aliphatic backbones, have been synthesised. Their structure can be easily manipulated to mimic individual structural features encountered in biological systems allowing observation of their direct effect on distance measurements. The use of model systems with a known chemical structure gives an easy access to distance predictions *via* increment models[33] or molecular dynamics simulations.[18c] Additionally, complex biological systems such as membrane receptors, ion pumps and ion channels have been found to be mechanically analogous to simplified geometrical structures.[34] Thus, studies regarding their conformational and structural changes can be performed on backbones mimicking the behaviour of the more complex systems. Chemical model systems have been previously used as tools for calibration of pulsed EPR experiments and study of the effects influencing distance measurements,[7a, 9b, 20b, 24] and represent the ideal starting point to scrutinise the impact of multi-spin effects on pulsed EPR distance measurements by performing both quantitative and qualitative experiments. These systems could be used as benchmarks to test and optimise existing and new methods for suppression of multi-spin effects currently affecting distance measurements on multiply labelled systems.

Development and synthetic strategies for synthesis of spin labels, aimed at introducing properties which would make them the optimal probes for EPR distance measurements, and model systems and their application are discussed in the next two sections.

1.4.1 Spin Labels

Spin labels are paramagnetic centres bearing a functionality that allows their coordination or covalent attachment to a diamagnetic system. Commonly, paramagnetic centres used for spin labelling consist of stable organic radicals such as nitroxides **1**–**4**, trityl radicals **5** or metal centres **6** in the form of ions or clusters (Figure 1.7).[27, 35] The latter can be attached to the system or replace native, diamagnetic metal ions.[36] Key properties that need to be taken into consideration when choosing or designing a spin label include stability, paramagnetic properties and reactivity. Additionally spin labels should be easily introduced or covalently attached onto biomacromolecules and should not affect the structures or functions of the systems.[37]

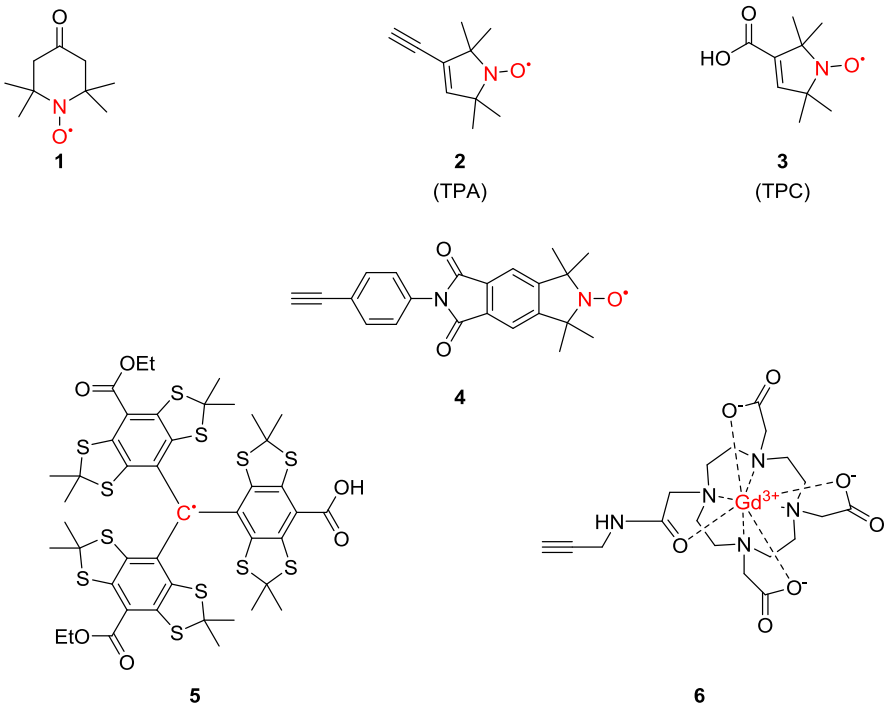

Figure 1.7: Spin labels commonly used for model systems.

Nitroxide radicals based on piperidine, pyrrolidine, pyrroline or imidazoline heterocycles are the most commonly used paramagnetic centres for spin labels,[35b, 38] due to their relative stability to redox reactions and ease of isolation, handling and introduction of different

functionalities. To date, the most commonly used nitroxide-based spin labels for synthesis of pulsed EPR model compounds are the pyrroline-based spin labels **2** and **3**.

These differ only in their functionality: the carboxylic acid in **3** allows its attachment, through esterification, to systems bearing free hydroxyl groups under mild conditions,[39] whereas **2** is commonly cross-coupled to an aryl or vinyl halide under Sonogashira conditions. In principle, the two methods are orthogonal and have proven to efficiently attach the spin label.

Increasing interest for *in vivo* pulsed EPR has recently fuelled the need for more stable spin labels that exhibit extended half-lives under reducing environments and improved stability at temperatures above 50 K. Recently, tetramethylpyrroline-based nitroxides,[40] trityl radicals[41] and Gd(III)-based complexes[42] have been proven to be promising spin labels for in-cell measurements. Trityl and gadolinium-based labels have already been used for labelling complex biological structures and give access to alternative pulsed EPR methods for distance measurements:[7a, 43] trityl-based spin labels allow DQC distance measurements with standard hardware,[41] while Gd(III)-based systems offer increased sensitivity using high-frequency EPR.[36]

When choosing the strategy for spin labelling, another aspect that should to be taken into consideration is the structure of the linking group and the chemistry for its attachment. The intrinsic flexibility of the spin label and conformational flexibility of the linking group can also give rise to the broadening of the distance distribution when measuring inter-spin distances, while the labelling chemistry should be highly selective and occur under mild conditions.[39] Thus, spin labels with a variety of functional groups, for example alkyne (compounds **2**, **4** and **6**) and carboxylic acid (compounds **3** and **5**) have been developed and their behaviour studied when attached to model compounds.

1.5 Model systems

Since the development of pulsed experiments for EPR distance measurements, synthetic efforts have been made to design systems for quantitatively studying parameters affecting distance measurements such as orientation selection, multi-spin effects or exchange couplings. Additionally, model compounds have played a fundamental role in testing the design of EPR experiments and validating their precision and accuracy.[9b, 19d, 38]

Biradical systems, in particular, have been extensively used for calibration of pulsed EPR distance measurements, including dead-time-free PELDOR or DEER,[7a, 14] a single-

frequency technique for refocusing (SIFTER)[44] and DQC,[12a, 45] while multiply labelled systems have been designed for quantifying multi-spin effects.[19a]

The synthesis of biradical and polyradical model systems is commonly approached by spin labelling a spacer or scaffold molecule bearing a specific functionality, such as a hydroxyl or aryl halide, to allow covalent attachment of the appropriate spin label. To fulfil their purpose as benchmarks, model compounds should usually be highly soluble in glass-forming solvents, preferred for distance measurements to reduce sample aggregation, and bear a well-defined structural rigidity. Poly(*para*-phenyleneethynylene)s represent one of the most extensively used scaffolds because of their relative restricted structural and conformational flexibility, which gives access to measurement of well-defined inter-spin distances for two-spin systems on length scales from 1.4 to 8 nm. [20b,18a, 18c, 39b] Examples of model systems also include linear and bent rigid systems, consisting of phenylacetylene or biphenyl units, [18b, 19a, 19b, 39] aliphatic chains[19d, 46] and condensed rings.[20a]

Systems bearing more than two spins, which typically consist of a phenyleneethynylene- or biphenyl-based backbone with up to four nitroxide moieties[19b, 39a], have been designed for quantifying multi-spin effects.[19a] Quantification of multi-spin effects becomes relevant for biological systems such as membrane channel proteins,[47] transport proteins[48] that commonly bear cysteine domains that will covalently bind to the MTSSL label. Furthermore, systems bearing two metal ions as paramagnetic centres[49] or their combination with nitroxide radicals[50] have been used for the optimisation of distance measurements involving these spectroscopically challenging spin centres. Biologically relevant examples include hemes[51] and iron-sulfur clusters.[52] Furthermore, biomaterial-inspired yardsticks such as bis-peptide molecular rods[53] or double-helical DNAs[54] have been reported. However, in the following the focus will be on syntheses and structures of synthetic model systems largely omitting biopolymers.

1.5.1 Biradicals

Most commonly experiments aim to extract a single distance between two electron spins; for this reason biradical model systems with a very narrow distribution of distances between the paramagnetic centres have been used as prototypical model compounds. These represent the most abundantly used model systems for pulsed EPR distances.[18a, 18c] Additionally, biradicals have also played a major role in studying specific properties directly affecting distance measurements; these include increased backbone flexibility,[19d, 46]

ferromagnetic and antiferromagnetic electron-electron exchange couplings[20] and distance measurements in the strong coupling regime.[55]

1.5.1.1 *Nitroxide-Based Biradicals*

One of the first examples of application of biradical model systems was used to study the basic principles of PELDOR distance measurements on the imidazole-based biradical **7** (Figure 1.8).[19d, 56] The same molecule has been used for testing further new experiments such as field-step ELDOR[57] and relaxation-induced dipolar modulation enhancement (RIDME).[58] Field-step ELDOR is an alternative pulsed EPR distance measurement technique; here the requirement of a second frequency source is avoided by switching the magnetic field. However, due to challenging hardware requirements the method is not commonly used. In a RIDME experiment, distance measurement is based on relaxation processes rather than microwave pulses for the inversion of coupled spins. The method has been applied at high field[59] and improved to a dead-time-free variant.[60]

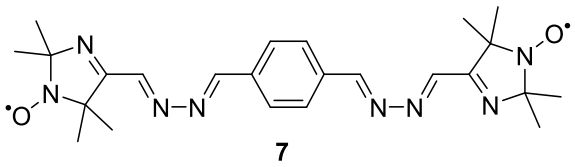

7

Figure 1.8: Imidazole-based biradical.

Imidazole-based nitroxide radicals have been the spin label of choice for the very first model systems for EPR distance measurements.[24] However, these spin labels have been in most cases replaced by pyrroline or piperidine-based nitroxides, such as **2** and **3**.[38] These, as opposed to the imidazole-nitroxide, have the unpaired electron localised on the N-O bond which is advantageous especially for the accuracy of measurements of short radical-radical distances.[39b]

A second example of a model system synthesised for calibration of pulsed EPR distance measurements is the anthraflavic acid-based biradical **8** (Figure 1.9).[17a] Here the spin label **3** was esterified to the anthraflavic acid backbone in the presence of pyridine and thionyl chloride.[61]

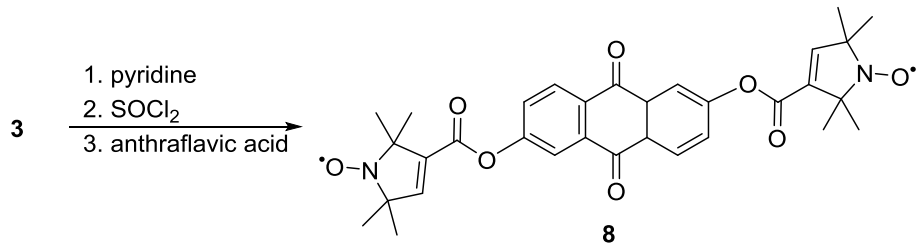

Figure 1.9: Esterification of anthraflavic acid to spin label **3**.

The PELDOR traces obtained from **8** are among the first to show an electron-electron dipolar modulation and gave direct access to the size of the dipolar coupling, thus inter-spin distance. In addition, the same model system was used for the first systematic consideration of orientation selection effects in PELDOR experiments. Orientation selection effects were studied by looking at a number of independent spectral positions.[17a, 62] The distance and geometry deduced from pulsed EPR were found to be in excellent agreement with a planar structural model.

The flexible systems **9**–**12** with increasing numbers of methylene units (Figure 1.10) were employed for studying conformational statistics and the resulting distributions of end-to-end distances by using the rigid biradical **8** as a reference for end-to-end distances and for determination of optimal experimental parameters.[46] The experiments proved the reliability of pulsed EPR methods for the extraction of distances in systems with large backbone flexibility.

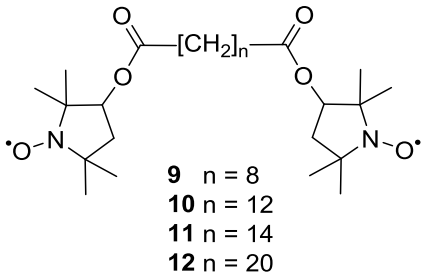

Figure 1.10: Structure of flexible biradical systems.

Scheme 1.1 reports representatives of an early, modular approach to the synthesis of biradicals as model systems for pulsed EPR distance measurements.[14] The systems were modelled to have different spin-spin distances of 1.4, 1.7, 1.9, 2.4 and 2.8 nm respectively, and are sufficiently rigid to allow extraction of narrow distance distributions. The convergent synthetic protocol entails of a *n*-BuLi and LiBr-mediated reactions of 4-

TEMPONE **1** with spacer building blocks bearing two terminal alkynes to give access to biradicals **13** and **14**. The same reaction also yielded the corresponding singly-labelled building blocks that were then dimerised *via* oxidative Hay coupling[63] to the give biradicals **15** and **16**. Compound **17** could be obtained by reaction of **1** with triisopropylsilylethyne in presence of *n*-BuLi and subsequent deprotection. Biradical **18** was obtained from the dimerization of **17**.

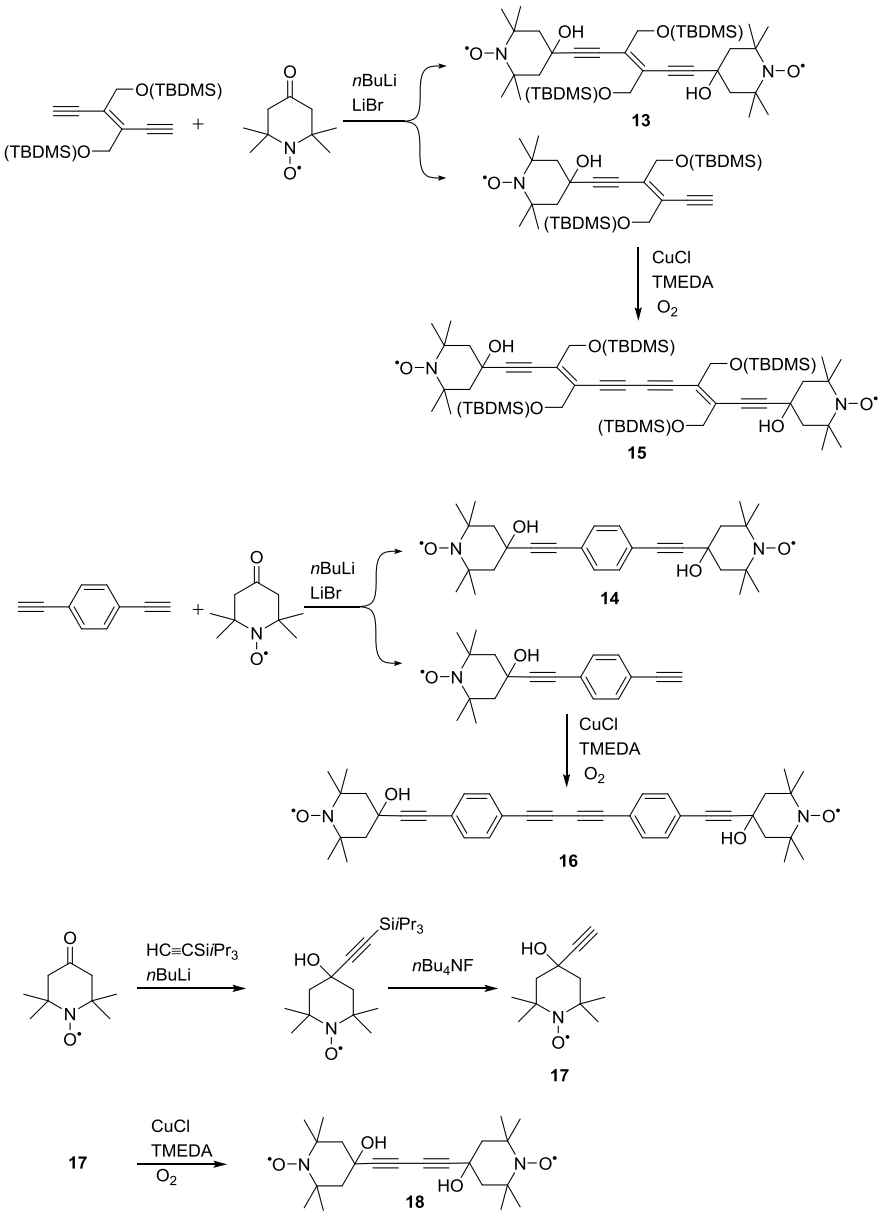

TMEDA: N,N,N',N'-tetramethylethylenediamine, TBDMS= tert-butyldimethylsilyl.

Scheme 1.1: Convergent synthesis of a series of biradical model systems.[14]

Distance measurements on these systems allowed to achieve two important advances in pulsed EPR: they demonstrated the accuracy of pulsed distance measurements with the use of the first series of biradicals with well-defined end-to-end distances. The measured distances were found to be in agreement, within 0.2 nm error, with the ones modelled by molecular dynamics. Additionally, measurements on model systems **14**, **16** and **19** (Scheme 1.2) were used to optimise and calibrate the extension of the original four-pulse experiment[14] to the asymmetric four-pulse dead-time-free sequence.[7a] The newly reported rigid biradical **19** was synthesised from a terminally hydroxylated poly(phenyleneethynylene) backbone **20** that was esterified to two equivalents of **3**. The reaction for attachment of the spin label using oxalyl chloride and pyridine, proceeds *via* the intermediate formation of the acyl chloride, thus facilitating the formation of the diester. The authors chose pyrroline-based **3** as spin-bearing group rather than the previously reported six-membered piperidine-based nitroxides, as it exhibits reduced flexibility and its carboxylic acid function allows formation of ester linkages. [7a]

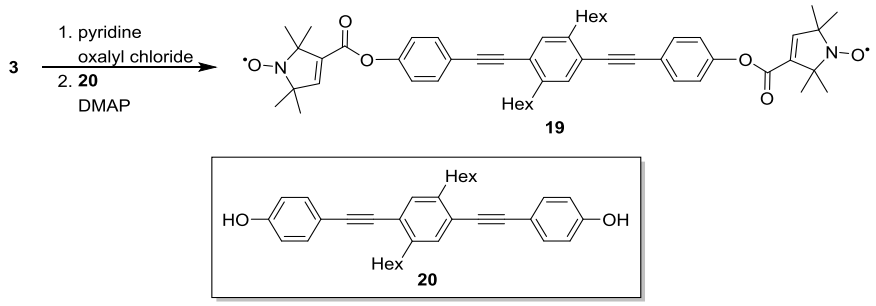

Hex: *n*-hexyl (C_6H_{13})

Scheme 1.2: Synthetic path for synthesis of **19** using oxalyl chloride and pyridine.

To streamline the synthesis of a series of biradical yardsticks a convenient route for accessing linear biradicals with inter-spin distances from 2.8 to 5.2 nm, as well as for generating a star-shaped three spin abacus, was later reported.[39b] The rod-like biradicals **19**, **21** and **22** bear poly(phenyleneethynylene) spacers synthesized by Sonogashira cross-couplings of substituted iodo- or diiodo-benzenes with a terminal alkyne building block bearing a tetrahydropyranyl (THP) protected phenol, such as **23**.

Building blocks of different lengths, such as **24** and **25**, were generated *via* addition of further segments by Sonogashira couplings. The free phenols could be isolated after

removal of the THP protective group. The spin label of choice, **2**, was then attached to the phenols *via* Steglich esterification (Scheme 1.3). [64] The same route has been used for the introduction of ^{2}H and/or ^{15}N-labelled **3**.[65]

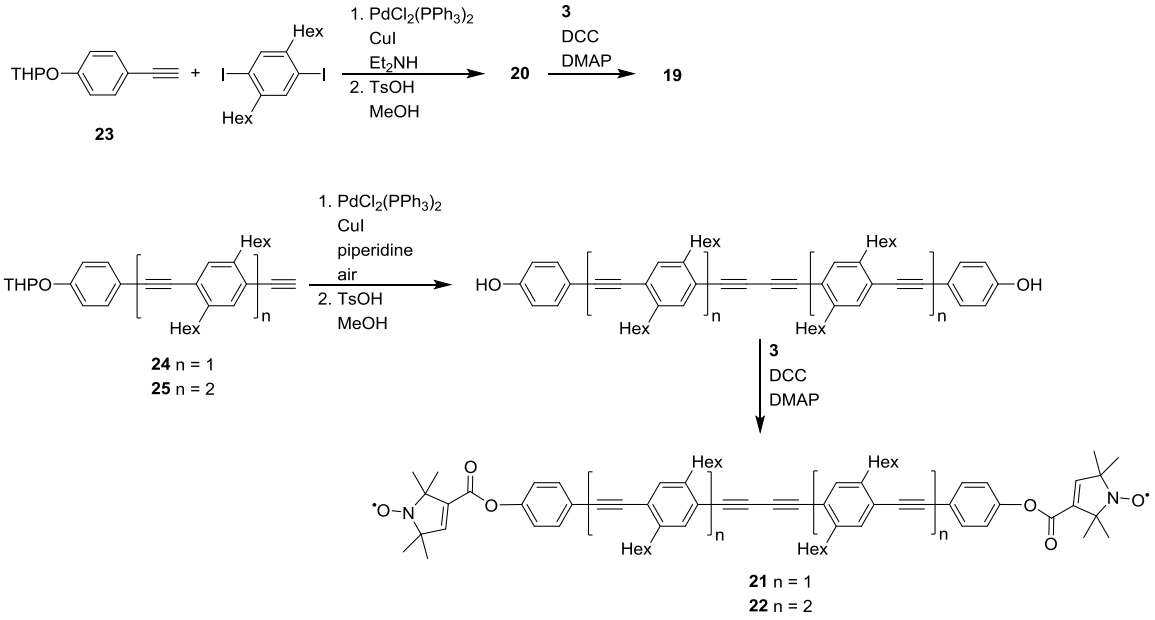

DCC: dicyclohexylcarbodiimide; DMAP: N,N-dimethylaminopyridine

Scheme 1.3: Synthesis of biradical model systems based on poly(phenyleneethynylene) backbones.

Poly(*para*-phenyleneethynylene)-based building blocks were also used for the synthesis of molecular rods with increasing lengths.[18c] The synthesis that yielded **21** and **22**[39b] was expanded to compounds **26** and **27** (Figure 1.11) giving access to a series of yardsticks with inter-spin distances of up to 7.5 nm.

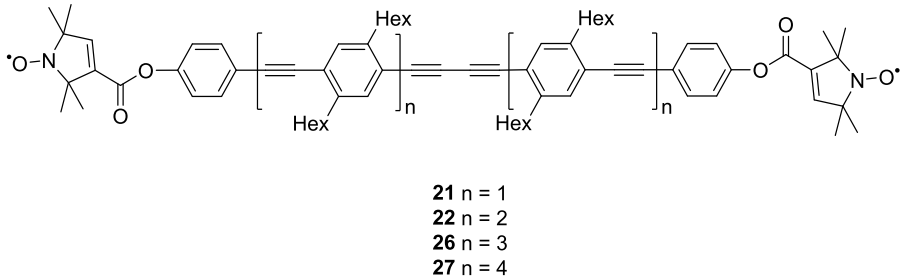

Figure 1.11: Poly(phenyleneethynylene)-based biradical yardsticks.

PELDOR distance measurements on **19**, **21**, **22**, **26** and **27** proved that the intrinsic flexibility of functional nanostructures bearing poly(*para*-phenyleneethynylene)-backbones could be accurately quantified using pulsed EPR methods. This could be achieved through the separation of the contribution of the rotational motion of the spin labels to the distance distributions.[18c] The same compounds have also been used to validate approaches for data processing [29-30, 66] and to test new experimental schemes as a variable-time variant of PELDOR/DEER.[67] The sensitivity enhancement achieved through this experimental set up allowed precise measurement of the 7.5 nm distance in **27**. However, this method is less robust and not recommended for protein samples due to the background function not necessarily being a smoothly decaying function, a behaviour that has been found to compromise the reliability of the separation of the dipolar coupling signal from the background function.[68] Additionally **19**, **21** and **22** have been used for the validation of the single-frequency technique for refocusing (SIFTER) dipolar couplings experiment.[44]

PELDOR measurements have also been used to study the dependence of backbone flexibility on temperature and structure. To this end, a series of oligo(*para*-phenylenebutadiynylene)- (**28**–**30**) and oligo(*para*-phenyleneethynylene)-based (**31**–**38**) biradicals with varying inter-spin distances were synthesised using similar synthetic strategies to those previously reported.[18c, 39b, 69] Additionally, variation in the model systems' structures has also been introduced by alternating **3** with conformationally unambiguous spin label **4**,[18a, 69] as reported in Figure 1.12. Because of the axiality of **4** the rotation of the label does not affect the width of the distance distributions. The authors emphasised the importance of choice of alkyl or ether linkages as side chains as they allow chromatographic separation of unwanted homo-coupled products, common side-products of Sonogashira cross-coupling reactions, and desired cross-coupled products by exploiting their difference in polarity. [18a]

The determination of the conformational flexibility of the model systems could be refined to higher accuracy by combining simulations and experimental data. Additionally, the variation of the spin label allowed the accurate estimation of the separate contributions from the spacer and label. Furthermore, the temperature dependence was investigated through the glass transition temperatures of the matrices used during measurements. As expected, the solvents with higher glass transition temperatures resulted in reductions in the mean distances and broader distance distributions, as indicated by the increased damping of dipolar oscillations.[18a]

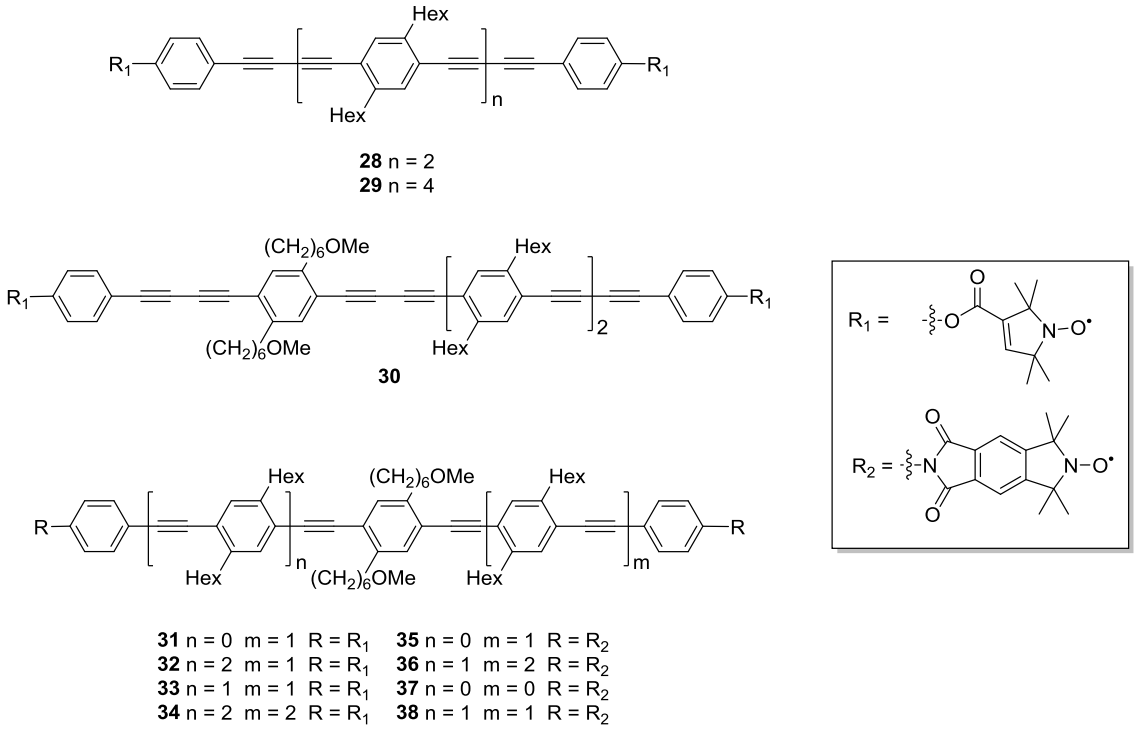

Figure 1.12: Oligo(*para*-phenyleneethynylene)- and oligo(*para*phenylenebutadiynylene)-based biradical yardsticks.

Biradical model systems based on phenylenes and ethynylenes were also used to determine flexibilities of the bent **39** and the linear **40** systems, reported in Figure 1.13,[18b] by studying the orientational correlations between the nitroxides and distance vector. These correlations can be studied by changing the spectral position of detection and pump pulses giving access to selective excitation of different subensembles of spins with specific molecular orientations in respect to B_0.[17a]

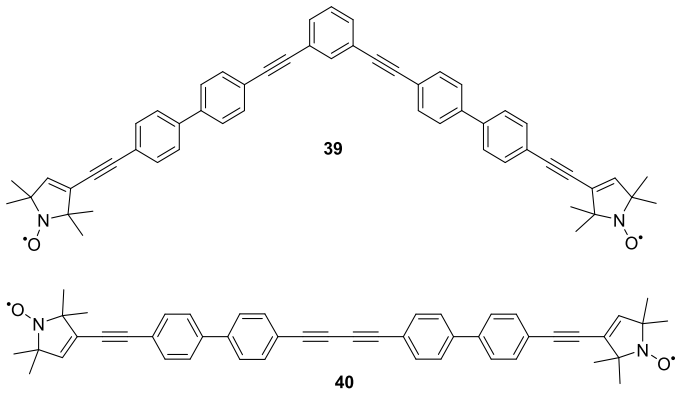

Figure 1.13: One linear and one bent biradical.

Analysis of orientation-selective X-band PELDOR traces gave access to an estimation of the conformational distribution of the molecules.[18b] The same concept was later employed to determine the dominant dynamic mode for double-helical DNA.[70] **40** has also been used for calibration of a wide variety of experiments and data analysis approaches including the extraction of orientations,[17b] library approaches,[71] out-of-phase PELDOR[72] or broadband inversion in PELDOR.[73]

Electron-electron exchange couplings have also been quantified using the combination of model systems and PELDOR distance measurements, as they can modify the frequency of the spin-spin coupling and, thus, affect distance measurements. This effect was the focus of a specific study that reported the synthesis, shown in Scheme 1.4, and analysis by PELDOR distance measurements of biradicals **41**–**44**.[20b] Compounds **41** and **42** have similar inter-spin distances dictated by the presence of a single phenyl ring spacer. Similarly **43** and **44** have two phenyl rings as spacers. The only difference within these pairs of systems is the spin label attached to the backbone: **2** in **41** and **43** or **3** in **42** and **44**. Due to their different functionalities, attachment of the two spin labels required different conditions, as previously discussed in Section 1.4.1.

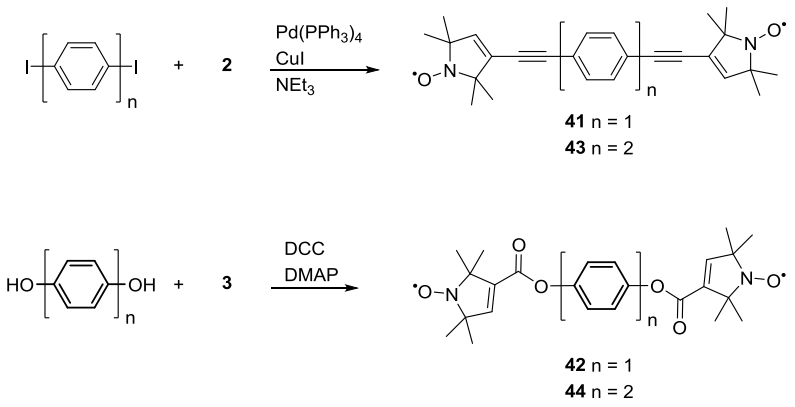

Scheme 1.4: Synthesis of biradical model systems with variable spacer length and conjugation.

The presence of ester bonds in **42** and **44** was expected to diminish the through-bond coupling; for this reason they were used as a reference for 'zero exchange coupling systems'. The linkages *via* ethynylene-groups in **41** and **43**, instead, give rise to a through-bond electron-electron exchange coupling between the radicals.[56] Distance measurements performed at S- and X-band frequencies (3 and 9 GHz, respectively) allowed for the exclusion of any hyperfine coupling contribution to the signal.[20a] Separation of the through-space dipole-dipole coupling from the through-bond exchange coupling was achieved by

performing orientation selection measurements based on the anisotropic nitrogen hyperfine interaction.[20b] The effects of electron-electron exchange coupling have also been studied in bis-nitroxides composed of annulated rings.[20a] The condensed structures of the model systems **45**, **46** and **47**, reported in Scheme 1.5, diminish rotational freedom of the nitroxides inducing very strong and easily resolved orientational correlations. Additionally, as for **41** and **43**, the full conjugation between the five-membered rings of the nitroxides gives rise to a non-vanishing electron-electron exchange coupling.

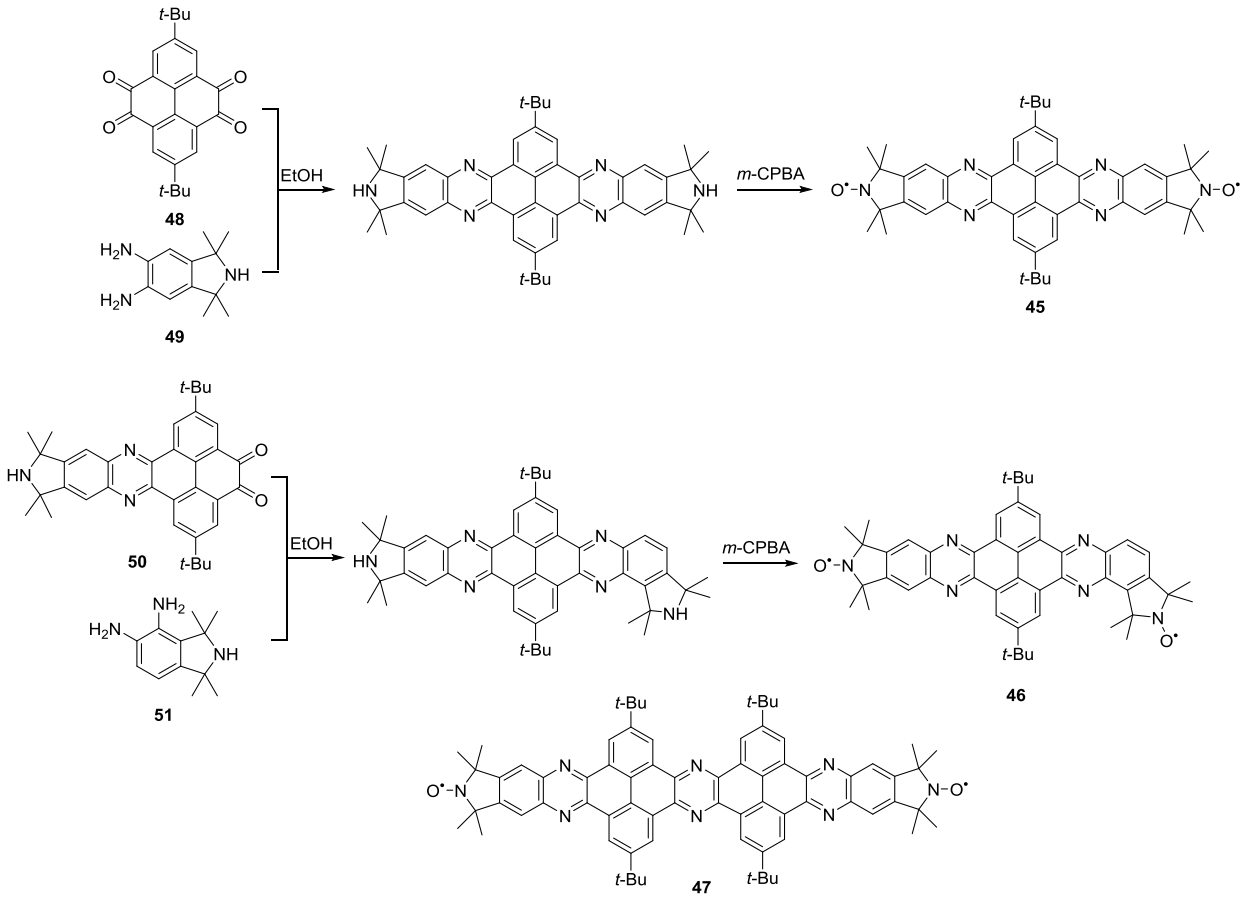

Scheme 1.5: Synthesis of rigid biradicals with different substitution patterns.

Fixing the relative orientations of the nitroxides in the model systems gave access to the extraction of both ferromagnetic and antiferromagnetic exchange couplings. The pyrroline precursors of the nitroxides were attached to the conjugated system using two different substitution patterns that gave rise to ferro- and antiferromagnetic interactions. The synthetic strategy is based on condensation between **48** and **49**, followed by generation of the nitroxide radical using *meta*-chloroperoxybenzoic acid (*m*-CPBA) to give the target molecule **45**. A similar approach was used for the synthesis of **46** for which **50** and **51** were

used as alternative starting materials leading to a different geometry and, thus, a different relative orientation of nitroxides. Additionally, the earlier reported **47** was used as reference for orientation selection in rigidly labelled DNAs.[74] The combination of simulations and experimental EPR distance data allowed the separation of the exchange and dipolar couplings. Angular correlations from compounds **45** and **46** could be extracted from distance measurements performed at W-band (95 GHz).[75]

Biradical model systems have also been used to optimise DQC experiments. This technique uses a single frequency pulse train to generate a double quantum coherence filter allowing isolation of the dipolar couplings.[76] An example of application of model systems for calibration of other pulsed EPR techniques is **52** (Figure 1.14). This model system was used to design an experiment for suppression of electron-nuclear effects when performing the single-frequency six-pulse experiment in protonated matrices.[77]

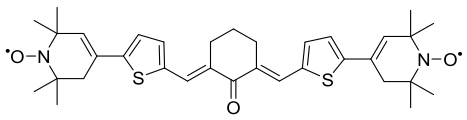

52

Figure 1.14: Structure of biradical used for calibration of DQC experiments.

1.5.1.2 *Trityl-Based Biradicals*

DQC[12b] represents an alternative pulsed EPR method for extraction of nanometre distances. This technique has been found to be more sensitive than PELDOR measurements, however DQC requires excitation of the full EPR spectrum, which is very challenging for standard hardware in the case of nitroxides, which usually present a field sweep 8 mT wide compared to the 0. 6 mT for the trityl radicals when measured at X-band frequencies. The comparatively narrow trityl EPR line is related to their vanishing *g*-anisotropy and small hyperfine couplings to abundant isotopes. Trityl radicals have recently been considered as alternative spin labels as they give access to measurements in biological systems at room temperature[43] and present a superior stability under in-cell reducing conditions compared to nitroxide radicals.[41]

As for PELDOR experiments, model systems have been synthesised for the optimisation of DQC measurements. Compound **53** is a trityl biradical and **54** exhibits one trityl and one nitroxide radical (Scheme 1.6).[41] Compound **53** was obtained by esterifying the dimer of **55** to two equivalents of trityl radical **5** using benzotriazol-1-

yloxytris(dimethylamino)phosphonium hexa-fluorophosphate (BOP) and 1-hydroxybenzotriazole (HOBT) as activating agents. **54** was obtained by cross-coupling **55** to **56** followed by esterification of the cross-coupling product to the trityl spin label **5**. The ether-linked alkyl side-chains present on the rod-like spacers, composed of a series of acetylene and phenylene units, help to improve solubility. The model systems were designed to have well-defined inter-spin distances of 3.5 (compound **53**) and 5 nm (compound **54**) well within the range of distances measured in biological systems.

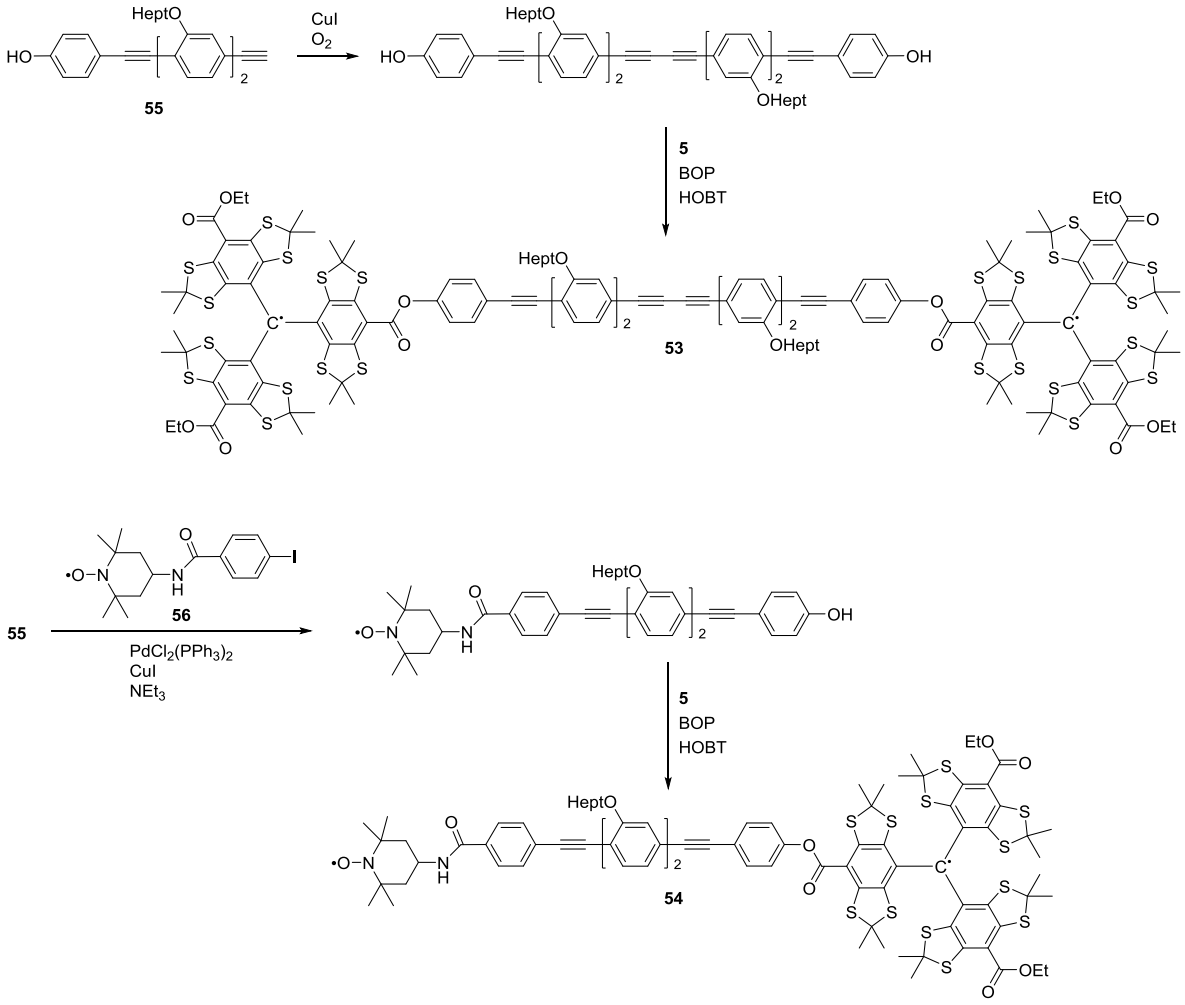

Scheme 1.6: Trityl-trityl and trityl-nitroxide model systems.

The same authors extended the series with two further bis-trityl systems, **57** and **58**, and one trityl-nitroxide biradical **59** (Scheme 1.7).[55] Cross-couplings were performed in presence of both free and THP-protected phenols. As opposed to the first **53** and **54**,[41] the trityl radicals in **57**, **58** and **59** were generated by reaction with trifluoroacetic acid after esterification of the trityl precursor (RH in Scheme 1.7). DQC distance measurements on the model systems proved that trityl-trityl inter-spin distances could be accurately extracted.

The mean inter-spin distances were obtained by taking into account the pseudo-secular part of the dipolar coupling, required when within the strong-coupling regime, and spin delocalisation of the trityl radical. Using this alternative approach the mean distances were measured to be 1.5 nm in **57**, 2.2 nm in **58** and 2.4 nm in **59**.[55] Overall, these studies demonstrated the potential of DQC distance measurements for systems of unknown structure using commercial pulsed X-band EPR hardware.[41, 55]

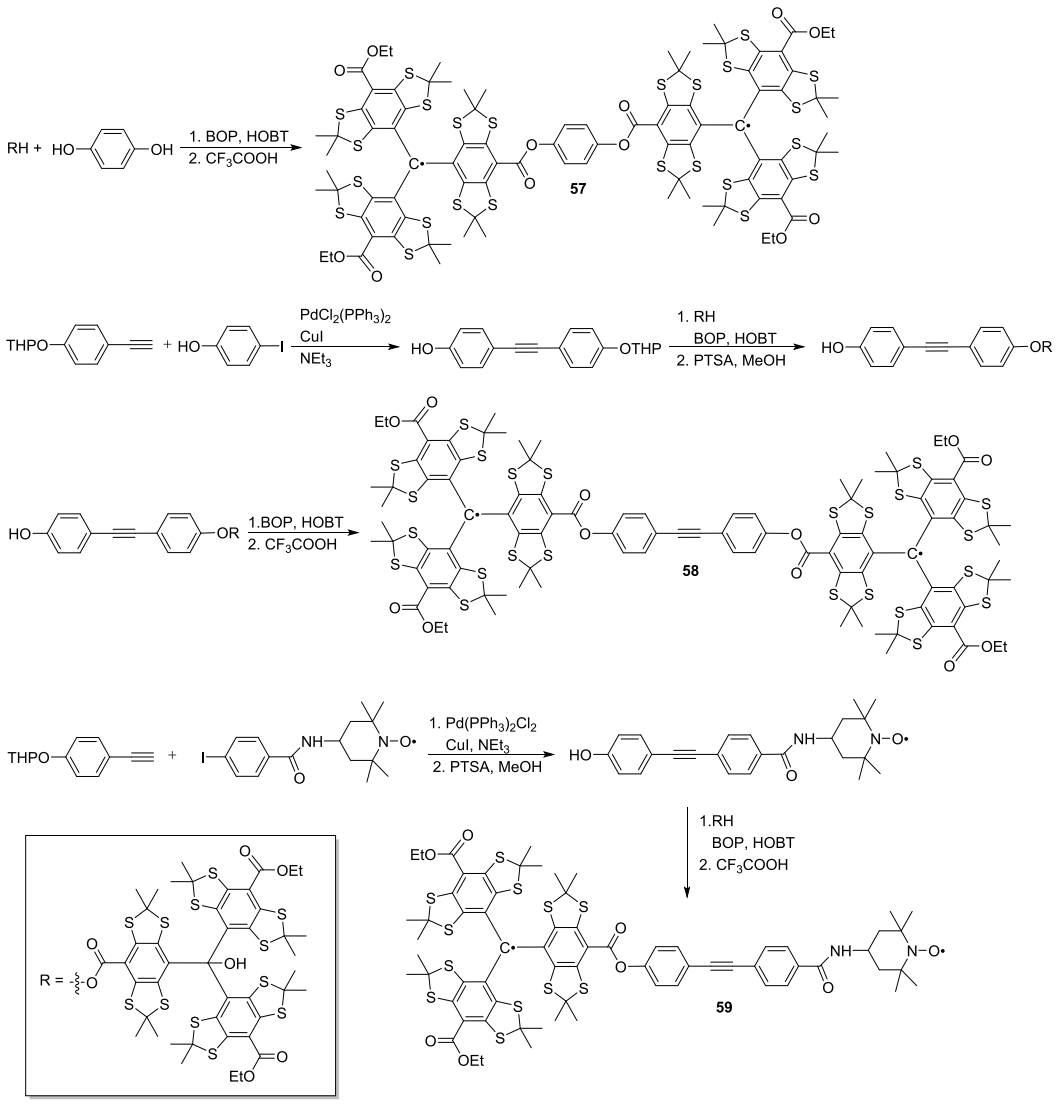

Scheme 1.7: Synthesis of shorter distance trityl-trityl and trityl-nitroxide model systems.

1.5.2 Polyradicals

Polyradical model systems have been developed mainly for two purposes: firstly for proving the concept of 'PELDOR spin counting'[19b-d] and secondly, for quantifying, and potentially suppressing, multi-spin contributions to the dipolar coupling.[19a, 78] Spin counting allows the number of interacting monomers in an oligomer to be determined, while multi-spin effects can complicate distance data analysis in systems with more than two unpaired electron spins.

For multi-spin model systems, the design of rigid spacers is often similar to those of yard-sticks. As for biradicals, multi-spin systems are commonly based on phenylene and ethynylene backbones bearing terminal functionalities allowing for attachment of spin labels such as **2**,[19b] **3**[39] or **4**.[69] In order to uniquely identify multi-spin effects, biradicals bearing the same general architecture are often employed as reference molecules.[18b, 19a] Thus, the additional contributions present in the multi-spin systems distance data, when compared to the results obtained for constituent biradicals, can be identified. One of the first syntheses of a series of polyradical model systems involved phenylene-based spacers bearing halogenated functional groups for the attachment of spin label **2**. The synthesis of polyradicals **60**, **61** and **62**, reported in Scheme 1.8, is based on cross-coupling of the spin labelled spacer **63** with aryl halides **64**, 1,3,5-triiodobenzene or 1,2,4,5-tetraiodobenzene using a convergent reaction scheme based on Sonogashira cross-couplings. **60**, **61** and **62** have well-defined inter-spin distances ranging between 2.2 and 3.8 nm and bear geometries that mimic aggregation states of biological complexes.[19b]

The bent biradical **39** (constituent biradical of **61**) is the product of the cross-coupling between 1,3-diethynylbenzene and **65**. **40**, instead, is a side product of the competing Glaser reaction of **63** during cross-couplings with aryl halides. The systems have been used to scrutinise a PELDOR-based method for spin-counting the number of interacting monomers and test its accuracy and limitations.[19b] Additionally, their restricted flexibility allowed quantitative distance measurements including the first resolution of three distances within a single molecule where two distances differed by less than 0.5 nm in **62**.[19b]

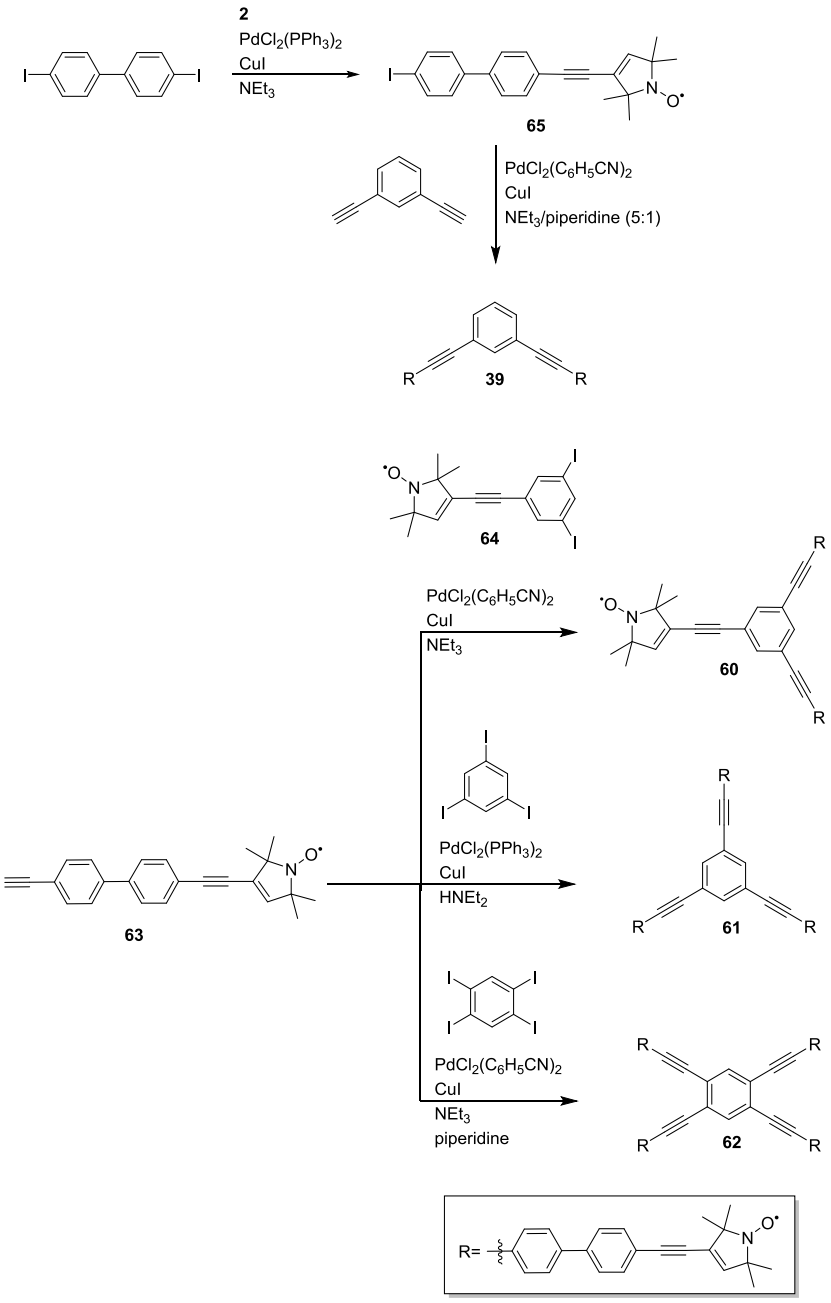

Scheme 1.8: Convergent synthesis of two triradicals and a tetraradical.

A series of multi-spin model systems **66**–**70** (Figure 1.15) were used for the isolation of the spin-pair contribution from the multi-spin PELDOR signal. The synthetic strategy is similar to the one previously reported,[39b] with the exception that either **3** or **4** are used as alternative spin labels.

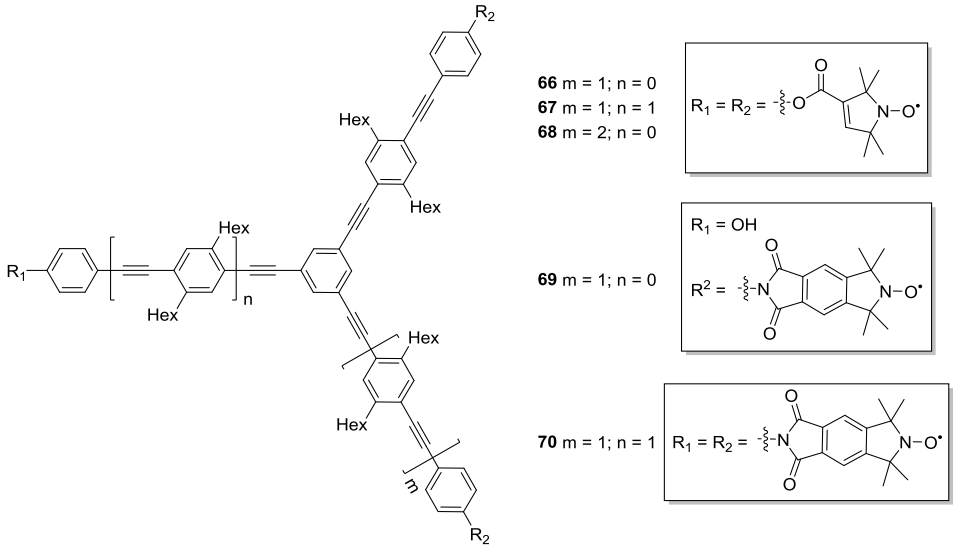

Figure 1.15: Multi -spin systems with different symmetries.

Compounds **21** and **67** have been measured at both X- and W-band to quantify, together with modelling based simple geometric models, the orientation selection effects on distance measurements in both bi- and tri-radicals.[19a, 79] The mutual orientations and their dynamics could be predicted from geometric models and verified by orientation selective PELDOR experiments. Measurements on **38** and **69** allowed calibration of orientation selection experiments at Q-band (34 GHz) frequencies.[80]

1.5.3 Metal Ions

A significant number of biological systems bear catalytically-active or structurally-relevant metal centres. These metal centres are frequently paramagnetic in one or more functional states of the biological system, or can often be substituted by a paramagnetic one.[81] Native metal ion-binding sites in biological systems are an interesting target for distance measurements. PELDOR, in particular, has proven to be an accurate tool for the measurement of distances not only between nitroxides,[68] but also between paramagnetic metal centres[51-52, 82] and paramagnetic cofactors.[62] Systems containing a single paramagnetic metal centre require the presence of at least one further spin centre for inter-spin distance measurements, which is commonly introduced by SDSL using nitroxide radicals.[51] Model systems have been synthesised to test the potential of pulsed EPR distance measurements in systems containing metal centres. PELDOR distance measurements have been found to be challenging due to their fast relaxation, broad EPR spectra, pronounced

anisotropies and strong ESEEM effects.[36] The design of model systems incorporating metal centres commonly involves the synthesis of a chelating ligand, often bearing a rod-like spacer, which is attached to a second ligand or a stable radical, followed by coordination to one or more metal centres. In contrast to some cases involving nitroxide spin labelling, the paramagnet is most commonly introduced into the ligand as the very last step. This is often performed by dissolving the salt containing the metal ion in water and suspending the ligand in this solution. Distance measurements involving copper(II)-nitroxide,[50b] copper(II)-copper(II),[81b] gadolinium(III)-gadolinium(III),[49b, 83] cobalt(II)-nitroxide[73] pairs and iron-sulfur clusters and nickel-iron centre pairs[52] have been reported.

One of the first studies performed on metal-nitroxide model system **71** proved that contribution of the Cu(II)-nitroxide coupling could be separated from the nitroxide-nitroxide coupling in the three-spin system, given in Scheme 1.9.[50b] The model system was synthesised by esterifying a rigid terpyridine spacer-ligand to spin label **3** to yield the spin labelled terpyridine-ligand **72**. Two equivalents of this ligand were coordinated to Cu(II) ions. This design yielded **71** which exhibits a well-defined coordination geometry around the Cu(II) centre.

The combination of density functional theory (DFT) calculations and force-field structures allowed an accurate estimation of the distance between the paramagnetic centres.[50b] The nitroxide-nitroxide distance was isolated by choosing frequencies coinciding with the nitroxide spectrum while the Cu(II)-nitroxide distance could be measured by changing one frequency to make it exclusively excite the spins on Cu(II). This was an early experiment to address specific distances between different spin centres by spectral selection.[50b]

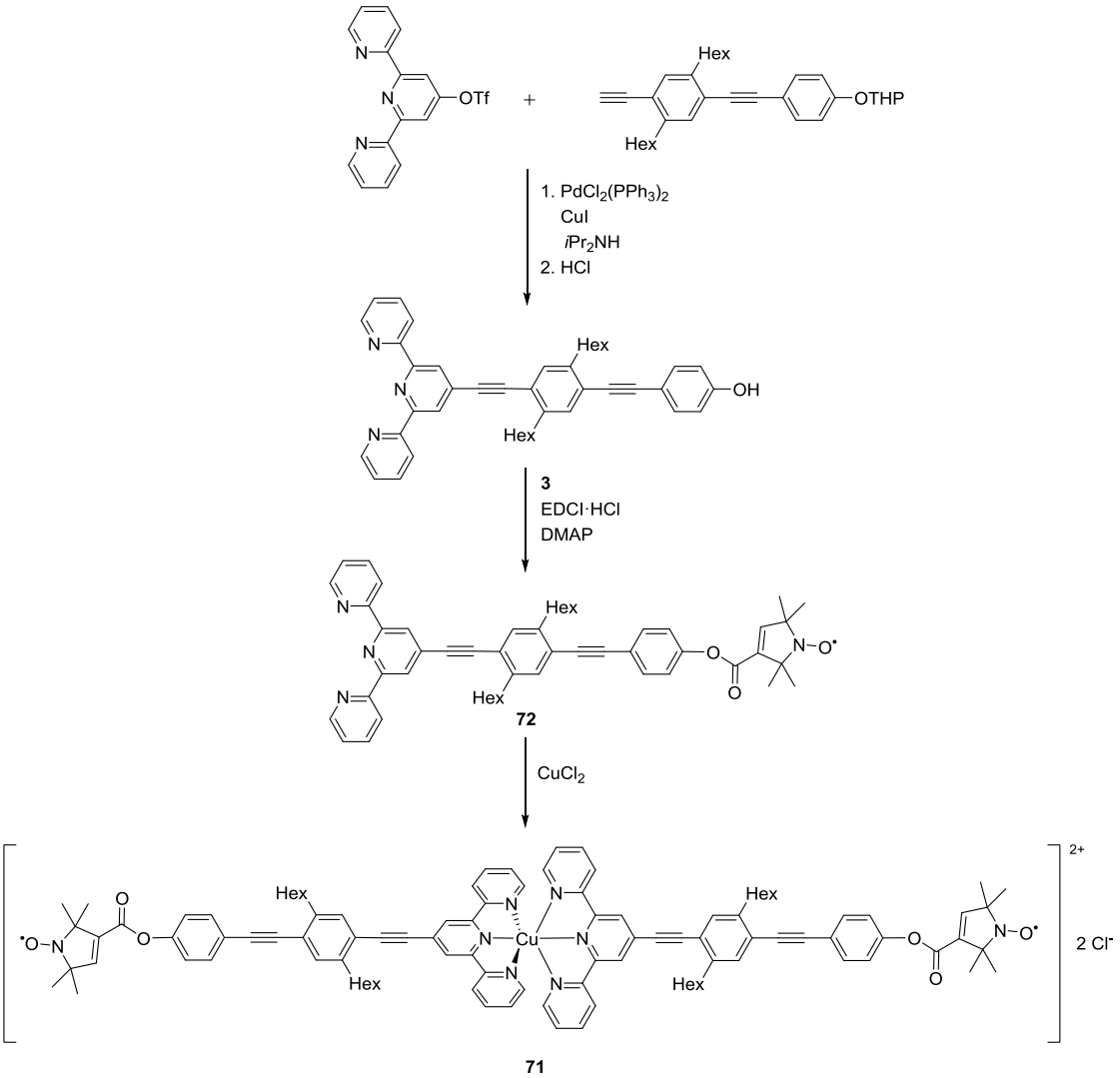

Scheme 1.9: Synthesis of a rigid Cu(II) bisnitroxide system.

The metal-nitroxide biradical **73** (Scheme 1.10) was synthesised to evaluate the achievable accuracy of distance measurements between the two different paramagnetic centres.[50a] This study also gave access to quantification of additional effects such as orientation selection, conformational flexibility and spin density distribution. The porphyrin moiety mimics the binding motives found in biological systems and introduces a moderate delocalisation of spin density from the metal onto the ligand. The synthesis of the model system (Scheme 1.10) involved Steglich esterification of 4-hydroxy-4′-iodobiphenyl **74** to **3** to form **75** and subsequent Sonogashira cross-coupling to an alkyne functionalized Cu(II)-octaethylporphyrin **76**. The alkyne functionality was introduced by a sequence of formylation of Ni(II)-octethylporphyrin, Wittig reaction to form the *meso*-chlorovinyl-porphyrin, metal exchange *via* the free base porphyrin and elimination of hydrochloric acid.

Separation of the electron-electron exchange coupling from the dipolar coupling could be achieved by the combination of simulation and experimental measurements. The study proved that Cu(II)-nitroxide distance measurements are also feasible in the presence of small through-bond exchange couplings.[50a]

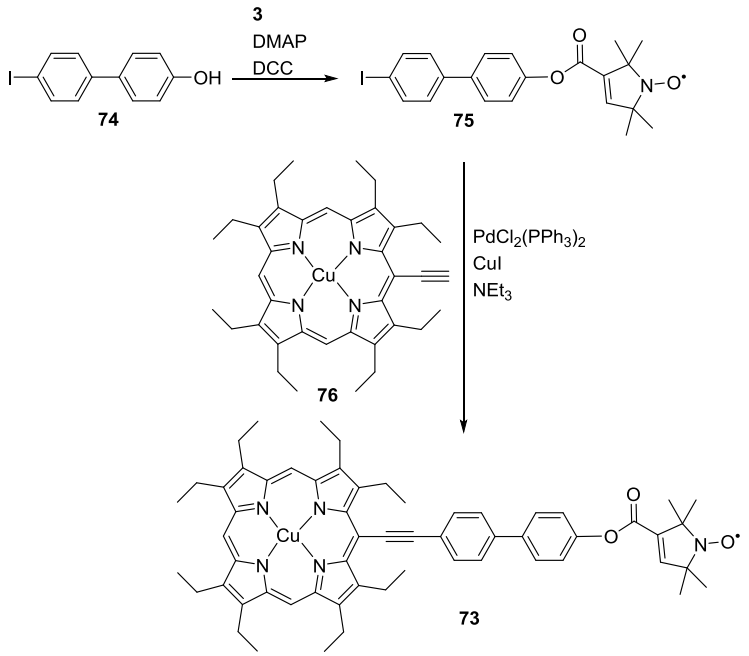

Scheme 1.10: Synthesis of Cu-nitroxide 'yardstick'.

The similar system **77** was used for isolation of electron-electron exchange coupling from distance measurements between a metal and a nitroxide-based paramagnetic centres.[84] The system has identical structure as **73**, except for introduction of **2** as spin label introducing a second alkyne bond. This creates a conjugated bridge that would be expected to induce an increase in *J*.[84] The synthetic path based on coupling between **65** and **76**, reported in Scheme 1.11, is similar to that reported for **73**.

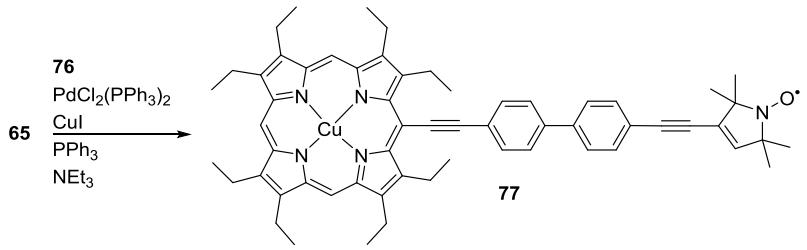

Scheme 1.11: Synthesis of Cu and Ni-based models with **2** used as spin label to introduce *J* coupling.

The dipolar oscillations were much more strongly damped for **77** than those for **73**, in which the conjugation is disrupted by the ester linkage. This damping could be quantitatively attributed to a significant electron-electron exchange coupling, which was confirmed by simulations. The extracted Cu-NO distance of 2.1 nm was also validated against crystallographic data obtained on the structurally homologous Ni(II) compound. [84]

With the continuous development of hardware and techniques for pulsed EPR methods, measurements can now be routinely performed on W- and Q-band frequencies. Measurements at Q-band frequencies have been found to improve sensitivity more than tenfold, allow for lower sample concentrations, and offer greatly reduced measuring times when compared to X-band.[85] The improvement in sensitivity is related to the increase in difference in the Boltzmann population between the spin states and in Zeeman energy, which increases by a factor of four and the increase in detection frequency by equally a factor of four.[85] Nitroxide radicals are not the ideal spin labels for high field measurements (W-band) as their spectral width increases with magnetic field.[36] Thus, the proportion of spins excited by the microwave pulses, and consequently the signal, commonly reduces with increasing magnetic field. The spectral width of Gd(III) ions, on the other hand, decreases with increasing magnetic field, thus they provide a feasible alternative for performing distance measurements at W- and Q-band. Model systems bearing novel Gd(III) ions based spin labels have been recently designed to test the potential of these metal centres for distance measurements. [36, 49b] These have also been successfully used extraction of inter-spin distances in biological systems at W and Q-band frequencies.[47c, 86]

To study the potential of Gd(III)-based spin labelling, high-field distance measurements have been performed on model system **78**. The model system is synthesised *via* Sonogashira cross-coupling of a 1,4-diethynylbenzene to two equivalents of pyridine-based chelator **79**.[49b] Hydrolysis followed by coordination to Gd(III) gives the wanted bis-gadolinium system **78** (Scheme 1.12).

This work demonstrated the potential for gadolinium as an alternative spin label to nitroxide radicals to perform distance measurements at high field, as they provide high sensitivity and present minor orientation selection effects.

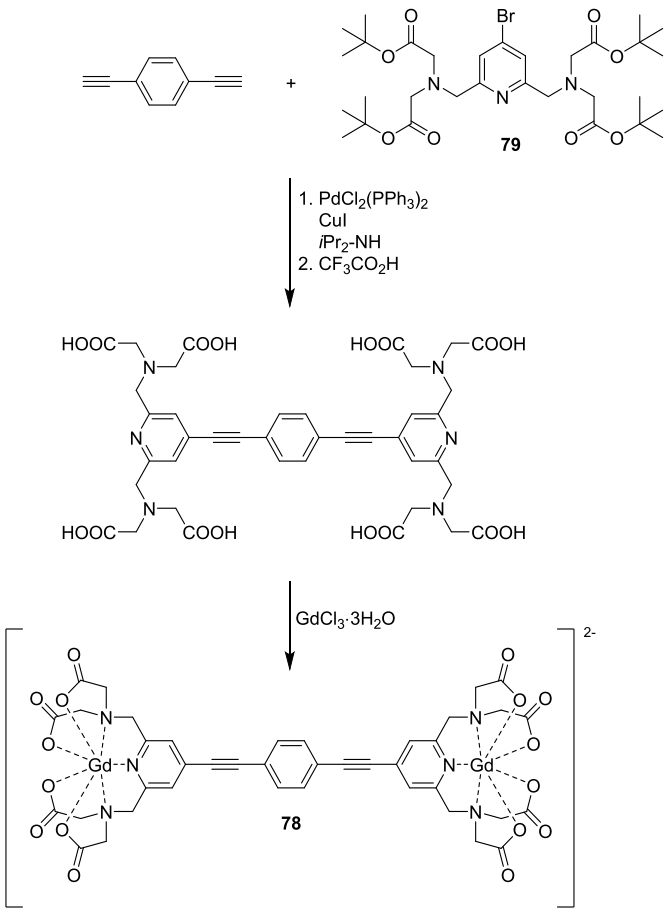

Scheme 1.12: Synthesis of rigid bis-Gd(III) model complex.

Another example of Gd(III)-Gd(III) distance measurements has been reported for model system **80** (Figure 1.16).[49a] The use of the flexible bridge was seen as an appropriate reference for biological systems. Flexible systems are considered to be challenging for distance measurements as their distance can be broadly distributed and the corresponding dipolar oscillations will be fully damped in the primary data.

The magnetic properties of Gd(III) should in principle allow measurement of longer PELDOR distances between Gd(III) ions than between nitroxides. This is due to combination of two factors: their short longitudinal relaxation times, allowing for more signal averaging over the same period of time, and long transversal time which allows a slower decay of the signal over time.[87]

Gd(III) was shown to be complementary to established nitroxide radicals for distance determination in rigid and flexible systems.[49a] Gd(III)-nitroxide distance measurements were first performed employing **72** ligated to the metal ion.[88]

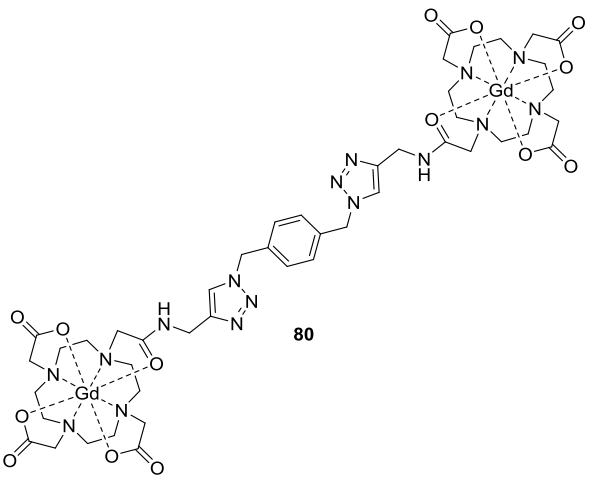

Figure 1.16: Flexible bis-radical based on Gd(III) paramagnetic centres.

1.6 PELDOR measurements in multi-spin systems

Distance measurements using PELDOR have been proven accurate and reliable when extracting inter-spin distances from a dipolar coupling between two interacting spins.[9, 19a, 78b] Recently there has been growing interest in large protein and nucleic acid complexes composed of two or more monomers because of their important biological activities. Examples include membrane proteins,[47c] membrane channel proteins [47a, 47b, 89] and ion channels,[90] DNA[25, 70, 91] and RNA.[28, 31] This same method, however, does not always give access to accurate extraction of inter-spin distances when measuring complexes bearing more than two paramagnetic centres.[19a, 78a, 89] This has been found to be related to the so called multi-spin effects. These are introduced when more than one dipolar coupling is excited by the pulse sequence used for measurement of inter-spin distances. In a two spin system a single dipolar frequency is isolated by flipping of the B spins by the pump pulse. All other interactions are refocused by the echo sequence.[9a] The same experiment when performed on systems bearing more than two spin labels leads to excitation of multiple dipolar couplings. The resulting signal contains a combination of two or more dipolar frequencies that complicates extraction of inter-spin distances.[19a, 19b, 78b]

In a biradical system the PELDOR signal, once inter-molecular interactions are excluded by background correction, for a two spin system can be described by Equation 1.6:[92]

$$V(t)_{intra} = V_0\left[(1 - \lambda_B(1 - cos\omega_{AB}t)\right] \quad (1.6)$$

where

$$\omega_{AB} = \omega_{dd} + 2\pi J_{AB}$$

and

$$\omega_{dd} = \frac{\mu_0 \hbar}{4\pi} \frac{\gamma_A \gamma_B}{r^3_{AB}} (1 - 3cos^2\theta)$$

where V_0 is the echo intensity at t=0, ω_{AB} is the dipolar frequency between spins A and B, λ_B is the fraction of B spins coupled to detected A and excited by the pump pulse and J_{AB} is the through bond exchange coupling.

The fraction of pumped spins depends on the pump pulse the flip angle, excitation bandwidth, frequency and on the EPR spectrum. Additionally, presence of orientation effects may affect the overall efficiency of the pump pulse.[78a] For a typical pump pulse

with a flip angle $\beta = \pi$, when applied to the maximum of the EPR absorption spectrum of a nitroxide at X-band, λ varies between 0.3 and 0.5 for pulse lengths of 12/20/32 ns.[19a] In a biradical the modulation depth Δ of the signal equals the probability of flipping the B spins by the pump pulse.[93]

Excitation of multiple dipolar frequencies in multi-spin systems leads to the signal containing not only the sum of contributions from spin pairs, as in a two-spin system, but the sum of products of the different frequencies.[19a] Thus, the PELDOR signal from multi-spin systems has to be described by Equation 1.7:[78]

$$V(t)_{intra} = V_0\langle \sum_{A=1}^{N} \prod_{\substack{B=1 \\ B\neq A}}^{N} (1 - \lambda_B(1 - cos\omega_{AB}t)) \rangle \qquad (1.7)$$

with N being the number of spins present within the labelled system and $\langle ... \rangle$ is the averaging over values of r_{AB}, J_{AB} and θ (Equation1.6).[19b]

Expansion of Equation 1.7 allows grouping the frequency contributions of the signal into pairs that oscillate with a single frequency and into triples, quadruples etc. oscillating with a product of frequencies. The signal modulation depth Δ will contain pair and multi-spin contributions and be dependent on the number of spins N within the system and on the experimental λ, as expressed by Equation 1.8 and shown in Figure 1.17:[78b]

$$\Delta = 1\text{-}(1\text{-}\lambda)^{N\text{-}1} \qquad (1.8)$$

This equation reveals that if $N > 2$ the contributions to the modulation depth will contain high-order terms.

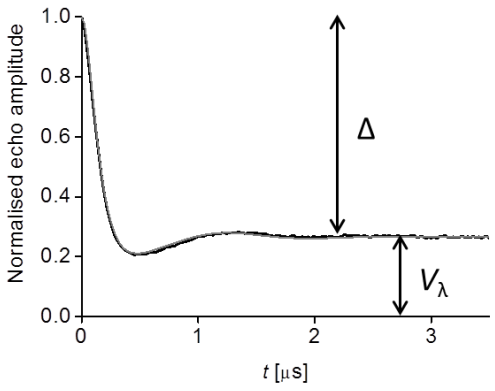

Figure 1.17: PELDOR background corrected trace from distance measurements on a tetraradical model system at X-band. The trace exceeds the modulation depth of 0.5 usually achieved when performing the same experiment on a biradical. This shows the effects from the behaviour outlined in Equation 1.8. V_λ is defined as $1\text{-}\Delta$.

The dependence described in Equation 1.8 can be simplified as Equation 1.9 to allow extraction of the number of coupled spins *N* present within the system once the term of modulation depth Δ is known:[19a, 78b]

$$N = 1 + \frac{\ln(1-\Delta)}{\ln(1-\lambda)} \tag{1.9}$$

In a system bearing more than two free radicals, spins A are coupling not only to a single spin B, but to two or more. A PELDOR experiment on these systems will thus excite multiple dipolar couplings giving a signal that modulates with the product of the dipolar frequencies of all possible pairs. This leads to the PELDOR signal containing sum of products of the excited dipolar frequencies.[9a, 78a] Presence of sum and difference frequencies violate assumptions of Tikhonov regularisation in DeerAnalysis, based on a kernel function for a two-spin system. [30, 78b] Artefacts are commonly found at shorter distances as a result of the presence of sum frequencies, emulating the presence of strong dipolar couplings that translate into short distances. Combination of difference frequencies leads to a frequency contribution close to zero, thus translating in very long distances. These may contribute to the distance distribution however, they are commonly suppressed by background correction.[27] Introduction of these artefacts challenges the accuracy and reliability of distance measurements on multiply labelled systems.[19a, 78a]

1.6.1 Spin-counting

When performing distance measurements on unknown multiply labelled systems it becomes important to determine the number of spins present within the system to test for the spin labelling efficiency *f*. This is commonly achieved by performing the so called spin-counting experiments. Initial studies revealed that number of spins present within the system taken under study directly affects the echo amplitude.[19d] This same concept was later used to successfully assess the number of spins within chemical model systems[19a] and monitor the oligomerisation of self-aggregating alamethicin[94] and of the Na^+/H^+ antiporter NhaA of *E. coli*.[19c]

Different methods for spin counting have been reported. To assess protein oligomerisation the relationship between Δ and *N* described in Equation 1.10 has been previously exploited: [19c]

$$\langle N \rangle = 1 + \frac{\log(1-\Delta)}{C} \quad (1.10)$$

where the parameter C depends on the excitation profile of the pump pulse and line shape of the nitroxide EPR field sweep spectrum.

In this study, rigid and flexible bi- and tri-radical model systems with varying inter-spin distances were used for calibration of λ, which was kept constant, and for the spin-counting method. The obtained results from the model systems were then used to accurately determine the number of paramagnetic centres present within the oligomerised system. The study allowed for determination of the dependence of dimerisation upon change of pH, which was found to be marginal.[19c]

Spin-counting by PELDOR distance measurements has also been performed on polynitroxide chemical model systems by exploiting the dependence of the number of spins *N* on Δ and λ, as described in Equations 1.9 and 1.10. [19b] This study represents the first attempt for experimental verification of spin counting by PELDOR distance measurements using fully characterised systems with up to four spins.[19b] The study proved that PELDOR distance measurements give access not only to accurate estimation of the number of spins present within a cluster, but also to information regarding their geometric arrangement. The same study also reports the first attempt for quantification of the fraction of monomers, dimers and higher oligomers in oligomeric mixtures. For this purpose, mixtures of bi-,tri- and tetra-radical model systems were measured using PELDOR methods. The behaviour of the modulation depth measured for each mixture could be rationalised only when taking into account the different phase memory times for each oligomer, the fraction of spins in each respective oligomer and the probability of exciting these by the pump pulse. Complications may arise when applying the same method to unknown biological systems where the fraction of spins in respective oligomers has to be quantified and the individual phase memory times are unknown.[19b]

The previously observed dependence of Δ upon gradual reduction of inversion efficiencies of the pump pulse for spin counting[19d] has been recently revisited.[19a] The dependence of Δ on the inversion efficiency λ was found to be described by a polynomial. This dependence allows to calculate the number of spins present within the systems by fitting this dependence to polynomials with increasing order *N*-1, until a satisfying agreement is obtained.[19a] To reveal the dependence of Δ on λ of a spin

labelled system to be fitted by a polynomial, PELDOR distance measurements are recorded while gradually reducing the microwave power and calculating the corresponding modulation depth. Reduction of λ was performed by lowering the pump pulse flip angle β and keeping the pump pulse length constant by increasing the main attenuator placed between the amplifier output and the probe head. The efficiency of the pump pulse λ is directly related to the cosine of its flip angle β, as shown in Equation 1.11:[19a]

$$\lambda = \lambda_{max}\,(1 - cos\beta)/2 \tag{1.11}$$

where λ_{max} is the maximum achieved flip angle achieved without using the main attenuator, thus presenting the highest λ achievable at that specific frequency and pulse length. The flip angle β is directly dependent on the microwave power, as expressed by Equation 1.12:

$$\beta = \pi \times 10^{-A/(20\ dB)} \tag{1.12}$$

where A indicates the microwave power attenuation.

This method was found to allow to overcome previously encountered limitations such as the need for calibration with known model systems and differences in inversion efficiencies between model compounds and unknown samples.[19a] The proposed method for spin counting, however, should not be used as an exclusive method to draw firm conclusions on the number of spins within the nano-object.

Reduction of λ was also found to yield the extraction of the spin-pair contribution from the PELDOR signal of multi-spin effects. Extraction of this contribution was found to reduce the broadenings and additional ghost peaks in distance distributions introduced by multi-spin effects, however at the price of loss in sensitivity.[19a] This is further discussed in Section 1.6.2.1 and in Chapter 3.

1.6.2 Methods for suppression of multi-spin effects to-date

Multi-spin effects have been reported to highly affect PELDOR distance measurements as they induce a faster damping of the PELDOR signal, lowering the resolution of dipolar oscillations, and by introducing broadening and additional distance ghost peaks.[19a, 78, 89] To date there are three approaches to suppression of multi-spin effects involving three different aspects of pulsed EPR distance measurements: experimental set-up, data processing and sample preparation. Each method has been

scrutinised by different research groups using chemical model systems[19a, 76a] and biological complexes.[47c, 95] In the next sections each approach will be discussed highlighting their advantages and disadvantages.

1.6.2.1 *Suppression by experimental methods*

To overcome challenges introduced by multi-spin effects in inter-spin distance measurements, it was firstly suggested to extract the spin-pair contribution from the complex of multiple dipolar frequencies and to analyse it using Tikhonov regularisation methods.[19a] The spin pair contribution can be processed by Tikhonov regularisation and should allow for accurate extraction of inter-spin distances. PELDOR distance measurements on bi- and tri-radical model systems **66** to **70** proved that the spin pair contribution can be extrapolated from three-spin correlations by reducing the flip angle of the pump pulse, and lowering the probability of flipping several B spins, thus several dipolar couplings.[19a]

The reduction of the pump pulse efficiency λ between 1 (λ_{max}) and 0.2 , by reducing the microwave power and consequently flip angle β of the pump pulse, allowed to obtain PELDOR data that can be fitted by a second order polynomial with vanishing constant term so that the spin pair and three-spin contributions could be isolated. [19a] Analysis of this dependence was made available by performing a series of PELDOR distance measurements with increasing attenuation, leading to a decreasing pump pulse flip angle β, as performed for spin-counting experiments previously discussed.[19a] The studies proved that analysis of the dependence of Δ on λ allow to separate the spin pair from the three-spin contribution, allowing for accurate distance measurements in three spin systems. [19a]

1.6.2.2 *Suppression by post-processing* methods

λ reduction experiments for suppression of multi-spin effects require experimental efforts in performing a number of experiments, varying the λ by changing the pump pulse flip angle β at high signal-to-noise ratios and they become prohibitive for application to biological samples.[78a] A later study accidentally found that superposition of the logarithm of the background corrected trace from a three-spin system with the logarithm of its spin pair contribution by linear scaling led to almost perfect agreement. This implies that linear scaling of the logarithm of the background corrected trace from a three spin system gives an identical trace to the corresponding two spin system. Thus,

scaling of traces containing contributions from more than one dipolar coupling should lead to traces that can be processed by DeerAnalysis, which assumes presence of contributions from pairs of spins.[78a] The optimum scaling factor is exclusively based on the number of spins *N* within the system. By linear scaling of the logarithm of the background corrected trace of a multi-spin system by a factor of 1/(*N*-1) ghost distance peaks from multi-spin effects were found to be efficiently suppressed.[78a] The newly introduced post-processing method, also referred to as power-scaling, was found to convert the total modulation depth of any multi-spin system to the Δ of a biradical. Scaling of a simulated PELDOR trace from a three-spin system has been found to provide data resembling the contribution of the spin pair. Power-scaling was found to suppress ghost distances introduced by multi-spin effects for simulated traces for systems bearing up to four spins assuming conditions typically found for experiments on nitroxides. For a five-spin system an intentional introduction of reduction of the inversion efficiency had to be introduced to obtain the desired effects.[78a] Specifically, power-scaling was found to suppress additional distances for λ up to 0.8 for a simulated triradical, up to $\lambda \leq 0.6$ for a tetraradical and up to $\lambda \leq 0.4$ for a pentaradical, above these λ values influence of ghost peaks could still be observed. The effects of power-scaling on PELDOR distance measurements performed on a triradical model system revealed that scaling by a factor of 1/(*N*-1) was not fully suppressing ghost peaks. It was concluded that power-scaling has a non-negligible effect on reduction of ghost distances integrals in distance distributions and does not require additional experimental efforts, however it does not lead to their full suppression. Additionally, power-scaling was found not to be as promising when applied to experimental data when compared to noise-free simulations and it may be lowered when applied to systems not bearing high symmetry.[78a] Presence of orientation selection effects is expected to lower the efficiency of the method.[78a] The authors recommend a combination of λ reduction and power-scaling for structural elucidation of unknown systems and that care should be taken when interpreting data where power-scaling of traces introduces important changes in distance distributions, and to perform further studies to quantify the influence of multi-spin effects.[78a]

1.6.2.3 *Suppression by sample sparse labelling*

To overcome challenges coming from multi-spin systems and allow accurate extraction of their inter-spin distances magnetic dilution, meaning the mixing of spin labelled and diamagnetic systems or of monomers with an activated spin label and monomers with a diamagnetic label, have been used and recently reported.[47c, 48] Dilution by addition of unlabelled systems has been used to prevent aggregation of doubly labelled self-aggregating systems whose spin labels would come to a distance close enough to be able to detect dipolar frequencies as a result of their interaction. Additionally, the high local concentration of spin labels gives fast decaying signals and broad distance distributions.[95-96] A recent study showed that dilution of a spin labelled sample of histidine kinase CheA with sufficient quantity of the same non-labelled protein helped towards elucidation of mechanism of its self-aggregation.[97] Magnetic dilution was performed by increasing the concentration of the unlabelled system while leaving the average concentration of the spin labelled system unaffected. The dilution allowed not only to reduce local concentration of the spin labelled proteins, but also left unaffected the average concentration of the spin labelled protein in the sample. Dilution showed to improve distance measurements as the spin pair contribution could be accurately extracted. This resulted in extraction of sharper distance distribution, reduction in the signal slope and generated the proof for self-aggregation of kinase CheA.[97] This dilution method, however, would not facilitate measurements on systems bearing more than two spins. Another method for magnetic dilution introduces diamagnetic analogues of spin labels in combination with paramagnetic labels to biological systems such as oligomeric systems and nucleic acids or by reducing the labelling efficiency.[48, 95] The second approach has been recently reported in a study on the hexamer proteorhodopsin.[47c] The authors labelled three sites of the complex - one near the oligomer interface, one on the peripheral, and one at the intracellular loop - with either nitroxide-based (MTSSL) or Gd(III) chelating spin labels. The hexamer samples were labelled with 33%, 55%, 80% and 100% Gd(III) or nitroxide occupancy/labelling, thus reducing the labelling efficiency *via* sparse labelling. Distance measurements on nitroxide sparsely labelled systems showed an improvement in extraction of inter-spin distances: distance peaks were narrower and background correction was also facilitated, in particular for the 33% labelled sample, however the longest distance peak could not be resolved.[47c]

1.7 Project aims

To date three methods have been proposed for suppression of multi-spin effects to improve extraction of distances from systems containing more than two spins: lambda reduction experiments, magnetic dilution or sparse labelling and power-scaling. Each method deals with suppression of multi-spin effects by optimising different parameters: experimental methods, sample optimisation and post-processing data treatment.

The aim of this project was to quantify the impact of multi-spin effects on distance measurements and to test known and alternative approaches to give access to accurate measurement of inter-spin distances from multiply-labelled systems. Suppression of multi-spin effects is key for structural elucidation and conformational studies of biological systems or oligomers, as often selective introduction of only two labels cannot be achieved. The combination of PELDOR distance measurements on chemical model systems and quantitative simulations has proven to be an effective method for designing pulsed EPR experiments.[14, 18b, 18c, 19b, 20a, 78b] Specifically, chemical model systems can be designed to have specific structural features, such as rigidity, symmetry and number of spin labels, to study specific effects, such as orientation selection and multi-spin effects. The behaviour of these structurally well-defined chemical backbones can be easily predicted by simulations on spin labelled polygons mimicking their geometries, making hypotheses to be easily tested and observed effects to be accurately quantified. Additionally, the measurement averaging times can be greatly reduced as sample concentrations can be easily modified.

In this project the combination of model systems and simulations was used for quantification of the effects introduced by the methods previously proposed, such as power-scaling[78a] and sparse labelling[47c] and to explore alternative experimental settings[98] towards suppression of multi-spin effects. The findings were validated on membrane channel proteins bearing seven and eight spin labels.

Chapter 2 - Synthesis of polyradical model systems

Parts of this chapter has been published in similar form in the following journals: *Journal of Organic Chemistry*, **2014**, *79* (17), 8313;[39a] *Chemistry - A European Journal*, **2016**, *22* (14), 4700;[98] *Molbank* **2015**, *2015* (3), M865.[99] The author designed and completed the synthesis of all polyradical model compounds. Dr. James E. Taylor and Dr. David S. B. Daniels contributed intellectual input into the syntheses analyses, Dr. Daniel Dawson and Prof. Sharon E. Ashbrook provided measurements and analysis of the solid state NMR spectra. Dr. Kasun S. Athukorala Arachchige and Prof. Alexandra M. Z. Slawin provided X-ray diffraction patterns and solved the crystal structures.

2.1 Project Background

The first step towards the understanding, quantification and suppression of multi-spin effects in PELDOR measurements in this work involved the synthesis of polyradical model systems with well-defined structures. The behaviour of these test compounds can be easily predicted, thus facilitating the quantification of effects induced by the presence of a third or fourth spin within the same system when interpreting experimental data. Additionally, their geometries allowed to build constituent biradicals to polyradicals and to mimic structures and aggregation states of biomolecules. Thus, model systems could be used to evaluate accuracy and limitations of known and novel pulsed EPR methods for biological applications.

Model systems should be rigid, rod-like, exhibit high symmetry and be designed to have inter-spin distances between 1.5 to 8 nm, a range that can be reliably measured by pulsed EPR techniques.[2b, 11] Rigidity limits the structural and conformational flexibility of the model system giving well-defined inter-spin distances, while symmetry minimises the number of different distances[18a, 18c] and facilitates the detection of deviations from an expected single peak.[78b] Figure 2.1 reports the three symmetrical core building blocks used for synthesis of symmetric polyradical model systems. An advantage of using commercially available 1,3-diethynylbenzene **81** and 1,3,5-triethynylbenzene **82** is that they have relatively high symmetry and the same angular geometry. In terms of multi-spin effects this means that any distortion induced by the presence of a third spin label could be separated from structural effects, as the triradical is the direct extension of the biradical. A tetrahedron-based tetraradical was approached using 1,3,5,7-tetrakis(4-ethynlphenyl)adamantane **83** as a building block.

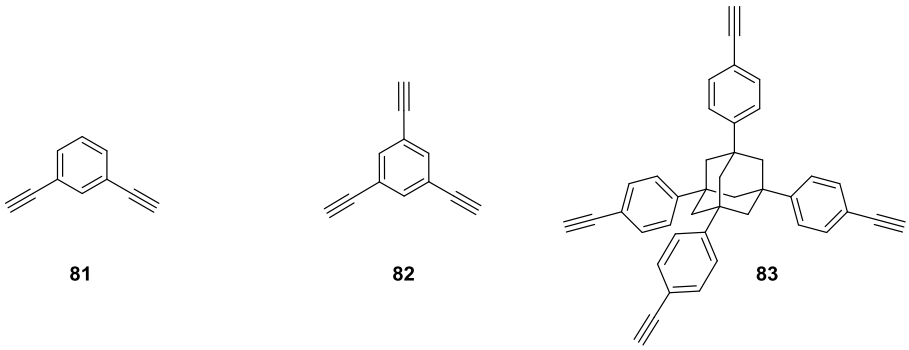

Figure 2.1: Symmetrical core building blocks for synthesis of polyradical model systems.

To validate whether findings from measurements on symmetric compounds were also valid on polyradicals bearing more than four spin labels and conformations that would give more than one distance, an asymmetric tetraradical and a system bearing a hexagonal symmetry were also envisaged. For this purpose 1,2,4,5-tetraethynylbenzene **84** and hexakis[(4-ethynyl)phenyl]benzene **85**, reported in Figure 2.2, were thought to be good templates.

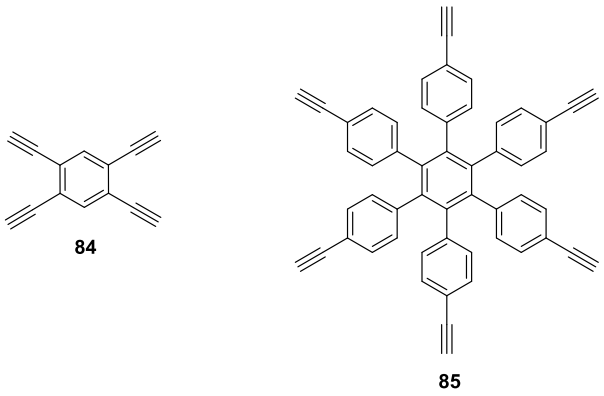

Figure 2.2: Core building blocks for synthesis of asymmetric tetraradical and hexagonal polyradicals.

2.2 Project aims

The aim of this project was to develop a common synthetic protocol for isolation of a variety of symmetric, asymmetric and rigid polyradical systems. These should consist of backbones of phenylene and ethynylene units, as they confer rigidity and chemical stability to the system,[18c, 39b] while introducing a specific functionality for covalent attachment of the spin label 1-oxyl-2,2,5,5-tetramethylpyrroline-3-carboxylic acid TPC **3**. This spin label can be readily introduced onto polyphenolic aromatic backbones through esterification under mild conditions. Additionally, it has been shown that the presence of multiple ester groups

largely diminishes the through-bond exchange coupling *J*, which would seriously complicate the interpretation of distance measurements.[20b, 39b] Different approaches were considered: one possibility is that 4 -hydroxy-4'-iodobiphenyl **74** (Scheme 1.10) could first be esterified with TPC **3** to give nitroxide radical **75**, which would be cross-coupled *N* times to a suitable precursor containing *N* terminal alkynes to form a series of polyradical systems (Scheme 2.1, route A). This procedure could be performed by following a similar strategy to what previously adopted.[19b] Alternatively, **74** could be first cross-coupled *N*-times to the terminal alkyne precursor to form a polyphenolic backbone that could then undergo global esterification with TPC **3** (Scheme 2.1, route B).[39b] In both cases **74** represents a yard-stick module that can be used to increase the inter-spin distance by approximately 1.12 nm, estimated using reported incremental bond lengths,[33] without compromising the rigidity of the system.

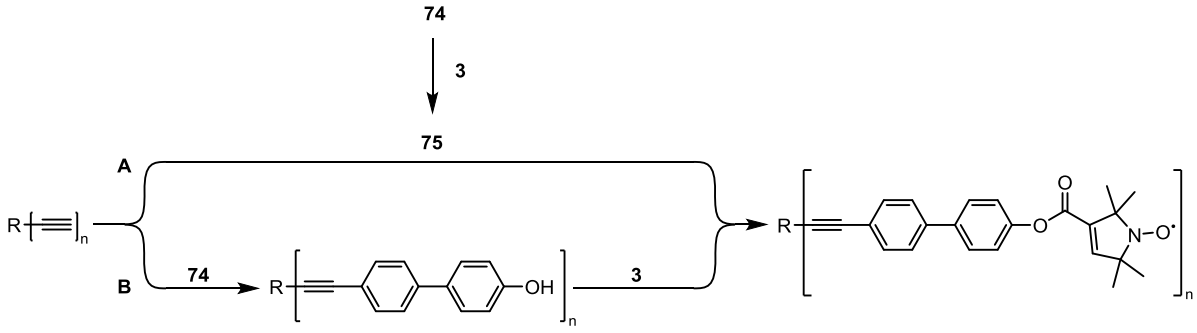

Scheme 2.1: Proposed synthetic routes for synthesis of rigid polyradicals.

2.3 Results and discussion

The development of a common protocol for the synthesis of polyradical model systems was developed in two stages: optimisation of esterification conditions for attachment of the spin label of choice TPC **3** to commercially available polyphenols followed by synthesis of polyphenolic backbones by cross-coupling building units bearing multiple terminal alkynes with spacer **74**.

2.3.1 Optimisation of esterification conditions

It was important to establish a reliable esterification protocol as a standard set of reference conditions for the synthesis of all polyradical model systems. The aim was to optimise conditions for an efficient final synthetic step as the introduction of a paramagnetic

centre would prevent quantitatively monitoring the reaction by NMR.[100] Different methods for esterification of spin label TPC to polyphenolic backbones had been previously reported, as shown in Scheme 2.2. One of the first examples, reported by Rosantzev,[61] involved the use of thionyl chloride in the presence of pyridine for attachment of TPC **3** to **86** and **87**. In this case the ester bond is formed by initial formation of the acid chloride, with chloride as a good leaving group. This strategy, however, gave target bi- and tri-radicals **88** and **89** in low yields, 23 and 14% resoectively, after sequential purification by column chromatography and recrystallization. A second method previously reported[20b] for esterification of TPC to hydroquinone **90** and 4,4'-biphenol **91** using Steglich conditions,[64] involved the use of less reactive reagents and gave biradicals **92** (11%) and **44** (16%).[39b]

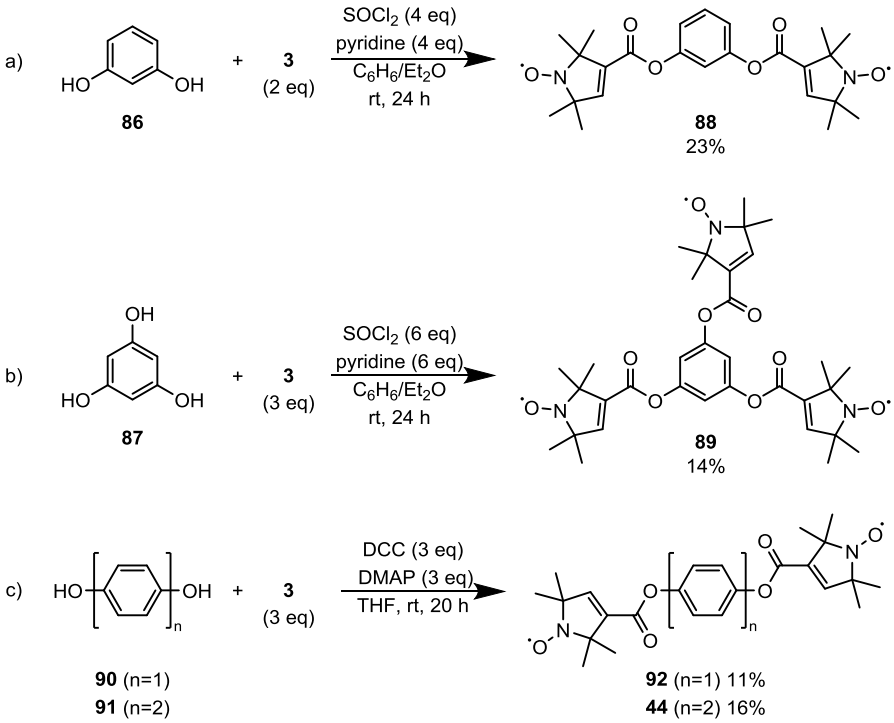

Scheme 2.2: Previously reported conditions for esterification of TPC **3** to polyphenolic backbones.[20b, 61]

For this reason it was initially decided to couple TPC to resorcinol **86**, 4-4'-hydroxybiphenol **91** and phloroglucinol **87** in the presence of dicyclohexylcarbodiimine (DCC) and dimethylaminopyridine (DMAP).[84] These reaction conditions gave the target biradicals, **88** and **44**, and triradical **89** in acceptable yields: 30%, 45% and 25% respectively, as reported in Scheme 2.3. Whilst these yields are an improvement on those previously reported the purifications proved to be challenging due the presence of the

dicyclohexylurea by-product. In an attempt to overcome these difficulties alternative esterification conditions were tested; these involved the use 1-ethyl-3-(3-dimethylaminopropyl) carbodiimide hydrochloride (EDCI·HCl) as the activating reagent in the presence of DMAP. In this case the urea by-product is completely water soluble and could be easily removed through an aqueous work-up. This led to an improvement in the isolated yields of biradicals **88** and **44** to 49% and 82% respectively (Scheme 2.3) after chromatographic purification on activity II aluminium oxide with 4% H_2O.[50a]

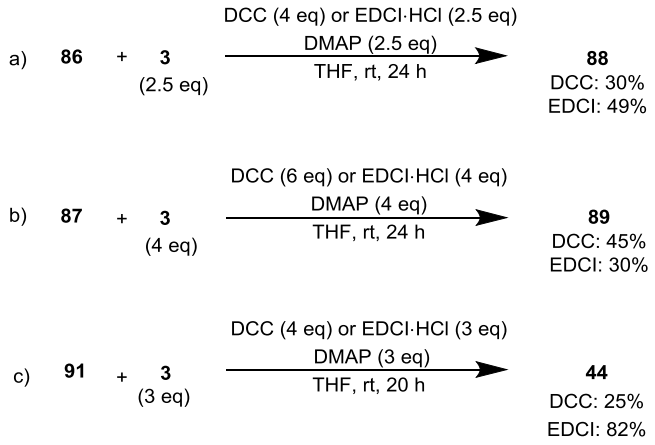

Scheme 2.3: Yield comparison between previously reported esterification conditions and the improved developed protocol.

The combination of EDCI and DMAP allowed overcoming the challenges of poor yields and difficult purification faced with previously reported methods. These improvements make these reaction conditions an ideal starting point for a general protocol for esterification of phenolic compounds to TPC **3**. Single crystal X-ray crystallographic analysis of biradical **88** revealed a nitroxide-nitroxide distance of 1.33 nm, based on the mid-point of the N-O bond, which is similar to the mean nitroxide-nitroxide distance of 1.32 nm (average of 1.39, 1.26 and 1.30 nm) obtained from structure of triradical **89**.[101] The approximation of triradical **89** being an overlay of three orientations of biradical **88** is therefore reasonably well fulfilled. The X-ray crystal structure of triradical **89** displayed a disorder related to multiple occupations, suggesting that at least two rotamers are of very similar in energy; this effect was not present in the X-ray crystal structures of biradicals **88** and **44**.[102]

2.3.2 Synthesis of polyradicals

The first synthetic strategy adopted for the synthesis of polyradical model systems was adapted from previously reported methods,[19b] here summarised in Scheme 2.4. This involved the cross-coupling of TPA **2** (Figure 1.7), which is similar to TPC **3** except for the presence of a terminal alkyne rather than a carboxylic acid functionality, followed by the cross-coupling of the alkyne bearing spin label to an iodinated poly(*para*-phenyleneethynylene) backbones.

Adoption of this synthetic strategy required a first esterification of 4-hydroxy-4' -iodobiphenyl **74** with **3**, to give **75** (Scheme 1.10).[50a] **75** was then cross-coupled *N* times to the alkyne-bearing core unit, as reported in Scheme 2.4. This first esterification, isolated using modified reaction conditions,[39a] was found to be efficient and easy to perform on large scales, as reported in Scheme 2.4, giving a 72% yield. For cross coupling of **75** to the alkyne-bearing core unit the reaction conditions similar to those previously reported[19b] were tested: $PdCl_2(PPh_3)_2$ (3 mol%), PPh_3 (30 mol%) and CuI (1 mol%) in a mixture of piperidine and triethylamine (Scheme 2.4). This gave the target biradical **93** in 12% yield. The same conditions were also tested on 1,3,5-triethynylbenzene **82**, however no product could be isolated on this occasion. Changes in reaction conditions, like equivalents of base, catalyst loading and temperature, were found not to improve the initial results.

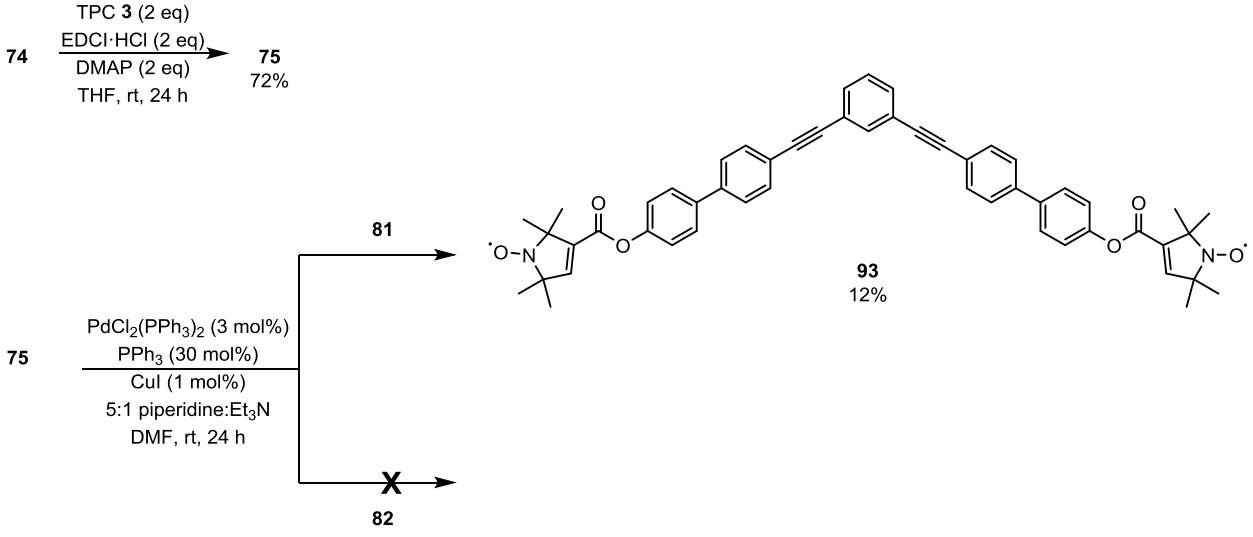

Scheme 2.4: Synthesis of bi-radical **93**

Multiple couplings in a single reaction step have been previously proven to be challenging due to the often limited yield for a single coupling and to the difficulties

encountered during separation of singly and multiply cross-coupled products.[19b] One possible explanation for the low yield is the competing Glaser reaction inducing the homocoupling of the alkyne;[19b] however the paramagnetic nature of the crude reaction mixture made identification of unwanted side-products difficult.[103] The disappointing results led to the exploration of the alternative approach reported in Scheme 2.1.

After consideration of all challenges encountered when using the previously reported method a straightforward solution would be to introduce the spin label in the very last step, thus building at first a polyphenolic backbone to which TPC **3** could be attached to give the target molecules. As esterification conditions of TPC **3** to the commercially available polyphenols had already been optimized, the attention was focused on designing a common protocol for synthesis of polyphenolic backbones. First attempts involved the use of standard Sonogashira conditions[19b] for cross-coupling of **81** or **82** and 4-hydroxy-4' –iodobiphenyl **74**. Disappointingly, none of the attempts gave the target polyphenols.

The alternative most straightforward strategy for synthesis of polyphenolic backbones appeared to involve the first cross-coupling of 4-hydroxy-4' –iodobiphenyl **74**, with which esterification of TPC **3** previously proved high yielding, to a building block bearing terminal alkynes (Scheme 2.1).A method for cross-coupling of halogenated compounds containing hydroxyl groups using a 0.5 M aqueous ammonia solution as a base,[104] instead of a mixture of piperidine and triethylamine[19b] in the presence of $PdCl_2(PPh_3)_2$ and CuI, was tested. In this case, 4-hydroxy-4'-iodobiphenyl **74** was first reacted with 1,3-diethynylbenzene **81** under aqueous ammonia Sonogashira cross-coupling conditions to afford biphenol **94** in 69% yield (Scheme 2.5).

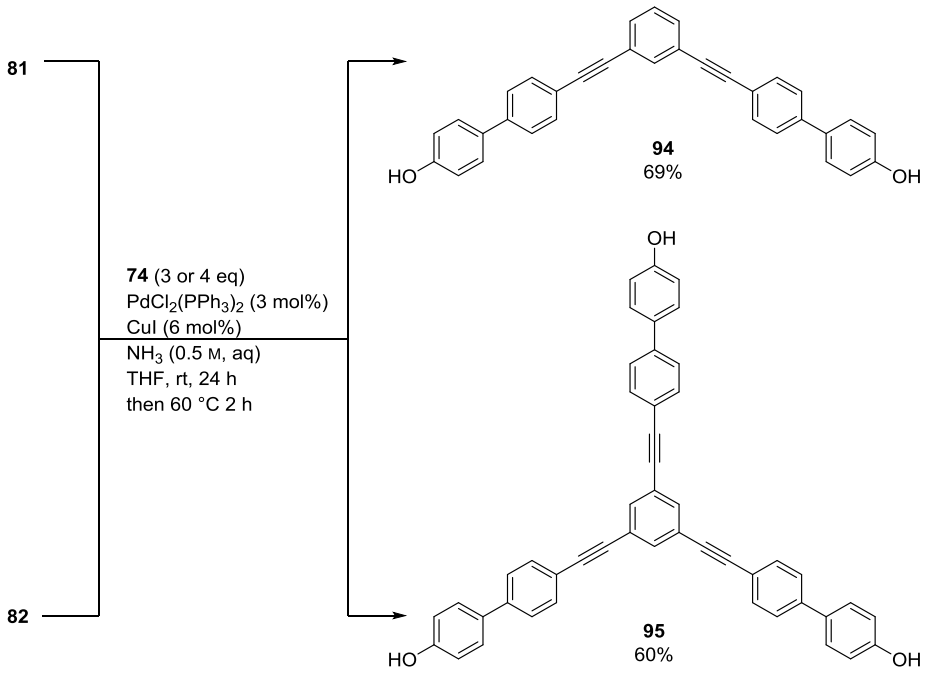

Scheme 2.5: One-step synthesis of bi- and tri-phenols using aqueous ammonia as base for cross-coupling.

The symmetric triphenol was synthesized in the same single step strategy from 1,3,5-triethynylbenzene **82** (Scheme 2.5). The triple cross-coupling process with 4-hydroxy-4'-iodobiphenyl **74** gave tris-phenol **95** in a 60% yield. The use of these alternative conditions gave access to the target polyphenols in good yields without need of protecting the phenol, thus reducing the number of steps.

From this strategy synthesis of target polyphenols **94** and **95** using commercially available **81** and **82** as core building blocks should only involve a single step. In the case of the adamantane-based tetraphenol a strategy for introduction of terminal alkynes was required. Synthesis of the tetrahedral tetraphenol was initially attempted using the same strategy as for the bi- and tri-phenols: Sonogashira cross-coupling under aqueous ammonia conditions of 4-hydroxy-4'–iodobiphenyl **74** to the core building block containing the required number of terminal alkynes relative to the number of phenolic groups for attachment of **3**.

The first step to synthesize the tetrahedral core **83**, suitable for onwards cross-coupling reactions, involved the treatment of 1-bromo adamantane **96** with tert-butyl bromide (3 eq) and a catalytic amount of $AlCl_3$ (10 mol %), and heated at reflux in benzene[105] to give tetraphenyladamantane **97** in 90% yield. Tetraphenyladamantane **97** was then iodinated using [bis(trifluoroacetoxy)iodo]benzene (4 eq) and iodine (2 eq) to give 1,3,5,7-tetrakis(4-

iodophenyl)adamantane **98** in 51% yield.[106] Next, TMS-acetylene was coupled to **99** followed by TMS deprotection to give the key tetrahedral tetraalkyne **83** in 67% yield over the two steps (Scheme 2.6).[107]

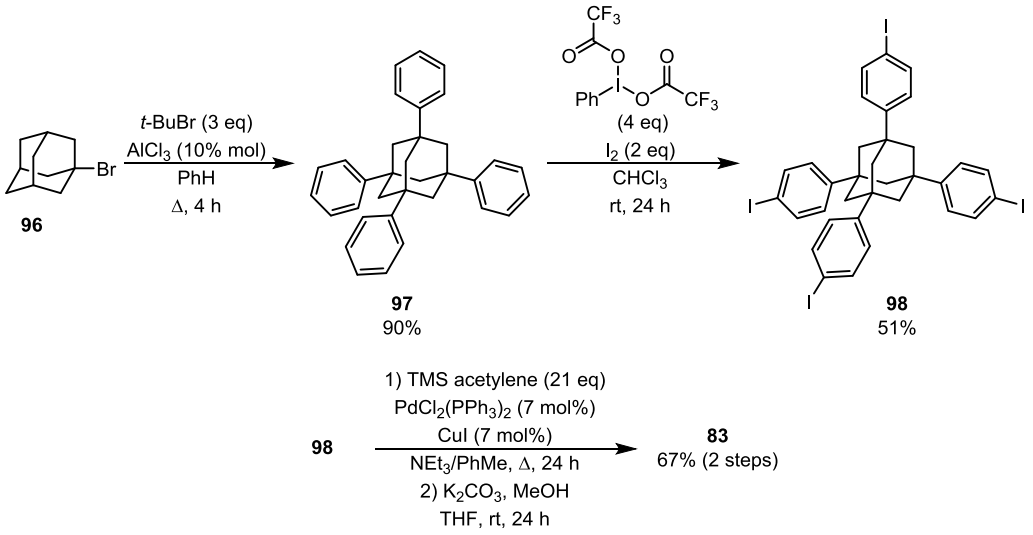

Scheme 2.6: Synthesis of poly-alkyne adamantane-based core building block.

Cross-coupling of **83** with 4-hydroxy-4'iodobiphenyl **74** using the aqueous ammonia Sonogashira conditions gave tetrakis-phenol **99**, but in a disappointing 35% yield (Scheme 2.8 A). Therefore, the order of the synthesis was changed in an attempt to provide a higher overall yield. Coupling of 4-hydroxy-4'-iodobiphenyl **74** with TMS-acetylene followed by silyl deprotection gave alkyne **100** in 80% yield over two steps (Scheme 2.7).[108]

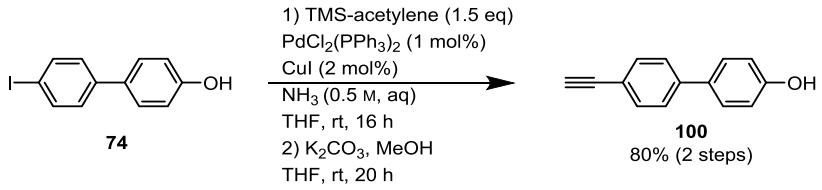

Scheme 2.7: Synthesis of poly-alkyne adamantane-base core building block.

Pleasingly, coupling of alkyne **100** with tetrakis-iodoadamantane **98** provided the desired tetrakis-phenol **99** in a much improved 60% yield (Scheme 2.8 B).

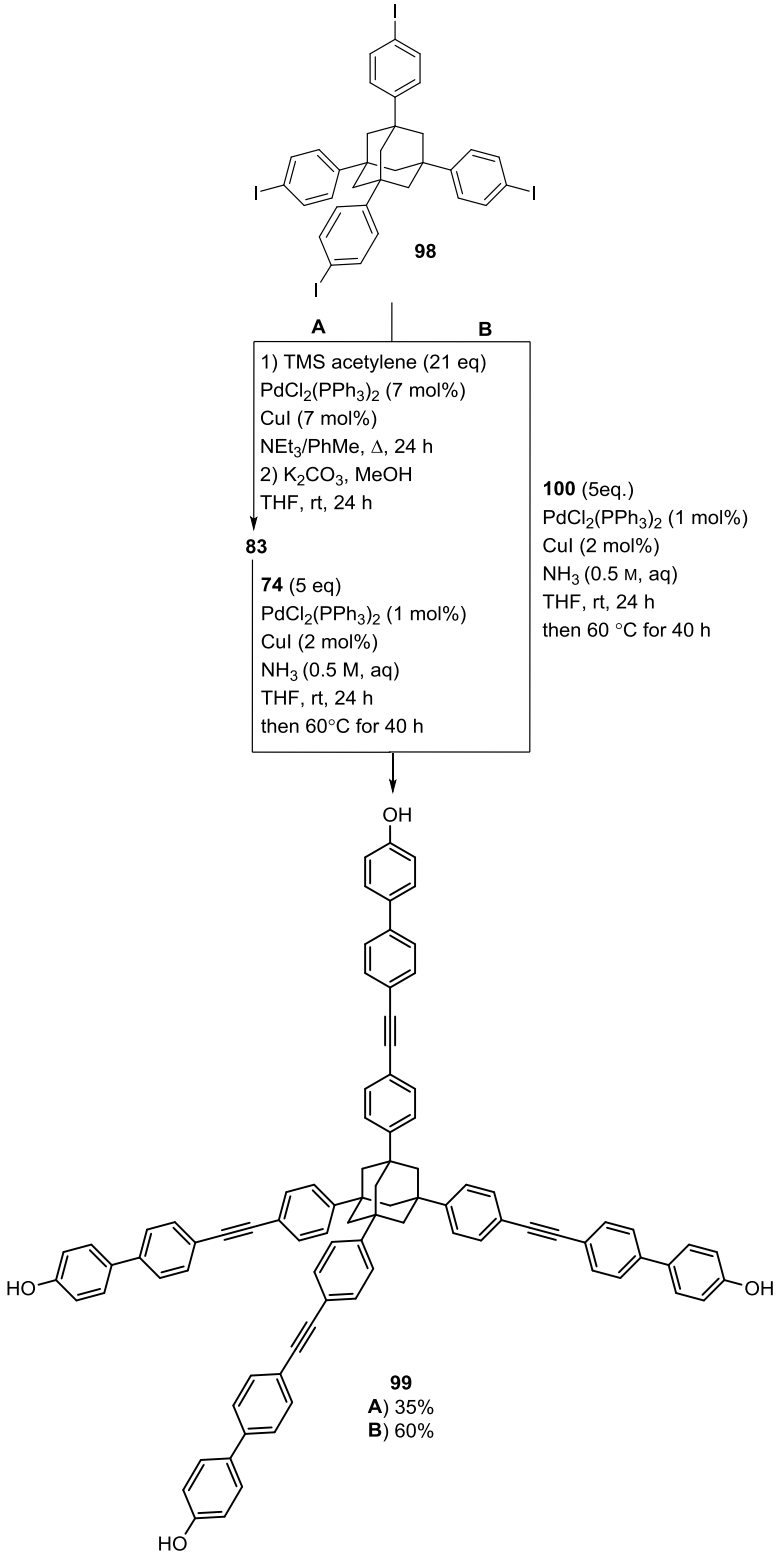

Scheme 2.8: Two synthetic strategies approached for synthesis of tetraphenol **99**.

The same synthetic strategy was used for synthesis of an asymmetrical tetraradical based on the cross-coupling of 4'-ethynyl-[1,1'-biphenyl]-4-ol **100** to the commercially available 1,2,4,5-tetrabromobenzene **101**. The aqueous ammonia cross-coupling gave the target asymmetric tetraphenol **102** in an 81% yield (Scheme 2.9).[98]

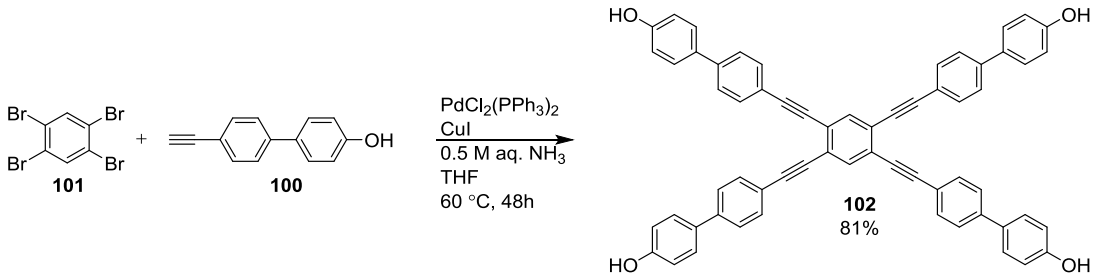

Scheme 2.9: Two synthetic strategies approached for synthesis of tetraphenol **102**.

Hexaphenol **103** was synthesised using a similar approach that lead to isolation of tetraphenol **99**: iodination of phenylated backbone **104** followed by coupling of 4'-ethynyl-[1,1'-biphenyl]-4-ol **100** (Scheme 2.10).[99]

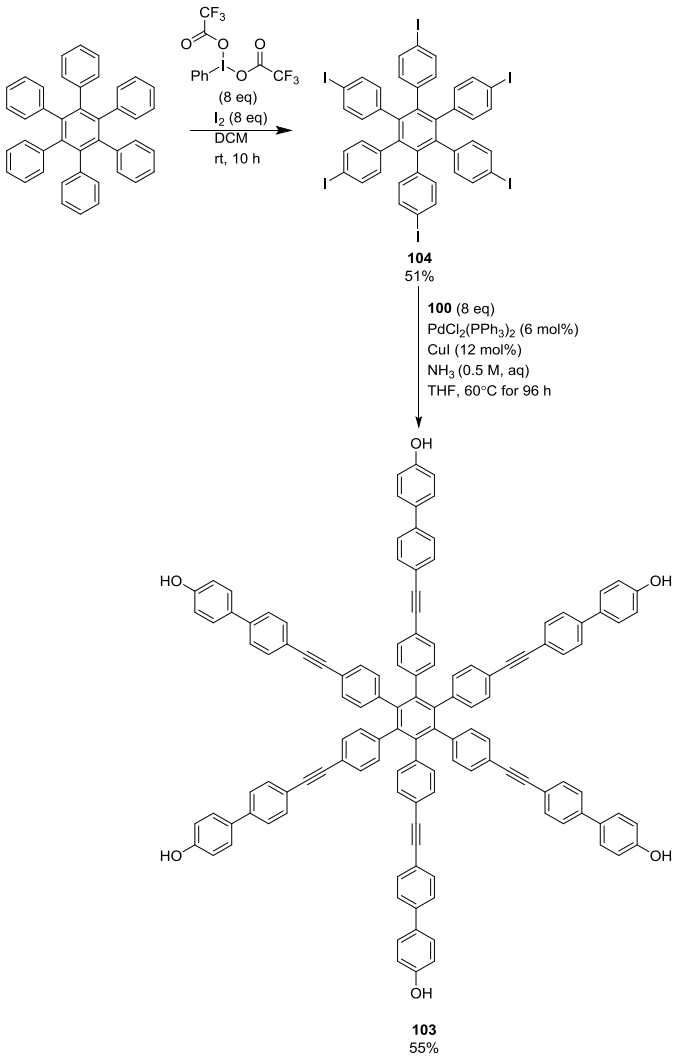

Scheme 2.10: Synthesis of hexaphenol **103** using the common synthetic protocol developed.

Esterification of the newly synthesised polyphenols to the spin label **3** was performed using conditions previously optimised on commercially available polyphenols: EDCI HCl and DMAP in THF at room temperature under inert atmosphere, as reported in Scheme 2.11.[23, 98]

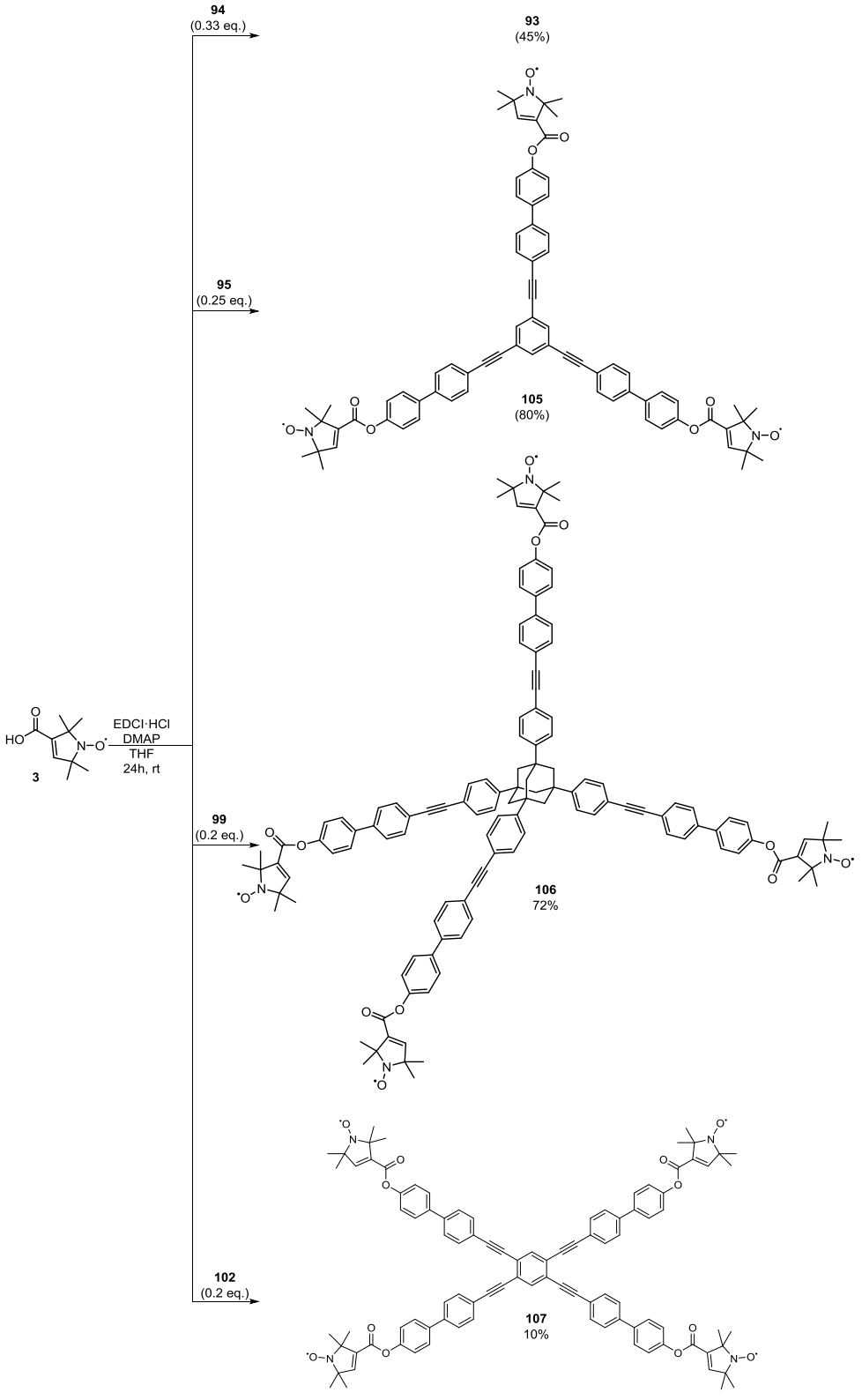

Scheme 2.11: Synthesis of polyradical model systems using a common synthetic protocol for synthesis of polyphenols and optimised conditions for esterification of TPC.

2.4 Conclusion

In conclusion an efficient modular approach for the synthesis a series of polyradical model systems for studying multi-spin effects in EPR distance measurements has been developed. Sonogashira cross-coupling of 4-hydroxy-4'-iodobiphenyl **74** to suitable symmetric polyalkynes under aqueous ammonia conditions provides a range of polyphenols without the need for phenolic protecting groups. EDCI·HCl mediated esterification of the polyphenols with the spin label TPC **3** gives the corresponding polyradical systems in good yield with a straightforward work-up and purification procedure. This common protocol has been successfully applied to the synthesis of bi-, tri- and tetraradical systems in a very few synthetic steps. Importantly, the synthesis of tetraradical **106** represents the first example of a non-planar polyradical with fixed inter-spin distances exhibiting tetrahedral shape.

Chapter 3 - Novel experimental approach for suppression of multi-spin effects

This chapter was published in similar form in *Chemistry - A European Journal*, **2016**, *22* (14), 4700.[98] The author performed synthesis, PELDOR measurements, simulations and data processing. Dr Katrin Ackermann contributed with preliminary measurements at Q-band and contributed modelling of distance distributions from crystal structure, Dr Hexian Huang and Dr. Christos Pliotas produced the spin labelled biological samples under the supervision of Prof. James H. Naismith. Bela Bode performed the λ reduction experiments at X-band on the biological systems.

3.1 Project background

PELDOR distance measurements have recently become an important addition to the techniques commonly used for elucidation of structural features of complex biological systems.[2b, 9] This technique gives access to the measurement of inter-spin distances between spin labels covalently bound to biological and chemical systems in the nanometre range. Measurement of long range distances can be a key element for assessing proteins conformational states.

To date the PELDOR method has only been proven reliable when performing measurements on doubly labelled systems (i.e. between exactly two spins).[19a, 78b] The traces obtained when measuring systems bearing two spin labels with this method can be easily processed in DeerAnalysis[30] to give accurate distance distributions.[19a, 19b, 78] Presence of additional factors such as restricted conformations, giving orientation selection effects, and strong *J* couplings require further analysis to accurately extract inter-spin distances when using this software.[18b, 20a, 71, 109]

In multiply labelled systems the multi-spin effects represent a continuing challenge for pulsed EPR distance measurements. Particularly, presence of more than two spins within the same nanoobject implies the existence of a number of different dipolar frequencies that make the PELDOR trace modulated with the product of the dipolar frequencies of all possible pairs. These lead to sum and difference frequencies, which could yield erroneous distances corresponding to the inverse cube of frequency dependence if multi-spin data was processed in DeerAnalysis.[19a, 78] Thus, processing of multi-spin data has been found to result in introduction of broadenings and additional peaks in distance distributions, which greatly compromises the accuracy of PELDOR

distance measurements on these systems.[47a, 78a] As previously discussed in Section 1.6.2, different methods have been proposed to suppress multi-spin effects and allow accurate extraction of distances in multiply labelled systems. One of the approaches previously proposed[19a] suggests that lowering of the pump pulse flip angle β allows for isolation of the spin-pair contribution to the signal, thus elimination of the combination frequencies.[19a, 78b] The same authors introduced a post-processing method, power-scaling, where isolation of the pair contribution could be achieved by scaling the PELDOR trace by a 1/(*N*-1) exponent. The method does not require additional experimental efforts or rely on a very high signal-to-noise ratio, as the former approach.[78a] Both methods, however, bring important limitations: substantial reduction in sensitivity (modulation to noise ratio)[78a] and loss of performance with increasing *N* and λ, respectively.[19a, 78b] The scaling method will thus not always be sufficient and the reduction of the pump pulse flip angle can become unaffordable in particular for multiply labelled biological systems that usually require long averaging times due to fast relaxation of the spin labels and requirement of long measuring time windows for resolution of long distances.[19a]

3.2 Project Aims

The first goal was to quantify the effects of λ reduction and power-scaling, and their combination for effectively diminishing multi-spin effects without overly compromising on sensitivity. The methods were tested on the two tetraradical model systems reported in Chapter 2 and on two membrane channel proteins. Measurements were focused on model system **106** and MscS S196R1 (Figure 3.1 a)). Symmetric molecules are more prone to manifest multi-spin effects in the attempt to measure their inter-spin distances.[78a] The asymmetric **107** and sWza Q335R1 (Figure 3.1 b)) were used as test systems to validate the effects of the two methods and their combination on complexes. The second goal of this project was to optimise settings for a modified variant of the PELDOR experiment aiming at the effective suppression of multi-spin effects together with overcoming the challenges and drawbacks imposed by the previously proposed methods. The alternative method would ideally give the optimum compromise between sensitivity loss and suppression of combination frequencies, and allow for accurate extraction of inter-spin distances in systems bearing more than two nitroxide spin labels.

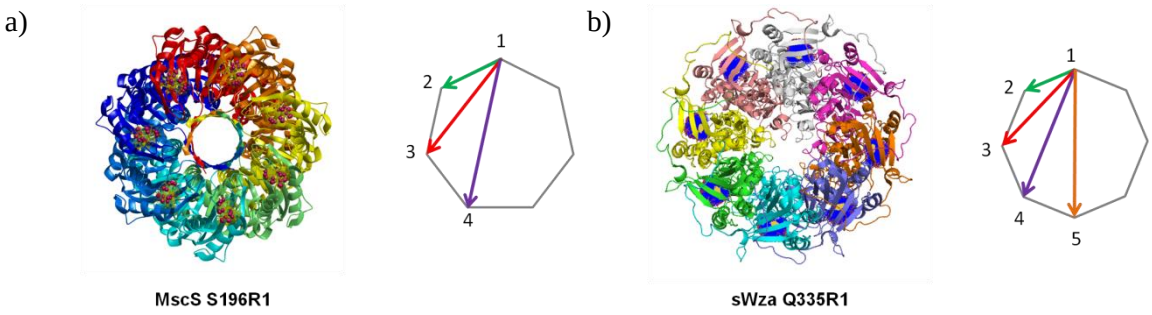

Figure 3.1: Crystal structures of membrane channel proteins MscS S196R1 a), sWza Q335R1 b) and corresponding polygons mimicking their geometries and expected distances.

3.3 Results and Discussion

The efficiency and drawbacks of the existing approaches to suppression of multi-spin effects, λ reduction and power-scaling, were carefully scrutinised on the chemical and biological systems. The effects of combination of λ reduction, power-scaling and of the alternative settings for the PELDOR experiment were initially tested and quantified at X-band using MD5 and MS3 resonators, with the latter giving access to a higher microwave field strength allowing shorter π-pulses. Similar experiments were then performed at Q-band.

3.3.1 Multi-spin effects suppression by λ reduction

To test the efficiency and limitations of λ reduction experiments (see Materials and Methods A.2.3.1) for suppression of multi-spin effects in distance measurements on multiply labelled systems, λ reduction experiments were performed on the tetra-radicals **106** and **107** reported in Chapter 2 and on heptameric and octameric membrane channel proteins MscS S196R1 and sWza Q335R1 (Figure 3.2). All distance distributions are shown with a colour-coding indicating the distance reliability ranges, as previously described in Section 1.3.[30] Initial results with reduced λ were obtained using a 5 mm dielectric ring (MD5) resonator that has large concentration sensitivity (when the sample amount is not limiting), as reported in Figure 3.2.

These preliminary results show that measurements using the commonly used setting for PELDOR distance measurements (see Materials and Methods A.2.3.1) exploiting the maximum pump pulse flip angle β to achieve the maximum λ (λ_{max}) give distance distributions with additional ghost peaks and broadenings. Progressive reduction of λ from λ_{max} shows decrease in intensity of the additional distance peaks and broadenings;

measurements performed with 20% of λ_{max} give distance distributions containing the expected single distance peak for the tetrahedral **106**, the sharper peaks for **107** and in good agreement with the models from the crystal structures for MscS S196R1 and sWza Q335R1 (Figure 3.2). Presence of actual ghost distances when using λ_{max} and reduction of these when reducing λ to 20% is confirmed by validations reported in Figure 3.3. Validation of distance distributions obtained by Tikhonov regularisation (see Materials and Methods A.2.4)allows performance of a systematic error analysis taking into consideration experimental factors such as noise levels and uncertainties in background correction. The validation tool in DeerAnalysis 2013 systematically varies the starting point for background correction to check the stability of the distance distributions against deconvolution of different background functions. Noise levels and background dimensionality can also be systematically varied. The validation provides error bars, here reported as grey areas delineating the lower and upper boundaries (Figure 3.3), suggesting the reliability of each point of the distance distribution, thus revealing the stability of the distance distributions against variation of the main parameters varied during data processing.[30, 110] The same λ reduction experiments were performed at X-band using a 3 mm split ring resonator (MS3) resonator that has a larger microwave field-strength than the MD5 and it is commonly recommended due to its absolute sensitivity (when the sample amount is a limiting factor) and higher achievable modulation depth (Figure 3.4).[68] In this case measurements were performed exclusively on the model systems, as the reduced concentration made repetition of the biological systems unfeasible (see Materials and Methods A.2.3.1). As for results obtained from measurements using an MD5 resonator, validations of distance distributions from MS3 resonator measurements show that the intensity of the ghost distance peaks in the λ_{max} experiments remain unaltered despite the change in the background function. Reduction of λ to 20% of λ_{max} confirms that ghost distances are efficiently suppressed (Figure 3.5).

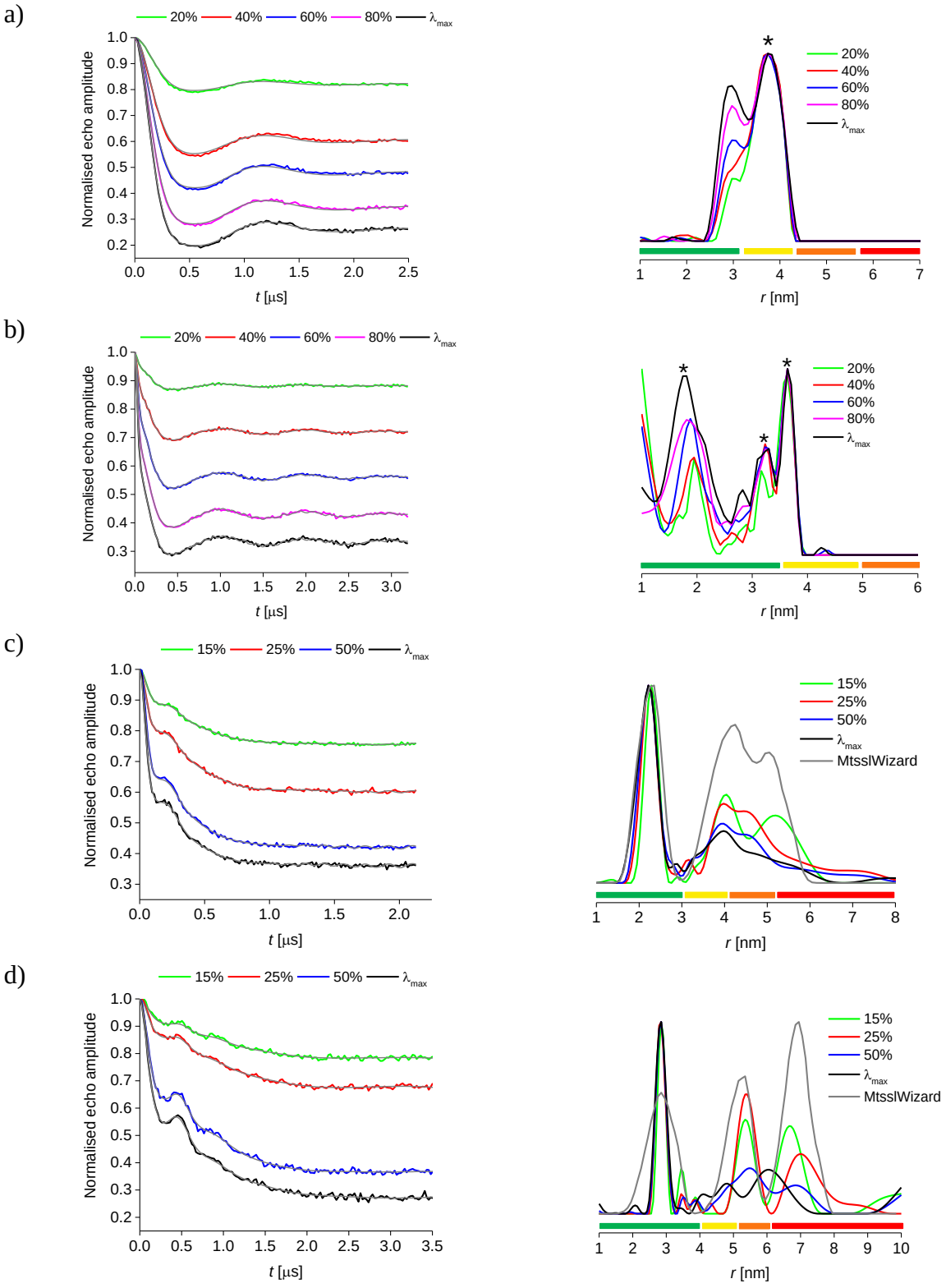

Figure 3.2: Background corrected PELDOR data with fit and corresponding distance distributions for **106** a), **107** b), MscS S196R1 c), and sWza Q335R1 d), measured at X-band with MD5 resonator. The * mark the true distances for **106** and **107**, the grey distance distributions are modelled from X-ray data of the proteins by the MtsslWizard software.[111] The coloured bars suggest the reliability of distances in relation to the measuring time window.

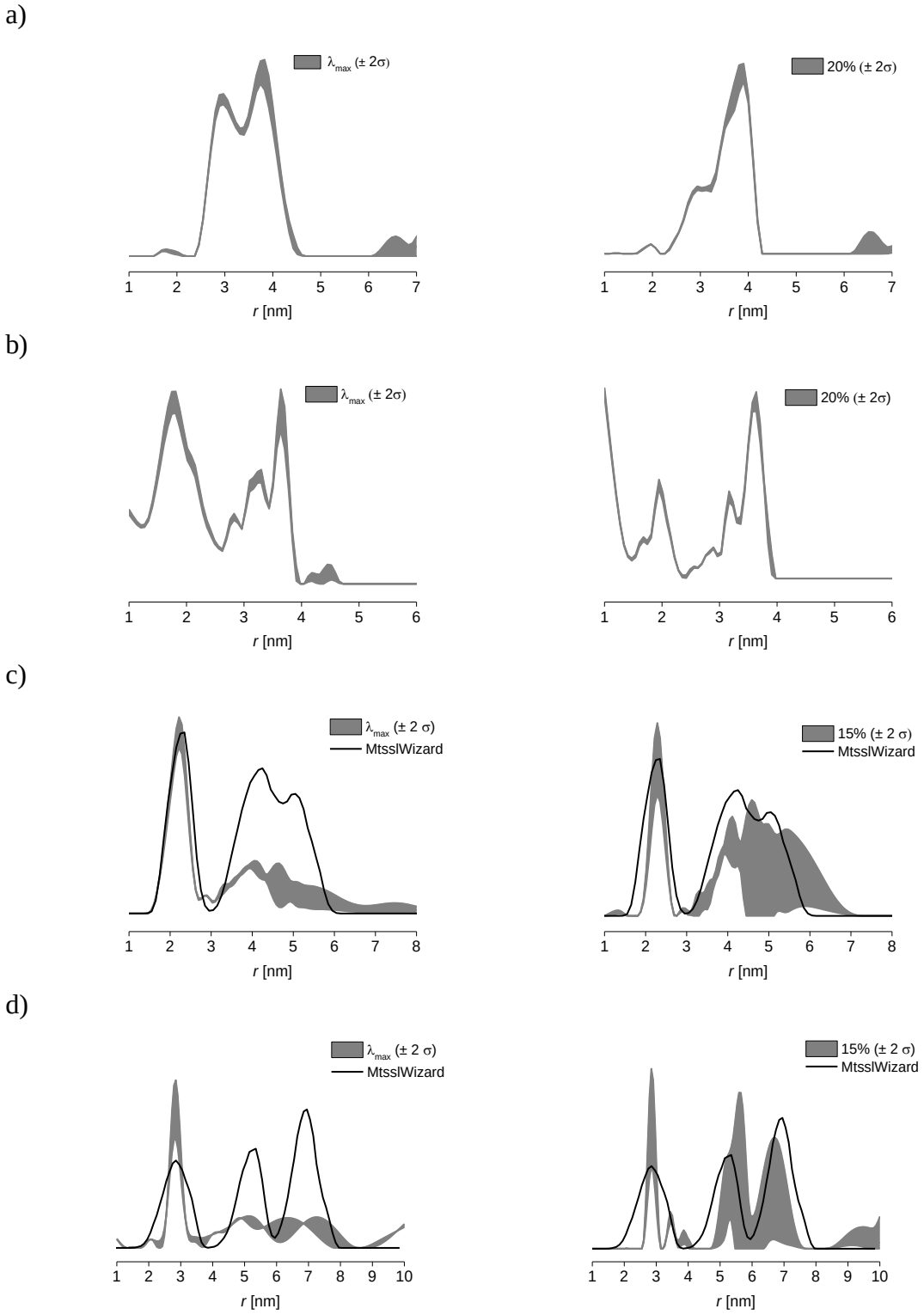

Figure 3.3: Validations for distance distributions PELDOR measurements at X-band using an MD5 resonator with λ_{max} and 20% on **106** a), **107** b), MscS S196R1 c) and sWza Q335R1 d) with MtsslWizard modelling from. The grey areas represent the error bars for each distance; the distance distributions in the white areas delineated by the grey-shaded error bars are stable to changes in background correction parameters, and thus are more reliable.

a)

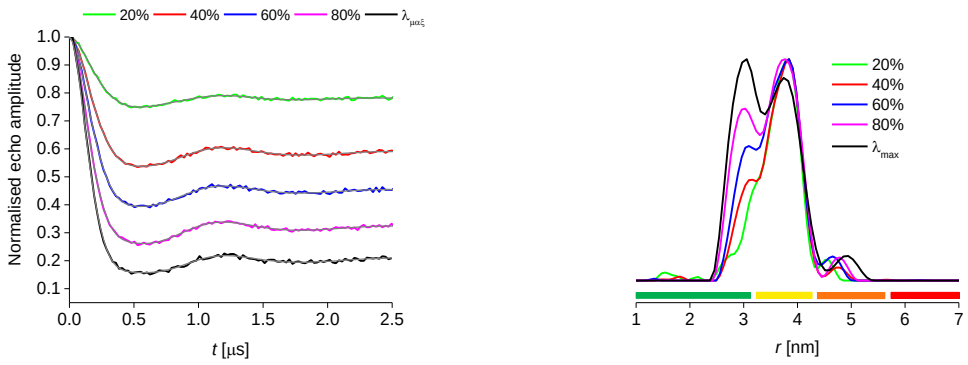

b)

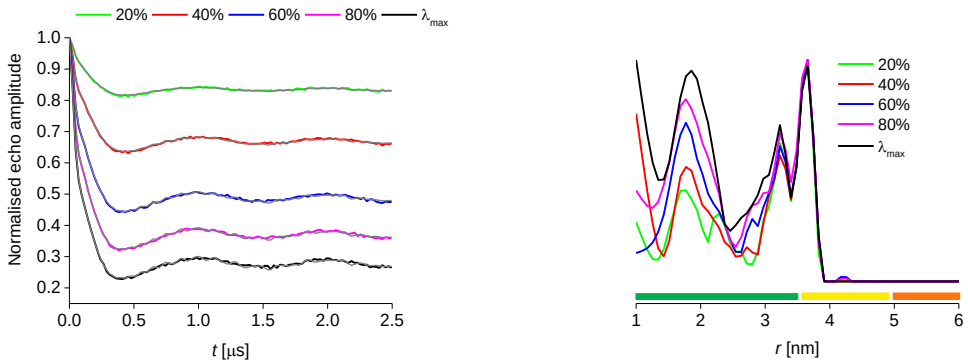

Figure 3.4: Background corrected PELDOR data with fit and distance distributions for tetra-radicals **106** a) and **107** b) measured at X-band (MS3 resonator). The coloured bars suggest the reliability of distances recovered.

a)

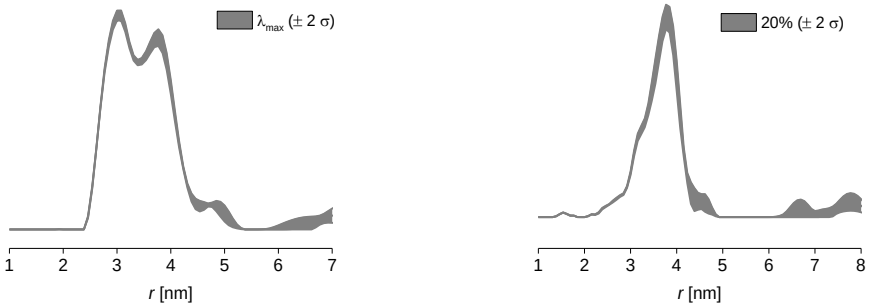

b)

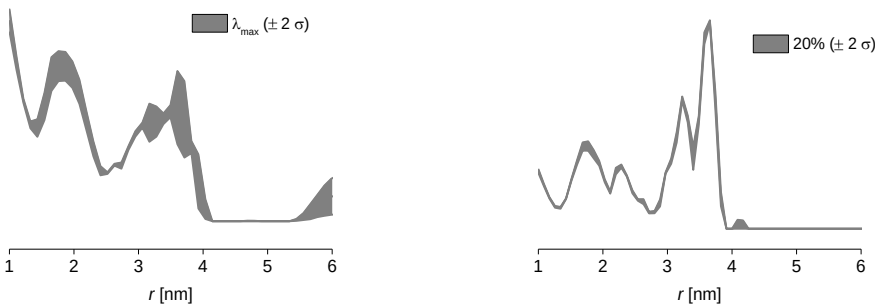

Figure 3.5: Validations for distance distributions for λ_{max} and 20% on **106** a), and **107** b) from PELDOR measurements at X-band with an MS3 resonator. The grey area, representing the error bar, delineates those distance distributions that are stable to changes in processing parameters.

a)

b)

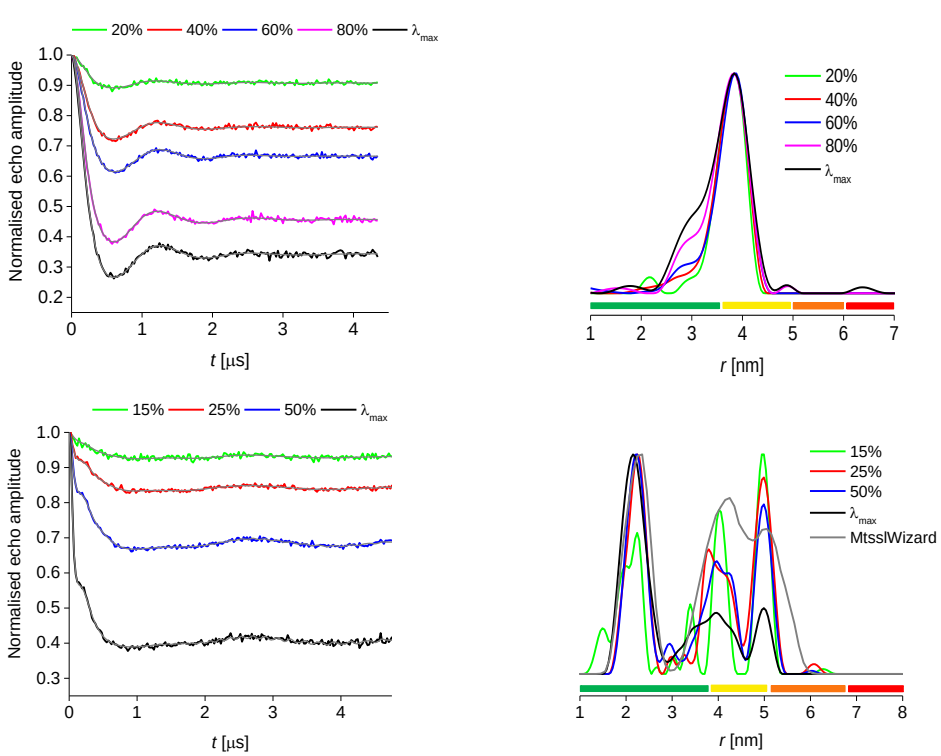

Figure 3.6: Background corrected PELDOR data with fit and corresponding distance distributions for tetra-radical **106** a) and MscS S196R1b) measured at Q-band. The coloured bars suggest the reliability of distances recovered.

a)

b)

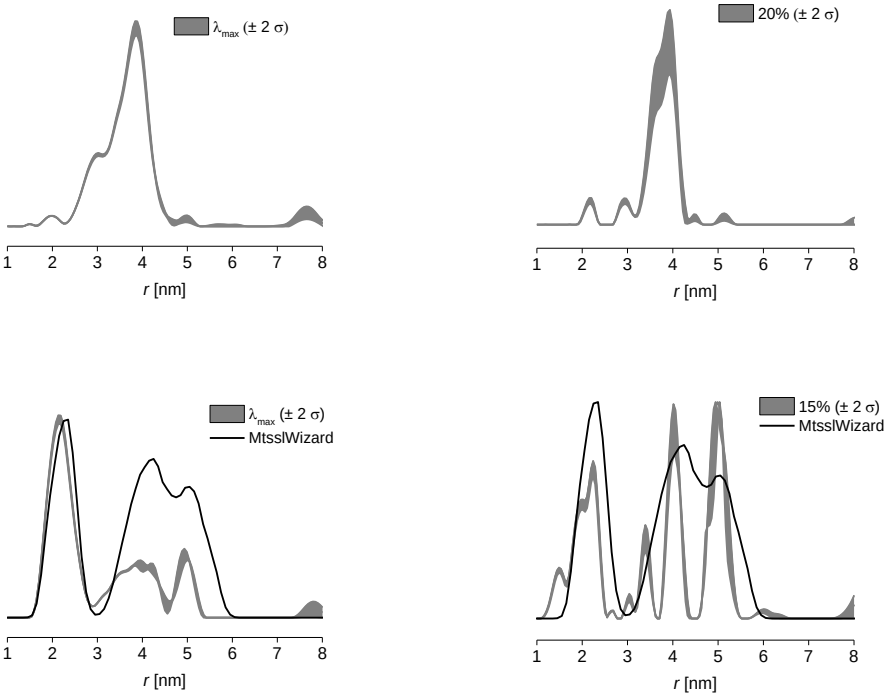

Figure 3.7: Validations for distance distributions for λ_{max} and 20% PELDOR measurements on **106** a), MscS S196R1 b) at Q-band. The grey area, representing the error bar, delineates those distance distributions that are stable to changes in processing parameters.

Recently, technical advances have allowed distance measurements to be expanded from 9 GHz to 34 GHz[80] and 95 GHz.[112] The same λ reduction experiments were performed at 34 GHz (Q-band) on **106** and MscS S196R1 (see Materials and Methods A.2.3.1). The sensitivity found at higher frequencies gives access to longer measuring time windows, particularly important for extraction of long distances in the heptameric channel protein MscS S196R1 (Figure 3.6). Here, efforts were focused on **106** and MscS S196R1. Validations of distance distributions reported in Figure 3.7 confirm the observations deduced from λ reduction experiments performed at X-band.The distance data from the chemical model systems (Figure 3.2 and Figure 3.4, a) and b) and Figure 3.6 a)) clearly demonstrates that reducing λ decreases the modulation depth Δ and diminishes the intensity of the ghost distance peaks introduced by multi-spin effects. When the same experiments performed on the biological systems show that decreasing λ allowed for the recovery of the second and third distance peaks (4.2 and 5 nm for MscS S196R1, 5.2 and 6.9 nm for sWza Q335R1); the fourth distance expected in sWza Q335R1 is, however, not resolved, as expected from the modelling performed on the crystal structure (Figure 3.2). This demonstrates the significant uncertainty related to the larger distances due to limited observation times, particularly when it comes to biological systems where all but the first distance are out of the range with a reliable shape of the PELDOR distance distribution (Figure 3.2). To test whether the observed behaviour was simply due to the limited time window achievable in the experiments, simulations based on geometric models mimicking the model systems and channel proteins[78b] were performed using a time window sufficient to resolve mean and width (Figure 3.8, see Materials and Methods A.2.2). Simulations also prove that additional ghost peaks and improper amplitudes in the distance distributions from multiply labelled systems obtained with increasing λ reported in Figure 3.2 to Figure 3.6 arise from multi-spin effects, as the observation time in the simulations was chosen long enough to avoid truncation artefacts. Additionally, distance distributions obtained from simulations show the expected true distributions upon reducing λ (grey traces in Figure 3.8). These are modelled from the geometry of the chemical model systems as tetrahedron (**106**) and rectangle (**107**) and as heptagon and octagon for MscS S196R1 and sWza Q335R1, respectively. These distributions are reasonably close to those modelled on the basis of the crystal structure of the membrane channel protein using MtsslWizard.[111]

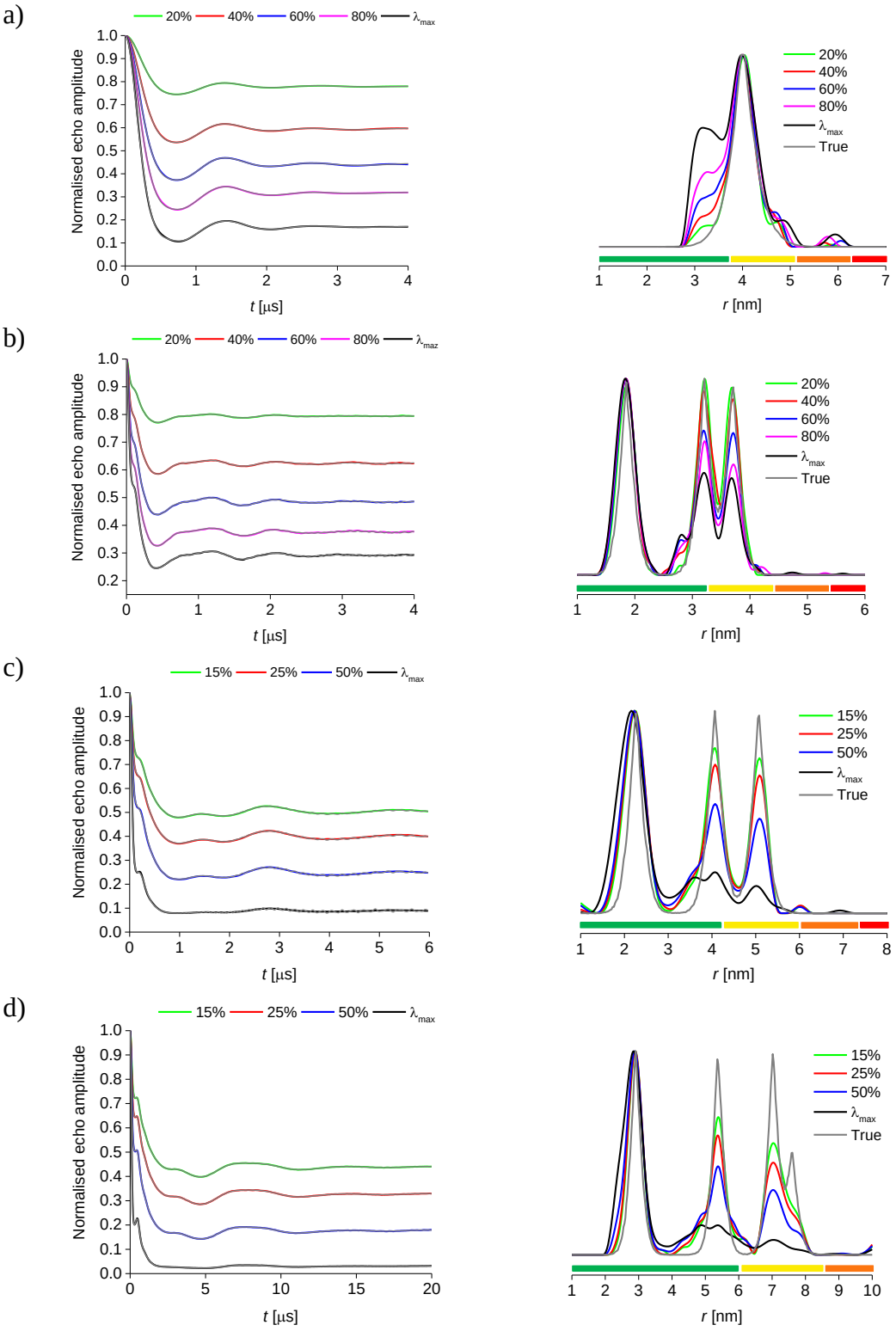

Figure 3.8: Simulated λ_{max} and λ reduced PELDOR traces with corresponding distance distributions (coloured) for a tetrahedron a), rectangle b), heptagon c) and octagon d) and expected true distance distributions (black). The coloured bars suggest the reliability of distances recovered.

Results for λ reduction experiments performed on these systems demonstrate that reduction of λ diminishes ghost distance peaks together with additional broadenings and appears to be particularly effective on the biological systems, where reliable distance intensity beyond the modal distance is recovered as confirmed by comparison with crystal structure based models. Suppression of ghost distance peaks comes at the price of reducing the signal modulation depth, thus decreasing the modulation effect with respect to noise and compromising sensitivity. This implies that measurements should be performed for a long averaging time to obtain the best achievable signal-to-noise ratio to minimise the loss in sensitivity and allow accurate extraction of distance distributions.[78a] Biological systems would particularly suffer from the necessity of a very good signal-to-noise level as they generally require longer averaging times due to faster relaxation, low sample concentration and often presence of incomplete labelling.[2b, 68] The impact of λ reduction on the experimental sensitivity is quantified in Section 3.3.4.

3.3.2 Multi-spin effects suppression by power-scaling

Power-scaling was tested on PELDOR traces obtained by λ reduced experiments with the aim to find the optimum combination of power-scaling and λ reduction. Comparison between non power-scaled and power-scaled distance distributions from tetraradical model systems **106**, **107** and biological systems MscS S196R1and sWza Q335R1 is reported in Figure 3.9. Power-scaling of **106** and **107** λ_{max} traces appears to reduce broadenings and additional ghost peaks intensities, however it is not as efficient as when using 20% of λ_{max}. Power-scaling of λ_{max} traces for MscS S196R1 and sWza Q335R1, on the other hand, does not give improvement to the same extent as when compared to the model systems (Figure 3.9). In particular power-scaling of the λ_{max} trace for sWza Q335R1 leads to misleading results as it suggests the presence of only two distance peaks, with the mean of the second peak not matching the expected distances.

Results suggest, in agreement with previous studies,[78a] that power-scaling applied on experiments with λ_{max} offers some improvement on the tetraradical model systems but its effectiveness is greatly reduced for systems bearing more than four spins. For these systems some intentional reduction of inversion efficiency λ is required in combination with power-scaling for extraction of accurate distance distributions.[78a]

a)

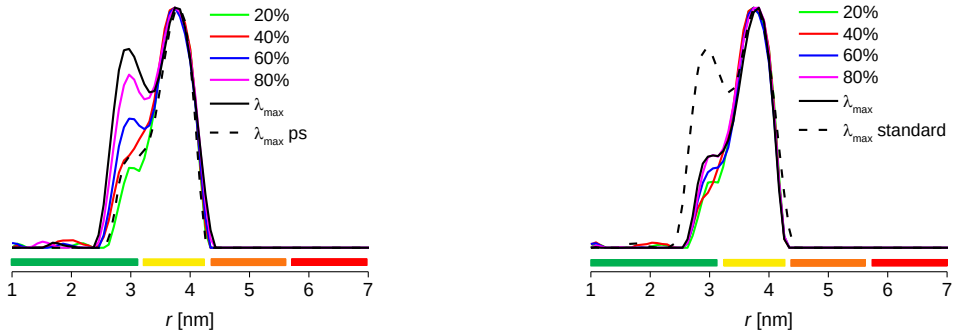

b)

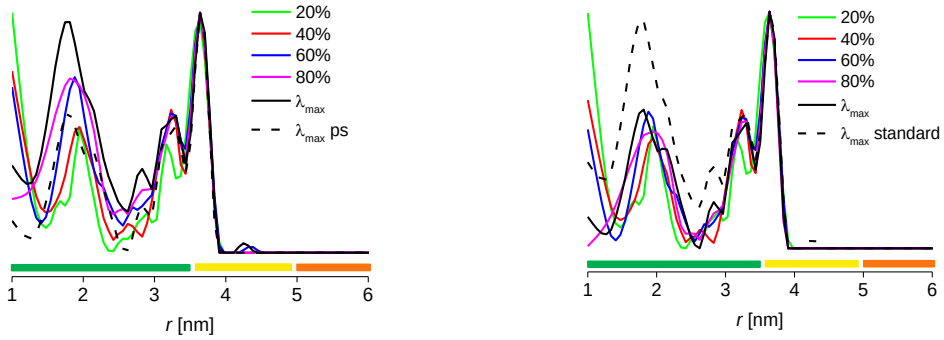

c)

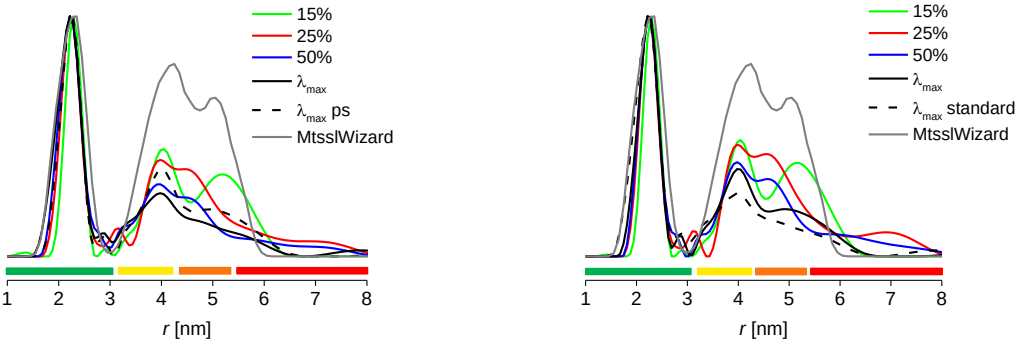

d)

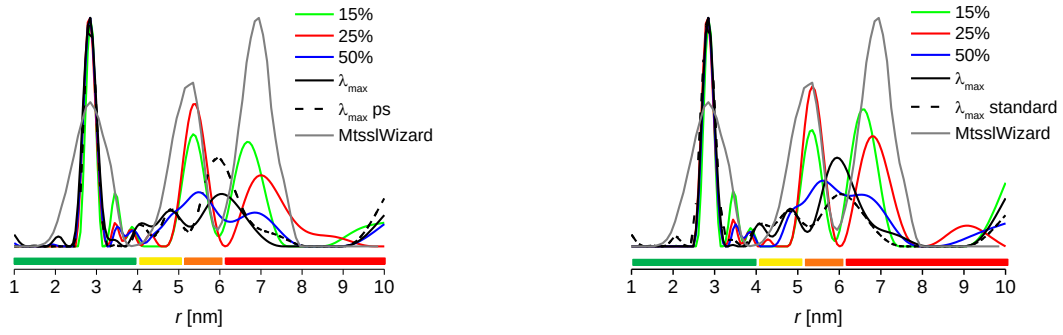

Figure 3.9: Distance distributions without (left) and with (right) power-scaling for tetraradicals **106** a) and **107** b), MscS 196R1 c), and sWza Q335R1 d) obtained from PELDOR measurements performed at X-band using an MD5 resonator. The coloured bars suggest the reliability of distances recovered.

The effects of the combination of these two approaches to suppress multi-spin effects on measurement sensitivity and distance distributions were investigated quantitatively aiming to develop recommendations for the combined use of λ reduction and power-scaling. It becomes important at this stage to calculate and evaluate effects on sensitivity that is highly affected by the λ reduction experiments. This was done by performing simulations on symmetric polygons bearing three to eight spins (see Materials and Methods A.2.2). Noise levels were varied between 0, 1 and 3% (Figure 3.10 to Figure 3.15). These simulations show that with a low noise level (0 and 1%) power-scaling efficiently suppresses distance distribution artefacts (ghost distances and broadenings) in measurements with $\lambda < 2\ (1/(N\text{-}1))$. This is quite remarkable as this tolerates substantial contributions from multi-spin effects (the maximum of the two-spin contribution manifests at $\lambda = (1/(N\text{-}1))$ and already here substantial distortions are observed in non-power-scaled data). With increasing noise (3%) ghost distances (or broadening and vanishing of distances) appear to be efficiently reduced in measurements with $\lambda < (1/(N\text{-}1))$. This was previously recommended as a maximum for the choice of λ.[113]

In the absence of noise power-scaling effectively suppresses ghost distances in systems bearing less than six spin centres, at $\lambda < 0.5$. When 1% noise is introduced in the simulated traces power-scaling is effective only for systems with $N < 4$. For systems with larger N power-scaling needs to be combined with reducing λ to 0.3 or even 0.2 to suppress ghost distances. Additionally combination of power-scaling and very small λ has a negative impact on sensitivity, as shown in the sensitivity quantifications. The relationship between λ and sensitivity shows that power-scaling comes at the price of reduced sensitivity because of the reduction in Δ which is larger than the reduction in noise (see Figure 3.10 to Figure 3.15 d) and e)).

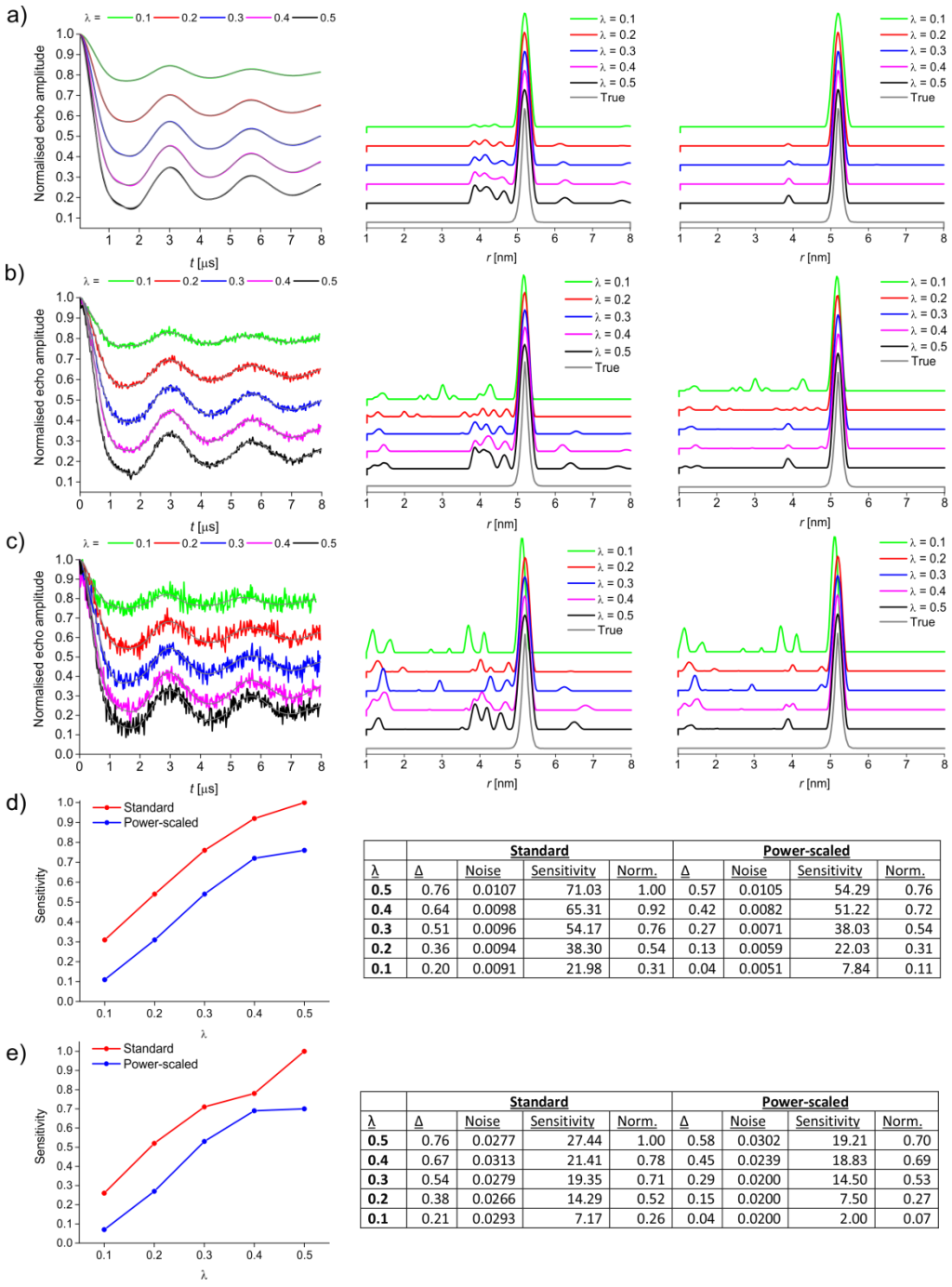

	Standard				Power-scaled			
λ	Δ	Noise	Sensitivity	Norm.	Δ	Noise	Sensitivity	Norm.
0.5	0.76	0.0107	71.03	1.00	0.57	0.0105	54.29	0.76
0.4	0.64	0.0098	65.31	0.92	0.42	0.0082	51.22	0.72
0.3	0.51	0.0096	54.17	0.76	0.27	0.0071	38.03	0.54
0.2	0.36	0.0094	38.30	0.54	0.13	0.0059	22.03	0.31
0.1	0.20	0.0091	21.98	0.31	0.04	0.0051	7.84	0.11

	Standard				Power-scaled			
λ	Δ	Noise	Sensitivity	Norm.	Δ	Noise	Sensitivity	Norm.
0.5	0.76	0.0277	27.44	1.00	0.58	0.0302	19.21	0.70
0.4	0.67	0.0313	21.41	0.78	0.45	0.0239	18.83	0.69
0.3	0.54	0.0279	19.35	0.71	0.29	0.0200	14.50	0.53
0.2	0.38	0.0266	14.29	0.52	0.15	0.0200	7.50	0.27
0.1	0.21	0.0293	7.17	0.26	0.04	0.0200	2.00	0.07

Figure 3.10: Triangle - Background corrected PELDOR data with fit (left), distance distributions without (standard, middle) and with power-scaling (right) for 0% (a), 1% (b) and 3% (c) noise. Graphs showing the relationship between λ and sensitivity for 1% (d, left) and 3% (e, left) noise. Tables (d, e, right) with corresponding values for λ, noise and sensitivity with and without normalisation (Norm.).

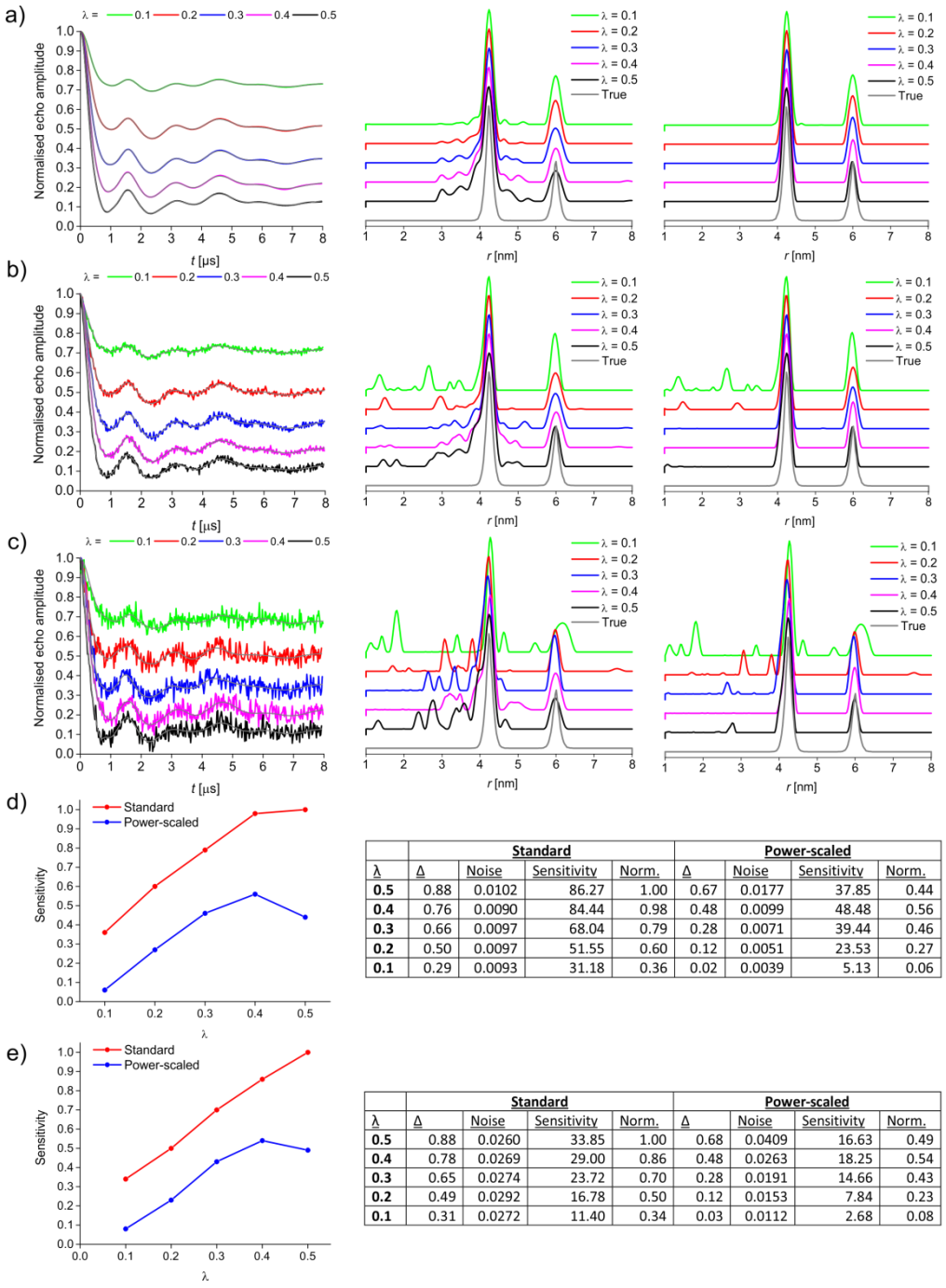

	Standard				Power-scaled			
λ	Δ	Noise	Sensitivity	Norm.	Δ	Noise	Sensitivity	Norm.
0.5	0.88	0.0102	86.27	1.00	0.67	0.0177	37.85	0.44
0.4	0.76	0.0090	84.44	0.98	0.48	0.0099	48.48	0.56
0.3	0.66	0.0097	68.04	0.79	0.28	0.0071	39.44	0.46
0.2	0.50	0.0097	51.55	0.60	0.12	0.0051	23.53	0.27
0.1	0.29	0.0093	31.18	0.36	0.02	0.0039	5.13	0.06

	Standard				Power-scaled			
λ	Δ	Noise	Sensitivity	Norm.	Δ	Noise	Sensitivity	Norm.
0.5	0.88	0.0260	33.85	1.00	0.68	0.0409	16.63	0.49
0.4	0.78	0.0269	29.00	0.86	0.48	0.0263	18.25	0.54
0.3	0.65	0.0274	23.72	0.70	0.28	0.0191	14.66	0.43
0.2	0.49	0.0292	16.78	0.50	0.12	0.0153	7.84	0.23
0.1	0.31	0.0272	11.40	0.34	0.03	0.0112	2.68	0.08

Figure 3.11: Square - Background corrected PELDOR data with fit (left), distance distributions without (standard, middle) and with power-scaling (right) for 0% (a), 1% (b) and 3% (c) noise. Graphs showing the relationship between λ and sensitivity for 1% (d, left) and 3% (e, left) noise. Tables (d, e, right) with corresponding values for λ, noise and sensitivity with and without normalisation (Norm.).

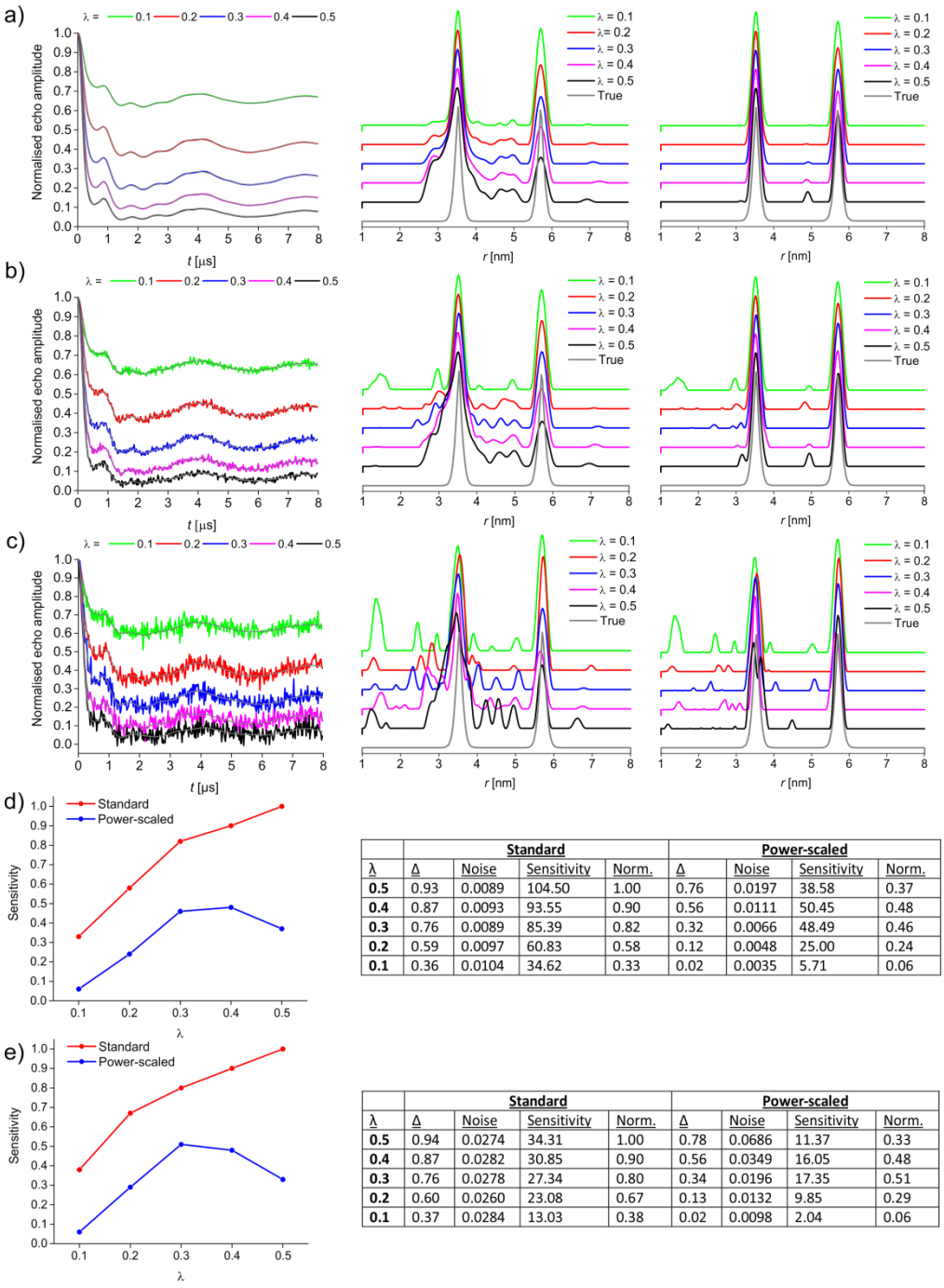

	Standard				Power-scaled			
λ	Δ	Noise	Sensitivity	Norm.	Δ	Noise	Sensitivity	Norm.
0.5	0.93	0.0089	104.50	1.00	0.76	0.0197	38.58	0.37
0.4	0.87	0.0093	93.55	0.90	0.56	0.0111	50.45	0.48
0.3	0.76	0.0089	85.39	0.82	0.32	0.0066	48.49	0.46
0.2	0.59	0.0097	60.83	0.58	0.12	0.0048	25.00	0.24
0.1	0.36	0.0104	34.62	0.33	0.02	0.0035	5.71	0.06

	Standard				Power-scaled			
λ	Δ	Noise	Sensitivity	Norm.	Δ	Noise	Sensitivity	Norm.
0.5	0.94	0.0274	34.31	1.00	0.78	0.0686	11.37	0.33
0.4	0.87	0.0282	30.85	0.90	0.56	0.0349	16.05	0.48
0.3	0.76	0.0278	27.34	0.80	0.34	0.0196	17.35	0.51
0.2	0.60	0.0260	23.08	0.67	0.13	0.0132	9.85	0.29
0.1	0.37	0.0284	13.03	0.38	0.02	0.0098	2.04	0.06

Figure 3.12: Pentagon - Background corrected PELDOR data with fit (left), distance distributions without (standard, middle) and with power-scaling (right) for 0% (a), 1% (b) and 3% (c) noise. Graphs showing the relationship between λ and sensitivity for 1% (d, left) and 3% (e, left) noise. Tables (d, e, right) with corresponding values for λ, noise and sensitivity with and without normalisation (Norm.).

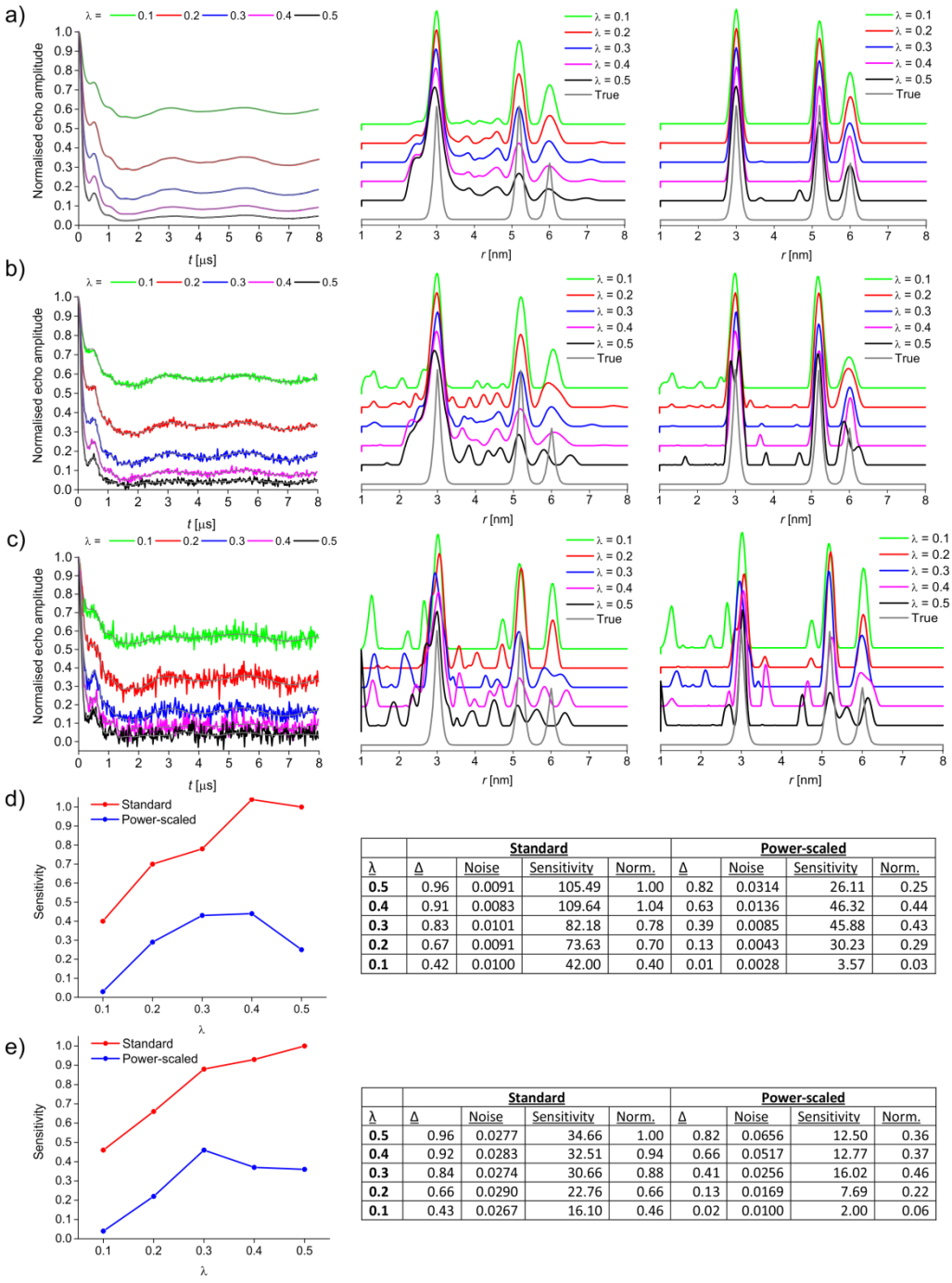

	Standard				Power-scaled			
λ	Δ	Noise	Sensitivity	Norm.	Δ	Noise	Sensitivity	Norm.
0.5	0.96	0.0091	105.49	1.00	0.82	0.0314	26.11	0.25
0.4	0.91	0.0083	109.64	1.04	0.63	0.0136	46.32	0.44
0.3	0.83	0.0101	82.18	0.78	0.39	0.0085	45.88	0.43
0.2	0.67	0.0091	73.63	0.70	0.13	0.0043	30.23	0.29
0.1	0.42	0.0100	42.00	0.40	0.01	0.0028	3.57	0.03

	Standard				Power-scaled			
λ	Δ	Noise	Sensitivity	Norm.	Δ	Noise	Sensitivity	Norm.
0.5	0.96	0.0277	34.66	1.00	0.82	0.0656	12.50	0.36
0.4	0.92	0.0283	32.51	0.94	0.66	0.0517	12.77	0.37
0.3	0.84	0.0274	30.66	0.88	0.41	0.0256	16.02	0.46
0.2	0.66	0.0290	22.76	0.66	0.13	0.0169	7.69	0.22
0.1	0.43	0.0267	16.10	0.46	0.02	0.0100	2.00	0.06

Figure 3.13: Hexagon – Background corrected PELDOR data with fit (left), distance distributions without (standard, middle) and with power-scaling (right) for 0% (a), 1% (b) and 3% (c) noise. Graphs showing the relationship between λ and sensitivity for 1% (d, left) and 3% (e, left) noise. Tables (d, e, right) with corresponding values for λ, noise and sensitivity with and without normalisation (Norm.).

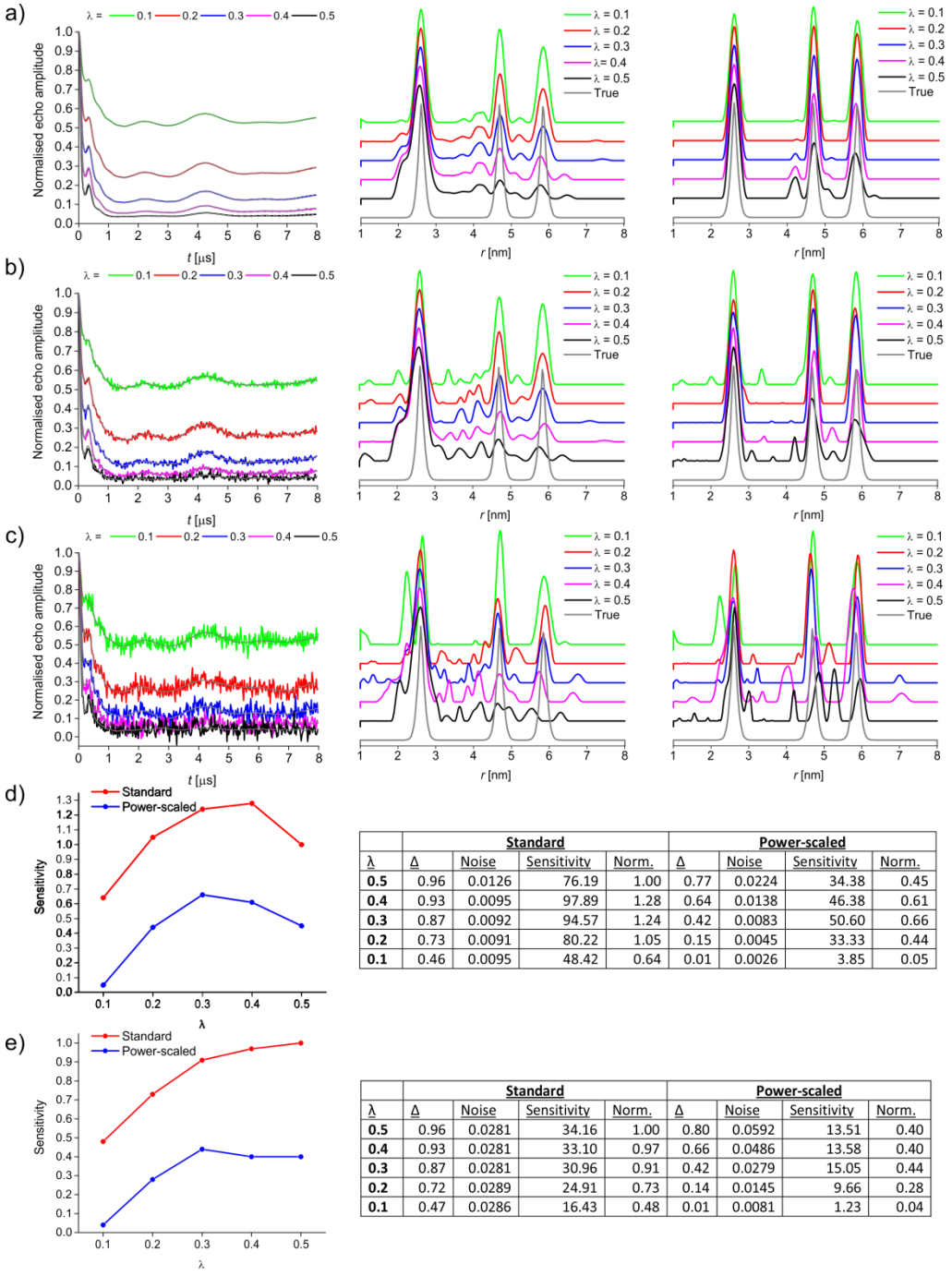

	Standard				Power-scaled			
λ	Δ	Noise	Sensitivity	Norm.	Δ	Noise	Sensitivity	Norm.
0.5	0.96	0.0126	76.19	1.00	0.77	0.0224	34.38	0.45
0.4	0.93	0.0095	97.89	1.28	0.64	0.0138	46.38	0.61
0.3	0.87	0.0092	94.57	1.24	0.42	0.0083	50.60	0.66
0.2	0.73	0.0091	80.22	1.05	0.15	0.0045	33.33	0.44
0.1	0.46	0.0095	48.42	0.64	0.01	0.0026	3.85	0.05

	Standard				Power-scaled			
λ	Δ	Noise	Sensitivity	Norm.	Δ	Noise	Sensitivity	Norm.
0.5	0.96	0.0281	34.16	1.00	0.80	0.0592	13.51	0.40
0.4	0.93	0.0281	33.10	0.97	0.66	0.0486	13.58	0.40
0.3	0.87	0.0281	30.96	0.91	0.42	0.0279	15.05	0.44
0.2	0.72	0.0289	24.91	0.73	0.14	0.0145	9.66	0.28
0.1	0.47	0.0286	16.43	0.48	0.01	0.0081	1.23	0.04

Figure 3.14: Heptagon – Background corrected PELDOR data with fit (left), distance distributions without (standard, middle) and with power-scaling (right) for 0% (a), 1% (b) and 3% (c) noise. Graphs showing the relationship between λ and sensitivity for 1% (d, left) and 3% (e, left) noise. Tables (d, e, right) with corresponding values for λ, noise and sensitivity with and without normalisation (Norm.).

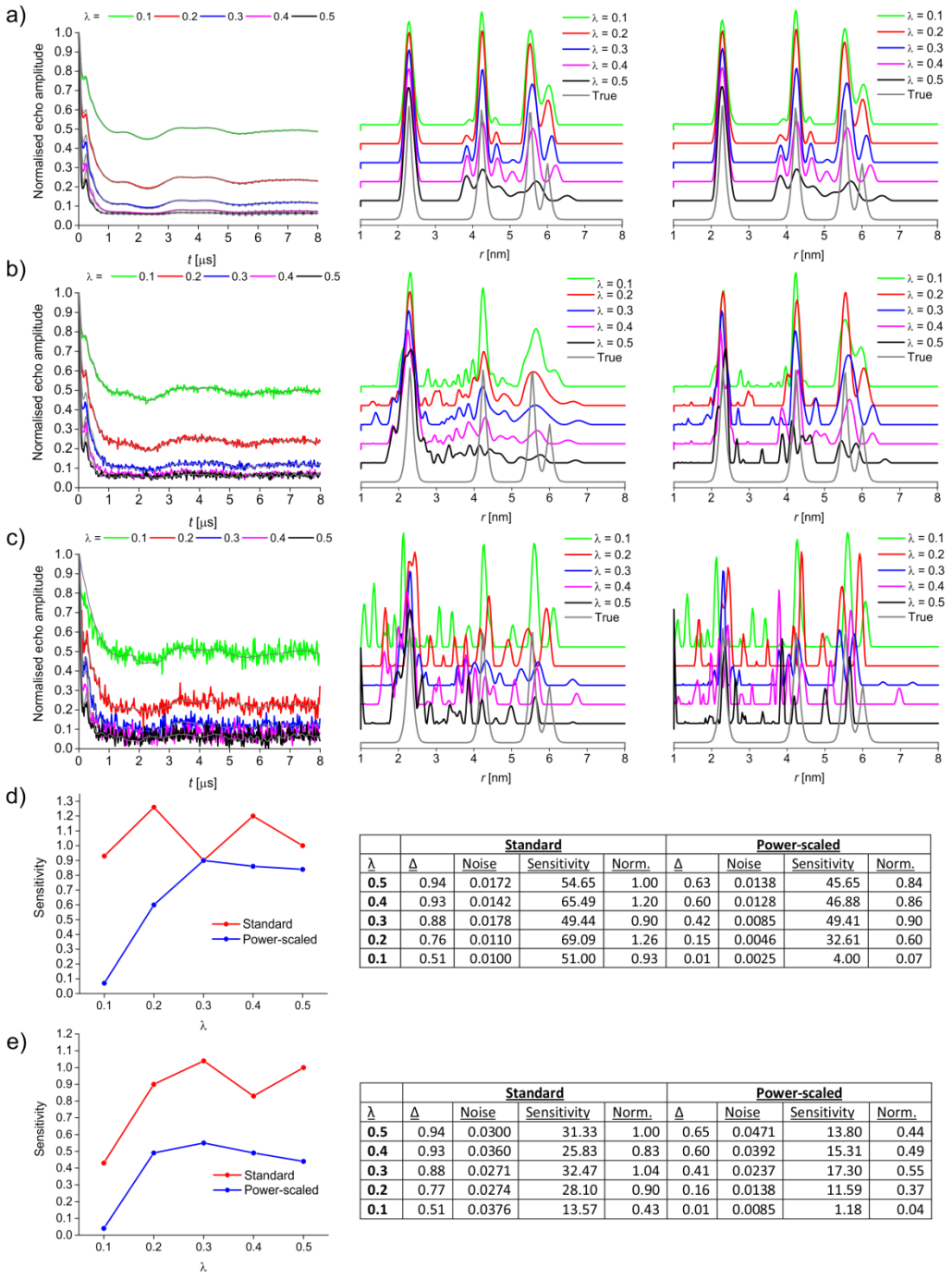

	Standard				Power-scaled			
λ	Δ	Noise	Sensitivity	Norm.	Δ	Noise	Sensitivity	Norm.
0.5	0.94	0.0172	54.65	1.00	0.63	0.0138	45.65	0.84
0.4	0.93	0.0142	65.49	1.20	0.60	0.0128	46.88	0.86
0.3	0.88	0.0178	49.44	0.90	0.42	0.0085	49.41	0.90
0.2	0.76	0.0110	69.09	1.26	0.15	0.0046	32.61	0.60
0.1	0.51	0.0100	51.00	0.93	0.01	0.0025	4.00	0.07

	Standard				Power-scaled			
λ	Δ	Noise	Sensitivity	Norm.	Δ	Noise	Sensitivity	Norm.
0.5	0.94	0.0300	31.33	1.00	0.65	0.0471	13.80	0.44
0.4	0.93	0.0360	25.83	0.83	0.60	0.0392	15.31	0.49
0.3	0.88	0.0271	32.47	1.04	0.41	0.0237	17.30	0.55
0.2	0.77	0.0274	28.10	0.90	0.16	0.0138	11.59	0.37
0.1	0.51	0.0376	13.57	0.43	0.01	0.0085	1.18	0.04

Figure 3.15: Octagon – Background corrected PELDOR data with fit (left), distance distributions without (standard, middle) and with power-scaling (right) for 0% (a), 1% (b) and 3% (c) noise. Graphs showing the relationship between λ and sensitivity for 1% (d, left) and 3% (e, left) noise. Tables (d, e, right) with corresponding values for λ, noise and sensitivity with and without normalisation (Norm.).

For the systems investigated here, when using a combination of power-scaling and λ reduction, the sensitivity was maximum at λ between 0.3 and 0.4. When using lower λ the sensitivity drops significantly. Thus, a combination of power-scaling and λ reduction appears to be efficient for suppression of artefacts when $\lambda < 1/(N\text{-}1)$, but not dramatically smaller.

3.3.3 Multi-spin effects suppression by frequency interchange

The loss in Δ that occurs when trying to reduce multi-spin effects *via* lowering λ suggested to revisit the experimental parameters used for distance measurements in multiply labelled systems. The most commonly used 4-pulse PELDOR experiment[7a, 11] for extraction of inter-spin distances is usually performed by placing the detection pulse sequence at the frequency corresponding to the low field maximum (at X-band, for nitroxides), and the π pump pulse, inverting B spins, on the most populated area of the EPR spectrum (see Materials and Methods A.2.3.1).[24] However, the high fraction of pumped spins achieved in this experiment is the root cause for large multi-spin effects and what is actually countered with lowering λ. On the other hand, swapping the position of detection and pump pulses will place the detection sequence at the frequency corresponding to the most populated area of the EPR spectrum, while pumping on the low filed maximum (see Materials and Methods A.2.3.2). This frequency interchange implies, when compared to the PELDOR experiment, that a lower fraction of B spins is pumped while a higher fraction of A spins is detected. This frequency-interchanged experiment should give an increased sensitivity at similar modulation depths when compared to the reduced λ experiment. This special case of the PELDOR or DEER experiment is **BA**sed on **M**inor **B**road **I**nversion and could be coined BAMBI-DEER.

The frequency-interchanged variant of the PELDOR experiment was tested on the model systems **106** and **107** together with MscS S196R1. First experiments focused on comparing the common PELDOR settings against the frequency-interchanged at X-band using MD5 (Figure 3.16, and validations Figure 3.17) and MS3 resonators (Figure 3.18, validations Figure 3.19). These initial measurements show that the alternative experimental setting leads to reduction in Δ and suppression of ghost distance peaks. Power-scaling of the PELDOR traces from measurements of **106** reported in Figure 3.16 a) and Figure 3.18 a) (black dashed line) appears to give similar results to the non-power-scaled frequency-interchanged ones (solid green line), suggesting that both

methods are similarly effective in suppressing ghost peaks. Validation of the non-power-scaled traces obtained on the model systems (Figure 3.17 a), b) and Figure 3.19 a), b)) proves the frequency-interchanged experiments give access to reliable and accurate extraction of inter-spin distances in systems with up to four spin labels.

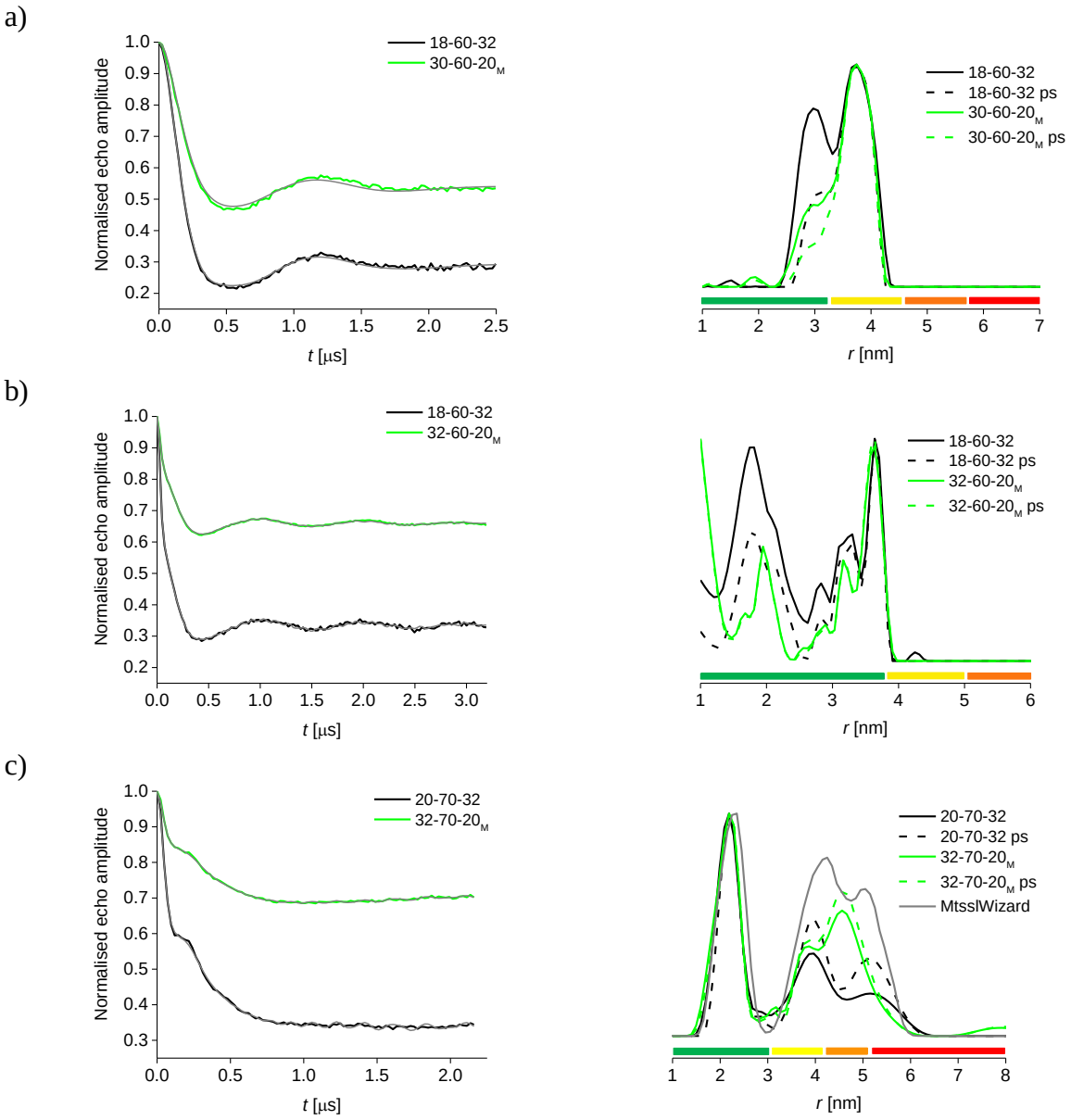

Figure 3.16: Comparison between background corrected traces and corresponding distance distributions without (solid line) and with power-scaling (dashed line) obtained by performing PELDOR (black) and frequency-interchanged (green) experiments with an MD5 resonator X-band frequencies for tetraradicals 106 a), 107 b) and MscS S196R1 c). The legend reports in the following order: pump pulse length – pulse offset – detection π pulse length. The subscript M indicates the position of the pump pulse on the maximum of the nitroxide field sweep spectrum. The coloured bars suggest the reliability of distances recovered.

a)

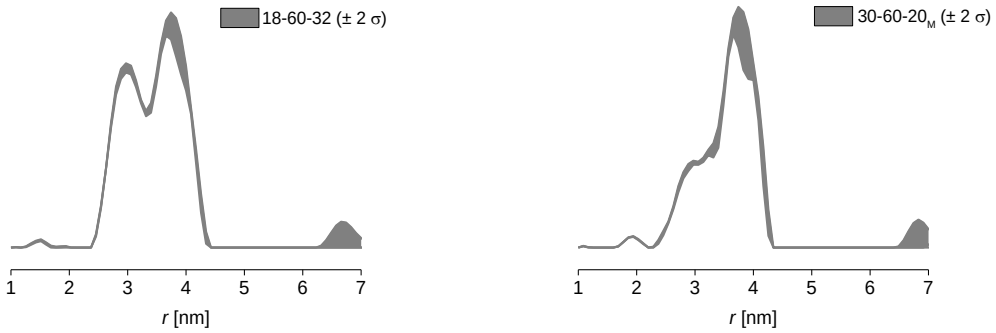

b)

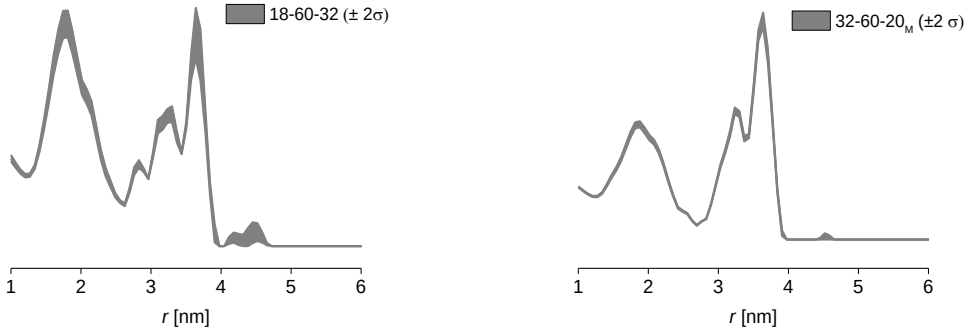

c)

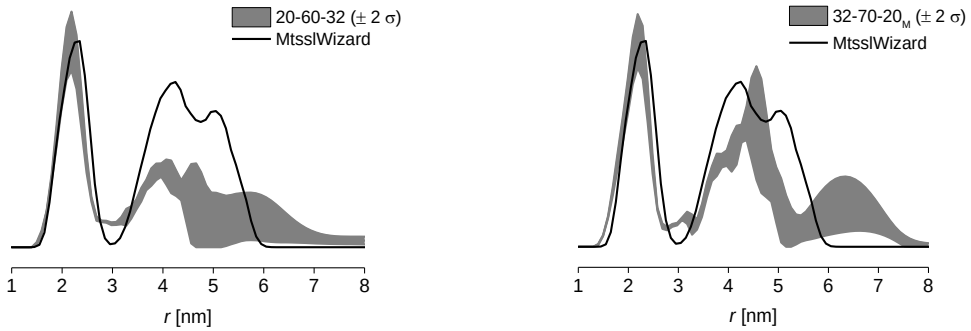

Figure 3.17: Validation of distance distributions obtained from PELDOR (left) and frequency-interchanged experiments on **106** a), **107** b) and MscS S196R1 at X-band (MD5 resonator). The grey areas represent the error bars for each distance; the distance distributions within the white areas are stable to changes in background correction parameters. The subscript M indicates the position of the pump pulse on the maximum of the nitroxide field sweep spectrum.

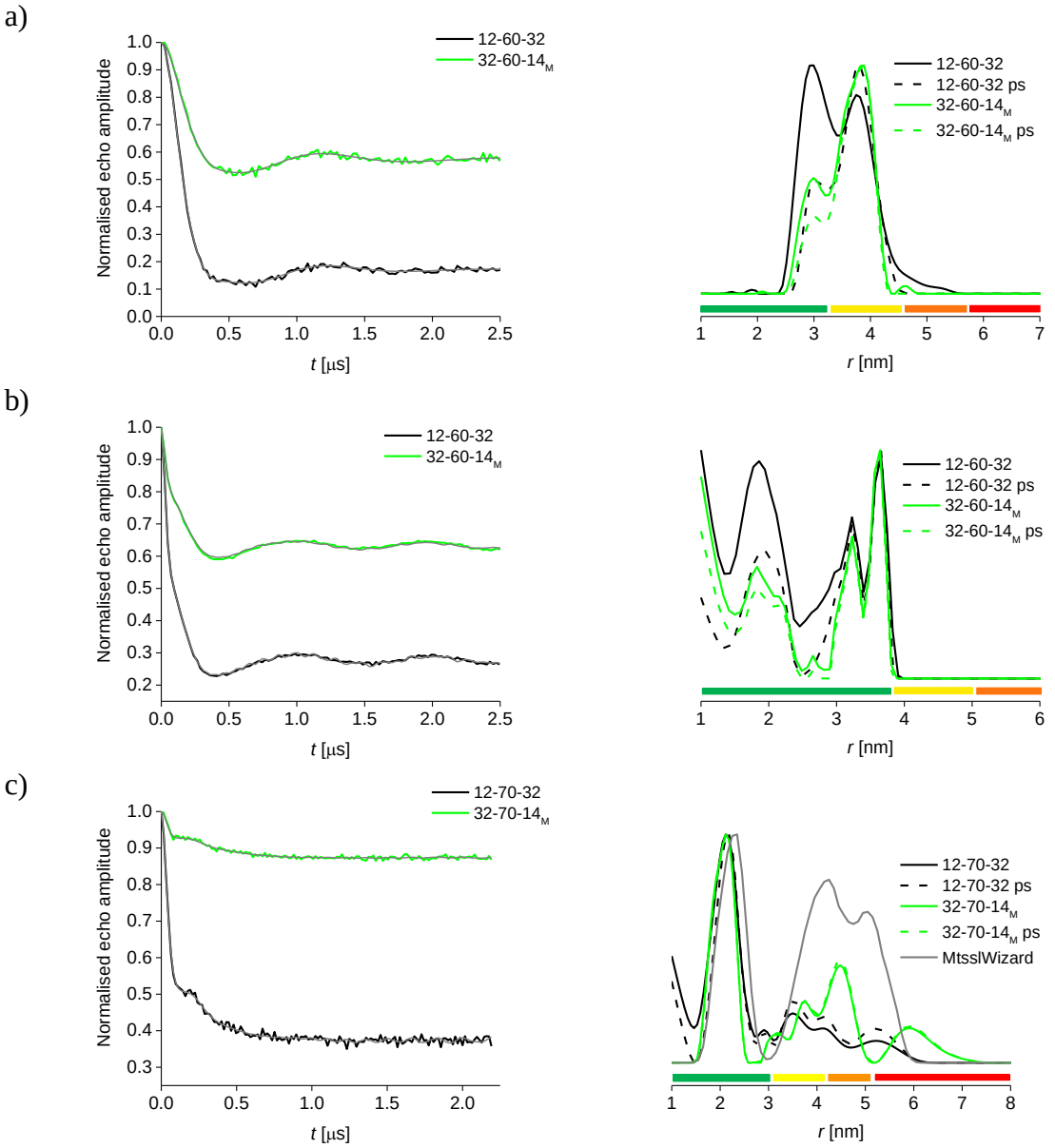

Figure 3.18: Comparison between background corrected traces and corresponding distance distributions without (solid line) and with power-scaling (dashed line) obtained performing PELDOR distance measurements using PELDOR (black) and frequency-interchanged (green) experiments with an MS3 resonator at X-band frequencies for tetraradicals **106** a), **107** b) and MscS S196R1 c). The legend reports the pump pulse length – pulse offset – detection π pulse length. The subscript M indicates the position of the pump pulse on the maximum of the nitroxide field sweep spectrum. The coloured bars suggest the reliability of distances recovered. The subscript M indicates the position of the pump pulse on the maximum of the nitroxide field sweep spectrum.

a)

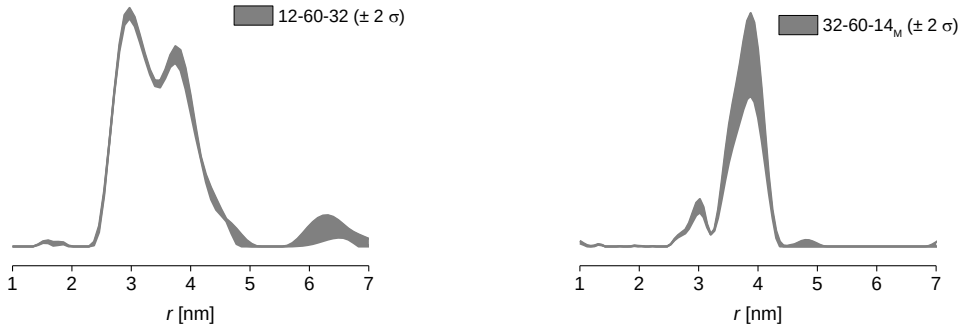

b)

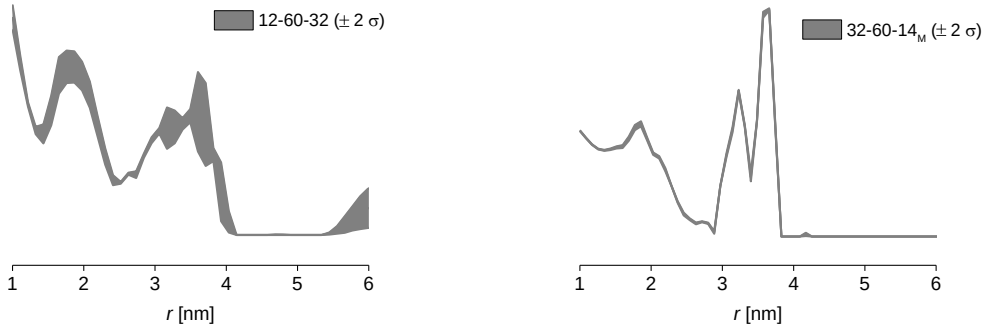

c)

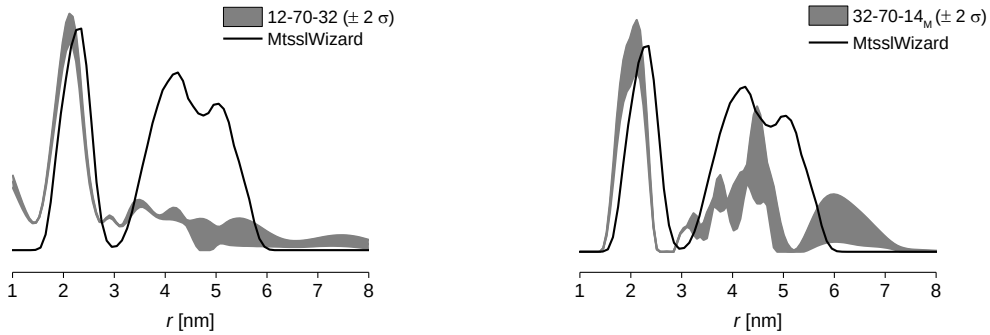

Figure 3.19: Validation of distance distributions obtained from PELDOR (left) and frequency-interchanged experiments on **106** a), **107** b) and MscS S196R1 at X-band (MS3 resonator). The grey area, representing the error bar, delineates those distance distributions that are stable to changes in processing parameters. The subscript M indicates the position of the pump pulse.

For MscS S196R1 conclusions cannot be firmly drawn because of the short measuring time window which introduces cut-off artefacts. Accurate extraction of long distances requires long measuring time windows to resolve the corresponding dipolar frequencies. If a too short time window is measured only part of an oscillation can be resolved possibly introducing cut-off artefacts. Background correction might lead to fitting an exponential that enhances the oscillatory behaviour of the end of the trace that can be interpreted as a dipolar oscillation and translated into a long distance peak. On

the other hand, a truncated oscillation might be fitted and removed as part of the background correction process. It was suspected that the mismatch between the second and third distance peaks from the PELDOR distance distributions of MscS S196R1 at X-band and those modelled by MtsslWizard (Figure 3.16 and Figure 3.18) could have been introduced by truncation of the time trace. To verify if the shift was related to cut-off artefacts the same experiments were performed at Q-band frequencies on **106** and MscS S196R1 allowing a longer measuring time window of 4.2 µs (Figure 3.20). Figure 3.20 shows that the mean of the longer distance peaks recovered by the frequency-interchanged experiment are now in good agreement with those expected from the MtsslWizard model, proving that the discrepancy found at X-band (Figure 3.16 and Figure 3.18) was indeed related to truncation of time windows. Additionally, Figure 3.20 shows that the frequency-interchanged experiment at Q-band introduces similar improvements as observed at X-band in recovering accurate distances from multiply labelled systems.

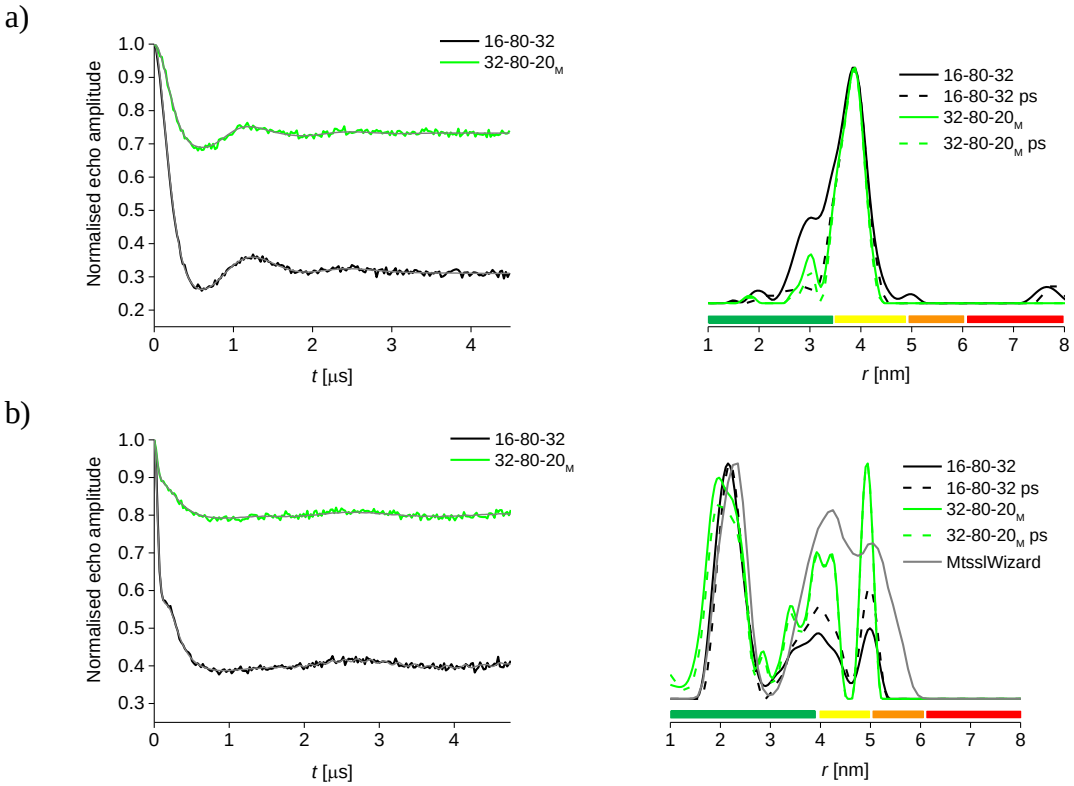

Figure 3.20: Background corrected traces and distance distributions without (solid line) and with power-scaling (dashed line) from PELDOR (black) and frequency-interchanged (green) experiments at Q-band for tetraradical **106** a) and MscS S196R1 b). The legend reports pump pulse length – pulse offset – detection π pulse. The subscript M indicates the pump pulse being on maximum of field sweep. The coloured bars suggest the reliability of distances recovered.

a)

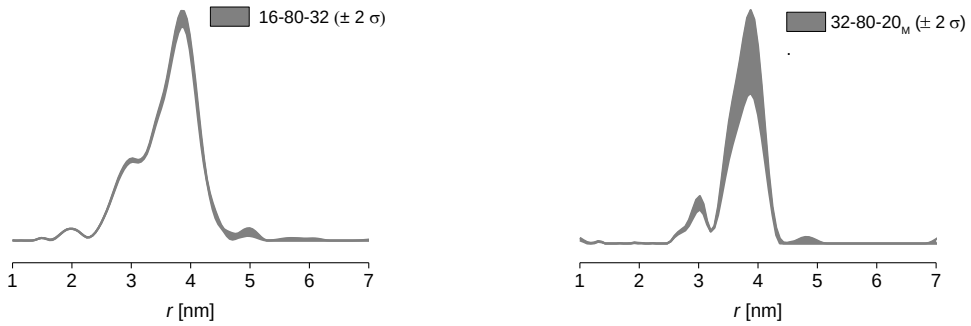

b)

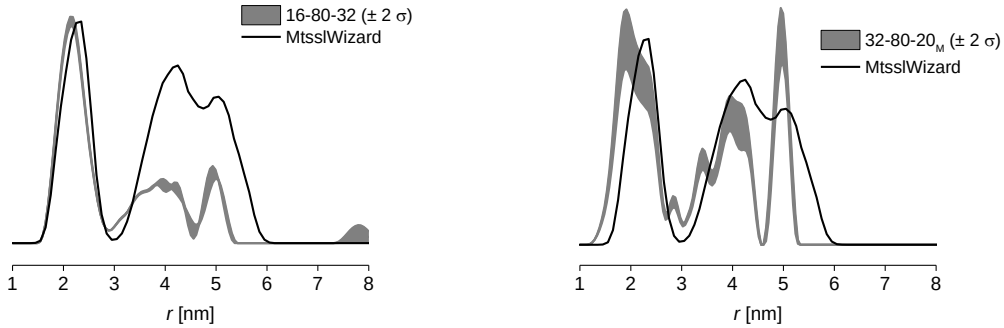

Figure 3.21: Validation of distance distributions obtained from PELDOR (left) and frequency-interchanged experiments on **106** a) and MscS S196R1 b) at Q-band. The grey areas represent the error bars for each distance; the distance distributions within the white areas are stable to changes in background correction parameters. The subscript M indicates the position of the pump pulse on the maximum of the nitroxide field sweep spectrum.

While the distance ghost peak in the PELDOR experiment on **106** (black trace in Figure 3.20) is less pronounced than the one obtained for the same experiment at X-band (Figure 3.16 and Figure 3.18), due to slightly lower achievable λ and a different spectral shape, MscS S196R1 still lacks intensity of the two longer distances at Q-band. These can be reliably recovered by the frequency-interchanged experiment, where the integrals of the longer distance peaks are recovered and their means are in good agreement with the modelling. The frequency-interchanged experiment also suppresses broadenings present in the distance distributions obtained from the PELDOR experiment to the same extent as power-scaling of the PELDOR experiment (Figure 3.20).Validation of the distance distributions obtained from measurements at Q-band shows the accuracy and stability of the distance distributions derived from of the frequency-interchanged experiments and confirms the suppression of the ghost distance

peak for **106** and recovery of the integrals of the longer distance peaks for MscS S196R1 (Figure 3.21).

3.3.4 Comparison of frequency-interchanged and λ reduction experiments

The performance of experiments based on a minor broad inversion shows consistent improvement in distance distributions when compared to PELDOR experiments at λ_{max} (Figure 3.22). The comparison of the frequency-interchanged with the λ reduction experiments with similar λ values shows that both methods reduce the modulation depth Δ together with broadenings and ghost distance peaks in a similar fashion when compared to λ_{max} and, as shown in Figure 3.22.

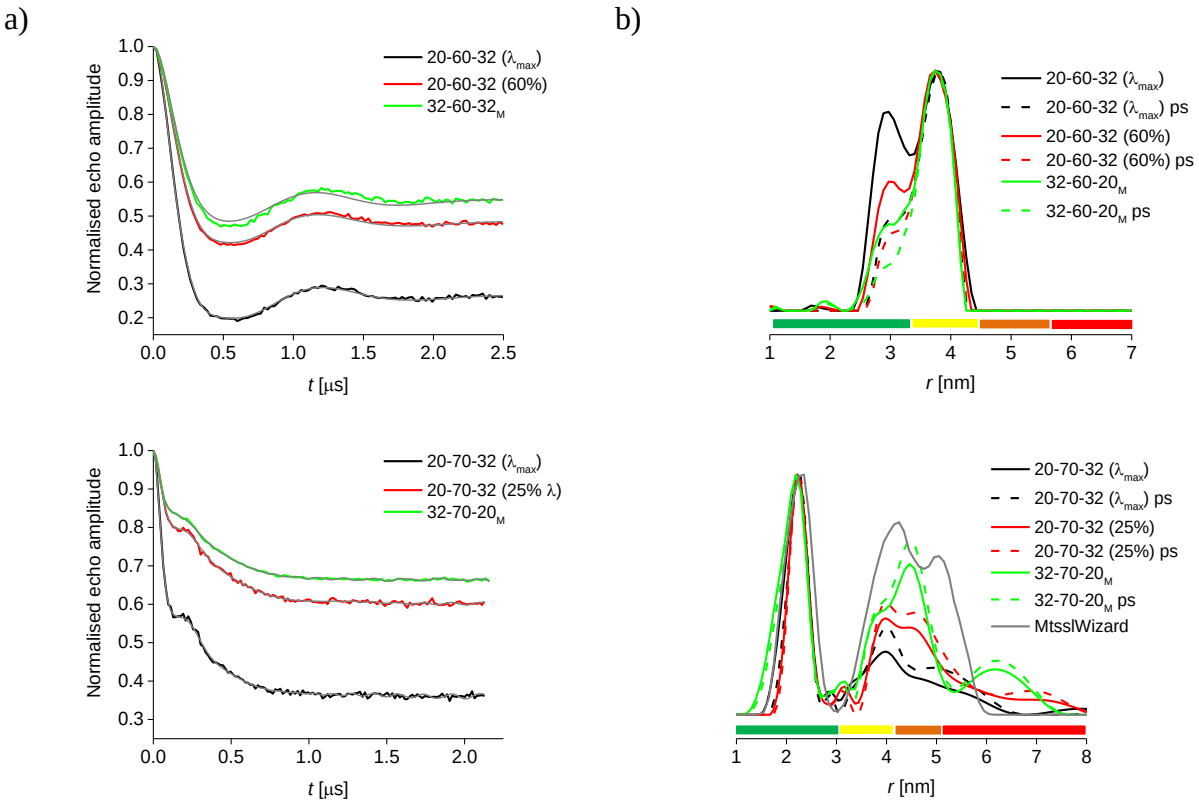

Figure 3.22: Comparison between background corrected traces and corresponding distance distributions without (solid line) and with power-scaling (dashed line) obtained performing PELDOR (black), frequency-interchanged (green) and λ reduced with similar λ to the frequency-interchanged (red) experiments at X-band frequencies (MD5 resonator) for model system **106** a) and MscS S196R1 b). The legend reports pump pulse length – pulse offset – detection π pulse. The subscript M indicates the pump pulse being on maximum of the field sweep. The coloured bars suggest the reliability of distances recovered.

Validation of the distance distributions obtained from measurements on **106** and MscS S196R1 without power-scaling (Figure 3.23) reveals that both ways of reducing λ improve the reliability of the PELDOR distance distribution when processing data from multiply labelled systems using Tikhonov regularisation.

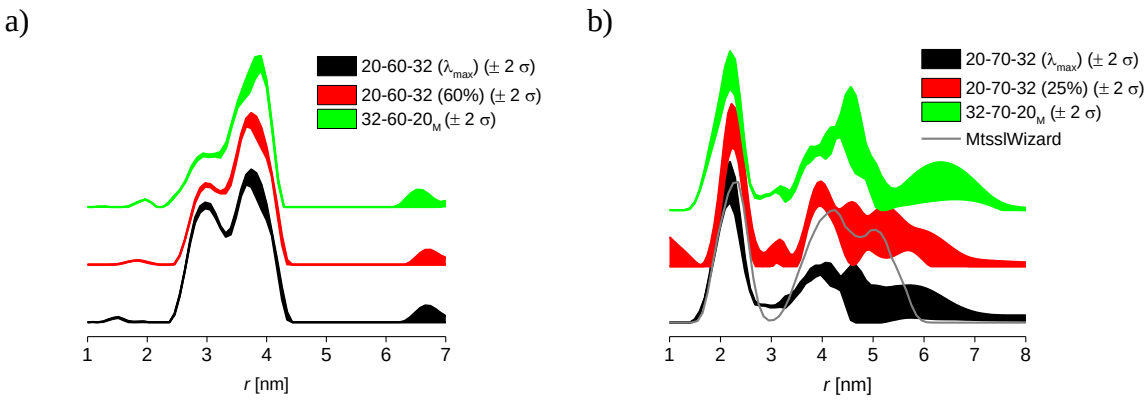

Figure 3.23: Validation of distance distributions for PELDOR with λ_{max} (black), λ reduced (red) and frequency-interchanged (green) experiments performed on **106** a) and MscS S196R1 b) at X-band (MD5 resonator). The coloured areas, representing the error bar, delineate those distance distributions that are stable to changes in processing parameters.

Similar measurements were performed at Q-band frequencies to allow for accurate extraction of longer distances present in MscS S196R1, as reported in Figure 3.24. Validation of the distance distributions in Figure 3.25 confirms the efficiency of frequency-interchanged experiments as well as λ reduction experiments in suppressing multi-spin effects and reliably recovering longer distances in MscS S196R1.

a)

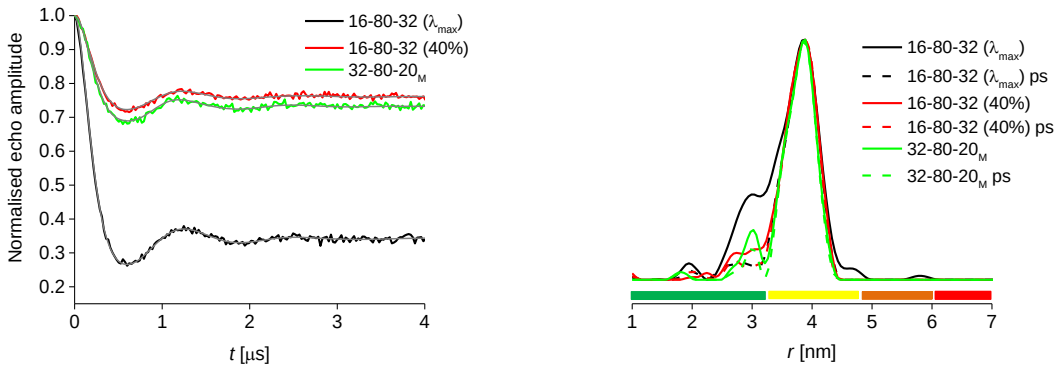

b)

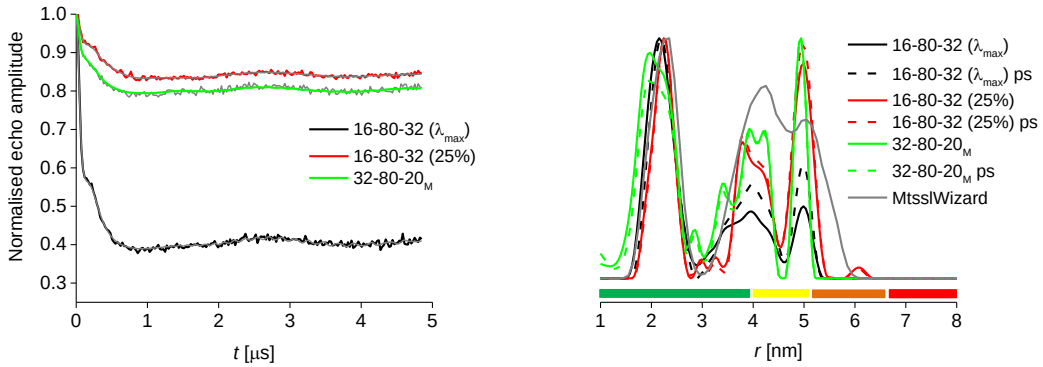

Figure 3.24: Comparison between background corrected traces and corresponding distance distributions without (solid line) and with power-scaling (dashed line) obtained performing PELDOR (black) and frequency-interchanged (green) experiments at Q-band frequencies for model system **106** a) and MscS S196R1 b). The legend reports pump pulse length – pulse offset – detection π pulse. The subscript M indicates the pump pulse being on maximum of field sweep. The coloured bars suggest the reliability of distances recovered.

a)

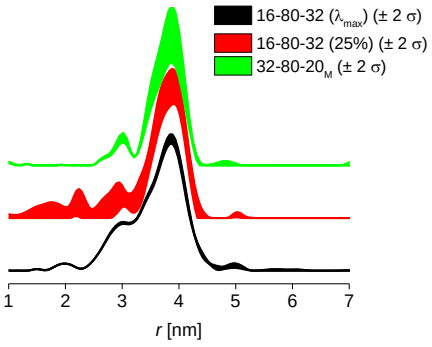

b)

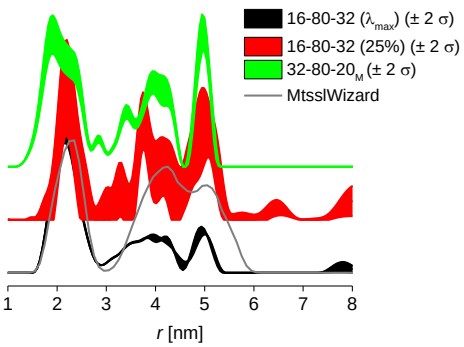

Figure 3.25: Validation of distance distributions for PELDOR with λ_{max} (black), reduced λ (red) and frequency-interchanged (green) experiments performed on 106 a) and MscS S196R1 b) at Q-band. The coloured areas, representing the error bar, delineate those distance distributions that are stable to changes in processing parameters. The subscript M indicates the position of the pump pulse on the maximum of the nitroxide field sweep spectrum.

Performance of λ reduction and frequency-interchanged experiments was evaluated by comparing their relative sensitivities. Table 3.1 and Table 3.2 report the nominal (Nom.) λ/λ_{max} values determined from nutation experiments using the pump frequency channel,[19a] and values for experimental (exp.) λ which were computed based on the experimental modulation depth Δ using Equation 3.1 (see Materials and Methods A.2.5):

$$\lambda = \lambda_{max} \sin^2 \frac{\beta}{2} \tag{3.1}$$

The exp. λ were then normalised to the λ_{max} achieved for each measurement series with percentages given in brackets (Exp. λ/λ_{max}). Noise and sensitivity values were calculated as described in Section A.2.5 of Materials and Methods. Sensitivity values were normalised to the maximum sensitivity value achieved in each series to facilitate comparisons. Values reported in Table 3.1 and Table 3.2 allow for comparison of sensitivity values between frequency-interchanged experiments and λ reduction measurements with similar λ, here highlighted in bold.

The hypothesis of using λ values equal to 1/(*N*-1) for extraction of the theoretical maximum of the two spin contribution[78b] which should allow full suppression of multi-spin effects in distance distributions, was tested. In Table 3.1 and Table 3.2 the 1/(*N*-1) values in brackets next to each heading are reported and all measurements with λ values falling under the threshold are highlighted in green. The results show that a λ = 1/(*N*-1) is not sufficient for suppression of multi-spin effects, as measurements with 80% and 100% of λ_{max} meet the λ < 1/(*N*-1) threshold and their corresponding distance distributions, as seen from Figure 3.2, still present residual artefacts. However, the combination of λ < 1/(*N*-1) with power-scaling (Figure 3.9) yields distance distributions already similar to those with the smallest λ tested. Thus, this approach appears to be effective when using λ values lower than 1/(*N*-1) where λ = ½/(*N*-1) seems to be sufficient for complete suppression of artefacts when combined with power-scaling.

106 λ reduction X-band - MD5 resonator						1/(*N*-1) = 0.33
Nom. λ/ λ max	**Noise**	**Δ**	**Sensitivity**	**Norm. Sens.**	**Exp. λ**	**Exp. λ / λ max**
20%	0.0021	0.18	84.29	0.23	0.06	18%
40%	0.0022	0.39	179.09	0.49	0.15	43%
60%	0.0023	0.52	225.22	**0.61**	0.22	60%
80%	0.0018	0.65	362.78	0.99	0.30	83%
100%	0.0020	0.74	368.00	1.00	0.36	100%
106 Frequency-interchanged X-band - MD5 resonator						
Nom. λ/ λ max	**Noise**	**Δ**	**Sensitivity**	**Norm. Sens.**	**Exp. λ**	**Exp. λ / λ max**
Std	0.0027	0.71	262.97	1.00	0.34	100%
Frq-int.	0.0032	0.46	143.75	**0.55**	0.19	56%
106 λ reduction Q-band						
Nom. λ/ λ max	**Noise**	**Δ**	**Sensitivity**	**Norm. Sens.**	**Exp. λ**	**Exp. λ / λ max**
20%	0.0041	0.09	22.44	0.22	0.03	11%
40%	0.0040	0.24	59.25	**0.57**	0.09	30%
60%	0.0045	0.33	74.00	0.71	0.13	43%
80%	0.0057	0.55	95.61	0.92	0.23	76%
100%	0.0064	0.66	103.75	1.00	0.30	100%
106 Frequency-interchanged Q-band						
Nom. λ/ λ max	**Noise**	**Δ**	**Sensitivity**	**Norm. Sens.**	**Exp. λ**	**Exp. λ / λ max**
Std	0.0064	0.66	103.75	1.00	0.30	100%
Frq-int.	0.0062	0.27	43.06	**0.42**	0.10	33%

Table 3.1: Comparison between sensitivity (Sens.) values for PELDOR λ reduced and frequency-interchanged experiments performed on **106** (1/(*N*-1) = 0.33).

MscS S196R1 λ reduction X-band - MD5 resonator						1/(*N*-1) = 0.17
Nom. λ/ λ max	**Noise**	**Δ**	**Sensitivity**	**Norm. Sens.**	**Exp. λ**	**Exp. λ / λ max**
15%	0.0032	0.24	76.25	0.48	0.04	27%
25%	0.0046	0.40	86.96	**0.55**	0.08	52%
50%	0.0034	0.58	170.88	1.08	0.14	88%
100%	0.0040	0.64	158.75	1.00	0.16	100%
MscS S196R1 Frequency-interchanged X-band - MD5 resonator						
Nom. λ/ λ max	**Noise**	**Δ**	**Sensitivity**	**Norm. Sens.**	**Exp. λ**	**Exp. λ / λ max**
Std	0.0027	0.63	232.22	1.00	0.15	100%
Frq-int.	0.0022	0.34	152.73	**0.66**	0.07	39%
MscS S196R1 λ reduction Q-band						
Nom. λ/ λ max	**Noise**	**Δ**	**Sensitivity**	**Norm. Sens.**	**Exp. λ**	**Exp. λ / λ max**
15%	0.0054	0.08	15.19	0.14	0.01	9%
25%	0.0038	0.18	46.05	**0.41**	0.03	20%
50%	0.0039	0.34	86.92	0.78	0.07	44%
100%	0.0055	0.61	111.09	1.00	0.15	100%
MscS S196R1 Frequency-interchanged Q-band						
Nom. λ/ λ max	**Noise**	**Δ**	**Sensitivity**	**Norm. Sens.**	**Exp. λ**	**Exp. λ / λ max**
Std	0.0055	0.59	107.82	1.00	0.15	100%
Frq-int.	0.0054	0.23	42.04	**0.39**	0.04	29%

Table 3.2: Comparison between sensitivity (Sens.) values for PELDOR λ reduced and frequency-interchanged experiments performed on MscS S196R1 (1/(*N*-1) = 0.17).

Sensitivity values for frequency-interchanged experiments for model system **106** are similar to the corresponding λ reduction experiment; no major difference was found when changing experimental settings and resonators. For MscS S196R1, X-band measurements suggest that the frequency-interchanged experiment brings an improved sensitivity, however at Q-band the performance of both experiments is similar. Table 3.1 and Table 3.2 also allow for comparison between the nominal and experimental λ. This comparison shows that the nutation experiments are a reasonably accurate method for the estimation of λ.

Given the similar sensitivity values of frequency-interchanged experiments with respect to λ reduction, PELDOR experiments with a fixed *t* of 0 but varying τ_2 (Figure 3.26 were performed to estimate the sensitivity of different PELDOR and frequency-interchanged PELDOR experiments. Furthermore, the predictive power of these relatively fast experiments varying the PELDOR time window was explored.

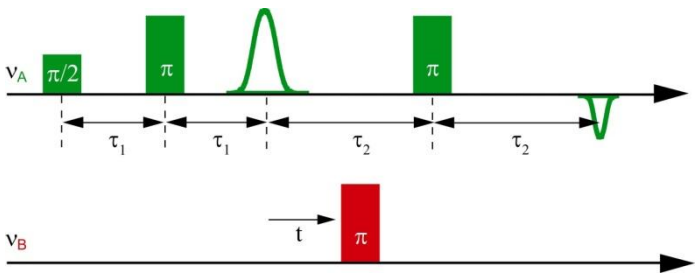

Figure 3.26: 4-pulse DEER (PELDOR) sequence.[7a]

These experiments were performed at the detection frequency of the PELDOR experiment; with the same pulse lengths and time intervals. Thus, except for the variation in τ_2 and $t = 0$, the experimental parameters remain the same as for the following PELDOR measurements. The axis size was chosen so that a full decay of the echo could be observed.

The relative values of the echo amplitude (Table 3.3), corresponding to the τ_2 of the respective PELDOR distance measurements, can be directly related to the relative signal-to-noise in the corresponding PELDOR experiments. This allows choosing the optimum pulse settings for the desired τ_2 of the PELDOR distance measurement.

Results from Table 3.3 suggest that performing the frequency-interchanged experiment keeping pump and detection pulse lengths of the PELDOR experiment (12-60-32_M) is in most cases the optimum choice because of lower experimental noise. However, due to its large modulation depth, it results in stronger multi-spin effects than other frequency-interchanged options.

106					
Experiment	**Echo amp. (*10^6)**	**Norm. echo amp.**	**Noise**	**Exp. λ**	**Norm. λ**
12-60-32	2.25	1.00	0.005	0.41	1.00
32-60-14_M	1.39	0.61	0.007	0.16	0.39
32-60-20_M	2.03	0.90	0.005	0.19	0.45
12-60-32_M	2.10	0.93	0.005	0.34	0.82
MscS S196R1					
Experiment	**Echo amp. (10^6)**	**Norm. echo amp.**	**Noise**	**Exp. λ**	**Norm. λ**
12-60-32	0.60	1.00	0.022	0.15	1.00
32-60-14_M	1.02	1.70	0.013	0.02	0.14
32-60-20_M	0.95	1.58	0.013	0.03	0.17
12-60-32_M	1.15	1.92	0.012	0.07	0.45
107					
Experiment	**Echo amp. (10^6)**	**Norm. echo amp.**	**Noise**	**Exp. λ**	**Norm. λ**
12-60-32 (2 μs)	3.47	1.00	0.0018	0.35	1.00
12-60-32 (4 μs)	1.34	0.39	0.0048	0.33	0.97
12-60-32_M (2 μs)	3.67	1.06	0.0017	0.27	0.77
12-60-32_M (4 μs)	1.30	0.38	0.0055	0.24	0.71
32-60-14_M (2 μs)	3.99	1.15	0.0018	0.14	0.40
32-60-14_M (4 μs)	1.29	0.37	0.0045	0.13	0.37
32-60-20_M (2 μs)	5.08	1.46	0.0017	0.15	0.44
32-60-20_M (4 μs)	1.72	0.50	0.0052	0.14	0.40

Table 3.3: Echo amplitude values, values normalised to the PELDOR settings together with noise and λ values for their corresponding PELDOR measurements. Measurements were performed using a MS3 split ring resonator.

In conclusion these experiments have been found to be a good method to estimate the optimum pulse sequence for PELDOR measurements in dependence of the τ_2 and consequently inter-spin distance that it is aimed to reliably measure. In the cases tested, frequency-interchanged experiments give better signal-to-noise when using a short τ_2; this is assigned to the increase of instantaneous diffusion effects induced by the detection pulse train being shifted to the most populated area of the field sweep spectrum, as further discussed in Section 4.1. In cases of short τ_2 frequency-

interchanged experiments give an improved signal-to-noise ratio compared to reducing λ for suppression of multi-spin effects in distance measurements.

3.4 Conclusion

It has been demonstrated that fully labelled multi-spin systems with up to eight spins per nanoobject can be reliably measured by PELDOR experiments in combination with power-scaling as long as pumping multiple spins is reduced by keeping $\lambda < 1/(N\text{-}1)$. This is in excellent agreement with earlier predictions.[78a] The previous findings were extended to the reliable extraction of experimental distance distributions in heptameric complexes and the estimate of the largest feasible λ. Additionally, effects of the combination of power-scaling and λ reduction on distance distributitons and measurement sensitivity was quantified and explicit recommendations made. The results suggest that a λ lower than the expected $1/(N\text{-}1)$ has to be used for accurate extraction of distance distributions. Additionally, power-scaling has been found to induce major losses in measurement sensitivity.

A variant of the experiment was tested on both model and biological systems, to verify if multi-spin effects could be largely suppressed without compromising sensitivity. Interchanging the positions of pump and detection pulses and their approximate excitation widths in the nitroxide spectrum allows an alternative route to significant reduction of multi-spin effects. The frequency-interchnaged experiment was found to reliably give accurate distance distributions matching with results obtained from models, however the performance of the experiment in terms of sensitivity gave mixed results when compared to λ reduced experiments performed with similar λ.It was found that the performance of these alternative experiments can be reliably predicted before the actual measurements allowing efficient use of instrument time for the most promising settings. Together, our results should be especially significant for the rising interest in distance measurements in multimeric membrane transporters.

Chapter 4 - Sparse labelling as method for suppression of multi-spin effects

The author performed the PELDOR measurements, preliminary simulations and data processing. Dr. C. Pliotas and Prof. J. H. Naismith provided the spin labelled mutants and Dr K. Ackermann contributed to the modelling of distance distributions from crystal structure.

4.1 Project background

Distance measurements have been found to be an important tool towards structural elucidation of biological systems.[2b, 68, 114] Commonly, one pair of spin labels is introduced into the system, giving access to the distance between the two labelled sites.[7b, 9b] However, labelling of exactly two specific sites is extremely challenging in case of homo-multimeric complexes. Even if each monomer only has one site for covalent attachment of a spin label, a cysteine in the case of labelling with MTSSL, the multimer will bear as many labelling sites as it has monomers. To reduce the number of labelling sites to exactly two can prove extremely challenging in these systems and is practically unfeasible in most cases. This makes accurate extraction of inter-spin distances in homo-multimeric systems more difficult due to the presence of multi-spin effects.[19a, 76] While these can be suppressed by the methodology developed in Chapter 3 another approach would be to dilute multi-spin effects, by addition of diamagnetic material.

The concept of magnetic dilution has also been initially introduced for CW EPR samples; it is commonly achieved by mixing unlabelled protein to a sample containing the corresponding spin labelled system.[115] Magnetic dilution is used to prevent short intermolecular spin-spin distances by aggregation of the labelled systems, which would introduce inhomogeneous broadening of the EPR signals and prevent accurate extraction of parameters such as hyperfine interactions used for structural information.[116] This type of dilution, however, cannot be used for multiply labelled systems, where the introduction of unlabelled protein would not affect the proximity of the multiple spin labels present within one system. To overcome challenges encountered in multiply labelled oligomeric systems the concept of reduction in number of labelled sites could be used for pulsed EPR distance measurements.

Complete labelling of complex biological systems can be challenging as the reaction between cysteines and the methanesulfonothioate groups of the MTSSL spin label is not always quantitative. One of the limiting factors is that thiol groups need to be in their reduced form during spin labelling to prevent inactivation of the cysteines by disulphide bridges. This process may require treatment with reducing agents that represent, at the same time, a threat for the nitroxide radical that may be quenched.[117] Incomplete labelling leads to mixtures of labelling degrees that affect PELDOR measurements by lowering modulation depth, and introducing uncertainties in data analysis.[78b] Specifically, in the presence of incomplete labelling in multiply labelled systems the modulation depth Δ becomes a function of λ, the fraction of spins excited by the pump pulse, and the labelling efficiency *f*, as shown in Equation 4.1:[118]

$$\Delta(\lambda f) = 1-(1- f\lambda)^{N-1} \qquad (4.1)$$

As discussed in Chapter 3, suppression of multi-spin effects comes at the price of loss in Δ, affecting the overall experiment sensitivity. From Equation 4.1 it can be deduced that suppression of multi-spin effects could be achieved by lowering either λ or *f*.

In the previous chapter it was confirmed that reducing λ either by reducing the flip angle β of the pump pulse, or by pumping on a less populated area of the EPR spectrum lead to reduction of multi-spin effects. In most cases the effect on sensitivity depends on the λ employed, but not how it was achieved. Specifically, the sensitivity of frequency-interchanged experiment is expected to be more strongly affected by instantaneous diffusion (ID) effects.[98] Briefly, ID is encountered even at relatively low concentrations of paramagnetic centres ($>10^8$ spins cm^{-3}). The dipolar interaction among a high number of close in space electron spins leads to a reduction in the phase memory time.[26, 68] Thus, the fraction of refocused A spins contributing to the PELDOR signal will be lowered and the sensitivity reduced.[68] By detecting a more intense area of the spectrum, as in the frequency-interchanged experiment, a higher proportion of the spins in the sample is inverted by the detection pulses leading to an increase of dephasing by ID effects, causing further loss in signal-to-noise.[119]

Reduction of multi-spin effects by the lowering the population of labelling sites within multimers might either be achieved by exchanging spin-labelled monomers with unlabelled monomers or by sparse labelling. The latter reduces the labelling efficiency *f*

by reacting a certain proportion of cysteines with a diamagnetic spin label analogue. This approach should allow reduction of multi-spin effects by performing PELDOR experiments on sparsely labelled samples. Furthermore, ID effects should be reduced due to the higher local dilution of spin labels, thus introducing a potential improvement in signal-to-noise.[26] To validate this method different labelling degrees would need to be tested to find a degree allowing to accurately extract inter-spin distances without overly compromising on sensitivity. Simulations on regular convex polygons mimicking rotationally symmetric membrane channels[78b] should allow predicting labelling efficiencies for experimental testing.

A recent study used the concept of sparse labelling to overcome multi-spin effects when studying the oligomeric structure of proteorhodopsin.[47c] The singly labelled monomers of the hexamer were labelled at three specific sites using 33%, 55%, 80% and 100% Gd(III) or nitroxide labelling probability, thus reducing the average number of spins per hexamer. The reduced probability for nitroxide-labelling was achieved by varying the ratios of unlabelled and nitroxide labelled monomers prior formation of the hexamer and by varying the amount of $GdCl_3$ added to the solution in case of the Gd(III) labelled samples. Results showed that for nitroxide spin labelled systems distance measurements on under-labelled systems improved the extraction of inter-spin distances and facilitated background correction.[47c] On Gd(III) sparsely and fully labelled samples the improvement in distance distributions was not as dramatic as for nitroxides.[47c] Other studies have been reporting the use of spin dilution to avoid complications arising from aggregation of singly and doubly labelled systems.[48, 95]

4.2 Project Aims

Initial studies reported in the literature highlight the requirement for quantifying the effects of sparse labelling on PELDOR distance measurements and to possibly design a protocol for its optimum application. The project aimed to test the potential of the sparse labelling, previously reported for both CW[116] and PELDOR,[47c] as alternative method for suppression of multi-spin effects. Initial studies involved the determination of labelling degrees for extraction of accurate distances in two mutants of the membrane channel protein MscS: S196R1 and D67R1. The effects of sparse labelling on distance measurements on multiply labelled systems was firstly tested by performing both PELDOR and frequency interchanged measurements on sparsely labelled samples of the

two oligomers at X-band and Q-band frequencies. Effects of sparse labelling on sensitivity were also quantified.

4.3 Results and Discussion

4.3.1 Simulations

Preliminary studies focused on finding the feasible labelling degrees for experimental testing. Therefore, two heptagons of different size, mimicking the structure of the two MscS mutants, were tested with respect to the stability of the PELDOR distance distribution when introducing increasing noise levels and reduction in λ; the stability was assessed on the basis of recovering the relative intensities and positions of distance peaks. The simulations were also used to explore the potential of sparse labelling and its combination with power-scaling (see materials and Methods A.2.2). The simulated labelling efficiencies were of 33, 66 and 100% and noise was varied between 1 and 3%.

These data (see Appendix A.3) indicate that 66% labelling is the most promising for extraction of inter-spin distances in rotationally symmetric heptamers, as introduction of noise does not greatly affect the distance distributions obtained from both mutants at different noise levels, while33% labelling is the best option in the presence of a good signal-to-noise level. Performance, stability and sensitivity of these degrees of sparse labelling were experimentally tested on sparsely labelled MscS samples at both X- and Q-band.

4.3.2 PELDOR experiments

4.3.2.1 *Sparse labelling: extraction of inter-spin distances*

Firstly, PELDOR experiments on the two different mutants (see Materials and Methods A.2.1) were performed at X-band using an MD5 resonator (Figure 4.1, see Materials and Methods A.2.3.1). When compared to the distance distributions modelled from the crystal structure of the two mutants (grey line), the 33% labelled samples (green line) show a better match to the expected distance distributions than the 66% (red line) or 100% (black line) labelled samples. These first results reflect the outcomes from the simulations, suggesting that sparse labelling represents a useful approach for extraction of accurate inter-spin distances in complex symmetric multi-spin systems. The preliminary experimental data shows that reduction of the labelling efficiency *f* to 33% seems to offer the best recovery of the longer distance peaks for measurements with a good signal-to-noise (Figure 4.1 a)). However, the time traces are too short to reliably extract the shape of the entire distance

distributions. Especially for MscS D67R1 resolving the second and third distance is unreliable, but reduced labelling recovers more overall intensity in this distance region (Figure 4.1 b)). These observations are in good agreement with the simulations on the polygons.

a)

b)

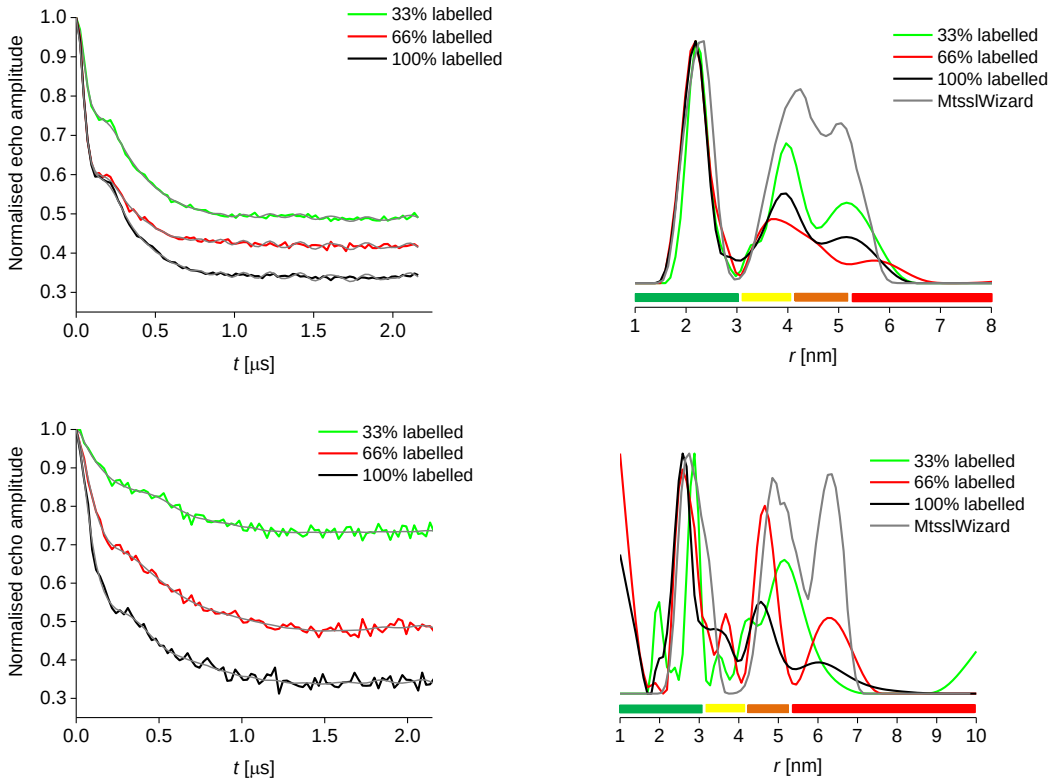

Figure 4.1: PELDOR X-band MD5 background corrected traces and with fits (grey) and corresponding distance distributions for 33, 66 and 100% labelled samples of MscS mutants S196R1 a) and D67R1 b). The "expected" grey distance distributions are derived from processing the X-ray data for each protein with the software MtsslWizard.[111] The coloured bars indicate the reliability of distances recovered as a function of the measuring time window.

Validation of the distance distributions (see Materials and Methods A.2.4) shows that reduction in labelling efficiency reduces the width of the shortest distance and recovers overall intensity of longer distances (Figure 4.2). However, it reveals that the preliminary data on MscS D67R1 is too noisy to draw firm conclusions on this mutant.

a) b)

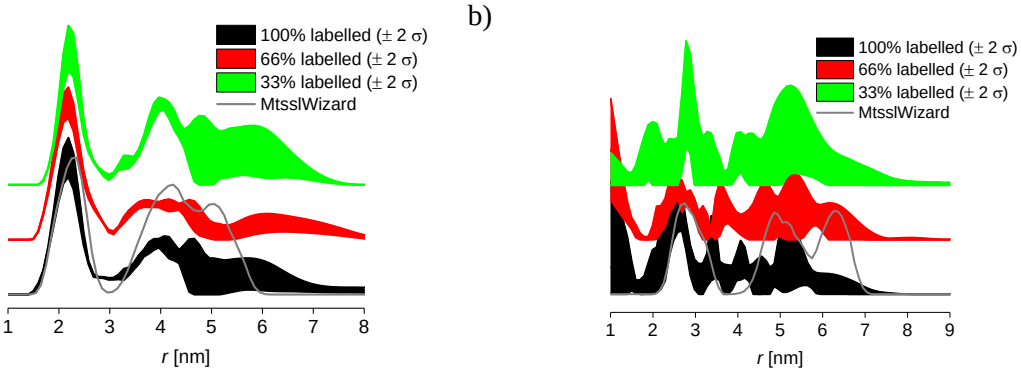

Figure 4.2: Validation of distance distributions obtained for 33, 66 and 100% labelled samples of MscS S196R1 a) and D67R1 b) mutants at X-band (MD5 resonator). The coloured areas, representing the error bars, delineate those distance distributions that are stable to changes in processing parameters.

Power-scaling allows to recover some intensity of the longer distance peaks when applied to PELDOR measurements on the fully labelled systems, however it appears not to be as efficient as reducing the labelling efficiency to 33%. The effects of power-scaling on the two sparsely labelled systems of each mutant appear not to be as prominent as for the fully labelled samples, as shown in Figure 4.3.

a)

b)

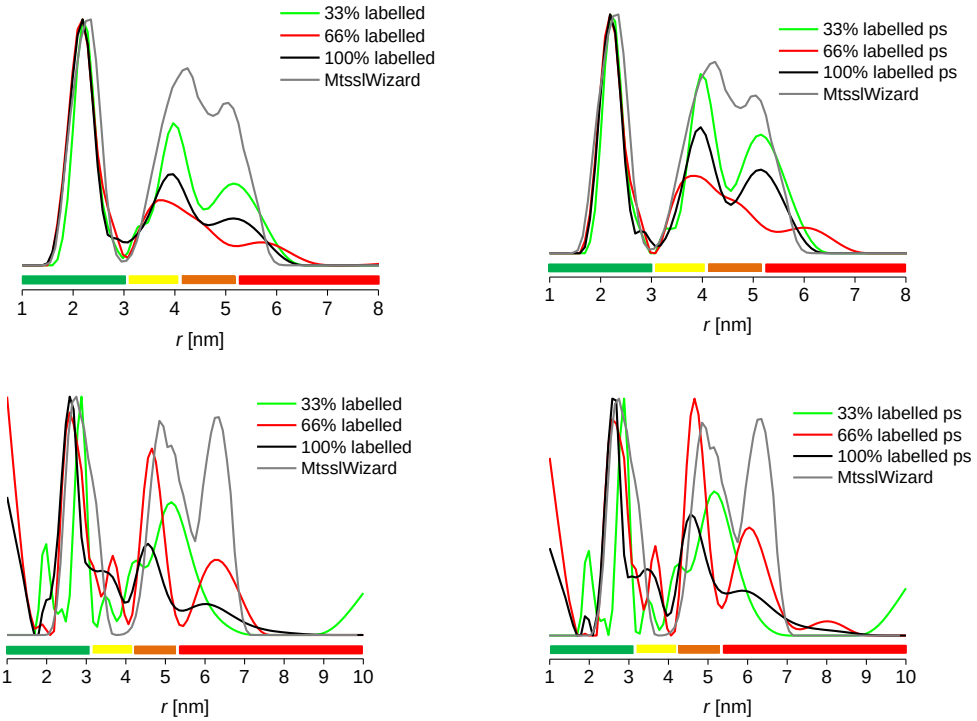

Figure 4.3: Distance distributions without (left) and with (right) power-scaling from PELDOR measurements performed on sparsely labelled samples of MscS S196R1 a) and MscS D67R1 b) at X-band (MD5 resonator). The coloured bars indicate the reliability of distances recovered as a function of the measuring time window.

Similarly to the results presented in Chapter 3 power-scaling alone is not sufficient for high quality distance distributions, but it offers further improvement when combined with sparse labelling.

The same qualitative trend was observed when using an MS3 resonator (see Materials and Methods A.2.3.1) . Here, the multi-spin effects are expected to be even more prominent as the achievable λ is larger than in the MD5 resonator.

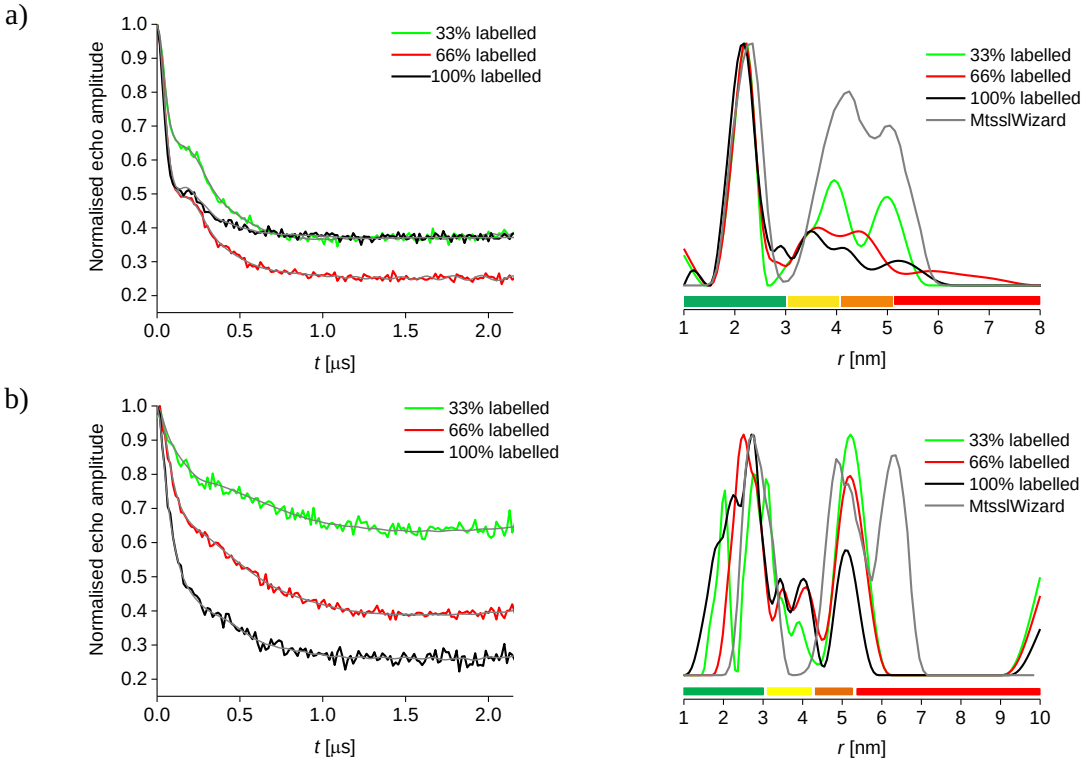

Figure 4.4: X-band MS3 background corrected traces with fits and corresponding distance distributions for 33, 66 and 100% labelled samples of MscS mutants S196R1 a) and D67R1 b). The coloured bars indicate the reliability of distances recovered as a function of the measuring time window.

Validation of the distance distributions shows that the 33% labelled sample of the MscS S196R1 allows to recover the second distance peak matching with the model from the crystal structure (Figure 4.5 a)), while the third distance is too long to be reliably extracted. MscS D67R1, however, shows a high level of uncertainity, suggesting that longer measuring time windows and better sensivity are required (Figure 4.5 b)).

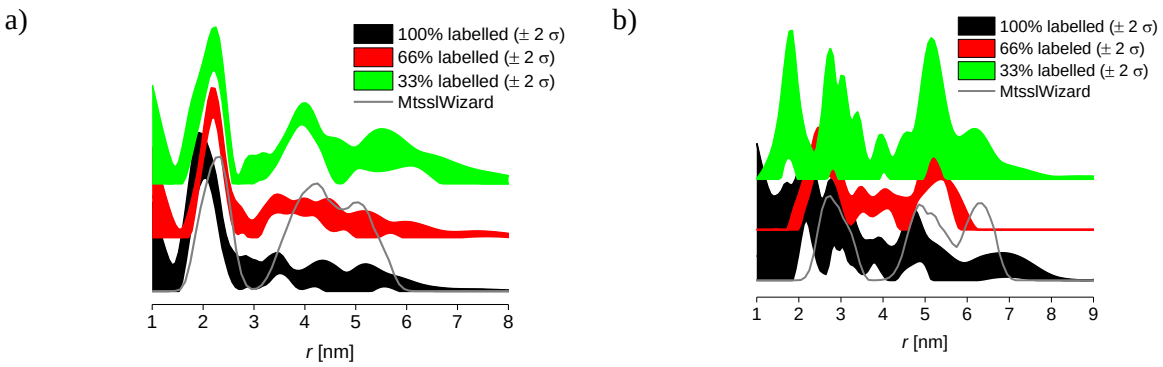

Figure 4.5: Validation of distance distributions obtained for 33, 66 and 100% labelled samples of MscS S196R1 a) and D67R1 b) mutants at X-band (MS3 resonator). The coloured areas, representing the error bars, delineate those distance distributions that are stable to changes in processing parameters.

Power-scaling of the traces obtained for measurements in the MS3 resonator recovers substantial long distances intensity in line with the MtsslWizard models (Figure 4.6). Improvements, however, appear to be more limited than what was observed with the MD5 resonator (and correspondingly smaller λ).

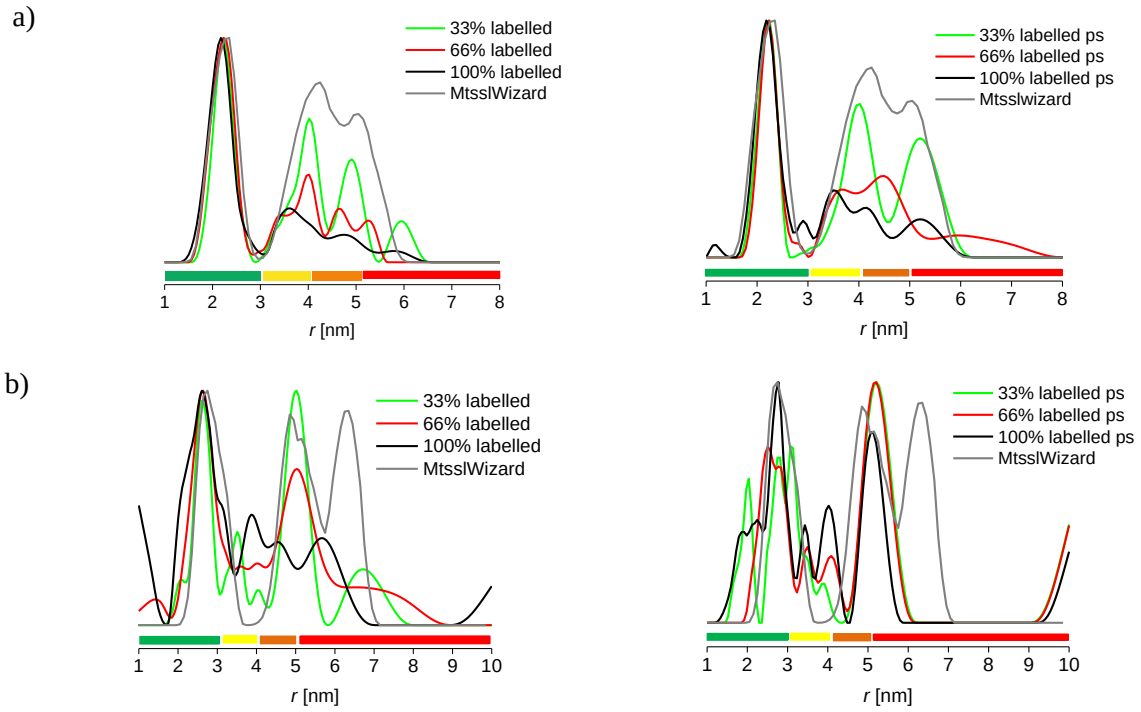

Figure 4.6: Distance distributions without (left) and with (right) power-scaling from PELDOR measurements performed on sparsely labelled samples of MscS S196R1 a) and MscS D67R1 b) at X-band (MS3 resonator). The coloured bars indicate the reliability of distances recovered as a function of the measuring time window.

Sparse labelling increases the accuracy of distance distributions from Q-band PELDOR data (see Materials and methods A.2.3.1), as shown in Figure 4.7. Validations demonstrate the increased reliability of the longest distance in MscS S196R1 and the medium distance in MscS D87R1 owing to the longer time window achievable (Figure 4.8).

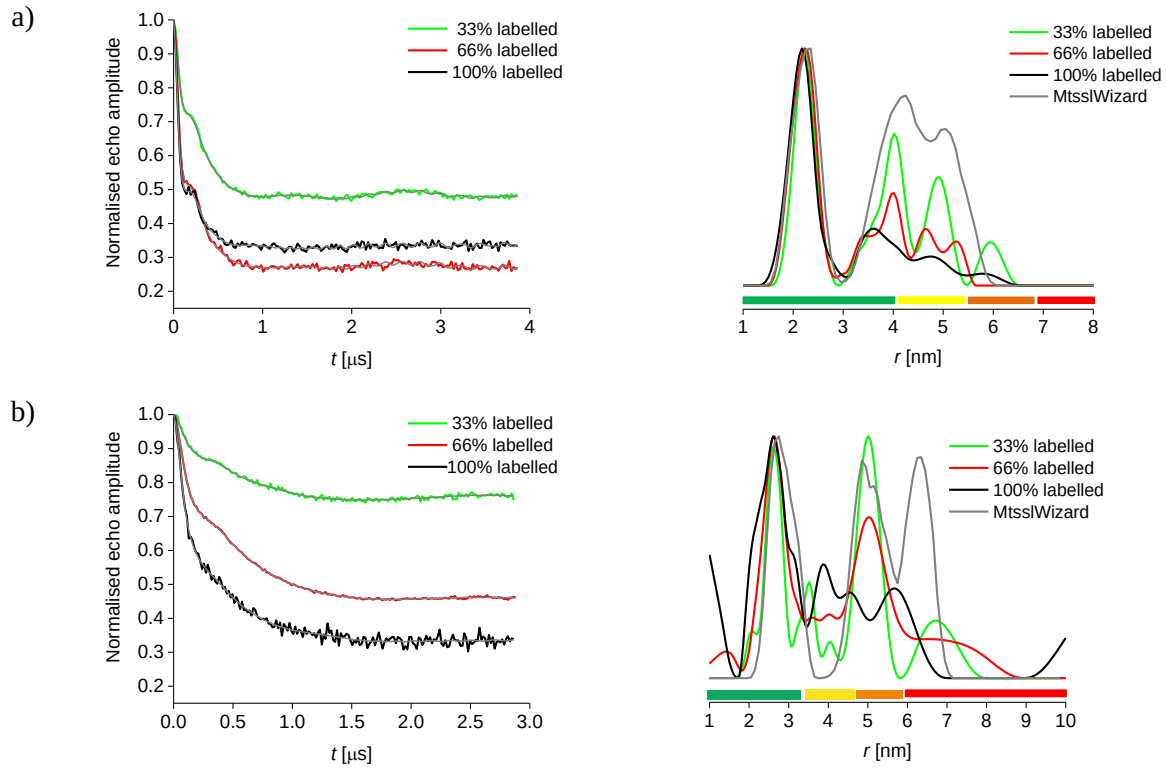

Figure 4.7: Q-band background corrected PELDOR traces with fits and corresponding distance distributions for 33, 66 and 100% labelled samples of MscS S196R1 a) and MscS D67R1 b). The coloured bars indicate the reliability of distances as a function of time window.

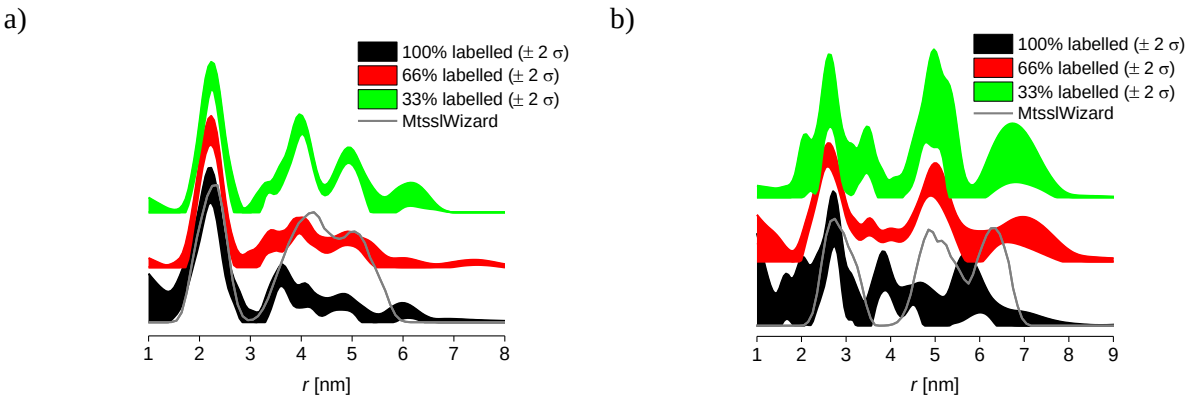

Figure 4.8: Validation of distance distributions obtained for 33, 66 and 100% labelled samples of MscS S196R1 a) and MscS D67R1 b) at Q-band. The coloured areas, representing the error bars, delineate those distance distributions that are stable to changes in processing parameters.

In agreement with X-band results power-scaling recovers intensity of longer distances (Figure 4.9).

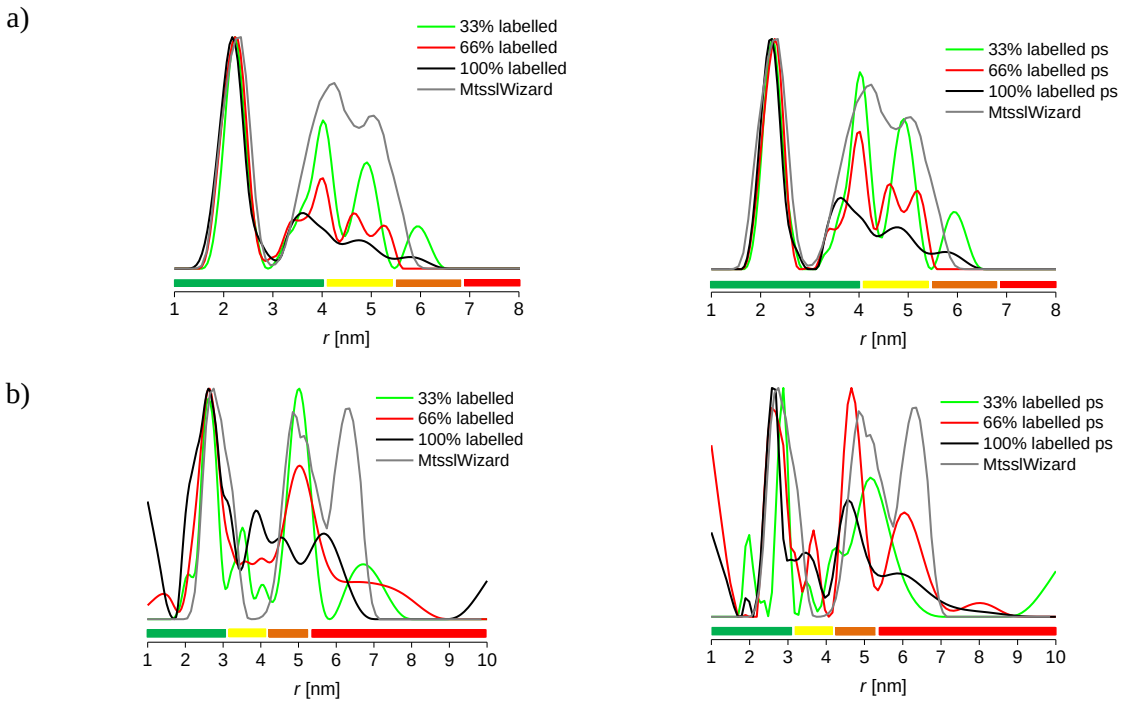

Figure 4.9: Distance distributions without (left) and with (right) power-scaling from PELDOR measurements performed on sparsely labelled samples of MscS S196R1 a) and MscS D67R1 b) at Q-band. The coloured bars indicate the reliability of distances recovered as a function of the measuring time window.

Preliminary results comparing the effects of different degrees of sparse labelling on distance measurements suggest that for both labelling positions tested on MscS both 66 and 33% labelled samples give a major improvement in recovery of distance peaks when compared to more common quantitative labelling. Q-band measurements show that 33% labelling gives results closest resembling to the expected distance distribution modelled by MtsslWizard. However, reduction of the labelling efficiency introduces an important loss in Δ, which affects sensitivity. This is quantified in the following section.

4.3.2.2 *Sparse labelling: effects on measurements sensitivity*

Sensitivity of PELDOR experiments performed on 33, 66 and 100% labelled samples of the two MscS mutants was calculated as the ratio between modulation depth Δ and noise, as described in Chapter 3 and Materials and Methods A.2.5. These values were then normalised against the sensitivity value calculated for the 100% labelled sample, as reported in Table 4.1. This corresponds to the labelling degree giving the commonly

desired high modulation depth and sensitivity achievable by PELDOR measurements. Initial experiments performed at X-band (MD5 resonator) show that an average 25% loss in sensitivity is introduced for both the 33 and 66% labelled samples for the S196R1 mutant, when normalised against the 100% labelled sample. For the D67R1 mutant the 66% labelled sample shows no loss in sensitivity, however a loss of 51% is calculated for the 33% sample. Thus, at X-band, under the experimental[98] and sample conditions used,[47a] sparse labelling appears to be a valid alternative for extraction of accurate inter-spin distances in symmetrical systems without excessively compromising on sensitivity.

Similar results were observed when using an MS3 resonator: sparse labelling introduces important improvements in recovery of longer distance peaks (Figure 4.4) without compromising, or in most cases, improving sensitivity values (Table 4.1). The method is efficient for all sparsely labelled samples, except for the 33% labelled D67R1 where the slight improvement in the intensity of longer distances does not necessarily justify the loss in sensitivity. Thus, for the S196R1 sample the optimum labelling efficiency appears to be 33% as it allows for recovery of the necessary distance peaks without compromising on sensitivity, while being 66% labelling for D67R1 represents the optimum compromise between distance recovery and gain in sensitivity, under the conditions chosen here.

Results obtained at Q-band show a gain in sensitivity when performing experiments on sparsely labelled samples for both mutants. PELDOR measurements on the 66% sample show a five-fold improvement in sensitivity compared to the values obtained on the fully labelled sample. This surprising result will have to be verified and might be due to different aggregation behaviour leading to different dephasing rates in these samples. Here, the gain in signal-to-noise overcompensates for the loss in Δ making sparse labelling a valid alternative method for accurate extraction of inter-spin distances. These results point out that, although additional effort is required for the preparation of sparsely labelled samples, reduction of labelling efficiency represents an emerging method for suppression of multi-spin effects while recovering sensitivity. Additionally, the preliminary simulations were found useful in exploring degrees of labelling efficiency to test experimentally. These predictive simulations minimise sample preparation and pulsed EPR measurements for testing different labelling degrees.

MscS S196R1_X-band MD5 resonator				
Labelling (*f*)	Δ	Noise	Sensitivity	Norm. Sensitivity
100%	0.66	0.0053	120	1.00
66%	0.58	0.0064	91	0.76
33%	0.49	0.0052	94	0.78
MscS D67R1_X-band MD5 resonator				
Labelling (*f*)	Δ	Noise	Sensitivity	Norm. Sensitivity
100%	0.66	0.0122	54	1.00
66%	0.52	0.0096	54	1.00
33%	0.27	0.0101	27	0.50
MscS S196R1_X-band MS3 resonator				
Labelling (*f*)	Δ	Noise	Sensitivity	Norm. Sensitivity
100%	0.63	0.0088	72	1.00
66%	0.75	0.0073	100	1.40
33%	0.65	0.0077	84	1.20
MscS D67R1_X-band MS3 resonator				
Labelling (*f*)	Δ	Noise	Sensitivity	Norm. Sensitivity
100%	0.74	0.014	52	1.00
66%	0.62	0.0031	200	3.80
33%	0.36	0.015	24	0.46
MscS S196R1_Q-band				
Labelling (*f*)	Δ	Noise	Sensitivity	Norm. Sensitivity
100%	0.68	0.0075	91	1.00
66%	0.73	0.0075	97	1.00
33%	0.52	0.0051	100	1.10
MscS D67R1_Q-band				
Labelling (*f*)	Δ	Noise	Sensitivity	Norm. Sensitivity
100%	0.66	0.0120	53	1.00
66%	0.54	0.0022	250	4.70
33%	0.27	0.0043	62	1.20

Table 4.1: Comparison of sensitivity between fully (100%) and sparsely (33 and 66%) labelled MscS S196R1 and D67R1 measured at X-band (MD5 and MS3 resonators) and Q-band. Sensitivity values were normalised against the quantitatively labelled samples for each mutant. All values are given to two significant figures.

4.3.3 Frequency-interchanged PELDOR experiments:

4.3.3.1 *Sparse labelling and frequency-interchange: effects on distance distributions*

PELDOR experiments on sparsely labelled systems showed to be efficient in reducing multi-spin effects while retaining or improving measurement sensitivities at Q-band. To test whether additional improvements could be achieved, the impact on sensitivity when combining frequency-interchanged experiments (see Materials and Methods A.2.3.2) and sparse labelling was quantified. Measurements were carried out under the same conditions as for the PELDOR experiments at both X-band, using MD5 and MS3 resonators, and Q-band, using QT2 resonator. Effects of power-scaling on both PELDOR and frequency-interchanged distance distributions were further explored.

First measurements on 100% labelled MscS S196R1 and D67R1 samples performed at X-band using an MD5 (Figure 4.10 with validations Figure 4.11 and Figure 4.12 with validations Figure 4.13) and MS3 (Figure 4.14 with validations Figure 4.15 and Figure 4.16 with validations Figure 4.17) resonators show, as expected from results previously reported in Chapter 3, an improvement in recovery of intensity of longer distances by the frequency-interchanged experiment, when compared to regular PELDOR measurements. The same figures show that for 66 and 33% labelled samples the frequency-interchanged experiments still bring some improvement in the distance distribution, however to a lower extent when compared to the 100% ones. This observation is not surprising as only minor contributions from multi-spin effects remain to be suppressed.

Validations, reported in Figure 4.11, Figure 4.13, Figure 4.15 and Figure 4.17, show that frequency-interchanged experiments recover some long distance intensity especially in fully labelled samples. However, the sensitivity is too poor to extract reliably distance distributions for MscS D67R1 (Figure 4.13).

a)

b)

c)

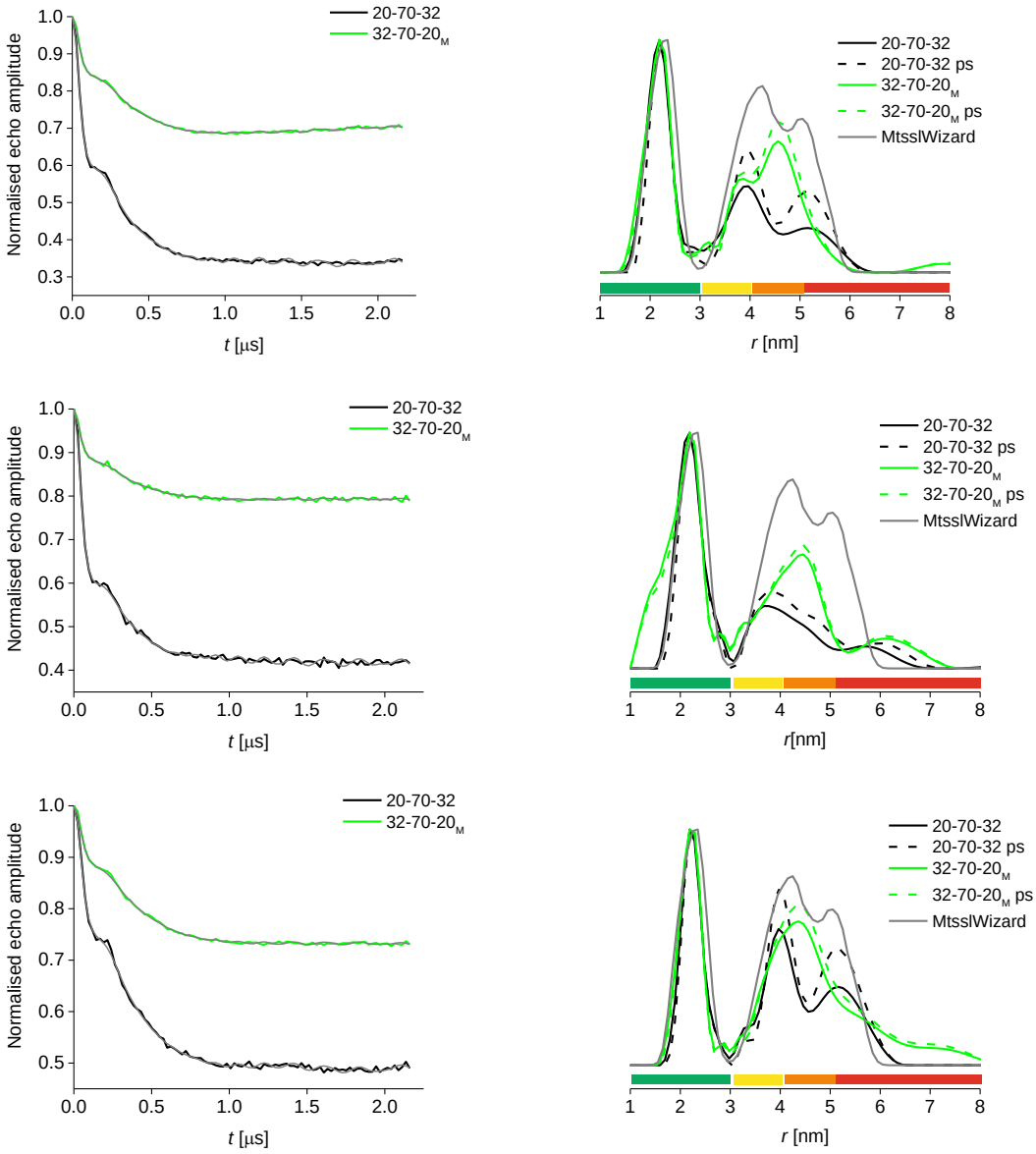

Figure 4.10: X-band MD5 background corrected traces with fits and corresponding distance distributions for 100 a), 66 b) and 33% c) labelled samples of MscS S196R1 obtained when performing PELDOR (black) and frequency-interchanged (green) experiments. The legend reports pump pulse length – pulse offset – detection π pulse. The subscript M indicates the pump pulse being on maximum of field sweep. The coloured bars indicate the reliability of distances recovered as a function of the measuring time window.

a)

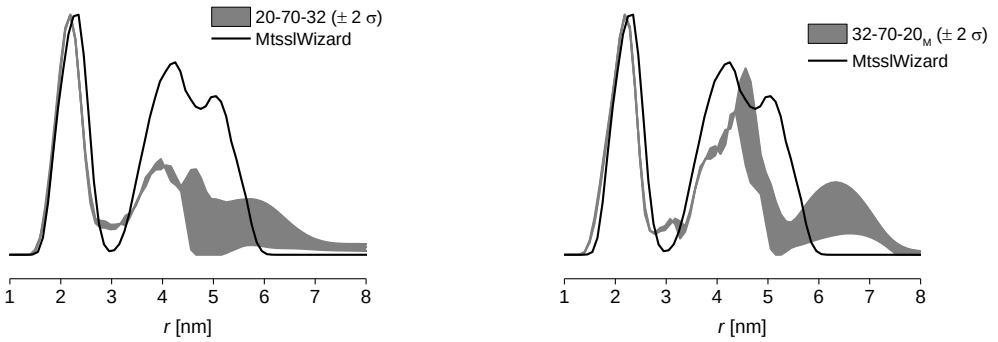

b)

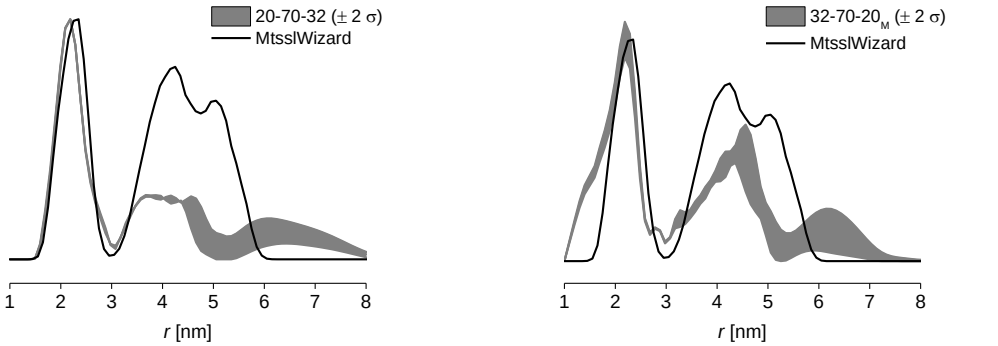

c)

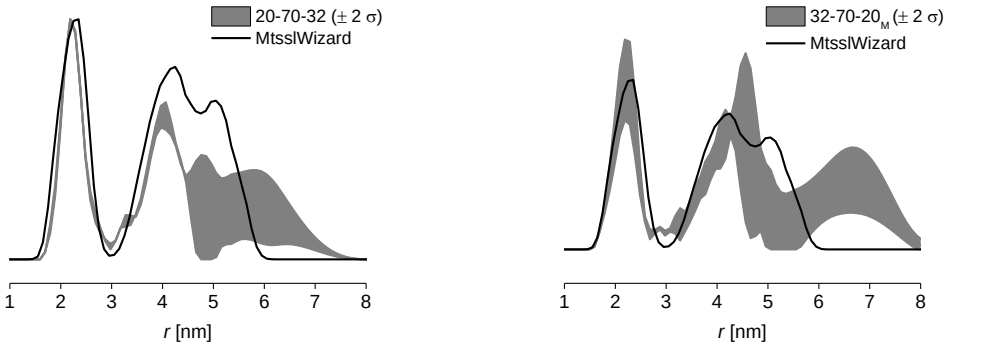

Figure 4.11: Validations of PELDOR (left) and frequency-interchanged (right) experiments on 100 a), 66 b) and 33 c) % labelled samples of MscS S196R1 at X-band (MD5). The grey areas represent the error bars for each distance; the distance distributions within the white areas are stable to changes in background correction parameters, thus more reliable. The subscript M indicates the position of the pump pulse on the maximum of the nitroxide field sweep spectrum.

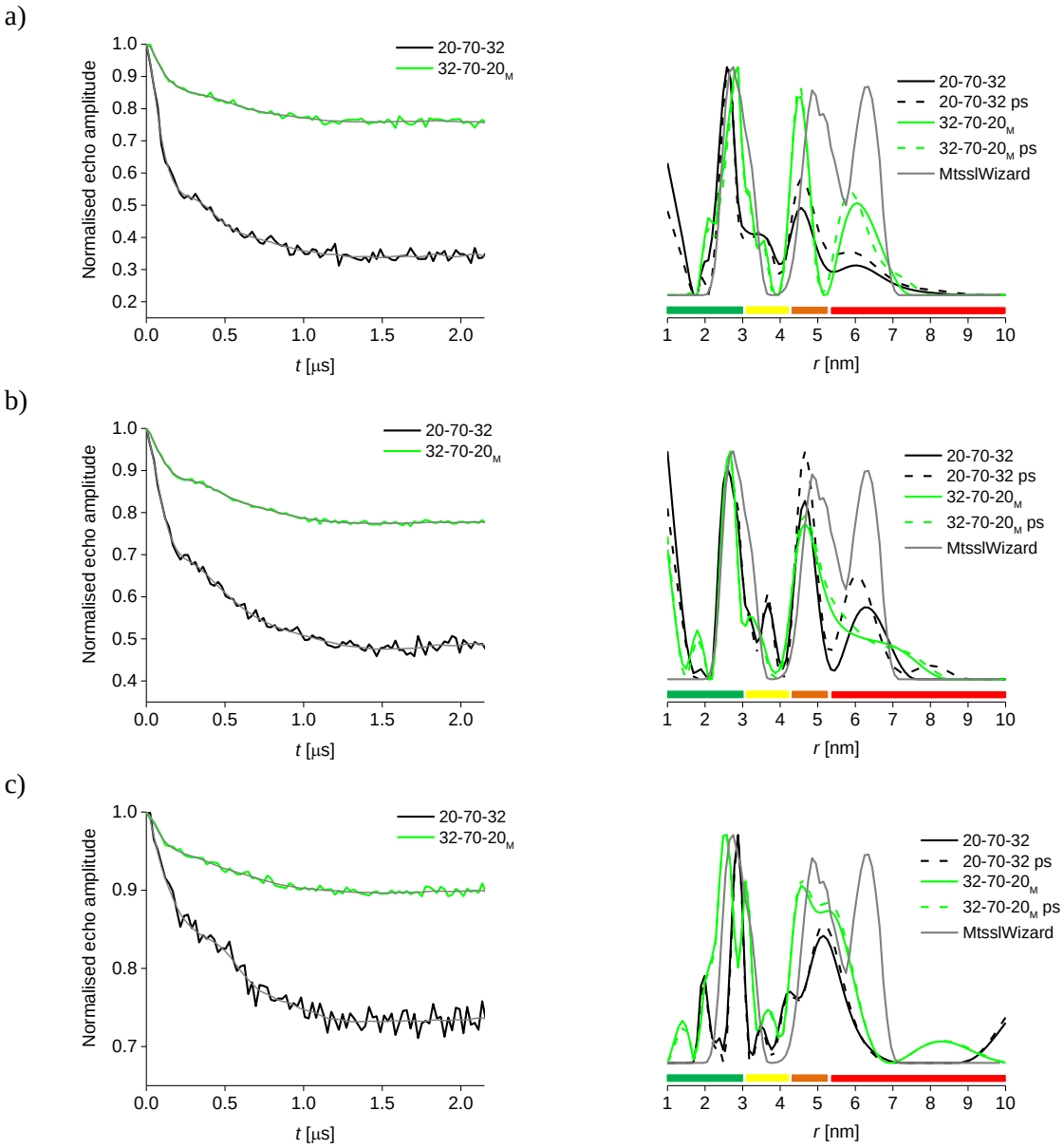

Figure 4.12: X-band MD5 background corrected traces with fits and corresponding distance distributions with (dashed) and without power-scaling (solid) for 100 a), 66 b) and 33% c) labelled samples of MscS D67R1 obtained when performing PELDOR (black) and frequency-interchanged (green) experiments. The legend reports pump pulse length – pulse offset – detection π pulse. The subscript M indicates the pump pulse being on maximum of field sweep. The coloured bars indicate the reliability of distances recovered as a function of the measuring time window.

a)

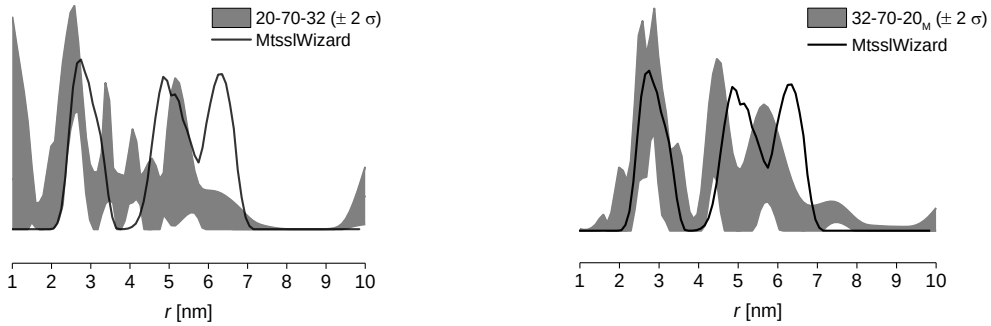

b)

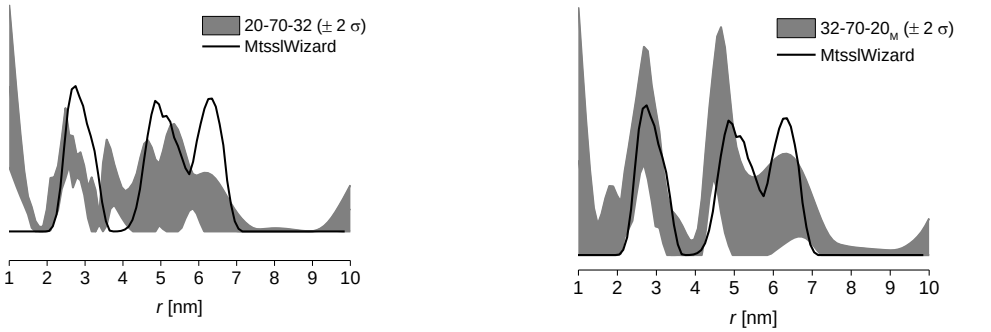

c)

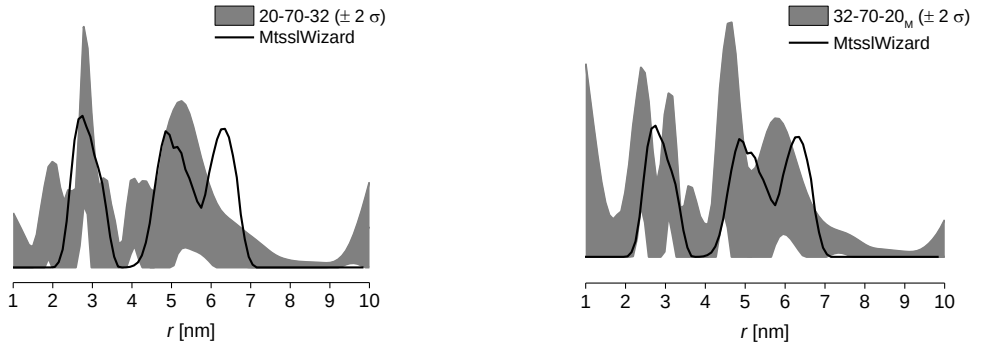

Figure 4.13: Validations of PELDOR (left) and frequency-interchanged (right) experiments on 100 a), 66 b) and 33 c) % labelled samples of MscS D67R1 at X-band (MD5). The grey area, representing the error bar, delineates those distance distributions that are stable to changes in processing parameters. The subscript M indicates the position of the pump pulse on the maximum of the nitroxide field sweep spectrum.

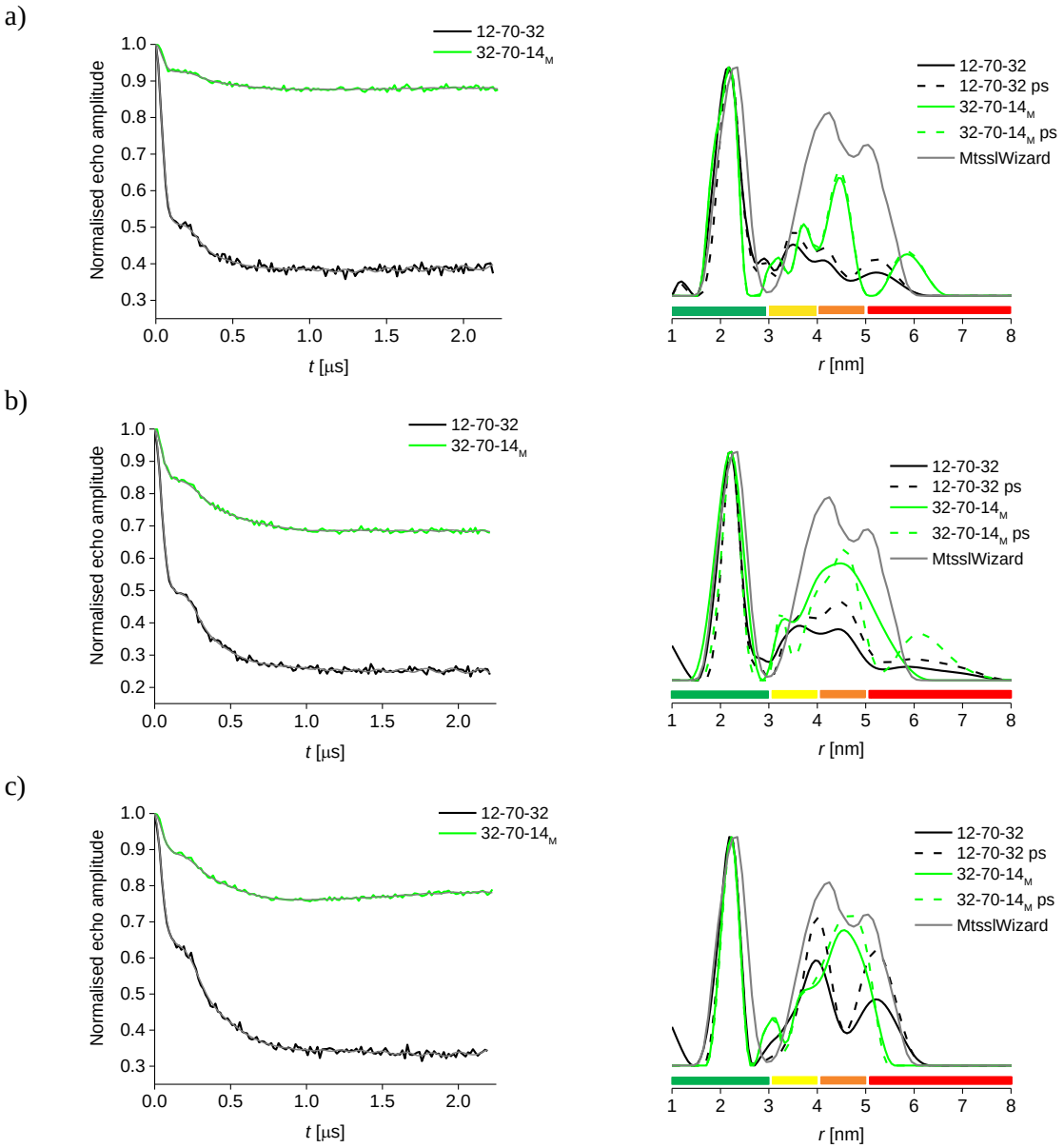

Figure 4.14: X-band MS3 background corrected traces with fits and corresponding distance distributions with (dashed) and without power-scaling (solid) for 100 a), 66 b) and 33% c) labelled samples of MscS mutant S196R1 obtained when performing PELDOR (black) and frequency-interchanged (green) experiments. The legend reports pump pulse length – pulse offset – detection π pulse. The subscript M indicates the pump pulse being on maximum of field sweep. The coloured bars indicate the reliability of distances recovered as a function of the measuring time window.

a)

b)

c)

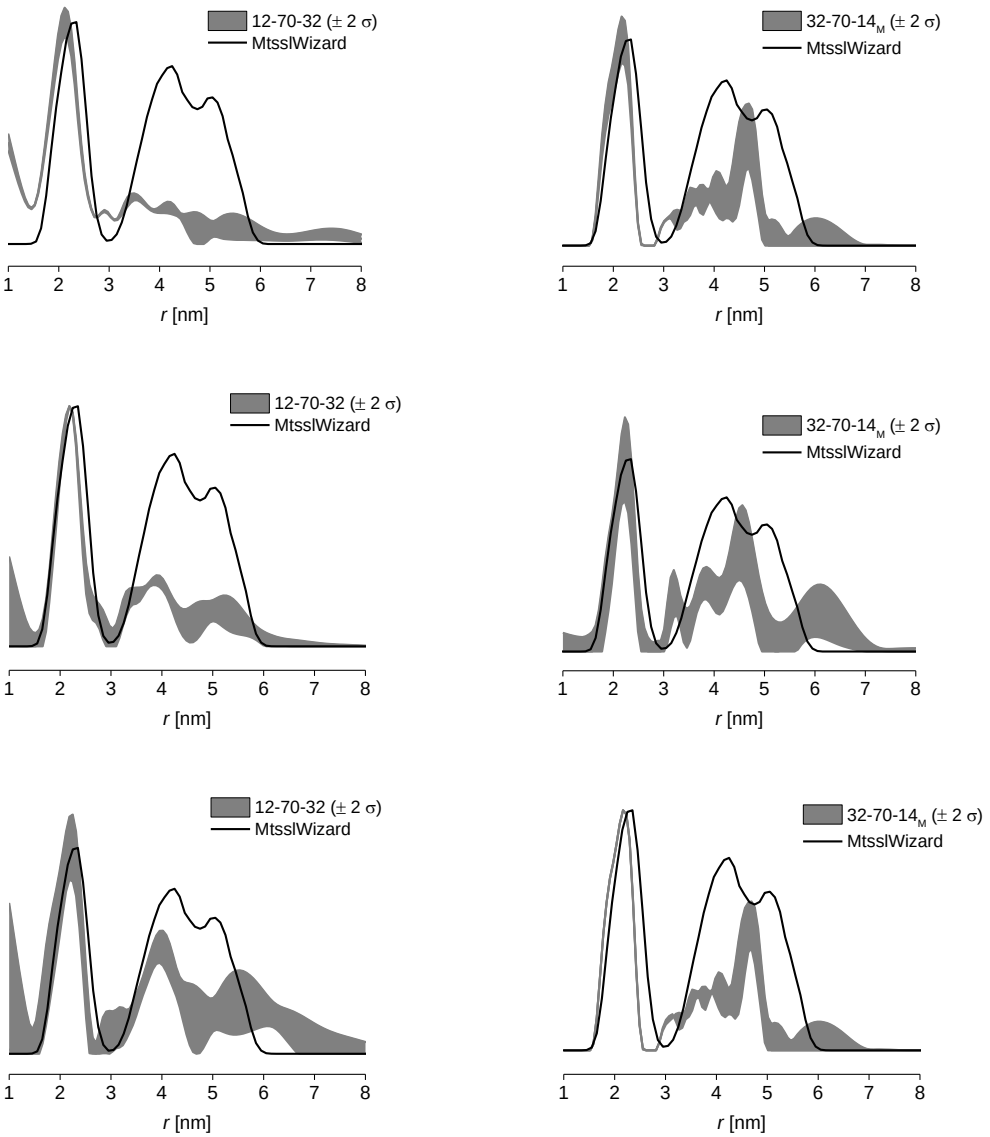

Figure 4.15: Validations of PELDOR (left) and frequency-interchanged (right) experiments on 100 a), 66 b) and 33 c) % labelled samples of MscS S196R1 at X-band (MS3). The coloured areas, representing the error bars, delineate those distance distributions that are stable to changes in processing parameters. The subscript M indicates the position of the pump pulse on the maximum of the nitroxide field sweep spectrum.

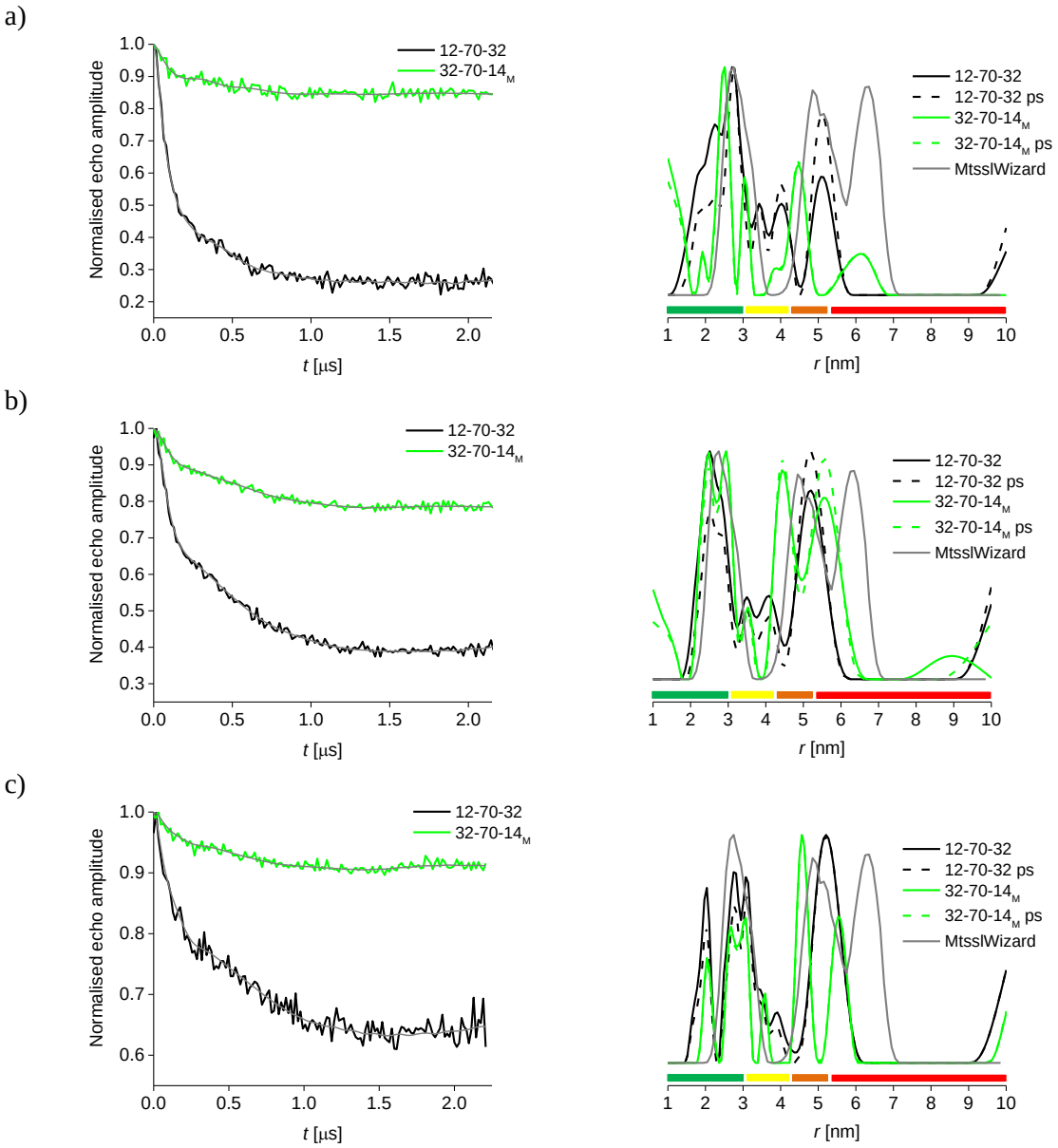

Figure 4.16: X-band MS3 background corrected traces with fits and corresponding distance distributions with (dashed) and without (solid) power-scaling for 100 a), 66 b) and 33% c) labelled samples of MscS mutant D67R1 obtained when performing PELDOR (black) and frequency-interchanged (green) experiments. The legend reports pump pulse length – pulse offset – detection π pulse. The subscript M indicates the pump pulse being on maximum of field sweep. The coloured bars indicate the reliability of distances recovered as a function of the measuring time window.

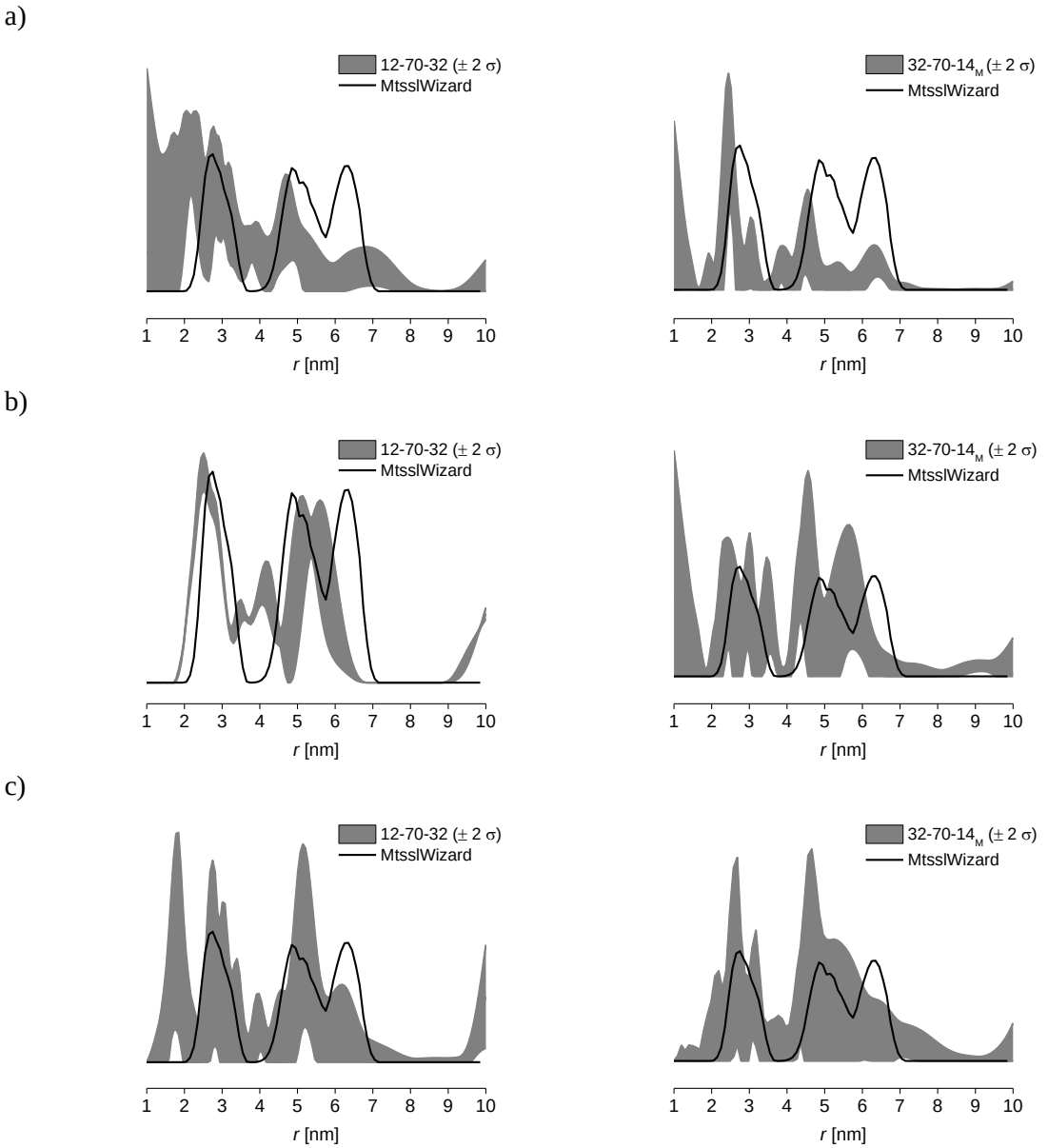

Figure 4.17: Validations of PELDOR (left) and frequency-interchanged (right) experiments on 100 a), 66 b) and 33 c) % labelled samples of MscS D67R1 at X-band (MS3). The coloured areas, representing the error bars, delineate those distance distributions that are stable to changes in processing parameters. The subscript M indicates the position of the pump pulse on the maximum of the nitroxide field sweep spectrum.

Measurements performed at Q-band frequencies show that frequency-interchanged experiments increase the intensities of longer distances. PELDOR experiments give improved distance distributions with decreasing degree of labelling, at least within the range that can be expected reliable. Frequency-interchanged experiments consistently further recover longer distance intensities, as shown in Figure 4.18 and Figure 4.20. Validation of MscS S196R1 distance distributions show good reliability for the

recovery of longer distances (Figure 4.19). However, the sensitivity still limits distance distributions of MscS D67R1, as suggested by validations of distance distributions reported in Figure 4.21.

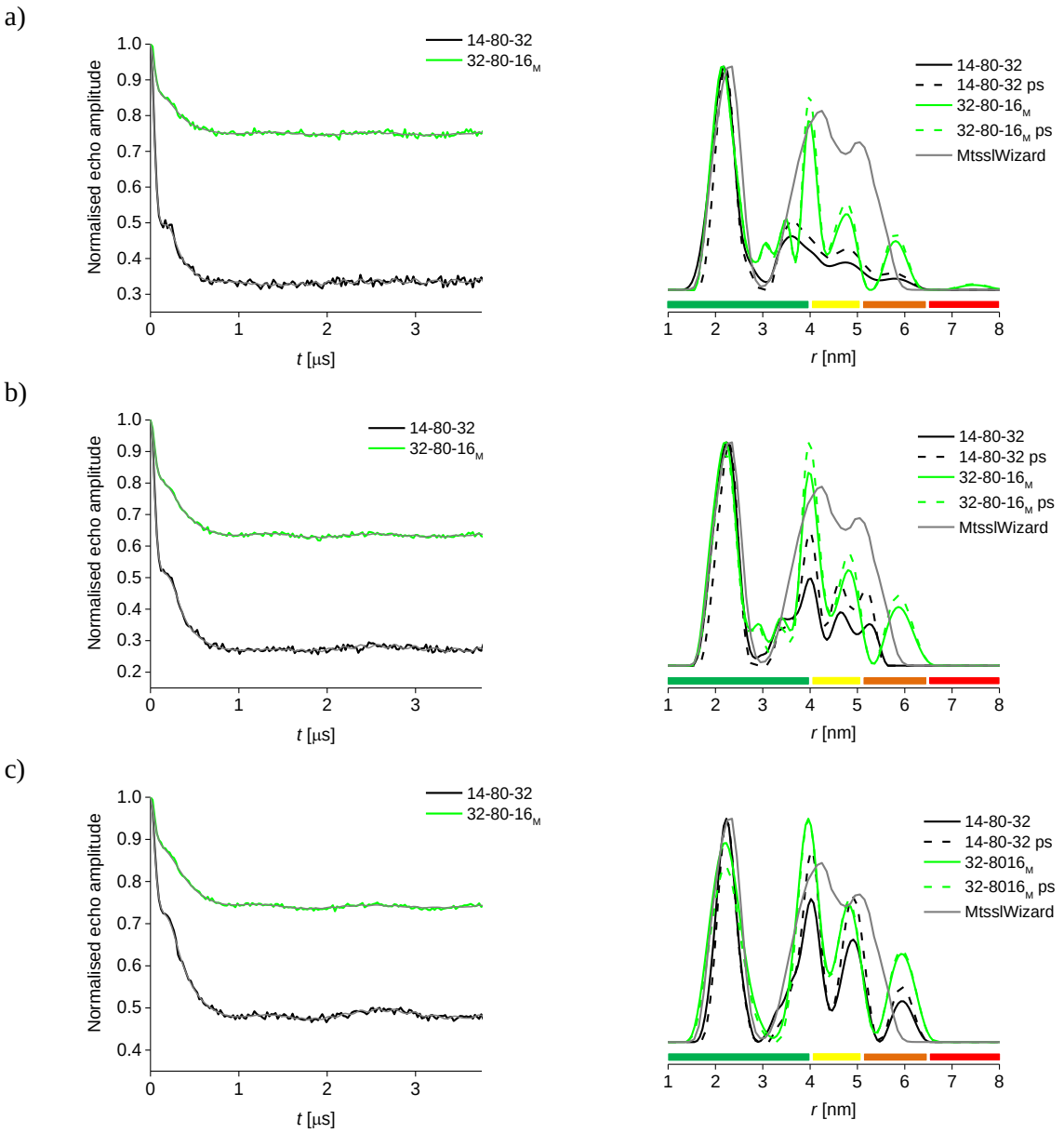

Figure 4.18: Q-band background corrected traces with fits and corresponding distance distributions with (dashed) and without (solid) power-scaling for 100 a), 66 b) and 33% c) labelled samples of MscS S196R1 obtained when performing PELDOR (black) and frequency-interchanged (green) experiments. The legend reports pump pulse length – pulse offset – detection π pulse. The subscript M indicates the pump pulse being on maximum of field sweep. The coloured bars indicate the reliability of distances recovered as a function of the measuring time window.

a)

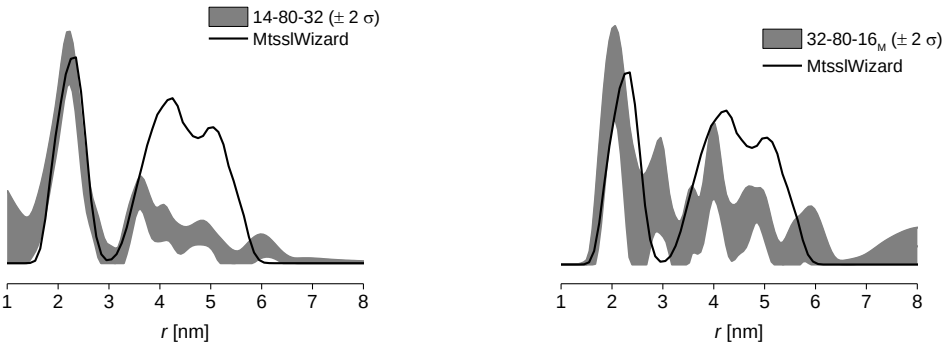

b)

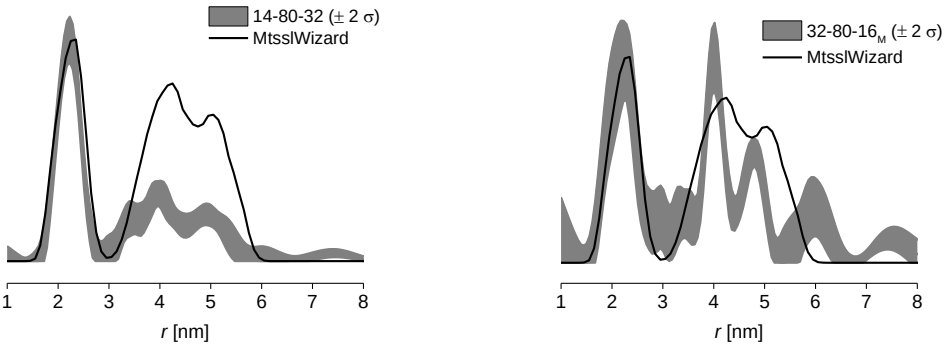

c)

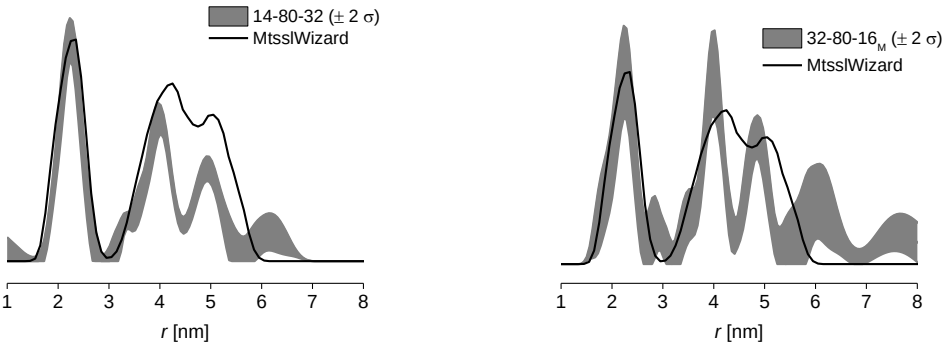

Figure 4.19: Validations of PELDOR (left) and frequency-interchanged (right) experiments on 100 a), 66 b) and 33 c) % labelled samples of MscS S196R1 at Q-band. The coloured areas, representing the error bars, delineate those distance distributions that are stable to changes in processing parameters. The subscript M indicates the position of the pump pulse on the maximum of the nitroxide field sweep spectrum.

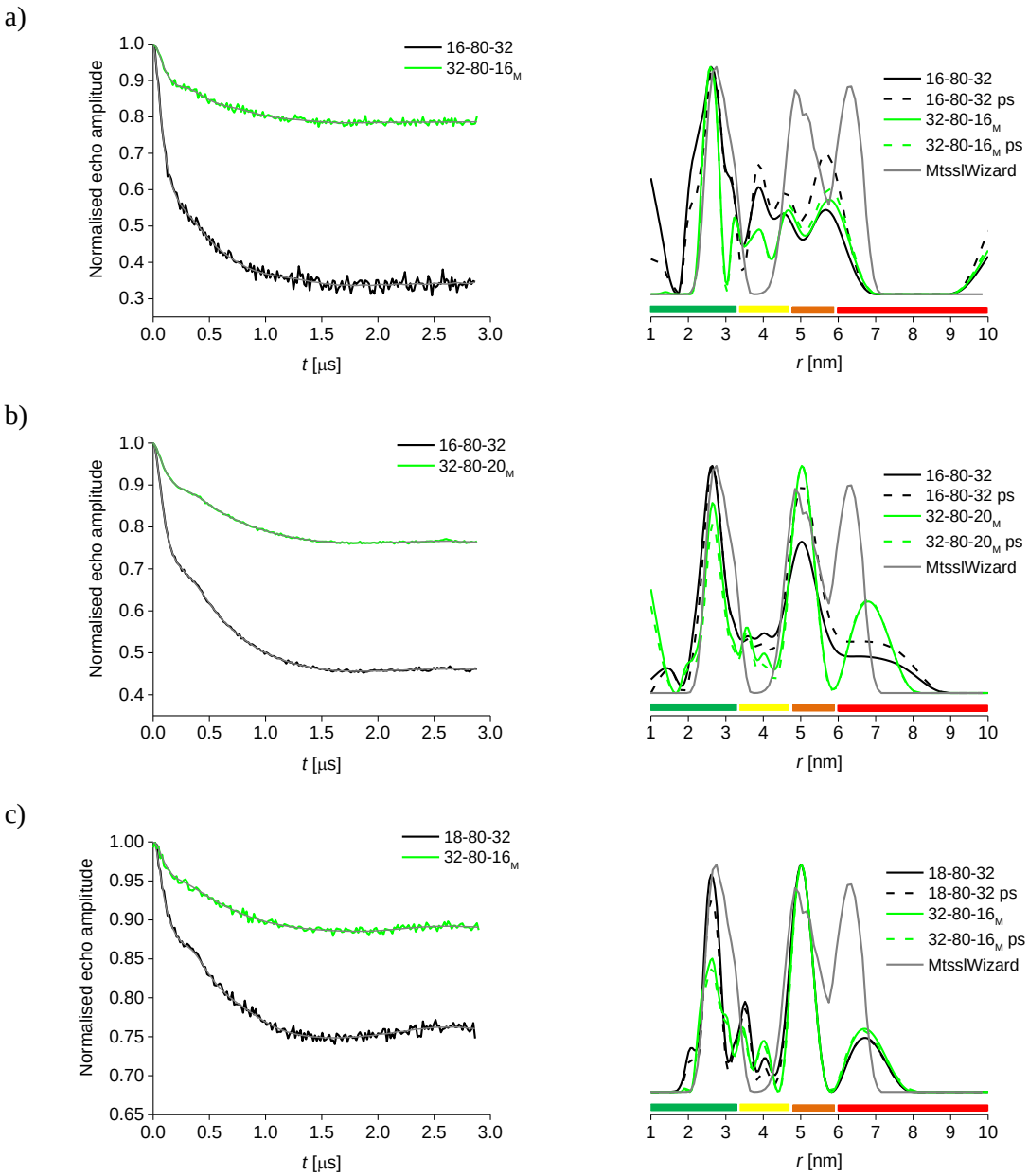

Figure 4.20: Q-band background corrected traces with fits and corresponding distance distributions with (dashed) and without (solid) power-scaling for 100 a), 66 b) and 33% c) labelled samples of MscS D67R1 obtained when performing PELDOR (black) and frequency-interchanged (green) experiments. The legend reports pump pulse length – pulse offset – detection π pulse. The subscript M indicates the pump pulse being on maximum of field sweep. The coloured bars indicate the reliability of distances recovered as a function of the measuring time window.

a)

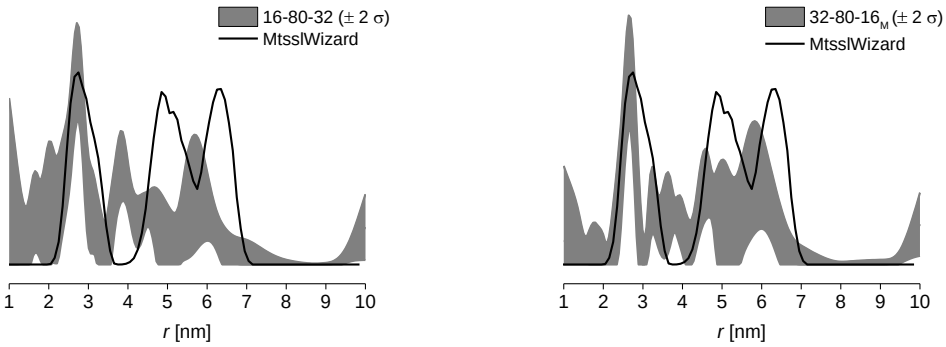

b)

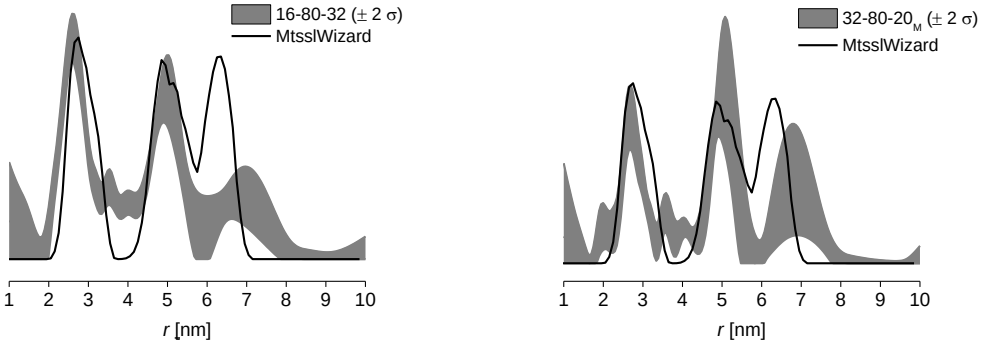

c)

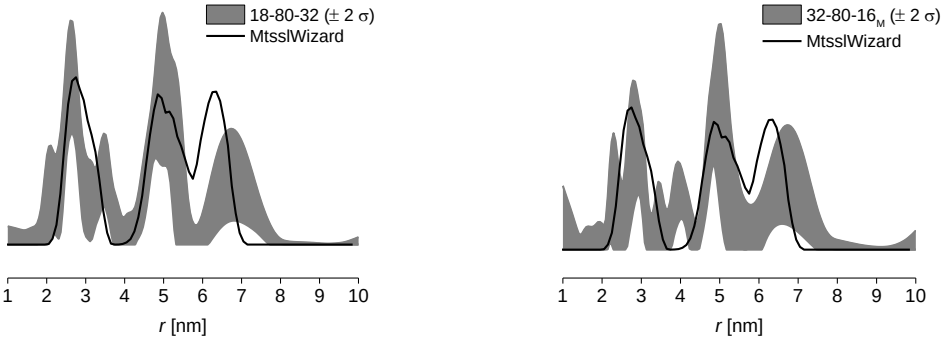

Figure 4.21: Validations of PELDOR (left) and frequency-interchanged (right) experiments on 100 a), 66 b) and 33 c) % labelled samples of MscS D67R1 at Q-band. The coloured areas, representing the error bars, delineate those distance distributions that are stable to changes in processing parameters. The subscript M indicates the position of the pump pulse on the maximum of the nitroxide field sweep spectrum.

Results reported in Figure 4.18 and Figure 4.20 suggest that Q-band measurements give access to extraction of accurate inter-spin distances in S196R1 sparsely labelled systems irrespective whether performing both regular PELDOR or frequency-interchanged experiments. The combination of frequency-interchanged experiment with 33% labelling brings some improvement in distance integrals for the S196R1 mutant (Figure 4.18), while broadening and loss of intensity of the first distance peak are introduced in the distance distribution for the D67R1 mutant (Figure 4.20 c)). In the next section recovery of the probability of long distances will be related to changes in sensitivity. This will allow quantifying the methods in question and drawing clear recommendations for sensitive and accurate distance measurements in multimeric systems.

4.3.3.2 *Sparse labelling and frequency-interchange: effects on sensitivity*

Sensitivity values reported in Table 4.2, Table 4.3 and Table 4.4 show a mixed performance from the frequency-interchanged experiments when compared to PELDOR measurements performed at X-band (MD5 resonator). Here, sensitivity values for both experiments performed on the fully and sparsely labelled samples of the same mutant are normalised against the sensitivity values obtained when performing PELDOR measurements on the fully labelled system. When comparing frequency-interchanged measurements on MscS S196R1 samples with the same labelling efficiency *f* with the corresponding experiments performed with PELDOR settings, these appear to give a minor reduction in sensitivity values except for the 33% labelled samples, for which a slight improvement is recorded for the frequency-interchanged measurements. This is due to the considerable lowering in noise levels, which overcompensates the loss in modulation depth. This phenomenon is probably related to the low labelling degree that reduces the ID effects, thus improving the noise levels.

MscS S196R1_X-band MD5 resonator				
PELDOR				
Labelling (*f*)	Δ	Noise	Sensitivity	Norm. Sensitivity
100%	0.66	0.0053	120	1.00
66%	0.58	0.0064	91	0.76
33%	0.49	0.0052	94	0.78
Frequency-interchanged				
Labelling (*f*)	Δ	Noise	Sensitivity	Norm. Sensitivity
100%	0.32	0.0026	120	1.00
66%	0.21	0.0033	64	0.53
33%	0.25	0.0024	100	0.83
MscS D67R1_X-band MD5 resonator				
PELDOR				
Labelling (*f*)	Δ	Noise	Sensitivity	Norm. Sensitivity
100%	0.66	0.0122	54	1.00
66%	0.52	0.0096	54	1.00
33%	0.27	0.0101	27	0.50
Frequency-interchanged				
Labelling (*f*)	Δ	Noise	Sensitivity	Norm. Sensitivity
100%	0.24	0.0067	36	0.66
66%	0.22	0.0026	85	1.60
33%	0.10	0.0031	32	0.60

Table 4.2: Comparison between sensitivity values obtained for PELDOR and frequency-interchanged experiments performed at X-band frequencies (MD5) on both MscS mutants S196R1 and D67R1 with a 100, 66 and 33% labelling efficiency *f*. All values are given to two significant figures.

X-band MD5 measurements for MscS D67R1, instead, show an improvement in sensitivity for the frequency-interchanged experiment on the 66% sample. However, frequency exchanged experiments with an MS3 resonator lead to slight loss in sensitivity for all labelling degrees of MscS S196R1 (Table 4.3). When going to MscS D67R1 the sensitivity significantly decreases further. This trend persists at Q-band: the frequency-interchanged experiments lead to a loss in sensitivity for both mutants (Table 4.4). This effect is dominated by the reduction in labelling lowering the number of spins per multimer available for excitation by the pump pulse, thus reducing Δ. Performance of the frequency-interchanged experiments is expected to decrease with lowering labelling efficiency, as the multi-spin effects are already partially countered by sparse labelling. Frequency-interchanged experiments of S196R1 at X-band using an MS3 resonator show a progressive

increase in sensitivity with lowering in labelling efficiency with the 33% samples giving a nearly three times improvement when compared to the frequency-interchanged experiment performed on the fully labelled sample. However, the same trend is not observed for the D67R1 sample where the frequency-interchanged experiments give the best sensitivity when applied on the 66% labelled sample. Thus, the change in measurement sensitivity when applying the frequency-interchanged experiment to sparsely labelled samples cannot be fully rationalised when comparing the results obtained from the two MscS mutants.

MscS S196R1_X-band MS3 resonator				
PELDOR				
Labelling (*f*)	Δ	Noise	Sensitivity	Norm. Sensitivity
100%	0.63	0.0088	72	1.00
66%	0.75	0.0073	100	1.40
33%	0.65	0.0077	84	1.20
Frequency-interchanged				
Labelling (*f*)	Δ	Noise	Sensitivity	Norm. Sensitivity
100%	0.13	0.0042	31	0.43
66%	0.30	0.0050	60	0.83
33%	0.26	0.0035	74	1.03
MscS D67R1_X-band MS3 resonator				
PELDOR				
Labelling (*f*)	Δ	Noise	Sensitivity	Norm. Sensitivity
100%	0.74	0.0141	52	1.00
66%	0.62	0.0031	200	3.80
33%	0.36	0.0152	24	0.46
Frequency-interchanged				
Labelling (*f*)	Δ	Noise	Sensitivity	Norm. Sensitivity
100%	0.15	0.0120	13	0.25
66%	0.22	0.0080	28	0.53
33%	0.09	0.0057	16	0.31

Table 4.3: Comparison between sensitivity values obtained for PELDOR and frequency-interchanged experiments performed at X-band (MS3 resonator) on both MscS mutants S196R1 and D67R1 with a 100, 66 and 33% labelling efficiency *f*. All values are given to two significant figures.

An improvement in signal-to-noise for both sparse labelling and frequency-interchanged experiments is observed. This is due to the reduction of dephasing by ID achieved through the reduction the local concentration of spin labels. The improvement of the

noise levels, however, shows not to be sufficient to fully compensate for the significant reduction in Δ by both sparse labelling and frequency interchange.

MscS S196R1_Q-band				
PELDOR				
Labelling (*f*)	Δ	Noise	Sensitivity	Norm. Sensitivity
100%	0.68	0.0065	100	1.00
66%	0.73	0.0063	120	1.20
33%	0.52	0.0056	93	0.93
Frequency-interchanged				
Labelling (*f*)	Δ	Noise	Sensitivity	Norm. Sensitivity
100%	0.25	0.0063	40	0.40
66%	0.36	0.0045	80	0.80
33%	0.26	0.0043	61	0.58
MscS D67R1 Q-band				
PELDOR				
Labelling (*f*)	Δ	Noise	Sensitivity	Norm. Sensitivity
100%	0.64	0.0110	54	1.00
66%	0.51	0.0021	240	4.40
33%	0.25	0.0041	61	1.10
Frequency-interchanged				
Labelling (*f*)	Δ	Noise	Sensitivity	Norm. Sensitivity
100%	0.20	0.0060	33	0.61
66%	0.22	0.0022	100	1.90
33%	0.11	0.0030	37	0.69

Table 4.4: Comparison between sensitivity values obtained for PELDOR and frequency-interchanged experiments performed at Q-band frequencies on both MscS mutants S196R1 and D67R1 with a 100, 66 and 33% labelling efficiency *f*. All values are given to two significant figures.

From these preliminary results it can be concluded that the combination of a high degree of sparse labelling and the frequency-interchanged experiment lead to a significant loss in sensitivity compromising the reliability of the distance distributions recovered. Further studies need to be performed to test whether the frequency-interchanged experiment is a practical alternative for extracting accurate distance distributions from samples with high *f* to the preparation of new samples with lower *f*.

4.3.4 Combination of lambda reduction and sparse labelling

After having tested the effects of the combination of sparse labelling and the frequency-interchanged experiments, it was investigated if λ reduction and sparse labelling were able to suppress multi-spin effects without compromising sensitivity to a similar extent. This would test the performance of sparse labelling in comparison to λ reduction and thus if efforts should be invested in sample preparation or measurement.

Experiments were performed on the 33% labelled sample performing PELDOR experiments with λ_{max} against the fully labelled sample measured with a λ value equivalent to 33% of the λ_{max}. The aim of this comparison was to test if the excitation of the most populated area of the EPR spectrum by the pump pulse of the 33% labelled sample would give similar results to measurement of the fully labelled samples with a reduced λ with a value equivalent to 33% of $\lambda_{max,}$ as only 33% of the spins are available for excitation when compared to the fully labelled sample. The comparison aimed at the observation for the accurate extraction of the expected distance peaks and sensitivity values obtained from the different experiments on the fully and sparsely labelled samples. Measurements were performed at Q-band as the time window achievable would allow accurate extraction of all distances excluding cut-off artefacts, at least for S196R1. The comparison between PELDOR experiments with λ_{max} for 33%, 66%, 100% labelled samples and PELDOR experiment with a reduced λ for fully labelled samples was made on both mutants (Figure 4.22). Measurements with λ_{max} on the sparsely labelled samples reflect the previously observed results: reduction in labelling efficiency leads to some loss in Δ and introduces improvements in recovery of long distance peaks. The λ reduced experiment on the fully labelled sample of MscS S196R1 shows a major loss in Δ, whose value is halved when compared to the 33% labelled sample, and gives the same distance distribution as for the 33% labelled sample. For the D67R1 sample the difference in Δ between measurements on the 33% labelled sample with λ_{max} and fully labelled sample with reduced λ, equivalent to 33% λ_{max}, is not as prominent (Figure 4.22). For both mutants, the recovery of distance peaks is similar; thus, when looking at distance distributions reduction in labelling efficiency and λ appear to perform with a similar trend.

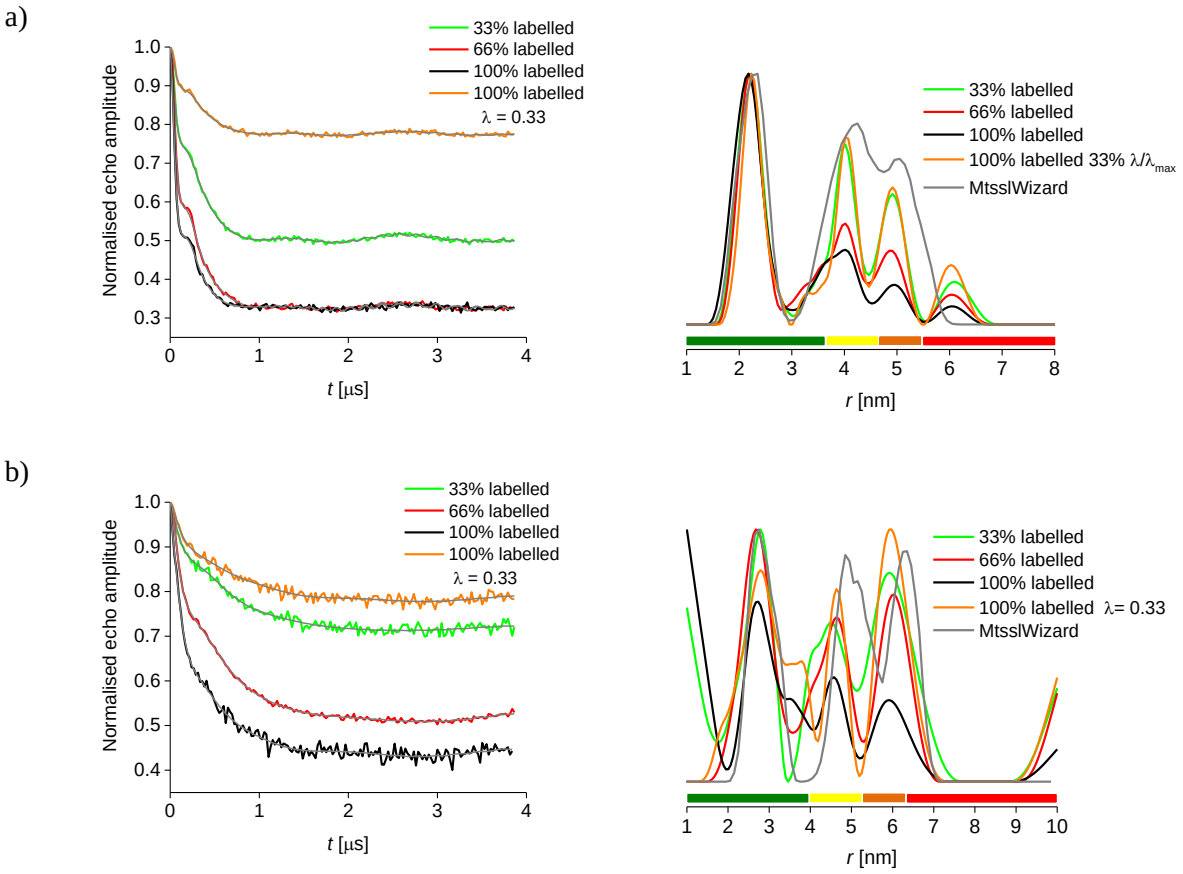

Figure 4.22: Comparison between PELDOR measurements performed at Q-band with λ_{max} on 33, 66 and 100% labelled samples together with 33% λ_{max} on the 100% labelled sample. The coloured bars indicate the reliability of distances recovered as a function of the measuring time window.

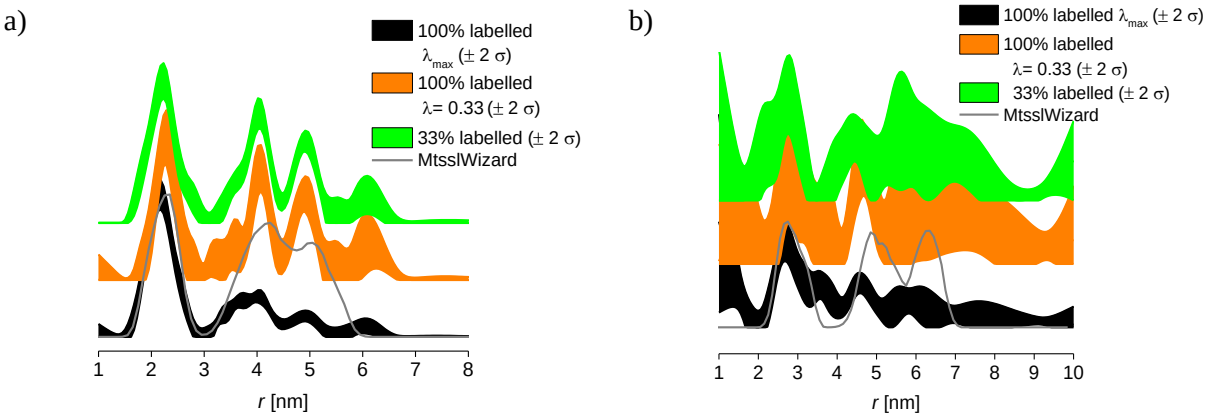

Figure 4.23: Validation of 100% (measured with λ_{max} and 33% λ_{max}) and 33% labelled (measured with λ_{max}) MscS mutants S196R1 a) and D67R1 b). The coloured areas, representing the error bars, delineate those distance distributions that are stable to changes in processing parameters.

Comparison of validations of the λ_{max} and 33% λ_{max} measurements performed on the fully labelled systems with measurements performed with λ_{max} on the 33% labelled mutants show that the least labelled system has the least level of uncertainty for S196R1 (Figure 4.23). Distances in S196R1 could be accurately resolved thanks to the extended measuring time window, however the third distance in D67R1 still requires a longer time window as suggested by the low reliability levels shown in the validation.

The effects on sensitivity for both methods were quantified as previously described in Section A.2.5 and are reported in Table 4.5. As expected from observations evident from the background corrected traces in Figure 4.22, reduction in *f* induces a very limited loss in sensitivity when compared to the fully labelled samples performed with λ_{max}. For MscS S196R1, reduction of λ on the 100% labelled samples shows to importantly lower the measurement sensitivity when compared to the value of the one obtained for the measurement performed on the 33% labelled one with λ_{max}. A similar result is observed for the second mutant where the gain in sensitivity when using sparse labelling is still significant compared to λ reduction.

MscS S196R1_Q-band				
PELDOR				
Labelling (*f*)	Δ	Noise	Sensitivity	Norm. Sensitivity
100%	0.67	0.0043	160	1.00
100% (33% λ/λ_{max})	0.22	0.0040	55	0.34
66%	0.67	0.0045	150	0.94
33%	0.50	0.0038	130	0.81
MscS D67R1_Q-band				
Frequency-interchanged				
Labelling (*f*)	Δ	Noise	Sensitivity	Norm. Sensitivity
100%	0.55	0.0100	54	1.00
100% 33% (λ/λ_{max})	0.20	0.0085	24	0.44
66%	0.50	0.0042	120	2.20
33%	0.28	0.0075	37	0.69

Table 4.5: Comparison between sensitivity values obtained for λ_{max} measurements performed on sparsely labelled samples and 33% λ_{max} experiments on 100% labelled mutants. All values are given to two significant figures.

The results presented here suggest that sparse labelling represents an alternative method for suppression of multi-spin effects in distance measurements of multiply

labelled oligomeric proteins. This method has been initially tested by simulations mimicking the conformational state of the two mutants of the MscS heptameric channel protein.. The effects of sparse labelling on measurement sensitivity and extraction of accurate inter-spin distances was tested in the presence of increasing levels of noise and in combination with the reduction of λ. The results demonstrate that sparse labelling is a valid alternative to λ reduction and power-scaling as it allows for extraction of accurate distances while minimising the loss or even introducing improvements in sensitivity levels when compared to reducing λ. .

4.3.5 Comparison between frequency-interchanged and sparse labelling

Up to this point frequency-interchanged experiment and the sparsely labelled methods have been tested as approaches to extract accurate distance distributions in multiply labelled systems without compromising on sensitivity. The two methods, in particular, have been tested on the two MscS mutants S196R1 and D67R1. Here, the distance distributions obtained from the labelling degree giving the most accurate distance distributions, 33% for both mutants, and from performing the frequency-interchanged experiment on the fully labelled systems are compared.

Figure 4.24 shows for both mutants that similar results are obtained when performing the PELDOR experiment on the 33% labelled systems and the frequency-interchanged experiment on the fully labelled system. The background corrected traces, however, show quite an important loss in Δ for the frequency-interchanged experiment when compared to PELDOR measurements on the least labelled 33% sample of MscS S196R1. For MscS D67R1 the difference in Δ does not appear to be as dramatic, however the signal-to-noise appears to be lowered for the frequency-interchanged experiment.

Table 4.6, reporting the sensitivity values for the experiments reported in Figure 4.24, confirms the observations from comparison of the background corrected traces: the frequency-interchanged experiment offers lower measurement sensitivity than the reduction in labelling efficiency. This is mainly related to discrepancy between the Δ achieved using the two methods, as suggested by value reported in Table 4.6, which suggests that lowering the number of spins within the system still allows for excitation of a larger fraction of spins than when performing the frequency-interchanged experiment.

a)

b)

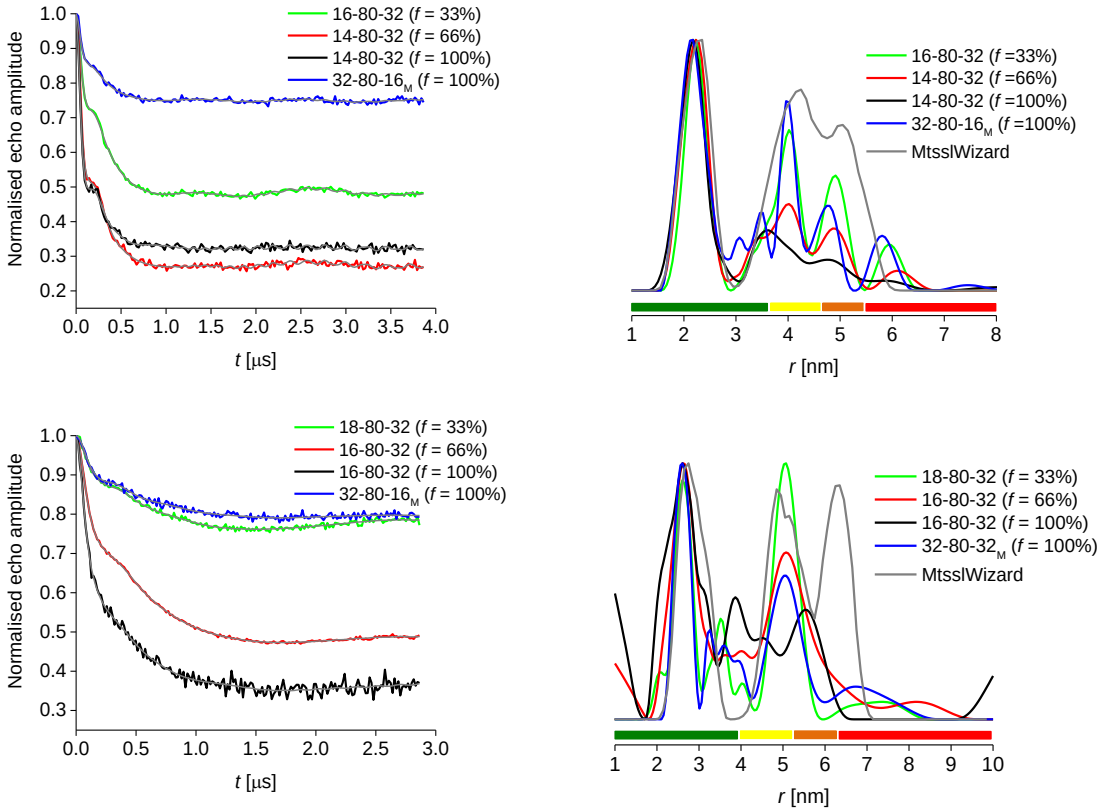

Figure 4.24: Background corrected traces and distance distributions obtained from PELDOR measurements on samples with labelling degree *f* 33% (green), 66% (red) and 100% (black) and for frequency-interchanged experiments (blue) on the fully labelled systems. The legend reports pump pulse length – pulse offset – detection π pulse. The subscript M indicates the pump pulse being on maximum of field sweep. The coloured bars indicate the reliability of distances recovered as a function of the measuring time window. The subscript M indicates the position of the pump pulse on the maximum of the nitroxide spectrum.

The improved recovery and gain in sensitivity obtained by sparsely labelled samples suggest that further improvements could be introduced in the frequency-interchanged experiment set-up. Further studies on other channel proteins are required to further establish the efficiency of both methods.

MscS S196R1_Q-band				
Labelling (*f*)	Δ	Noise	Sensitivity	Norm. Sensitivity
16-80-32_100%	0.68	0.0065	100	1.00
14-80-32_66%	0.73	0.0063	120	1.20
14-80-32_33%	0.52	0.0056	93	0.93
32-80-16_M_100%	0.25	0.0063	40	0.40
MscS D67R1_Q-band				
Labelling (*f*)	Δ	Noise	Sensitivity	Norm. Sensitivity
18-80-32_100%	0.64	0.0110	54	1.00
16-80-32_66%	0.51	0.0021	240	4.40
16-80-32_33%	0.25	0.0041	61	1.10
32-80-16_M_100%	0.20	0.0060	33	0.61

Table 4.6: Comparison of sensitivity values for PELDOR experiments performed on sparsely labelled systems and frequency-interchanged measurements on the fully labelled MscS S196R1 and D67R1 samples. All values are given to two significant figures.

4.4 Conclusion

Comparison and combination of sparse labelling with λ reduction and frequency-interchanged experiments together with power-scaling have been evaluated and their effects quantified. Sparse labelling, when performing PELDOR measurements with λ_{max}, gave access to accurate extraction of the expected distance peaks, matching the MtsslWizard predicted model. Here, losses in sensitivity were limited for X-band measurements, while at Q-band sensitivity values were not affected, or, in some cases, even improved when compared to measurements on the fully labelled samples with λ_{max}. Frequency-interchanged experiments on sparsely labelled samples introduced a limited improvement in distance distributions, however it led to some loss in sensitivity as the improvement in noise levels could not compensate the loss in Δ. Lastly, sparse labelling was proven to introduce the same improvement in recovery of longer distance peaks as λ reduction on a fully labelled sample, while retaining or improving the sensitivity.

Consequently, this method offers an alternative and efficient approach for suppression of multi-spin effects when performing distance measurements in multiply labelled systems.

Chapter 5 - Orientation selection and multi-spin effects in PELDOR distance measurements

The author performed the PELDOR measurements and data processing under the supervision of Dr. Bela Bode.

5.1 Introduction

Orientation selection effects are one the factors, together with multi-spin effects,[19a] strong *J* couplings[20b] and spin density distribution,[50a] that are neglected when processing data with DeerAnalysis;[30] these may require particular attention when interpreting distance measurements. Orientation selection effects in PELDOR are commonly induced by the presence of angular restraints between spin labels, usually induced by their geometry and backbone restricted conformational flexibility. The extent of orientation selection effects depends on the degree of correlation in the spin label orientations and resolution of the *g*-tensor.[120] In rigid systems the relative orientations between two or more radicals and the connecting distance vectors **r** are fixed introducing a non-random distribution of dipolar angles θ between **r** and B_0 contributing to the PELDOR signal. Presence of fixed molecular orientations with different resonance field values allows for selective excitation of spin labels with a specific orientation of their molecular axis system in relation to B_0 when varying the pump and detection frequencies.[2b] This leads to the dependence of the PELDOR signal not only on the inter-spin distances, but also on the angular correlations present within the rigid system.[2b, 90] Here, the nature and implications of orientation selection effects in PELDOR distance measurements are briefly described.

In spin labelled systems bearing an intrinsic flexibility, dictated by the structure and conformation of both the system and the spin label of choice, the mutual orientations of the molecular axis systems of the spin labels can be approximated to be random. In these cases the frequency and modulation depth Δ of a PELDOR experiment will be independent of the orientation of the excited spin labels in respect to B_0 and the distribution function of the dipolar angles can be described by the $\sin(\theta_{dip})$ distribution of a Pake pattern.[18b] Thus, the time trace will be independent of the pump and detection frequencies and the Δ will only depend on the probability of a spin to be flipped by the pump pulse. This statistical distribution of orientations can be easily analysed by Tikhonov regularisation methods.[29, 121]

In rigid systems the structural constraints present within the system lead to fixed relative orientations between the spin labels and connecting distance vectors. This can induce to a non-random distribution of dipolar angles and to the consequent excitation of a limited number of orientations that will contribute to the PELDOR signal. This factor will directly affect the line shape of the dipolar spectrum, which will now present features indicating the excitation of a specific set of orientations.[2b]

One method for studying orientation selection in PELDOR experiments at X-band is by variation of the pulses' offset. This is commonly performed by fixing the pump pulse on the maximum of the EPR spectrum, while varying the frequency of the detection pulse to excite different spectral areas to which correspond different molecular orientations of detected radicals in relation to B_0.[7a] Selection of specific orientations is thus dependent on the frequency of the detection sequence; this is due to the anisotropy of the nitroxide EPR spectrum[20b] being dominated at X-band by the ^{14}N hyperfine coupling, with only the tensor components A_{zz} being resolved as shown in Figure 5.1.[27]

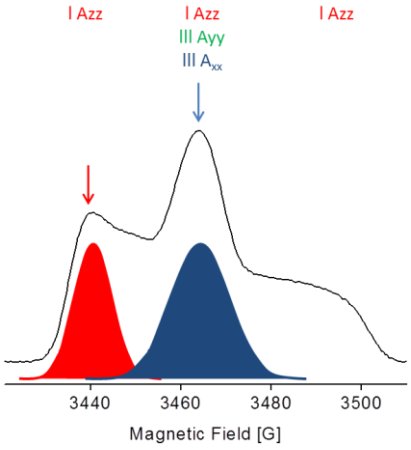

Figure 5.1: ^{14}N hyperfine tensor in anisotropic nitroxide EPR spectrum at X-band with a cartoon of the bandwidth and spectral position for detection (red) and pump (blue) pulses.[2b]

The position of the pump frequency is set at the maximum of the EPR spectrum, where all components A_{zz}, A_{yy} and A_{xx} of the anisotropic hyperfine are present, thus allowing excitation of all orientations.[17b, 74] By changing the position of the detection frequency from the low-field maximum towards the global maximum different intermediate orientations are excited. At the low field maximum predominantly the A_{zz} component of the ^{14}N hyperfine tensor dominates the spectral intensity; this corresponds

to spin labels with their molecular z-axis parallel to B_0 dominating the spectrum (Figure 5.1 and Figure 5.2).

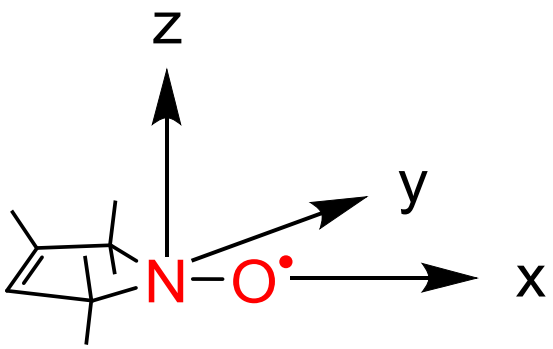

Figure 5.2: The principal molecular axes of the components of the hyperfine tensor in a nitroxide spin-label.

Several X-band studies used pulse offsets between 40 and 80 MHz allowing for a selection of spin labels with their molecular axis z largely perpendicular or parallel to B_0, respectively.[18b, 122] This manifests, in extreme cases, with a certain orientation of molecules detected and only certain orientations of pump spin molecules are found at certain dipolar angles θ. The dipolar frequency now depends on the dipolar angle which in turn is constrained by the orientations detected, while the modulation depth will be governed by the pump frequency or rather how many of the molecules connected to the specific orientations detected are pumped (i.e. resonant with the pump frequency).[120] The effects of different dipolar angles on the dipolar coupling are illustrated by Equation 1.2 and materialise in the Pake pattern (Figure 1.4).

Orientation selective PELDOR can give access to both distance and angular information; however several considerations have to be taken into account for collection and interpretation of orientation selective data. Several PELDOR experiments exciting different molecular orientations by the pump and detection pulses (e.g. by changing frequencies, or magnetic field or both) are required for identifying and determining possible constrained mutual orientations.[17a, 18c, 62, 74, 120]

Interpretation of these data cannot be performed in a model-free fashion and requires calculation of the individual contributions of each dipolar angle for the given subsets of pumped and probed spins.[50a, 71] This procedure cannot be currently performed in DeerAnalysis, as the gold standard of PELDOR data analysis, as the model free analysis is based on a random distribution of dipolar angles.[30] Particularly, it has been found that

interpretation of data from systems presenting strong angular correlations by DeerAnalysis can lead to erroneous results[18b, 50a, 71] and, if underestimated, to data misinterpretation.[74] Thus, analysis of distance data requires alternative methods for interpretation of orientation selective PELDOR data.[18b]

PELDOR data affected by orientation selection and multi-spin effects require caution and additional methods when extracting distance information, as excitation of specific orientations of the dipolar angle and presence of sum and difference frequencies, respectively, give a distorted dipolar spectrum which deviates from a superposition of Pake patterns.[2b, 78b] Previous studies and work reported in Chapters 3 and 4 have demonstrated the impact of multi-spin effects on PELDOR distance measurements, however their presence has not always been apparent in distance measurements on model systems with up to four spins[19b] or on a protein octamer.[47b] Notably, in the first study processing of data from PELDOR measurements on a tri- and tetra-radical model systems gave distance distributions where all peaks could be resolved almost quantitatively, with only a small artefact found in the distance distribution from the asymmetric tetraradical. Here, the simulation of the time trace based on the distance distribution without the additional peak showed that the additional distance was not significant within the signal-to-noise ratio.[19b] The study on the protein octamer revealed the shortest two of the four distances to be expected in a regular convex octagon were accessible within the achievable measuring time window. Their distance peak positions nicely agreed with crystallographic data on the spin-labelled protein.[47a] These observations point to a discrepancy in the literature and the field. While some studies[19a, 78a], and Chapters 3 and 4 herein, find multi-spin effects a major obstacle in accurate extraction of distances, these results above were in excellent agreement with models and predictions even though completely neglecting multi-spin effects. A study rationalising all these findings in a single model is currently lacking.

A further issue in distance measurement arises from electron spin echo envelope modulation (ESEEM). The ESEEM frequencies correspond to forbidden electron-nuclear transitions that can be introduced into distance measurements by spectral overlap of pulses. ESEEM is another abundant, but unwanted, contribution to the PELDOR signal.[9b] Nuclear modulation frequencies could be erroneously translated into distance peaks, thus hampering distance measurements.[9b] Replacement of protons by

deuterium is a common method used for facilitating distance measurements by extending the transverse relaxation time, thus extending the achievable time window.[68]

In a non-deuterated environment the signal can often decay within 2 μs, limiting the measurement of distances to a maximum of 3-4 nm, while in perdeuterated solvent this often extends to 5-6 μs pushing the distance limit ~1.5 nm further.[123] Total deuteration of protein and buffer has been shown to give access to a measuring time window up to 36 μs and 10 nm distances.[124] However, perdeuteration of the protein is very challenging and costly,[68] making it unlikely to become a standard method. The perspective of measuring longer time windows and consequently of accurately extracting long distances becomes particular appealing for large biological systems. It has to be considered, however, that at X-band frequencies the deuterium modulations at approximately 2.3 MHz, would correspond to a distance of about 2.8 nm when mistaken for a dipolar frequency. Proton modulations at ~14.5 MHz at X-band, on the other hand, correspond to a distance of 1.5 nm, right at the lower distance limit of PELDOR measurements.[9b, 113] It has recently been shown that these nuclear modulation artefacts can be suppressed to a good extent by nuclear modulation averaging. This is achieved by incrementing the inter-pulse delay between the first two detection pulses and summation of the time traces with varying initial pulse delays.[29, 113]

Commonly, protonated solvents are used for measurement of short distances and deuterated ones are employed for longer distances. However, when measuring protonated biological systems in deuterated solvents for elucidation of longer distances both proton and deuterium nuclear modulations can occur and averaging is commonly only set for one nuclear modulation during a PELDOR experiment.

5.2 Project aims

The aim of this study was to resolve the discrepancies around the prominence and importance of multi-spin effects in measurements of polyradical model systems. To this end measurement, sample and processing parameters were screened on chemical poly-nitroxide model systems **93**, **105** and **106** previously synthesised and reported in Chapter 2.[39a] Their symmetry should lead to a single narrow distance peak, while their rigidity introduces conformational restraints introducing orientation selection effects in PELDOR measurements. The study also aimed to look at the impact of the choice of protonated and deuterated solvents on PELDOR distance measurements.

5.3 Results and Discussion

5.3.1 Solvent effect

The effect of using protonated, deuterated toluene or protonated *o*-terphenyl on distance measurements within the model systems was studied and the use of ESEEM suppression were tested (Figure 5.3). First analyses of distance measurements performed in different solvents (see Materials and Methods A.2.1) show that the modulation depth obtained in time traces of model systems **93**, **105** and **106** is reduced for the *o*-terphenyl samples compared to the toluene ones; this might be related to the higher possibility of sample aggregation. The time traces recorded for samples in *o*-terphenyl also show a faster damping of dipolar oscillations when compared to measurements of samples in toluene, suggesting that the systems assume a broader range of conformations, also in agreement with the broadened distance distributions (green traces, Figure 5.3). This is in good agreement with the fact that the melting point of *o*-terphenyl (56-59° C) is much higher than that of toluene (-95° C). Assuming the individual molecules will be trapped in their individual conformations when the solvent solidifies, the molecules will sample a much larger conformational space before freezing in *o*-terphenyl due to the larger thermal energy.

Similarly, the widths of distance distributions of phenyleneethylnylene-based model systems have been shown to increase when solvents with higher glass transition temperature are used, as perdeuterated *o*-terphenyl.[18a] This also manifests in slightly quicker damping of dipolar oscillations. Deuteration of toluene alone does not appear to have an important impact on distance measurements, except for triradical **105** where the modulation depth is slightly reduced and the distance distribution appears broader than for the other solvent. This discrepancy is likely to be related to hardly reproducible sample conditions due to low solubilities of the model compounds. Further investigations would be needed to confirm this observation.

Suppression of deuterium ESEEM by nuclear modulation averages, performed by varying the first inter-pulse delay eight times by 56 ns (see Materials and Methods A.2.3.3), shows the presence of some deuterium ESEEM in non-suppressed traces (black), however the intensity of the 2.7 nm distance peak is only marginally reduced by the suppression.

a)

b)

c)

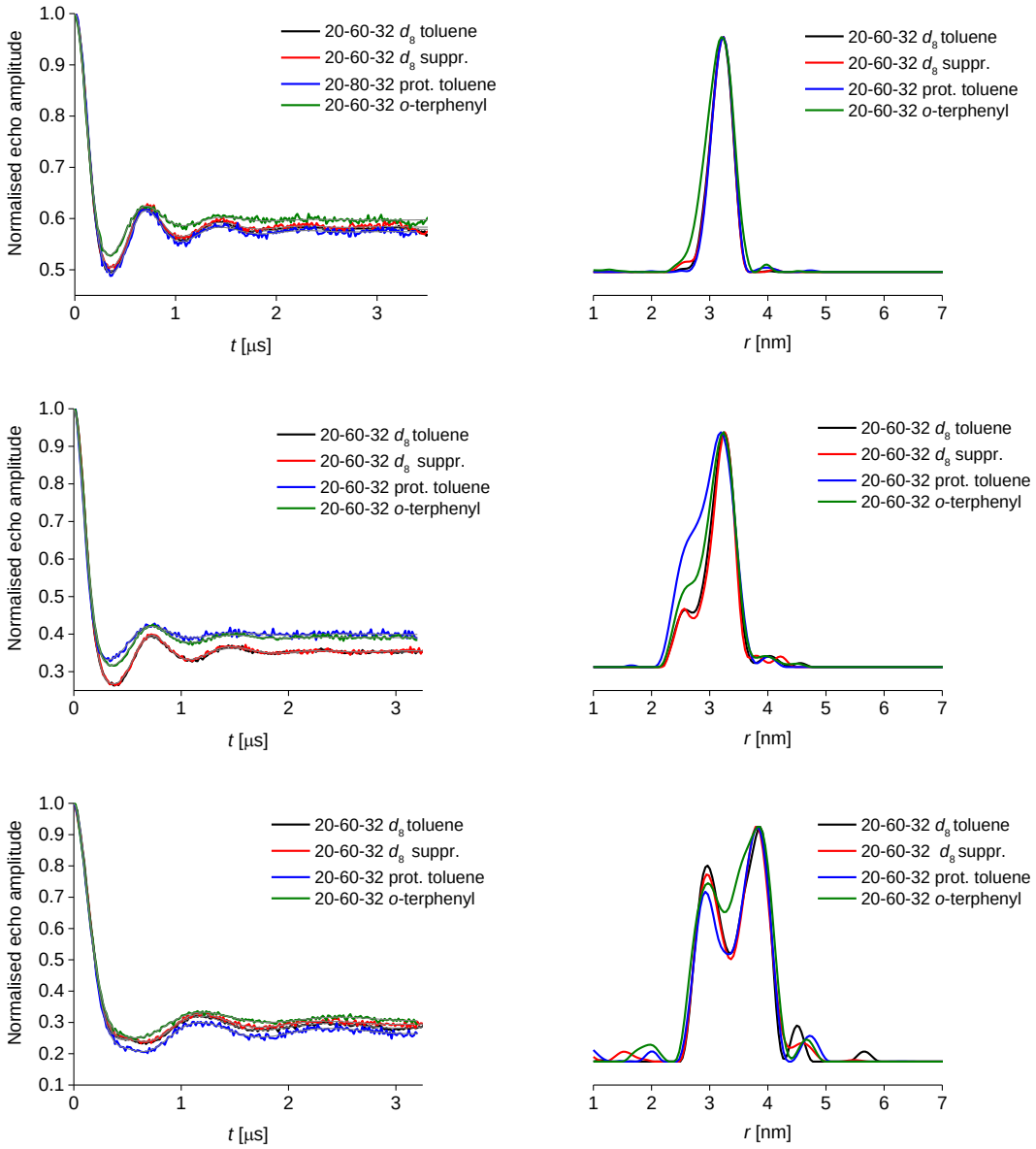

Figure 5.3: Background corrected traces PELDOR with fits and corresponding distance distributions obtained when performing distance measurements of samples in d_8 toluene without (black) and with deuterium ESEEM averaging (red), protonated toluene (blue) and *o*-terphenyl (green) measured on model systems **93** a), **105** b) and **106** c). The legend reports: pump pulse length – pulse offset – π pulse length.

From these preliminary results it can be concluded that samples in deuterated toluene, in combination with deuterium ESEEM suppression, give access to sharp distributions. Thus, the combination of deuterated solvents, ESEEM suppression and extended time windows represent the ideal measuring conditions for accurate extraction of inter-spin distances.

5.3.2 Orientation selection and multi-spin effects

Presence and impact of orientation selection effects on PELDOR distance measurements was tested by varying the offset between detection and pump pulses from 40 to 60 and 80 MHz, while maintaining the position of the pump pulse at the maximum of the nitroxide spectrum (see Materials and Methods A.2.3.3).[17a] The preliminary results in Figure 5.4 show the dependence of the signal modulation depth Δ and PELDOR oscillation frequency on pulse offsets, suggesting for the presence of orientation selection effects.[18b, 50a] The PELDOR background corrected traces show a reduced Δ for all measurements performed with a 40 MHz offset. This might be related to the spectral overlap between the detection and pump pulses and selection of specific combinations of orientations with a reduced number of pumped spins per detected spin.[98, 123] For **93** and **105** the 80 MHz traces show a slightly reduced modulation depth, which seems not to be the case for **106** when compared to measurements performed with the common 60 MHz offset.

The effects of orientation selection can also be observed from the line shape of the dipolar spectrum extracted from each measurement performed with different pulse offsets (Figure 5.4).[2b, 20a, 122] The enhanced intensity at the edges of the Pake pattern corresponding to $2\omega_{dd}$ indicates that the smallest offset increasingly excites a sub ensemble of molecules with the dipolar vector parallel to the external magnetic field. The 60 MHz offset shows the parallel and perpendicular components of a Pake pattern (Figure 1.4) in a proportion close to the one expected for a random distribution, suggesting that excitation of a statistical distribution of orientations is achieved.[18c] The 80 MHz offset reduces the edge of the Pake pattern, thus indicating that more dipolar vectors perpendicular to B_0 are excited corresponding to the 'horns' of the dipolar spectrum at ω_{dd}.

The distance distributions obtained when processing the PELDOR data from the experiments performed with different pulse offsets using DeerAnalysis are reported in Figure 5.5 (see Materials and Methods A.2.4). The data shows that to an increase in pulse offset correspond increasingly narrower distance distributions.

a)

b)

c)

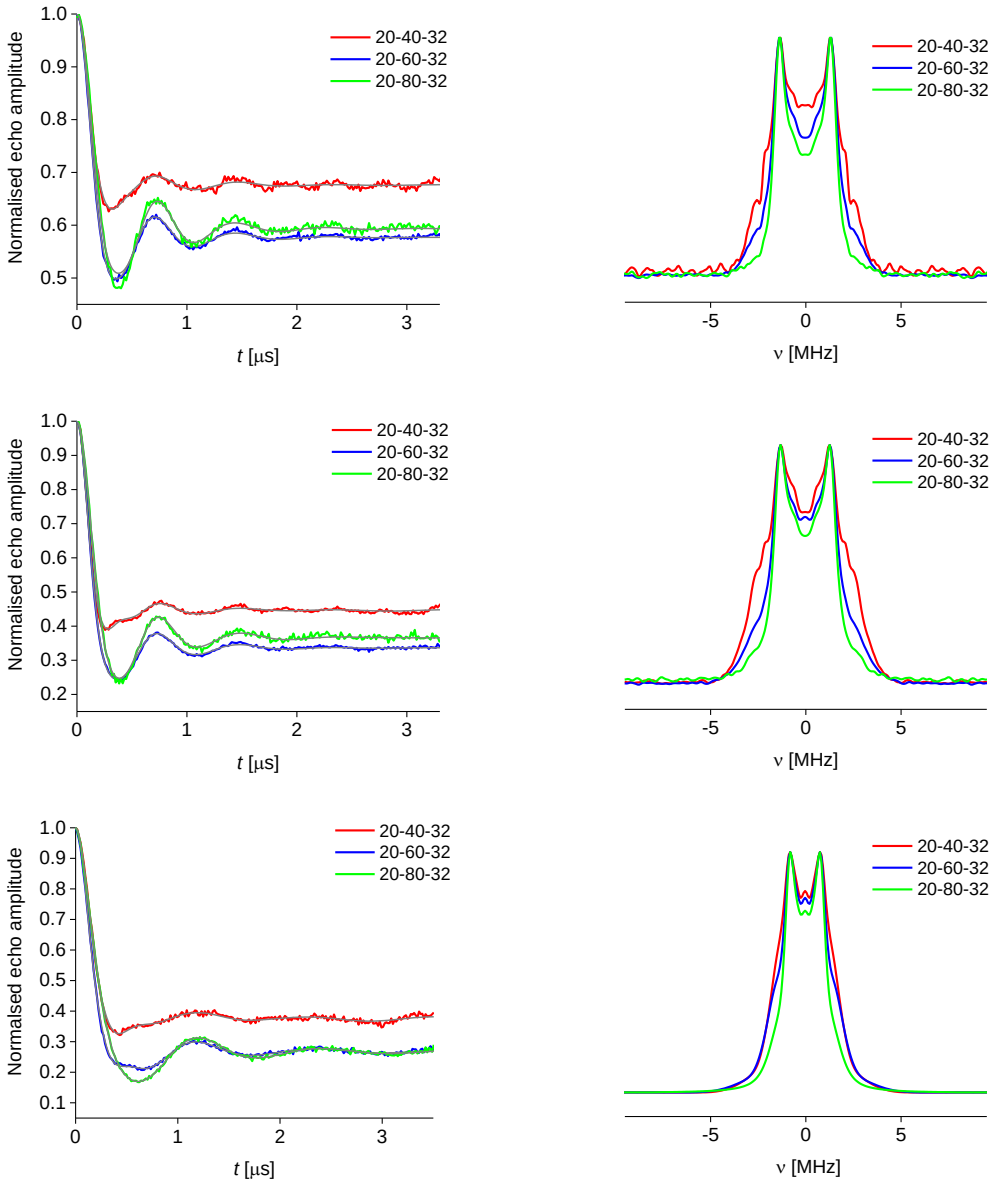

Figure 5.4: Background corrected PELDOR traces with fits for measurements performed with 40 (red), 60 (blue) and 80 (green) MHz pulse offset and corresponding dipolar spectra on **93** a), **105** b) and **106** c). The legend reports: pump pulse length – pulse offset – π pulse length.

a)

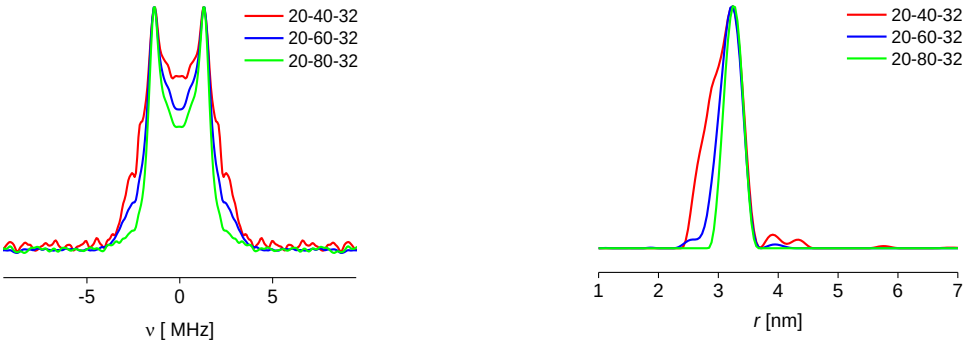

b)

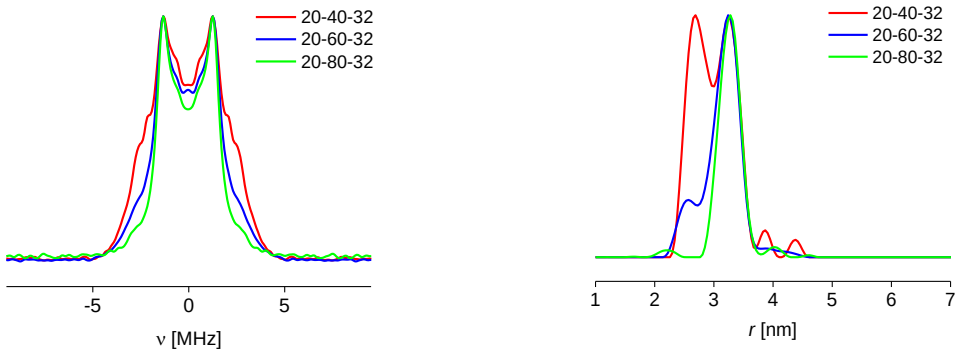

c)

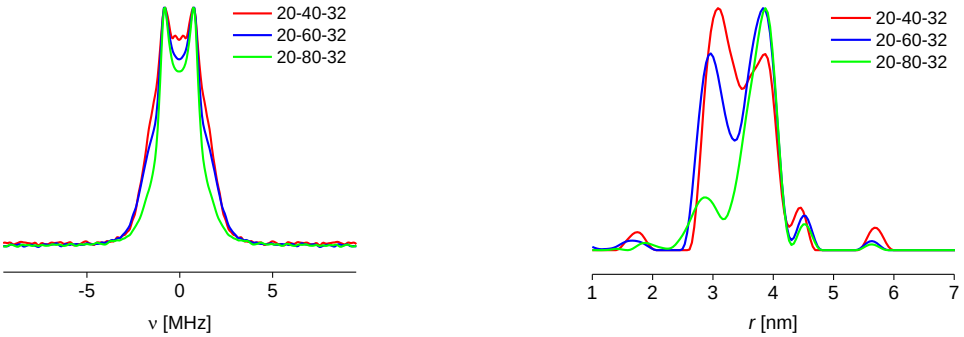

Figure 5.5: Distance distributions and corresponding Pake patterns obtained from PELDOR traces for measurements performed with 40 (red), 60 (blue) and 80 (green) MHz pulse offset on **93** a), **105** b) and **106** c). The legend reports: pump pulse length – pulse offset – π pulse length.

Validations of distance distributions (Figure 5.6) show that the observations from Figure 5.5 are significant even with systematic variation in background correction, confirming that 80 MHz measurements give the narrowest distance distributions while additional peaks are present in the 40 and 60 MHz experiments (see Materials and Methods A.2.4).

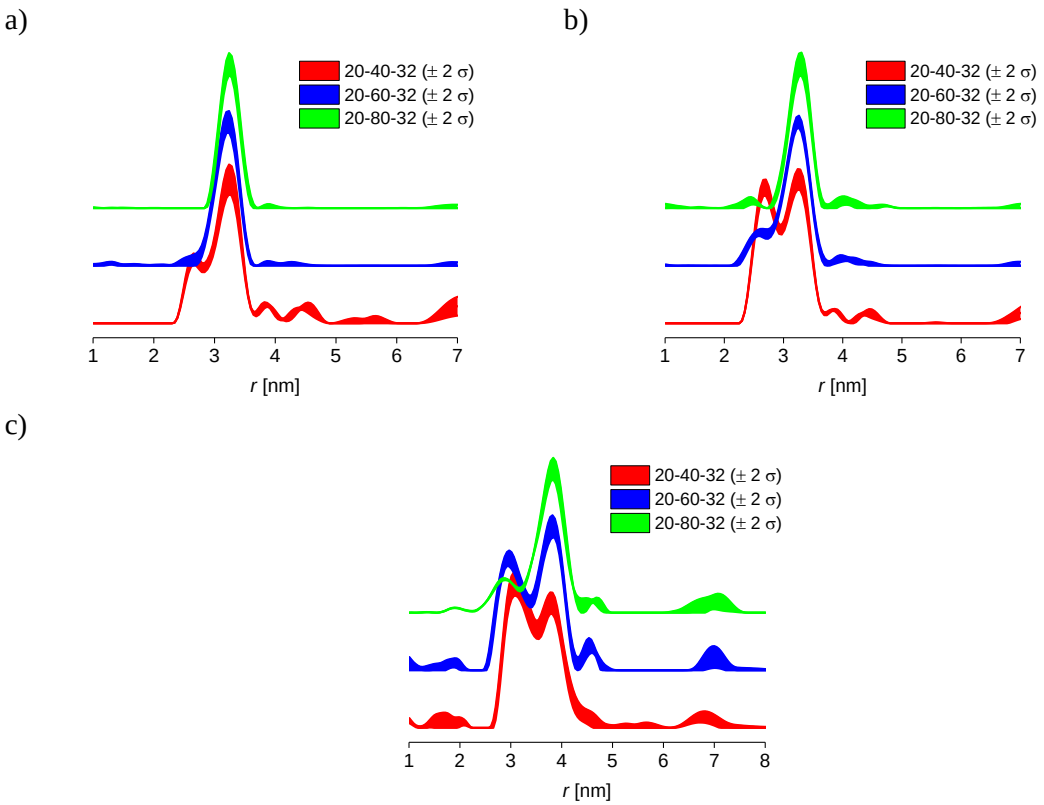

Figure 5.6: Validation of distance distributions from measurements with 40 (red), 60 (blue) and 80 (green) MHz offset on **93** a), **105** b) and **106** c). The coloured areas, representing the error bars, delineate those distance distributions that are stable to changes in processing parameters. The legend reports: pump pulse length – pulse offset – π pulse length.

The presence of multi-spin effects was tested by looking at the effects of power-scaling (Figure 5.7). Power-scaling of the tri- (**105**) and tetra- (**106**) radical time traces at different pulse offsets only partially reduces the integral of the additional distance peaks from measurements performed at 40 MHz. Further improvement of the PELDOR distance distribution is observed at 60 MHz offset. Measurements performed with 80 MHz offset convert to single peak distributions, here power-scaling has no visible effect on **105** (Figure 5.7 a)) and suppresses the small additional distance peak present in **106** (Figure 5.7 b)).

a) b)

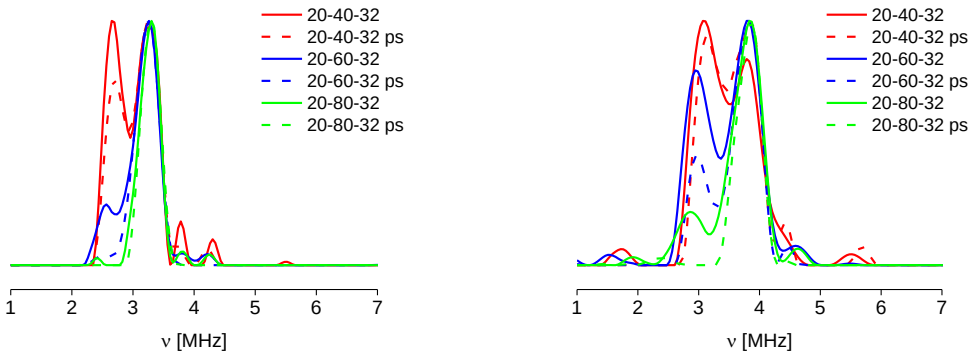

Figure 5.7: Power-scaled (dashed lines) and non-power-scaled (solid) distance distributions obtained from PELDOR measurements performed on **105** a) and **106** b) with 40 (red), 60 (blue) and 80 (green) MHz offset. The legend reports: pump pulse length – pulse offset – π pulse length.

The minor effect of power-scaling on the measurements performed with the 40 MHz offset could be due to a selection of the spins corresponding to a dipolar axis parallel B_0 giving a stronger weight of double frequencies. These frequencies are not expected to be affected by power-scaling as they are not combination frequencies. The minor improvement in distance distributions extracted from 80 MHz measurements suggest that only minor multi-spin effects are present. The effects observed for the 60 MHz traces are similar to those noticed in Chapter 3, thus indicating the presence of multi-spin effects which are partially suppressed by the post-processing method.

DeerAnalysis generates a fit to the experimental time trace (see Section 1.3) and a corresponding dipolar spectrum using Tikhonov regularisation methods from which distance distributions are extracted. The dipolar spectrum itself reveals the dipolar frequencies present in the PELDOR trace. The fit is generated on the assumption that all orientations of dipolar vectors are excited and that only pairs of interacting spins are contributing to the PELDOR signal.[19a, 19b, 78b] Figure 5.8 shows the comparison between the dipolar spectra obtained for biradical **93**, with 60 MHz offset (red), triradical **105** with 60 (blue) and 80 (green) MHz. These two model systems can be directly compared as they have the same geometry and inter-spin distance so that any effects caused by the presence of a third spin label can be separated from structural effects. Measurements on biradical **93** with a 60 MHz offset should represent the ideal conditions for accurate extraction of inter-spin distances using DeerAnalysis: absence of combination frequencies and minimum orientation selection; thus it can be used as a reference

system. Multi-spin effects are expected to affect measurements in **105**, by means of introduction of sum and difference frequencies.[19a, 19b] These appear in the experimental dipolar spectra (Figure 5.8 a)) for the 60 MHz trace (blue) where the intensity for the 0 frequency is increased together with the edges of the spectrum, when compared to the one dipolar spectrum of **93** trace (red) at 60 MHz. Combination frequencies from two times the most prominent dipolar frequency (the horns of the Pake distribution) lead to zero frequency (difference) and double frequency (sum) contributing to the lineshape of the dipolar spectrum.[19a]

a) b)

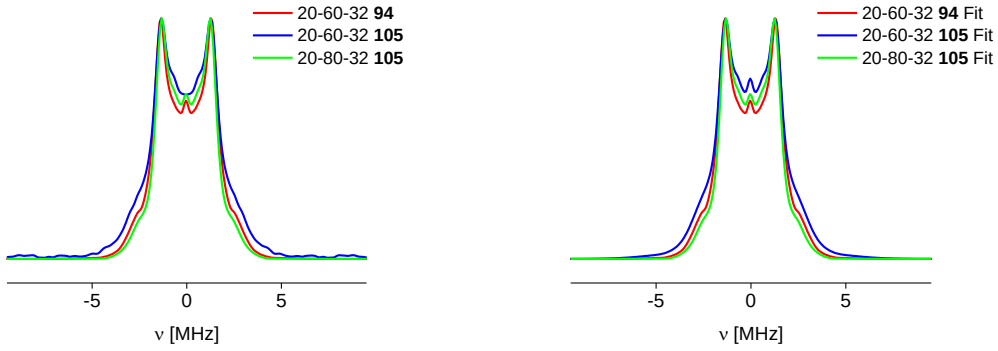

Figure 5.8: Comparison between experimental dipolar spectra a) and corresponding DeerAnalysis fits b) obtained from PELDOR measurements at 40, 60 and 80 MHz performed on biradical **93**. The legend reports: pump pulse length – pulse offset – π pulse length.

PELDOR measurements performed on **105** with an 80 MHz offset, however, do not present the features expected from combination frequencies.[19a] Instead, it shows the same dipolar line shape as biradical **93**. This dipolar spectrum corresponds to a narrow distance distribution lacking the additional distance peak previously observed when using 60 MHz as offset. The DeerAnalysis fits of the experimental data, shown in Figure 5.8 b), accurately reflect the experimental dipolar spectra, except for the measurement of **106** with a 60 MHz offset where the fit displays even less intensity on the edge (double frequency) than the experiment. Figure 5.5 and Figure 5.8 show that increasing the offset suppresses frequencies corresponding to the θ=0° (edge) of the Pake pattern. This double frequency can then be reintroduced by multi-spin effects.

To further investigate the shape of the dipolar spectrum and its effect on distance distributions the match between the experimental and fitted dipolar spectra was studied for different offsets (Figure 5.9). Measurements performed on **93** are not affected by

multi-spin effects, thus DeerAnalysis experimental data fitting can be studied in the presence (at 80 MHz) and absence (at 60 MHz) of orientation selection effects.

For the 60 MHz measurement on **93** a good match between fit and experimental data is observed, confirming the excitation of the majority of orientations. For the 80 MHz offset, however, the fit produces the expected double frequency which is lacking in the experimental data due to orientation selection. Due to the non-negativity constraint on the distance distribution a lack of intensity in the dipolar spectrum does not lead to additional distance peaks. However, excess intensity will lead to additional peaks or broadening of the distance distribution. The same comparison is performed for the multi-spin systems **105** and **106** for which a good match between fit and experimental data is found. The 80 MHz measurements give an overall narrower dipolar spectrum, which is reproduced by the fit. This can be rationalised by the multi-spin effects in 80 MHz measurements on **105** 'filling' the missing intensity of the dipolar spectrum of **93** with combination frequencies. However, when going to 60 MHz offset **105** shows a dipolar spectrum resembling all orientations and the addition of combination frequencies broadens the dipolar spectrum and thus the distance distribution (Figure 5.5). For 80 MHz offsets this means that the combination of the two counteracting effects gives a dipolar spectrum for **105** which now shows the dipolar spectrum as for the biradical **93** where all orientations assumed by the spin labels within the system are selected. Thus, multi-spin effects are being compensated by orientation selection effects resulting in a "lucky error compensation" diminishing multi-spin effects

This lucky error compensation between multi-spin effects and orientation selection represents a reasonable explanation for the discrepancies between the severities of multi-spin effects observed in literature.

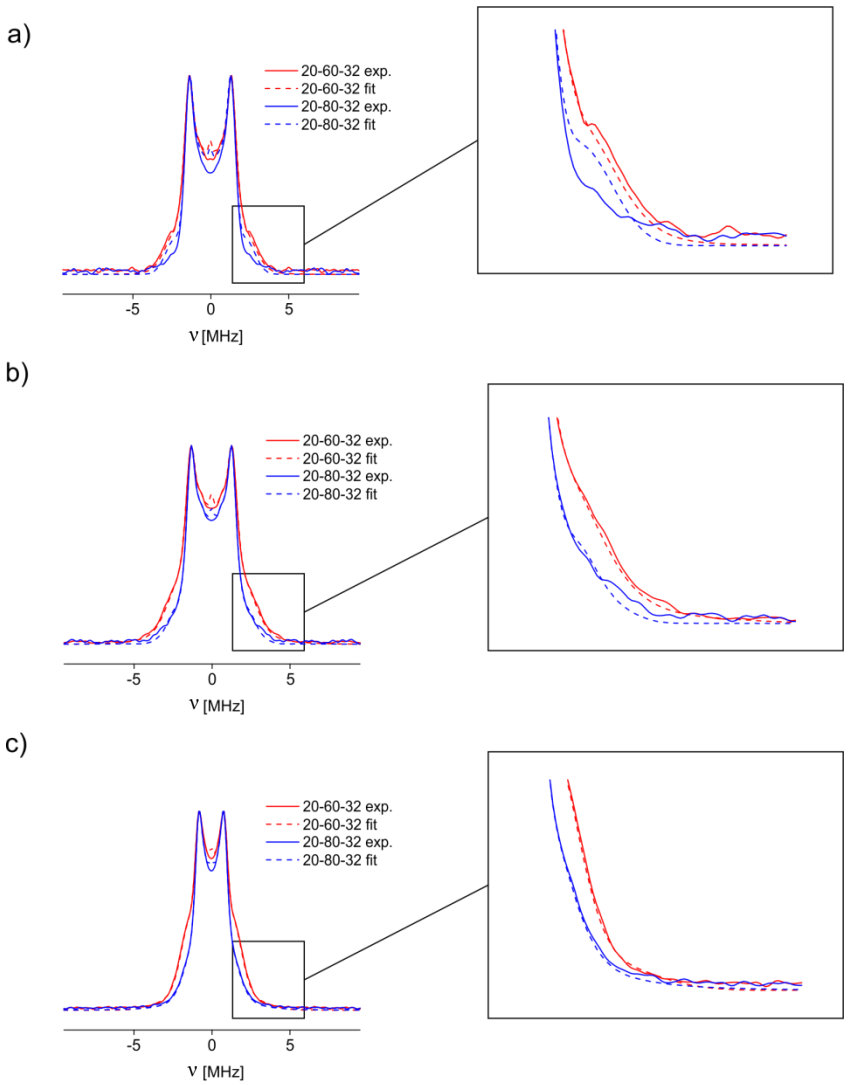

Figure 5.9: Pake patterns of **93** a) **105** b) and **106** c), from measurements performed at 60 (red lines) and 80 MHz (blue lines) as solid lines with respective DeerAnalysis fits as dashed lines. The legend reports: pump pulse length – pulse offset – π pulse length.

5.3.3 Orientation averaging

To further test the hypothesis that the absence of multi-spin effects is merely caused by a "lucky error compensation" for multi-spin effects by orientation selection an orientation averaging experiment was performed.[18c] The experiment should allow for averaging of orientation selection effects, thus giving a trace that reflects random orientation of the dipolar vector. The experiment involves the variation of the magnetic field so that the observer position is swept between the low-field maximum and the overall maximum of the nitroxide spectrum (see Materials and Methods A.2.3.3). The difference between pump and observer frequency is kept constant at 60 MHz.[18c] Figure

5.10 and Figure 5.11 report the PELDOR traces and corresponding dipolar spectra resulting from the addition of all 14 traces recorded for each 2 G field step for the three model systems **93**, **105** and **106** while maintaining a constant offset of 60 MHz. The traces show a reduced modulation depth when compared to standard measurements performed with a 60 MHz offset. This is expected as the pump position moves away from the global maximum of the spectrum. This is demonstrated by the reduction in modulation depth when increasing the magnetic field position at each step, as shown in the orientation resolved traces in Figure 5.12. The distance distribution for the orientation averaged (OA) experiment on biradical **93** gives a similar result to the 60 MHz standard PELDOR experiment. The same behaviour can be observed for triradical **105**, while for **106** the orientation averaged distance distribution appears to give a lower intensity of the first ghost peak (Figure 5.10). This can be related to the lower average λ achieved during the orientation averaged experiments, due to the sweeping of the observer position between the low-field and the global maximum. These results suggest for the presence of multi-spin effects, also justified by the dipolar spectra of each orientation averaged dipolar spectra, shown in Figure 5.11, measured in deuterated solvent while performing deuterium averaging, parameters which exclude the presence of orientation selection and deuterium ESEEM effects. When comparing the dipolar spectra of **93**, to **105** a) and **106** b) it can be seen that additional broadenings are introduced by double frequencies introduced by multi-spin effects (Figure 5.11).

These experiments show that multi-spin effects are still present in the PELDOR measurements on triradical **105** and tetraradical **106**. It also confirms that orientation selection effects can affect appearance of multi-spin effects in rigid systems as distance ghost peaks are present in the orientation averaged experiments while they are largely absent in the distance distributions from the 80 MHz PELDOR experiments.

a)

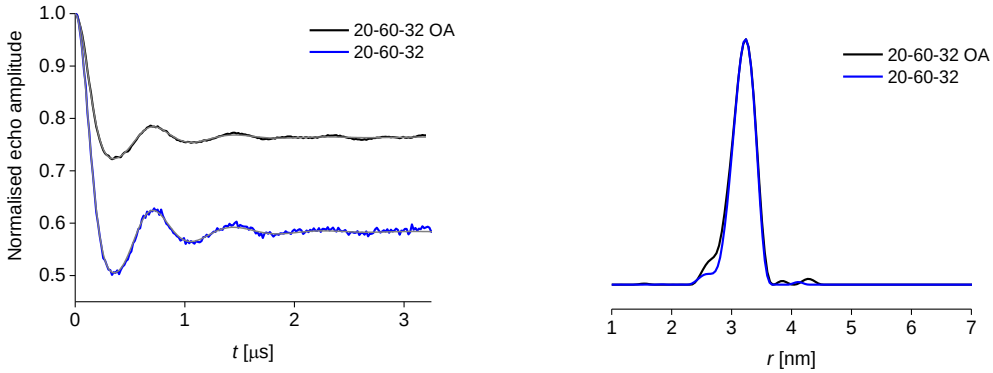

b)

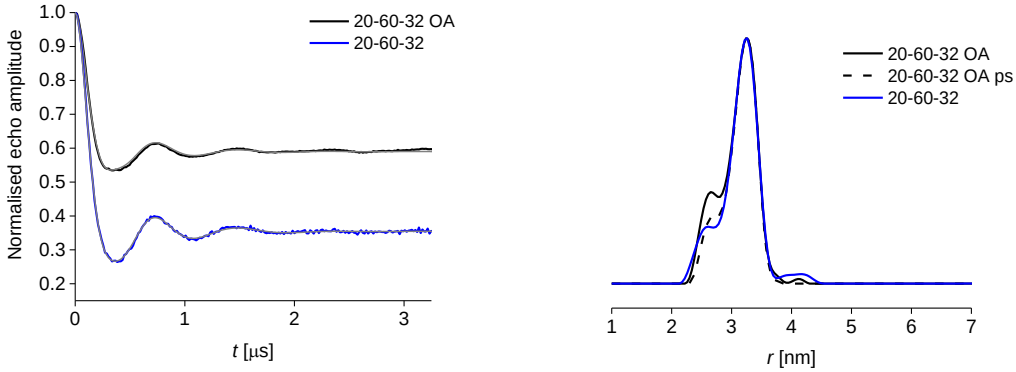

c)

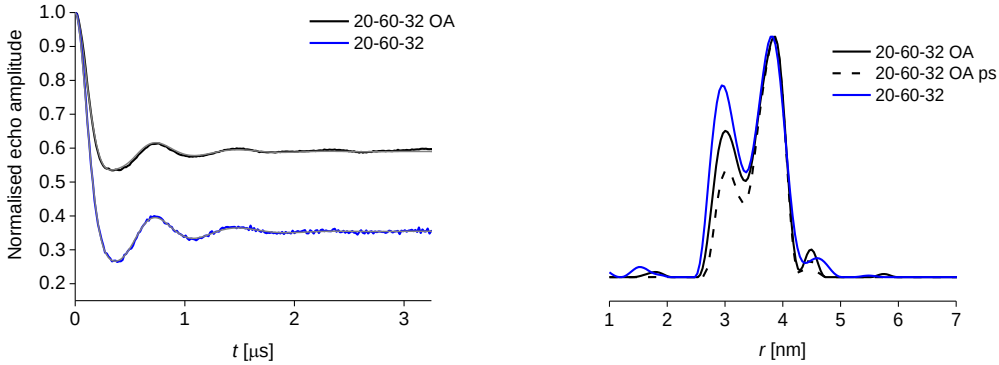

Figure 5.10: Comparison between background corrected traces for orientation averaged (OA) experiments on **93** a), **105** b) and **106** c) (black) and PELDOR together with their corresponding distance distributions (black) with (dashed) and without (solid) power-scaling. The legend reports: pump pulse length – pulse offset – π pulse length.

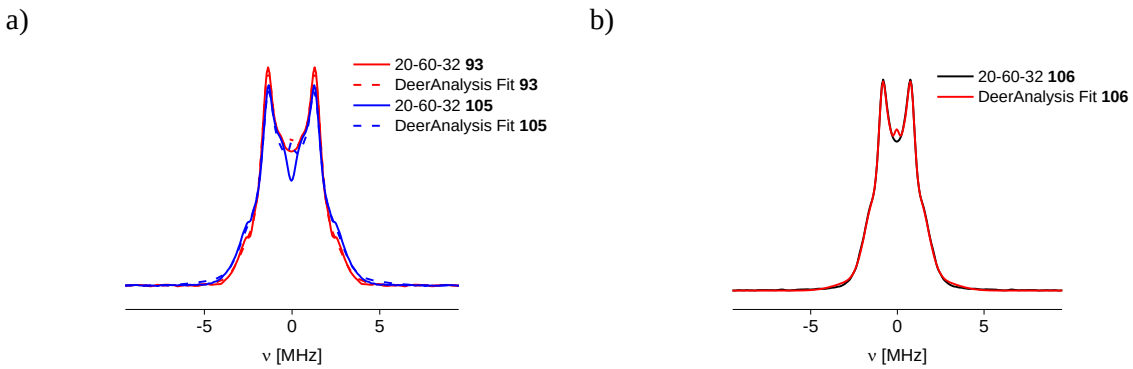

Figure 5.11: Comparison between dipolar spectra from orientation averaged experiments on **93** and **105** a) and dipolar spectrum from measurements on **106** b) (solid) with corresponding DeerAnalysis fits (dashed). The legend reports: pump pulse length – pulse offset – π pulse length.

When looking at individual traces before averaging (Figure 5.12), the effects of spectral selection on Δ can be directly observed. The distance distributions obtained from these "orientation resolved" measurements reflect the observations derived when comparing measurements at 40, 60 and 80 MHz. Initial shifting of the detection position towards the global maximum, up to 1.2 mT from the low field maximum, induces excitation of the parallel component of the dipolar interaction and consequent introduction of double frequencies and broadenings in the distance distribution, as observed for 40 MHz PELDOR measurements. Further shifting towards the global maximum leads to a progressive excitation of the perpendicular component of the dipolar tensor giving progressively narrowing distance distributions. The +2.4 mT measurements give distance distributions very similar to the ones obtained for the 80 MHz PELDOR experiments. Selective excitation of the perpendicular component of the dipolar interaction leads to narrow distance distributions making presence of multi-spin effect not apparent.

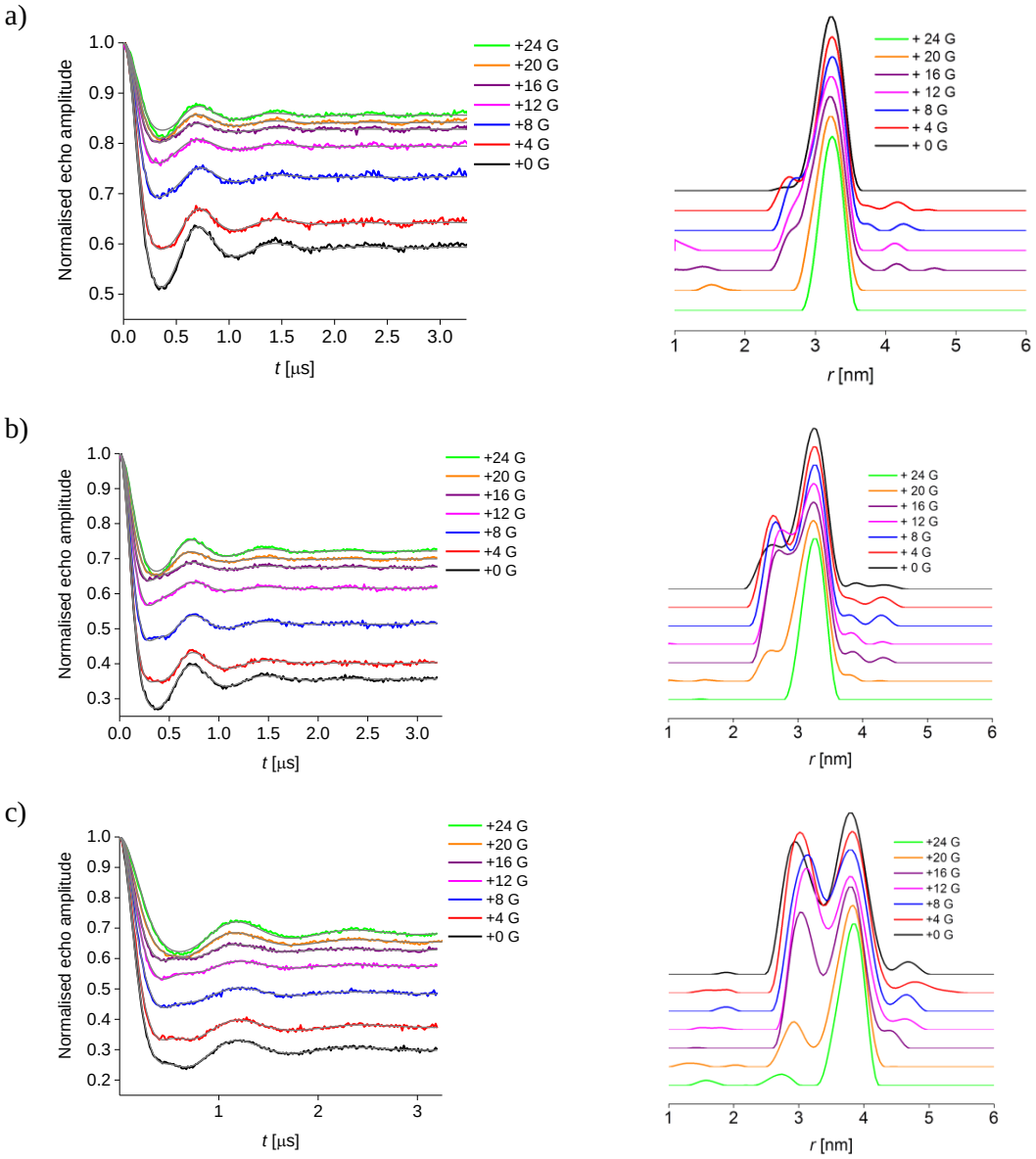

Figure 5.12: Background corrected traces with fits and corresponding distance distributions from orientation resolved experiments performed with 2 G steps of the magnetic field during performance of the orientation averaged experiment on **93** a), **105** b) and **106** c).

The orientation resolved and averaged experiments confirm that orientation selection effects can greatly affect distance measurements and that processing of PELDOR data on rigid systems and it can give misleading results when processing orientation selective data using a method based on random orientation of the dipolar vector. This can mask multi-spin effects, whose presence and impact had previously been observed in measurements performed at 60 MHz and reported in Chapter 3.

5.4 Conclusion

Orientation selection effects observed on the reported polyradical model systems were found to compensate multi-spin effects giving a narrower distance distribution when compared to measurements allowing excitation of all orientations. This demonstrates how appearance of multi-spin effects can be easily masked by choice of offset in measurements of multiply labelled systems presenting a specific geometry. These observations suggest that measurements on multi-spin systems performed with different offsets may give divergent distance distributions showing multi-spin effects, in more or less pronounced fashion. In these cases multi-spin effects and orientation selection cancel each other by a "lucky error compensation", diminishing multi-spin effects. These results highlight the importance of determining the presence of both multi-spin and orientation selection effects prior to qualitative and quantitative analysis of distance measurements data. Interpretation of PELDOR neglecting the presence of orientation selection effects can lead to data misinterpretation suggesting that no multi-spin effects are affecting measurements on multiply labelled systems. This assumption would contradict previous observations previously reported.[19a, 47a, 78, 98] Recording a number of traces with varying magnetic field seems a very effective way of identifying and largely suppressing orientation selection effects. Individual traces also effectively suppress multi-spin effects.

Conclusions and Outlook

The work showcased in this thesis contributes to the understanding and suppression of one of the major challenges encountered when performing pulsed EPR distance measurements. Multi-spin effects have been found to affect significantly distance measurements in systems bearing more than two spin labels by introducing broadenings, additional "ghost" distance peaks and suppressing longer distances. This had been found previously and verified in this project, to be misleading with the danger of data misinterpretation.

In this work alternative approaches for suppression of multi-spin effects have been tested and scrutinised on novel rigid and symmetric model systems and on two different mutants of a heptameric channel membrane protein. Simulated PELDOR data for polygons and a polyhedron, reflecting the spin label geometry of the systems under study, allowed exploring the influence of more than two spins on data in distance and time domain *in silico*. The findings from measurements on the model systems were then validated on the biological samples, reconfirming that chemical model systems can be valid benchmarks for testing of experimental set ups for distance measurements.

A common synthetic protocol for the synthesis of multiply labelled chemical model systems has been developed. This protocol gave access to a variety of symmetric and asymmetric model systems. The synthesised model systems also allowed us to look at the impact of the presence of both orientation selection and multi-spin effects on distance distributions extracted using Tikhonov methods. Here, it is observed for the first time, how orientation selection effects could hinder the appearance of multi-spin effects giving narrow distance distributions virtually free of artefacts for multiply labelled systems. Additionally, these chemical systems were used to test alternative experimental approaches quantitatively. The BAMBI or frequency-interchanged experiments were demonstrated as alternative method for suppression of multi-spin effects, giving access to the extraction of accurate distances in the nanometre range. The sensitivity has been shown to be superior in several cases and the performance can be reliably predicted from quick preliminary experiments making the application of the alternative really practical. Sparse labelling, a concept previously introduced in CW EPR, was scrutinised for its potential for extraction of accurate distances from multiply labelled systems. The method was found to give distance distributions in good agreement with the predicted models from crystal structures while offering good

sensitivity. Both proposed methods, frequency-interchanged and sparse labelling, are effective against multi-spin effects. However, the frequency-interchanged and λ reduction experiments require only require changes in experimental parameters and not in sample preparation. Both methods offer similar sensitivity and combine efficiently with power-scaling, while sparse-labelling offers improved sensitivity when compared to frequency-interchanged and λ reduction experiments on fully labelled systems.

Further work would include testing of sparse labelling and frequency interchanged experiments on other biological systems to test their efficiency and versatility. In particular, sparse labelling should also be tested on the model systems to test for its efficiency in suppressing distance "ghost" peaks while limiting the loss in sensitivity on other biological systems. Simulations would allow further understanding and justifying the experimental observations discussed regarding the "lucky error compensation" of multi-spin effects by orientation selection.

The results presented in this thesis in combination with further systematic studies will strengthen PELDOR as method for extraction of accurate inter-spin distances in multiply labelled systems. Further insights into the implications of distance measurements in multiply labelled systems will be provided by quantitative studies employing different methods for suppression of multi-spin effects on chemical and biological systems.

Materials and Methods

A.1 Synthesis General Methods

Moisture and air sensitive reactions were carried out under a nitrogen atmosphere using standard Schlenk techniques and dry solvents. All glassware was flame-dried and cooled under vacuum before use. Solvents (THF, CH_2Cl_2 and toluene) were obtained anhydrous and purified by a solvent purification system (SPS) alumina column. All other solvents and commercial reagents were used without further purification. Solvents used for cross-coupling reactions were degassed using freeze-pump-thaw cycles (× 3). ^{1}H and $^{13}C\{H^{1}\}$ nuclear magnetic resonance (NMR) spectra were acquired on either a 400 MHz ^{1}H, 100 MHz ^{13}C or a 500 MHz ^{1}H, 125 MHz ^{13}C NMR spectrometer at ambient temperature, if not otherwise stated, in the deuterated solvents reported. All chemical shifts are reported in parts per million (ppm) relative to TMS with the solvent used as an internal standard. All coupling constants *J* are reported in Hz. Multiplicities are reported as: s (singlet), d (doublet), m (multiplet). Solid-state NMR spectra were acquired at 14.1 T (^{13}C Larmor frequency of 151 MHz) with magic angle spinning (MAS) rates between 11 and 12.5 kHz. Cross polarization from ^{1}H was employed to enhance sensitivity and high-power ^{1}H decoupling was applied during acquisition to enhance resolution. Chemical shifts are reported relative to TMS using the CH_3 resonance of L-alanine (δ = 20.5 ppm) as an external reference. FT Infrared spectra were recorded using an attenuated total reflectance (ATR) probe and only characteristic peaks are reported. Melting points recorded are uncorrected. Mass spectrometry (*m/z*) data were acquired using electron spray (ES), atmospheric solids analysis probe (ASAP) and matrix-assisted laser desorption/ionization matrix-assisted laser desorption ionization (MALDI). CW EPR spectra were obtained with an X-band spectrometer operating at ~9.7 GHz with 100 kHz modulation. Samples were dissolved in deuterated toluene and deoxygenated by saturation nitrogen. Samples were contained in 4 mm OD quartz tubes sealed with rubber septa. Solution and solid state NMR and CW EPR spectra together with X-ray crystallography data can be found in the Appendix.

General Procedure A: Esterification of TPC **3**. The appropriate phenol, TPC **3** and DMAP were dissolved in anhydrous THF. The flask was covered in aluminum foil before addition of EDCI·HCl. The reaction mixture was stirred under a nitrogen atmosphere at room temperature (rt) for the time stated. The reaction mixture was filtered to remove the urea precipitate, and washed with CH_2Cl_2. The organic filtrate was washed with water (× 3) before being dried over $MgSO_4$ and filtered. Solvents were removed under reduced pressure to give the crude product, which was purified *via* 4% H_2O aluminum oxide column chromatography.

General Procedure B: Aqueous ammonia Sonogashira coupling. The appropriate aryl iodide was dissolved in anhydrous THF before $PdCl_2(PPh_3)_2$ and CuI were added. The obtained solution was degassed *via* freeze-pump-thaw cycles (× 3). The appropriate alkyne was then added portionwise as a solid, or dropwise as a degassed solution in THF. The reaction mixture was degassed once more before dropwise addition of a 0.5 M aqueous ammonia solution (2 eq.), which had been purged with nitrogen for 3 min. The reaction mixture was stirred at rt and/or heated for the time stated. The two phases were separated and the aqueous layer extracted with EtOAc. The combined organic layers were washed with 10% HCl and water before being dried over $MgSO_4$ and filtered. Solvents were removed under reduced pressure to give the crude product that was purified *via* silica column chromatography or trituration.

Biradical (**44**). 4-4'-Biphenol **91** (0.10 g, 0.54 mmol), TPC **3** (0.30 g, 1.63 mmol), DMAP (0.20 g, 1.64 mmol) and EDCI·HCl (0.16 g, 1.03 mmol) in THF (10 mL) were reacted according to general procedure A. The reaction mixture was stirred 24 h. The crude product (0.31 g) was purified (4% H_2O aluminum oxide, CH_2Cl_2, R_f 0.2) to give **44** as yellow crystals (0.23 g, 82%). Data are in accordance with the literature:[20b] mp 211-213 °C; FT-IR (ATR): 2976 (w), 2931 (w), 1732 (s), 1490 (m), 1346 (m), 1286 (m), 1244 (m), 1194 (s), 1147 (s), 1024 (s), 1001 (s), 792 (s), 759 (s); HRMS [NSI, ion trap] $[M+H]^+$ calcd for $C_{30}H_{35}N_2O_6$ 519.2490, found 519.2476; Anal. Calcd. for $C_{30}H_{34}N_2O_6$: C, 69.48; H, 6.61; N, 5.40, found: C, 69.30; H, 6.75; N, 5.54. Room temperature continuous wave EPR displays a characteristic three line nitroxide spectrum: $a_{iso}(^{14}N)$ =1.42(1) mT.

Monoradical (**75**). 4-Hydroxy-4'-iodobiphenyl **74** (0.10 g, 0.34 mmol), TPC **3** (0.12 g, 0.67 mmol), EDCI·HCl (0.10 g, 0.67 mmol), DMAP (0.08 g, 0.67 mmol) in THF (15 mL)

were reacted according to general procedure A. The reaction mixture was stirred 24 h. The crude product (0.20 g) was purified (4% H_2O aluminum oxide, 3:2 CH_2Cl_2, ethyl acetate, R_f 0.8) to give **75** as a yellow solid (0.08 g, 72%). Data in accordance with literature:[50a] mp 157-158 °C; FT-IR (ATR): 2978 (w), 1730 (s), 1624 (m), 1477 (s), 1458 (m), 1442 (m), 1344 (m), 1282 (m), 1197 (s), 1182 (s), 1165 (s), 1149 (s), 1014 (m), 999 (s), 760(s); MS [ESI, ion trap] $[M+H]^+$ calcd for $C_{21}H_{22}INO_3$ 463.31, found 463.32.

*1,3,5,7-Tetrakis(4-ethynlphenyl)adamantane (**83**)*. Following the procedure described by Lu *et al.*,[107] **99** (1.20 g, 1.27 mmol), trimethylsilylacetylene (2.7 g, 27.49 mmol), $PdCl_2(PPh_3)_2$ (0.062 g, 0.09 mmol) and CuI (0.37 g, 1.92 mmol) in toluene (25 mL) and triethylamine (11 mL). The crude product (2.30 g) was suspended in anhydrous MeOH (38 mL) together with K_2CO_3 (4.20 g, 30.39 mmol). The reaction was stirred for 24 h. The crude product (0.50 g) was purified *via* silica column chromatography (10% CH_2Cl_2 in hexane, R_f 0.28) to give **83** as a white solid (0.7 g, 67%). Data are in accordance with the literature:[107] mp 178-180 °C; FT-IR (ATR): 3284 (s), 2924 (m), 2899 (m), 2850 (m), 2106 (w), 1606 (w), 1504 (s), 1446 (w), 1402 (w), 1357 (m), 1259 (w), 1112 (w), 1016 (m), 893 (w), 830 (s), 790 (s); ^{1}H NMR (400 MHz, Chloroform-*d*) δ 7.52 – 7.46 (m, 8H), 7.45 – 7.38 (m, 8H), 3.06 (s, 4H), 2.12 (s, 12H); HRMS [ASAP, ion trap] (SOLID) $[M+H]^+$ calcd for $C_{42}H_{33}$ 537.2577, found 537.2572.

*Biradical (**88**)*. Resorcinol **86** (0.08 g, 0.73 mmol), TPC **3** (0.33 g, 1.82 mmol), EDCI·HCl (0.28 g, 1.82 mmol) and DMAP (0.22 g, 1.82 mmol) in THF (10 mL) were reacted according to general procedure A. The reaction mixture was stirred 24 h. The crude product (0.25 g) was purified (4% H_2O aluminum oxide, CH_2Cl_2, R_f 0.3) to give **88** as a pale yellow solid (0.16 g, 49%): mp 169-171 °C {lit.[61] mp 183-185 °C (benzene-heptane)}; FT-IR (ATR): 2980 (m), 2929 (m), 1730 (s), 1597 (s), 1344 (m), 1286 (m), 1244 (s), 1154 (s), 1130(s), 1026 (s), 805(s), 754 (s); HRMS [ASAP, ion trap] (SOLID) $[M+H]^+$ calcd for $C_{24}H_{31}N_2O_6$ 443.2177, found 443.2176; Anal. Calcd. for $C_{24}H_{30}N_2O_6$: C, 65.14; H, 6.83; N, 6.33, found: C, 65.18; H, 6.94; N, 6.38. Room temperature continuous wave EPR displays a characteristic three line nitroxide spectrum: $a_{iso}(^{14}N)$ =1.42(1) mT.

*Triradical (**89**)*. Phloroglucinol **87** (0.04 g, 0.32 mmol), TPC **3** (0.23 g, 1.27 mmol), EDCI·HCl (0.19 g, 1.27 mmol) and DMAP (0.15 g, 1.27 mmol) in THF (10 mL) were reacted according to general procedure A. The reaction mixture was stirred 48 h. The crude

product (0.13 g) was purified (4% H_2O aluminum oxide, CH_2Cl_2, R_f 0.1) to give **89** as a bright yellow solid (0.06 g, 30%): mp 214-216 °C {lit.[61] mp 225-226 °C (benzene-heptane)}; FT-IR (ATR): 2978 (w), 2931 (m), 1732 (s), 1604 (m), 1456 (m), 1348 (m), 1286 (s), 1168 (s), 1128 (s), 1030 (s), 752 (m); HRMS [ASAP, ion trap] (SOLID) $[M+H]^+$ for $C_{33}H_{43}N_3O_9$: calcd. 625.2994, found 625.2989; Anal. Calcd. for $C_{33}H_{42}N_3O_9$: C, 63.45; H, 6.78; N, 6.73, found: C, 63.31; H, 6.85; N, 6.81. Room temperature continuous wave EPR displays a characteristic three line nitroxide spectrum: $a_{iso}(^{14}N)$ =1.41(1) mT.

*Biradical (***93***)*. Bis-phenol **94** (0.09 g, 0.19 mmol), TPC **3** (0.09 g, 0.5 mmol), DMAP (0.06 g, 0.49 mmol) and EDCI·HCl (0.08 g, 0.52 mmol) in THF (15 mL) were reacted according to general procedure A. The mixture was left stirring 40 h. The crude product (0.25 g) was purified (4% H_2O aluminum oxide; CH_2Cl_2, R_f 0.4) to give **93** as a pale yellow solid (0.07 g, 45%): mp 212-214 °C; FT-IR (ATR): 2933 (w), 2868 (w), 1730 (s), 1490 (m), 1346 (m), 1286 (m), 1185-1149 (s), 999 (s), 800 (s); HRMS [ESI, ion trap] $[M+NH_4]^+$ calcd for $C_{52}H_{50}N_3O_6$ 812.3694, found: 812.3697; Anal. Calcd. for $C_{52}H_{46}N_2O_6$: C, 78.57; H, 5.83; N, 3.52, found: C, 78.47; H, 5.84; N, 3.42. Room temperature continuous wave EPR displays a characteristic three line nitroxide spectrum: $a_{iso}(^{14}N)$ =1.42(1) mT.

*Bis-phenol (***94***)*.4-Hydroxy-4'-iodobiphenyl **74** (0.30 g, 1.01 mmol), $PdCl_2(PPh_3)_2$ (0.01 g, 0.02 mmol), CuI (0.005 g, 0.02 mmol) and 1,3-diethynylbenzene **81** (0.09 mL, 0.61 mmol), 0.5 M aqueous ammonia solution (5 mL) in THF (5 mL) were reacted according to general procedure B. The mixture was stirred for 24 h before being heated to 60 °C for 2 h. The crude product (0.48 g) was purified (silica gel, 10% EtOAc in CH_2Cl_2, R_f 0.5) to give **95** as a pale brown solid (0.32 g, 69%): mp 272-274 °C; ^{1}H NMR (300 MHz, DMSO-d_6) δ_H 9.67 (s, 2H), 7.81–7.46 (m, 16H), 6.87 (4H, d, *J* 8.6); $^{13}C\{^1H\}$ NMR (101 MHz, DMSO-d_6): δ_C δ 157.7, 140.6, 133.9, 132.0, 131.4, 129.7, 129.4, 127.9, 126.1, 123.1, 119.7, 115.9, 90.3, 88.7.; HRMS [NSI, ion trap] $[M-H]^-$ calcd for $C_{34}H_{21}O_2$ 461.1547, found: 461.1544.

*Tris-phenol (***95***)*. 4-Hydroxy-4'-iodobiphenyl **74** (0.27 g, 0.91 mmol), $PdCl_2(PPh_3)_2$ (0.02 g, 0.03 mmol), CuI (0.003 g, 0.02 mmol) and 1,3,5-triethynylbenzene **82** (0.05 g, 0.3 mmol), 0.5 M aqueous ammonia solution (15 mL) in THF (15 mL) were reacted according to general procedure B. The reaction mixture was stirred at room temperature for 24 h and heated to 60 °C for 2 h. The crude product (0.26 g) was purified (silica gel, dry-load, 2% MeOH in CH_2Cl_2, R_f 0.5) to give **95** as a colorless oil, which turned into pale brown flakes

when washed with CH_2Cl_2 (0.09 g, 60%): mp 134-136 °C; ^{1}H NMR (300 MHz, DMSO-d_6) δ_H 9.68 (s, 3H), 7.76–7.55 (m, 21H), 6.88 (6H, d, *J* 8.6); ^{13}C{^{1}H} NMR (101 MHz, DMSO-d_6) δ_C 157.7, 140.7, 133.6, 132.1, 129.7, 127.9, 126.1, 123.9, 119.5, 115.9, 91.1, 87.9; HRMS [NSI, ion trap] $[M-H]^-$ calcd for $C_{48}H_{29}O_3$ 654.2122, found: 654.2122.

*1,3,5,7-Tetraphenyladamantane (***97***)*. 1-Bromo adamantane **96** (6.00 g, 27.89 mmol) was reacted following the procedure previously described[105] in the presence of *tert*-butyl bromide (9.5 mL, 84.59 mmol) and $AlCl_3$ (0.37 g, 2.77 mmol) to give **97** as a white solid after chloroform Soxhlet extraction (11.50 g, 90%): mp >300 °C; FT-IR (ATR): 3020 (m), 1597 (m), 1494 (m), 1442 (m), 1355 (m), 1078 (m), 1031 (m), 750 (s); ^{13}C CP/MAS NMR (14.1 T) δ_C (ppm) 39.2, 45.1, 51.3, 124.7, 127.2, 129.1, 130.2, 149.8.

*1,3,5,7-Tetrakis-(4-iodophenyl)adamantane (***98***)*. Following the procedure described by Drew *et al.*,[106] **97** (2.00 g, 4.54 mmol) was reacted with iodine (4.60 g, 9.06 mmol) and [bis-(trifluoroaceteoxy)iodo]benzene (4.00 g, 9.30 mmol). The crude product (4.80 g) was purified *via* silica column chromatography (5:1 hexane in CH_2Cl_2, R_f 0.13) to give **98** as a white solid (2.20 g, 51%) with data are in accordance with the literature: mp 236-238 °C {lit.[106] 250 °C ($CHCl_3$, MeOH)}; FT-IR (ATR): 2920 (w), 2897 (w), 2850 (w), 1483 (s), 1446 (w), 1388 (m), 1355 (m), 1211 (w), 1176 (w), 1064 (m), 1002 (s), 887 (w), 821 (s), 775 (s); ^{1}H NMR (400 MHz, Chloroform-*d*) δ 7.72 – 7.61 (m, 8H), 7.23 – 7.14 (m, 8H), 2.06 (s, 12H); HRMS [ASAP, ion trap] (SOLID) $[M]^+$ calcd for $C_{34}H_{28}I_4$ 943.8364, found 943.8366.

*Tetrahedral tetrakis-phenol (***99***)*. **98** (0.5 g, 0.53 mmol), $PdCl_2(PPh_3)_2$ (0.02 g, 0.03 mmol) and CuI (0.002 g, 0.01 mmol) were dissolved THF (10 mL). 4'-ethynyl-[1,1'-biphenyl]-4-ol **100** (0.53 g, 2.72 mmol) was dissolved THF (5 mL) in a separate flask. The two flasks were degassed using freeze-pump-thaw cycles (× 3). The alkyne solution was added dropwise to the first flask. The obtained mixture was degassed once more before dropwise addition of 10 mL of a 0.5 M aqueous ammonia solution. The reaction mixture was heated to 60 °C under nitrogen atmosphere for 40 h before being heated at reflux for 30 min. The two phases were separated and the aqueous layer extracted with EtOAc. The organic layer was dried over $MgSO_4$ and solvents removed. The obtained solids (3.5 g) were triturated with toluene and filtered to give **99** as a brown solid (0.65 g, 60%): mp > 300 °C; FT-IR (ATR): 2927 (w), 2922 (w), 1609 (m), 1589 (m), 1506 (s), 1491 (m), 1437

(m), 1354 (w), 1259 (s), 1226 (m),1171 (m), 1107 (w), 1018 (m), 1001 (m), 982 (m), 804 (s), 777 (m), 760 (m); ^{1}H NMR (400 MHz, DMSO-d_6) δ_H 9.66 (s, 4H), 7.64–7.54 (m, 40H), 6.86 (d, *J* 8.2, 8H), 2.12 (s, 12H); ^{13}C{^{1}H} NMR (126 MHz, DMSO-d_6, T= 80 °C) δ_C 157.6, 150.1, 140.2, 131.9, 131.5, 131.2, 129.7, 128.8, 127.8, 126.0, 125.8, 120.2, 115.9, 89.9, 89.1, 45.7; HRMS [MALDI, TOF] [M]+ calcd for $C_{90}H_{64}O_4$ 1208.4805, found 1208.4633.

*4'-ethynyl-[1,1'-biphenyl]-4-ol (***100***)*. 4-Hydroxy-4'-iodobiphenyl **74** (2.00 g, 6.75 mmol), $PdCl_2(PPh_3)_2$ (0.05 g, 0.07 mmol), CuI (0.04 g , 0. 21 mmol), trimethylsilylacetylene (1.5 mL, 10.54 mmol) and 0.5 M aqueous ammonia solution (35 mL) in THF (120 mL) were reacted according to general procedure B. The reaction was stirred at room temperature for 16 h. The crude product (2.16 g) was purified (silica gel, 10% MeOH in CH_2Cl_2, R_f 0.16). The obtained product (1.62 g, 6.08 mmol) and K_2CO_3 (1.00 g, 7.24 mmol) were dissolved in dry methanol (20 mL). The solution was left stirring under nitrogen atmosphere for 20 h. The reaction mixture was taken up in EtOAc and washed with water (× 3). The organic phase was dried over $MgSO_4$ and solvents were removed under reduced pressure. No further purification was carried out giving **100** as a pale brown solid (1.18 g, 80%). Data in accordance with literature:[108] mp 152-154 °C; FT-IR (ATR): 3373 (w), 3356 (w), 1595 (m), 1522 (m), 1477 (m), 1259 (m), 1246 (m), 997 (m), 800 (s); ^{1}H NMR (400 MHz, Chloroform-*d*) δ_H 7.59–7.43 (m, 6H), 6.91 (d, 2H), 4.86 (s, 1H); HRMS [ASAP, ion trap] $[M+H]^+$ calcd for $C_{14}H_{11}O$ 195.0804, found 195.0805.

*Asymmetric tetrakis-phenol (***102***)*: 1,2,4,5-tetrabromobenzene **101** (0.15 g, 0.38 mmol) was dissolved in 15 mL of dry THF together with $PdCl_2(PPh_3)_2$ (0.01 g, 0.01 mmol). 4′-ethynyl-[1,1′-biphenyl]-4-ol **100** (0.33 g, 1.7 mmol) was dissolved in 15 mL of dry THF in a separate flask. Both flasks were degassed *via* freeze-pump-thaw cycles (3 ×). The alkyne solution was added drop-wise to the flask containing the aryl halide. CuI (0.002 g, 0.008 mmol) was added to the mixture. The 0.5 M ammonia solution was prepared and deoxygenated by bubbling nitrogen gas through it. 7.8 mL of a 0.5 M aqueous solution of ammonia were added drop-wise to the mixture. The reaction mixture was heated to 60°C for 48 h. The two phases were separated and the aqueous layer was extracted with EtOAc and washed with 10% aqueous HCl and water. The organic layer was dried over sodium sulfate and solvents were removed *in vacuo* to give the crude product (0.43 g) that was purified (silica gel; 10% EtOAc in CH_2Cl_2, R_f 0.3) to give **102** as a dark brown solid

(rotameric mixture) (0.32 g, 81%): mp >300 °C; FT-IR (ATR) 2362 (w), 1587 (m), 1496 (s), 1172 (s), 1732 (s), 1020 (s), 981 (s), 820 (s), 721 (s), 692 (s); ^{1}H NMR (500 MHz, DMSO-d_6) δ_H 9.72 (s, 4H), 7.82 (s, 1H), 7.64 – 7.52 (m, 24H), 6.86 (d, J = 8.1, 8H); ^{13}C NMR (126 MHz, DMSO-d_6, 80°C) δ_C 158.40, 141.58, 134.94, 132.44, 130.25, 128.22, 126.61, 125.33, 120.23, 116.51, 96.50, 88.24; MS [ESI, ion trap] $[M - H]^-$ calcd for $C_{62}H_{37}O_4$ 845.2697, found 845.2689.

*Hexakis-phenol (***103***)*: **104** (0.1 g, 0.08 mmoles) was dissolved in dry THF (10 mL) together with $PdCl_2(PPh_3)_2$ (6% mol., 0.003 g, 0.005 mmoles). 4′-Ethynyl-[1,1′-biphenyl]-4-ol **100** (0.12 g, 0.62 mmoles) was dissolved in a separate flask in dry THF (10 mL). Both solutions were degassed before drop-wise addition of the alkyne solution to the first solution. The new mixture was degassed once more before addition of CuI (12%, 0.01 g, 0.08 mmol). A 0.5 M aqueous ammonia solution (2.5 mL, 1.3 mmoles) was added drop-wise to the new mixture, which was left stirring at 65 °C for 4 days. The reaction crude (0.2 g) was purified via silica column chromatography (10% EtOAc in CH_2Cl_2, R_f 0.1). **103** was isolated as a brown solid (0.07 g, 55%). FT-IR (ATR): 2916 (m), 2848 (m), 1662 (m), 1589 (m), 1492 (m), 1274 (m), 1172 (m), 1047 (s), 1022 (s), 997 (s), 821 (s).^{1}H NMR (500 MHz, DMSO-d_6) δ 9.66 (s, 6H), 7.56 (dd, J = 37.2, 7.2 Hz, 36H), 7.18 (d, J = 7.9 Hz, 12H), 7.01 (d, J = 8.0 Hz, 12H), 6.84 (d, J = 8.3 Hz, 12H). ^{13}C NMR (126 MHz, DMSO) δ 157.62, 140.27, 132.07, 131.89, 131.54, 131.46, 130.06, 128.83, 128.73, 127.77, 125.93, 119.96, 115.85, 89.81, 89.55. MS [MALDI] $[M+H]^+$ calcd for $C_{126}H_{78}O_6$ 1687.6, found 1687.6

*Hexakis(4-iodophenyl)benzene (***104***)*: was prepared using modified literature procedures.[125] Hexaphenylbenzene (2 g, 3.7 mmoles) was dissolved in dry CH_2Cl_2 (150 mL). To the obtained solution freshly ground iodine (3.8 g, 15 mmoles) was added together with [bis-(trifluoroaceteoxy)iodo] benzene (6.4 g, 15 mmoles); 3.2 g was added just after addition of iodine and the remaining half was added after 30 minutes. The obtained mixture was left stirring in the dark under nitrogen atmosphere overnight. Hexane was added to the yellow solution to encourage precipitation. The solids were isolated by filtration. The obtained solids were dissolved in chloroform; the solution was washed with 5% sodium bisulfite aqueous solution followed by water and brine. The organic layer was dried over sodium sulfate and solvents removed under reduced pressure. The obtained solids were recrystallized from chloroform to give **104** as a white solid (0.35 g, 51 %) FT-IR (ATR):

1487 (m), 1384 (m), 1138 (m), 1058 (m), 1003 (s), 823 (m). ^{1}H NMR (300 MHz, Chloroform-*d*) δ 7.23 (s, 12H), 6.54 – 6.39 (m, 12H).[125]

*Triradical (***105***)*. Tris-phenol **95** (0.05 g, 0.08 mmol), TPC **3** (0.06 g, 0.33 mmol), DMAP (0.03 g, 0.25 mmol) and EDCI·HCl (0.05 g, 0.32 mmol) in THF (10 mL) were reacted according to general procedure A. The reaction mixture was stirred 48 h. The crude product (0.08 g) was purified (4% H_2O aluminum oxide; 10% EtOAc in CH_2Cl_2, R_f 0.7) to give **105** as a yellow solid (0.1 g, 80%): mp 159-160 °C; FT-IR (ATR): 2974 (w), 2927 (w), 1730 (m), 1490 (m), 1286 (m), 1203(s), 1180(s), 1002 (s), 798 (s); HRMS [NSI, ion trap] $[M+NH_4]^+$ calcd for $C_{75}H_{70}N_4O_9$ 1171.5170, found: 1171.5174; Anal. Calcd. $C_{75}H_{66}N_3O_9$: C, 78.10; H, 5.77; N 3.64, found: C, 77.86; H, 5.85; N, 3.54. Room temperature continuous wave EPR displays a characteristic three line nitroxide spectrum: $a_{iso}(^{14}N)$ = 1.42(1) mT.

*Tetrahedral tetraradical (***106***)*. Tetraphenol **99** (0.15 g, 0.12 mmol), TPC **3** (0.12 g, 0.65 mmol), DMAP (0.08 g, 0.65 mmol) and EDCI·HCl (0.10 g, 0.64 mmol) in THF (20 mL) were reacted according to general procedure A. The reaction mixture was stirred 48 h. The crude product (0.30 g) was purified (4% H_2O aluminum oxide; 20% ethyl acetate in CH_2Cl_2, R_f 0.03) to give **106** as a dark orange solid (0.23 g, 72%): mp > 300 °C; FT-IR (ATR): 3034 (w), 2974 (w), 2927 (w), 1732 (m), 1504 (m), 1490 (m), 1288 (m), 1200 (s), 1002 (s), 831 (m), 800 (m); MS [MALDI, TOF] $[M+H]^+$ calcd for $C_{126}H_{113}N_4O_{12}$ 1875.8, found 1875.9; Anal. Calcd. for $C_{126}H_{113}N_4O_{12}$: C, 80.74; H, 6.02; N, 2.99, found: C, 80.65; H, 6.15; N, 3.12. Room temperature continuous wave EPR displays a characteristic three line nitroxide spectrum: $a_{iso}(^{14}N)$ =1.43(1) mT.

*Asymmetric tetraradical (***107***):* **102** (0.1 g, 0.12 mmol) was dissolved in 20 mL of dry THF. **3** (0.11 g, 0.6 mmol) was added to the solution together with dimethylaminopyridine (DMAP) (0.07 g, 0.6 mmol). EDCI·HCl (0.1 g, 0.6 mmol) was added in the dark. The reaction was left stirring in the dark at room temperature under nitrogen atmosphere for 40 h. The reaction mixture was filtered to remove urea precipitate and extracted with CH_2Cl_2. The organic layer was washed three times with water before being dried over magnesium sulfate. Solvents were removed under reduced pressure to give the crude product (0.16 g) that was further purified using column chromatography (aluminium oxide 4% H_2O; 5% EtOAc in CH_2Cl_2, R_f 0.48) to give **107** as an orange solid (0.02 g, 10%); mp 227-233 °C; FT-IR (ATR) 2976 (w), 2927 (w), 2866 (w), 2362 (w), 1732 (s), 1494 (s),

1288 (s), 1203 (s), 1165 (s), 1001 (s), 798 (s); MALDI-MS $[M + H]^+$ calcd for $C_{98}H_{87}N_4O_{12}$ 1511.6, found 1511.6.[126] Anal. Calcd for $C_{98}H_{86}N_4O_{12}$: C, 77.86; H, 5.73; N, 3.71, found: C, 77.71; H, 5.63; N, 3.8.

A.2 PELDOR General Methods

A.2.1 Sample preparation

Samples of model systems **93**, **105**, **106** and **107** (Chapter 3) were prepared from toluene or CH_2Cl_2 solutions (100 μM spin concentration). The solutions were transferred into 4 mm or 3 mm quartz EPR tubes (Wilmad), solvents were removed under reduced pressure and replaced with freshly molten *o*-terphenyl for measurements reported in Chapter 3, or by deuterated or protonated toluene and *o*-terphenyl for Chapter 5. Our collaborators C. Pliotas, H. Huang and J. H. Naismith prepared samples of the mechanosensitive channel of small conductance (MscS) from *E. coli* (Figure 3.1) were as previously described.[47a] MscS was spin labelled at residue S196, i.e. the serine residue was mutated to a cysteine and subsequently modified with the spin label (MscS S196R1) (1-Oxyl-2,2,5,5-tetramethylpyrroline-3-methyl) methanethiosulfonate (MTSSL). The labelling efficiency of MscS S196R1 was accurately quantified.[127] The soluble construct of the translocation channel Wza (sWza) spin labelled at residue glutamine 335 (Q335R1)[47b] was prepared as previously described. All protein samples were measured in deuterated buffer, with MscS S196R1 incorporated into phospholipid bicelles.[47a, 89]

Samples for measurements with the MD5 resonator (4 mm quartz tube) were filled with ≥ 100 μL of sample corresponding to ≥ 12 mm filling height, while for the split-ring MS3 resonator ≥ 65 μL of sample were transferred into a 3 mm quartz tube corresponding to ≥ 17 mm filling height. The MS3 resonator would allow volumes down to 30 μL, however the same sample tubes were measured at Q-band where the active length is 16 mm.

The sparsely labelled samples (Chapter 4) were prepared in a similar fashion by C. Pliotas under the supervision of J. H. Naismith. The two mutants of the heptameric membrane proteins MscS S196C and D67C were labelled S196R1 and D67R1 respectively using 33, 66 and 100% labelling. Sparse labelling was achieved by labelling each monomer with a ratio between EPR-active nitroxide-based spin labels and their diamagnetic analogues, a protonated MTSSL label. The percentages used as

identifier for each sample indicate the portion of EPR-active spin labels used for preparation of each sample.[47a, 89]

Samples for orientation selection studies (Chapter 5) were prepared from original solutions of biradical **93**, triradical **105** and tetraradical **106** with a 300 or 400 μM spin concentration in protonated toluene. 100 μL of each solution was transferred into a 4 mm Wilmad quartz tubes. The solvent was evaporated and replaced with an equivalent volume of liquid *o*-terphenyl (mp 60° C) or d_8 toluene; samples were immediately immersed into liquid nitrogen. Protonated toluene solutions were transferred into the same tubes and frozen in liquid nitrogen.

A.2.2 Simulations

A.2.2.1 Polygons

Simulations for a regular convex heptagon and octagon (mimicking MscS S196R1 and sWza Q335R1, respectively) were performed as described by Giannoulis *et al.*[78b] without adding noise or intermolecular dipolar interactions (Chapter 3). Dipolar evolution times were chosen to correspond to experimental conditions. However, the heptagon simulations had the time window extended to exclude cut-off artefacts and thus giving access to accurate extraction of all distances. The spin label positions for the tetrahedron representing **106** were derived by displacing each of the four vertices in a random direction in space from a regular tetrahedron of an edge length of 4 nm. Displacements are characterised by the standard deviation of 0.4 nm of a Gaussian distributed random length and λ was set to 0.45. The rectangle representing **107** was constructed as a regular convex hexagon[78b] with a diameter of 3.7 nm, having two opposite vertices (e.g. 1 and 4) removed. 100% λ was set to 0.4. The standard deviation of vertex displacement was set to 4% of the diameter.

Simulations for testing the efficiency of combination of λ reduction and power-scaling (Section 3.3.2) were performed on polygons bearing from 3 to 8 spins. In this case noise levels of 0, 1 and 3% of the maximum intensity of the simulated time trace were introduced. Polygons were set to have a 6 nm diameter and vertex displacement fixed to 0.1 nm. A time window of 8 μs was used to reliably extract mean and width of distances up to 6 nm. A regularisation parameter of 1 was used for all polygons, except for the octagon where 0.1 was required to accurately resolve the last distance peak.

Intermolecular dipolar interactions were excluded from the simulations allowing removal of a constant offset as background.[78b]

Modelling for extraction of expected distance distributions from proteins crystal structure has also been described in the Appendix of Chapter 3.Simulations to estimate the optimum labelling efficiencies (Chapter 4) were performed in a similar fashion. In this case two heptagons with an internal diameter of 5 and 6 nm for the two mutants of MscS, S196R1 and D67R1 respectively, were used as templates for studying effects of sparse labelling. A λ_{max} of 0.4 was set, the typical value representing the portion of spins excited by the pump pulse at X-band, together with a label displacement of 0.2 nm. The noise was varied between 1 and 3% and labelling efficiency per monomer varied between 30, 60 and 100%. The time window was set to 5 μs to allow extraction of all distances. Distance distributions were plotted for each noise level and labelling efficiency for the two mutants; power-scaling was also applied to test for effects on recovery of distances for each condition.

A.2.3 EPR experimental methods

A.2.3.1 PELDOR and λ reduced experiments pulses set-up

PELDOR measurements were recorded at X-band using both a MD5 resonator, and a split-ring (MS3) resonator and at Q-band. For all measurements at X-band detection and pump pulse offsets were varied between 60 MHz for model systems **106** and **107** and between 70 and 75 MHz for proteins (MscS S196R1 and sWza Q335R1, respectively). For all Q-band measurements an offset of 80 MHz was used. τ_1 was set to 380 ns for protein samples in deuterated buffer and to 200 ns when using protonated *o*-terphenyl matrices for measurement of model systems **106** and **107**. τ_2 for X-band measurements was set to 2.4 μs or 3.8 μs for protein samples and to 3.8 μs for model systems **106** and **107**. For Q-band measurements τ_2 could be extended to 5 μs for all measurements. Shot repetition times between 2 and 3 ms were used.

Experiments reducing the probability of pumping spins (λ) while retaining the spectral excitation profile were performed similarly to those previously described.[19a] The inversion efficiencies as a function of the pump channel attenuation were determined by an echo-detected electron spin nutation experiment. The pump pulse flip angle β is optimised to achieve maximum inversion of the Hahn echo at that specific frequency. Calibration of the reduced λ or pump pulse flip angle β is performed by the

nutation experiment. A nutation π pulse of variable time *t* is applied followed, after a time delay *T*, by two detection pulses π and π/2 for generation of a Hahn echo. The change in polarisation induced by the variable length of the nutation pulse is detected by the echo generated by the following two pulses, as shown in Figure A.1.

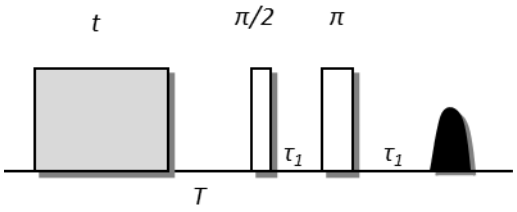

Figure A.1: Echo-detected spin nutation experiment pulse train used for calibration of pump pulse flip angle β.

The experiment generates a cosine wave as function of the change of longitudinal magnetisation over the increasing length of nutation pulse, as shown in Figure A.2. The first minimum of the cosine wave occurs at the pump pulse length required for achieving β equivalent to π. Thus, it determines which ELDOR pulse length is required for achieving an inversion pulse with a flip angle of π.

a) b)

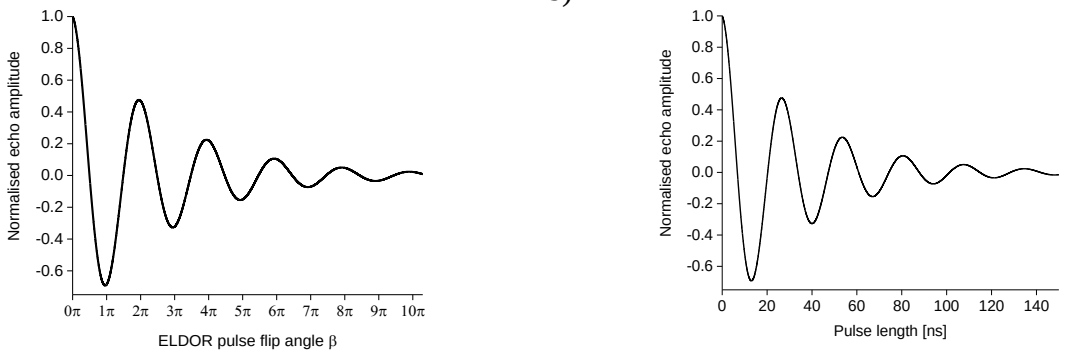

Figure A.2: ELDOR nutation experiment showing the occurrence of a 180° inversion of the spin echo after pulses with a flip angle of odd multiples of π (a) and its corresponding time trace (b).

An increase in the pump channel attenuation will require a longer pump pulse to achieve a flip angle β of π necessary to give the full echo inversion. The flip angle β of the pump pulse relative to the maximum inversion (λ(β)/ λ(π)) at a given attenuation and exciting a specific area of the EPR spectrum, can be calculated using the Equation A.1:

$$\frac{\lambda(\beta)}{\lambda(\pi)} = \sin^2\frac{\beta}{2} \qquad \text{(A.1)}$$

where $\lambda(\beta)$ is the inversion efficiency obtained for a certain flip angle β and $\lambda(\pi)$ is the inversion efficiency obtained for a π pump pulse. Here, λ was reduced by keeping the pump pulse length constant, but reducing the pulse power. For experiments reducing λ the fraction λ / λ_{max} (or $\lambda(\beta)/ \lambda(\pi)$) is given as a percentage.

A.2.3.2 Frequency-interchanged experiments

A typical PELDOR pulse sequence performed at X-band with an MD5 probe uses a $\pi/2$ pulse of 16 ns followed by a π pulse of 32 ns, and a 18/20 ns π pump pulse. This allows in a two spin system to trade the detected number of spins for larger Δ resulting from excitation of a larger fraction of B spins by the pump pulse (Figure A.3 a) and c)). The use of this or similar experimental settings on systems bearing more than two spins has been found to give traces containing sum and difference frequencies that cannot be correctly processed by DeerAnalysis, if not in combination with λ reduction and power-scaling.[19a, 78a, 89] In an attempt to suppress the contribution of multi-spin effects to the PELDOR signal from multiply labelled systems the respective frequencies of detection and pump pulses were swapped. At X-band this leads to the detection of A spins on the maximum of the nitroxide field sweep spectrum and pumping of B spins on the low field maximum (Figure A.3 b) and d)). In this case the pulse lengths were modified from the original PELDOR experiment settings as follows: a 10 ns $\pi/2$ pulse, followed by a 20 ns π pulse is applied at the detection frequency, while a 32 ns π pulse is applied at the pump frequency. At Q-band the new settings lead to the detection pulses being set at the first field sweep maximum while the pump pulse is applied on the second maximum, as shown in Figure A.3 d). In this case the pulse lengths were modified as follows: 8 to 10 ns $\pi/2$ pulse, followed by a 16 to 20 ns π pulse is applied at the detection frequency, while a 32 ns π pulse is applied at the pump frequency. This longer pump pulse exhibits a smaller excitation bandwidth than the typical 18/20 ns pump pulse used in PELDOR experiments, thus allowing excitation of a lower fraction of B spins.

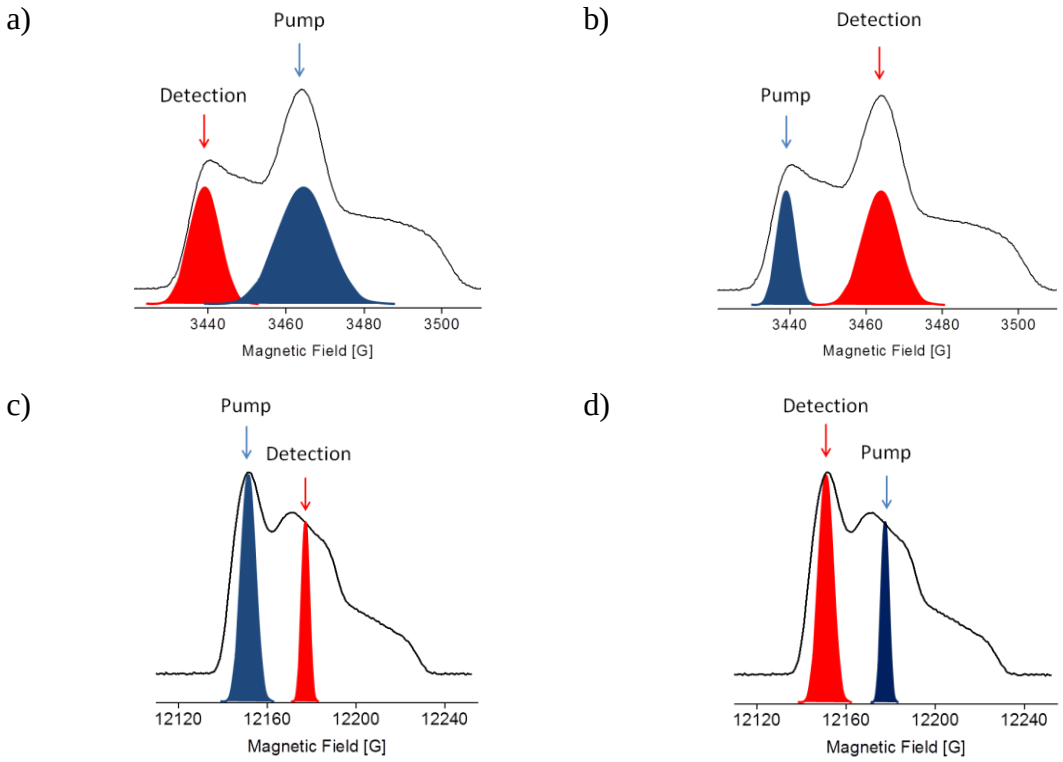

Figure A.3: Estimated pulses profiles on nitroxide EPR field spectra at X-band for a PELDOR a) and frequency-interchanged b) and Q-band for a PELDOR c) and frequency-interchanged d) settings.[27, 90, 128]

Additionally, the expected loss in sensitivity, due to reduced Δ, should be compensated by detection of a larger fraction of A detection spins. Pulse lengths were adjusted depending on the resonator and frequencies used, as shown in Table A.1, Table A.2 and TableA.3. The legend for each measurement reports the pump pulse length [ns] – the frequency offset between pump and detection pulses [MHz] – the detection π pulse length [ns], in this order. For all frequency interchanged experiments a subscript "M" has been added after the detection π pulse length to indicate its position on the maximum of the nitroxide field sweep spectrum.

Standard PELDOR parameters			
	X-band MD5	X-band MS3	Q-band QT2
π/2 detection [ns]	16	16	16
π detection [ns]	32	32	32
π pump [ns]	12*/18/20	12	12/16

Table A.1: Pulse lengths used for standard PELDOR settings. *A 12 ns pump pulse was found to give maximum modulation depth when performing standard PELDOR measurements of MscS S196R1 and sWza Q335R1 with an MD5 resonator. For all other experiments 18 or 20 ns pump pulses were required for maximum inversion.

It is common to use a 12 or 18/20 ns pump pulse, a length at which the maximum inversion of the Hahn echo is achieved when using an MS3 split-ring and MD5 resonators respectively (Table A.1).[9a]

Frequency-interchanged PELDOR parameters X-band MD5 and Q-band		
	X-band MD5	Q-band QT2
π /2 detection [ns]	10	8-10
π detection [ns]	20	16/20
π pump [ns]	30/32	32

Table A.2: Pulse lengths used for frequency-interchanged PELDOR at X-band (MD5 resonator) and Q-band.

Frequency-interchanged PELDOR parameters X-band MS3			
π /2 detection [ns]	8	10	16
π detection [ns]	14	20	32
π pump [ns]	32	32	12

Table A.3: Pulse lengths used for frequency-interchanged PELDOR at X-band (MS3 resonator).

Measurements on sparsely labelled MscS samples were carried out at both X- and Q-band frequencies. Standard PELDOR and frequency-interchanged experiments performed at X-band using MD5 and MS3 resonators and at Q-band frequencies were carried out as previously described, as reported in Table A.4 and Table A.5. Specifically for frequency-interchanged experiments the following pulse sequences, reported in Table A.5, were used:

Standard PELDOR parameters			
	X-band MD5	X-band MS3	Q-band QT2
π/2 detection [ns]	16	16	16
π detection [ns]	32	32	32
π pump [ns]	20	12	12/16

Table A.4: Pulse lengths used for frequency-interchanged PELDOR at X-band (MD5 and MS3 resonators) and Q-band.

Frequency-interchanged PELDOR parameters X- and Q-band			
	X-band MD5	X-band MS3	Q-band QT2
π/2 detection [ns]	10	8	8-10
π detection [ns]	20	14	16/20
π pump [ns]	32	32	32

Table A.5: Pulse lengths used for frequency-interchanged PELDOR at X- and Q-band.

A.2.3.3 Orientation selective and orientation averaged experiments

Orientation selective PELDOR measurements were recorded at X-band using an MD5 resonator as previously reported.[129] The offset between detection and pump pulse offset was varied between 40, 60 and 80 MHz. This range corresponds to the smallest frequency offset that avoids strong pump/probe frequency overlap, and therefore large nuclear modulation artefacts, and the largest possible frequency offset that excites the edge of the nitroxide spectrum whilst still pumping the global maximum.[90] PELDOR measurements were performed as previously described[98] with exception of τ_2 being set to 3.8 μs for all measurements and shot repetition times varied between 2 and 2.5 ms. The first inter-pulse delay was also varied eight times by 8 and 56 ns each time in order to average the proton and deuterium nuclear modulation respectively.[29] Orientation averaged experiments were performed by varying the magnetic field so that the observer position is varied between the low-field maximum of the nitroxide spectrum and the global maximum in 14 steps of 2 G. The difference between pump and observer frequencies was kept constant at 60 MHz.[18c] Traces were then added and normalised to give orientation averaged traces. Individual traces were used for orientation resolved experiments. All orientation resolved experiments were performed on d_8 toluene samples and d_8 ESEEM being suppressed.

The legend of each measurement reports: length of the pump pulse, pulse offset and length of the π pulse of the detection sequence, respectively.

A.2.4 Data processing: DeerAnalysis parameters

Raw data was fitted by a monoexponential decay to remove the intermolecular background, followed by Tikhonov regularization in DeerAnalysis2013.[30] The optimum regularization parameter α was chosen by the L-curve criterion: α = 10 was found to be optimum for all cases except for tetraradical **107** where α = 1 was required. In **107** two equivalent short distances (*ortho*), two equivalent medium distances (*meta*) and two equivalent long distances (*para*) are present. As similar angular fluctuations will broaden the *ortho*-distance more than the *para*-distance each of the three distance pairs would require different Tikhonov regularization parameters to capture their distribution. A value of 1 was found not to broaden the long distances and not to split the short distance distributions.[32] Traces were power-scaled[78a] as indicated using the implementation in DeerAnalysis2013. Distance distributions were validated by varying the background start point using the validation tool in DeerAnalysis2013. For all traces in Chapter 3 validations were performed by varying the start time from 5% to 95% of the total time window length, and 19 trials (every 5%) were performed, followed by pruning of the trial results with a prune factor of 1.15 (i.e. retaining only those data sets exceeding the lowest rmsd (root mean square deviation) by a maximum of 15%). If less than 50% of trials were retained upon pruning, traces were cut in steps of 15% of the time window length (here, resulting either in cuts of 15 or 30%) until at least half of the trials were within 15% of the lowest rmsd. Distance distributions show the 2 × σ confidence interval (± 2 × rmsd). For all traces reported in Chapter 4 the start time was varied from 5% to 80% of the total time window length, and 16 trials (every 5%) were performed, followed by pruning of the trial results with a prune factor of 1.15. The noise was increased to a level of 1.5 (i.e. by 50%) and 50 trials were performed.

The time domain simulations were fitted by a zero order polynomial for background correction to remove a constant offset, as all the simulated traces were lacking on the intermolecular background, followed by Tikhonov regularization in DeerAnalysis2013.[30]

A.2.5 Sensitivity calculation and noise estimation

Sensitivity values were calculated as the ratio between modulation depth (Δ) and noise. Noise was estimated using the rmsd of the background fit (error of the background model) given in DeerAnalysis2013. This solution was found to be more stable than using the error of the fit due to differences in the quality of fit between standard and frequency-interchanged experiments. It was found that the fit generated by DeerAnalysis for the frequency-interchanged experiments did not match the experimental data as well as for traces from PELDOR experiments. This mismatch increases the error of fit, thus the noise level for all frequency-interchanged experiments would be increased. To avoid this bias towards the frequency-interchanged experiments the estimation was performed within the background range corresponding to the last third of the trace. The value was estimated by taking the average rmsd within the range in which the rmsd values were most consistent (i.e. where the fit was most stable).

The experimental λ values for λ reduction and frequency-interchanged experiments were calculated from the experimental modulation depths (Equation A.2):[78b]

$$\lambda = 1 - (1 - \Delta)^{\frac{1}{N-1}} \tag{A.2}$$

with Δ being the experimental modulation depth and N the number of spins in the system. These λ values were used to compare the expected fraction of λ calculated for the λ reduction experiments from the ELDOR nutation experiment.

References

1. (a) Bernal, J. D., Crowfoot, D., X-ray photographs of crystalline pepsin. *Nature* **1934,** *133*, 794-795; (b) Garman, E. F., Developments in X-ray crystallographic structure determination of biological macromolecules. *Science* **2014,** *343* (6175), 1102-1108.
2. (a) Albrecht, C., Joseph R. Lakowicz: principles of fluorescence spectroscopy, 3rd Edition. *Anal. Bioanal. Chem.* **2008,** *390* (5), 1223-1224; (b) Schiemann, O.; Prisner, T. F., Long-range distance determinations in biomacromolecules by EPR spectroscopy. *Q. Rev. Biophys.* **2007,** *40* (01), 1-53.
3. (a) Lee, J.-S.; Khitrin, A. K., High-precision measurement of internuclear distances using solid-state NMR. *Concepts Magn. Reson., Part A* **2008,** *32A* (1), 56-67; (b) Wütrich, K., *NMR of proteins and nucleic acids*. Wiley: New York, 1986; (c) Bonvin, A. M. J. J.; Boelens, R.; Kaptein, R., NMR analysis of protein interactions. *Curr. Opin. Chem. Biol.* **2005,** *9* (5), 501-508.
4. Cooke, J.; Brown, L., Distance measurements by continuous wave EPR spectroscopy to monitor protein folding. In *Protein folding, misfolding, and disease*, Hill, A. F.; Barnham, K. J.; Bottomley, S. P.; Cappai, R., Eds. Humana Press: 2011; Vol. 752, pp 73-96.
5. (a) Zheng, J., FRET and its biological application as a molecular ruler. In *Biomedical applications of biophysics*, Jue, T., Ed. Humana Press: Totowa, NJ, 2010; pp 119-136; (b) Jares-Erijman, E. A.; Jovin, T. M., FRET imaging. *Nat Biotech* **2003,** *21* (11), 1387-1395.
6. (a) Liu, J.; Lu, Y., FRET study of a trifluorophore-labeled DNAzyme. *J. Am. Chem. Soc.* **2002,** *124* (51), 15208-15216; (b) Watrob, H. M.; Pan, C.-P.; Barkley, M. D., Two-step FRET as a structural tool. *J. Am. Chem. Soc.* **2003,** *125* (24), 7336-7343; (c) Sale, K.; Faulon, J.-L.; Gray, G. A.; Schoeniger, J. S.; Young, M. M., Optimal bundling of transmembrane helices using sparse distance constraints. *Protein Sci* **2004,** *13* (10), 2613-2627.
7. (a) Pannier, M.; Veit, S.; Godt, A.; Jeschke, G.; Spiess, H. W., Dead-time free measurement of dipole–dipole interactions between electron spins. *J. Magn. Reson.* **2000,** *142* (2), 331-340; (b) Kovacs, F. A.; Fowler, D. J.; Gallagher, G. J.; Thompson, L. K., A practical guide for solid-state NMR distance measurements in proteins. *Concepts Magn. Reson., Part A* **2007,** *30A* (1), 21-39.
8. (a) Salnikov, E.; Rosay, M.; Pawsey, S.; Ouari, O.; Tordo, P.; Bechinger, B., Solid-state NMR spectroscopy of oriented membrane polypeptides at 100 K with signal enhancement by dynamic nuclear polarization. *J. Am. Chem. Soc.* **2010,** *132* (17), 5940-5941; (b) Maly, T.; Debelouchina, G. T.; Bajaj, V. S.; Hu, K.-N.; Joo, C.-G.; Mak–Jurkauskas, M. L.; Sirigiri, J. R.; van der Wel, P. C. A.; Herzfeld, J.; Temkin, R. J.; Griffin, R. G., Dynamic nuclear polarization at high magnetic fields. *J. Chem. Phys.* **2008,** *128* (5), 052211-052211.
9. (a) Borbat, P. P.; Freed, J. H., Pulse dipolar electron spin resonance: distance measurements. In *Structural information from spin-labels and intrinsic paramagnetic centres in the biosciences*, Timmel, C. R.; Harmer, J. R., Eds. Springer Berlin Heidelberg: 2013; Vol. 152, pp 1-82; (b) Jeschke, G., DEER distance measurements on proteins. *Annu. Rev. Phys. Chem.* **2012,** *63* (1), 419-446.
10. (a) Hubbell, W. L.; Altenbach, C., Investigation of structure and dynamics in membrane proteins using site-directed spin labeling. *Curr. Opin. Struct. Biol* **1994,** *4* (4), 566-573; (b) Hubbell, W. L.; Gross, A.; Langen, R.; Lietzow, M. A., Recent advances in site-directed spin labeling of proteins. *Curr. Opin. Struct. Biol*, **1998,** *8* (5), 649-656.

11. Milov, A. D.; Salikhov, K. M.; Shirov, M. D., Application of double resonance method of electron spin echo in a study of the spatial distribution of paramagnetic centres in solids. *Fiz. Tverd. Tela* **1981,** *23*, 975-982.
12. (a) Borbat, P. P.; Freed, J. H., Multiple-quantum ESR and distance measurements. *Chem. Phys. Lett.* **1999,** *313* (1–2), 145-154; (b) Saxena, S.; Freed, J. H., Double quantum two-dimensional Fourier transform electron spin resonance: distance measurements. *Chem. Phys. Lett.* **1996,** *251* (1–2), 102-110.
13. Bowman, A.; Hammond, C. M.; Stirling, A.; Ward, R.; Shang, W.; El-Mkami, H.; Robinson, D. A.; Svergun, D. I.; Norman, D. G.; Owen-Hughes, T., The histone chaperones Vps75 and Nap1 form ring-like, tetrameric structures in solution. *Nucleic Acids Res.* **2014,** *42* (9), 6038-6051.
14. Martin, R. E.; Pannier, M.; Diederich, F.; Gramlich, V.; Hubrich, M.; Spiess, H. W., Determination of end-to-end distances in a series of TEMPO diradicals of up to 2.8 nm length with a new four-pulse double electron electron resonance experiment. *Angew. Chem., Int. Ed.* **1998,** *37* (20), 2833-2837.
15. Jeschke, G.; Pannier, M.; Spiess, H. W., Double electron-elctron resonance: methodological advances and application to disordered systems. In *Biological magnetic resonance*, Berliner, L. J.; Eaton, S. S.; Eaton, G. R., Eds. Kluwer Academic/Plenum Publishers: New York, 2000; Vol. 19.
16. Yu, D. T.; Milov, A. D.; Maryasov, A. G., Pulsed electron–electron double resonance (PELDOR) as EPR spectroscopy in nanometre range. *Russ. Chem. Rev.* **2008,** *77* (6), 487.
17. (a) Larsen, R. G.; Singel, D. J., Double electron–electron resonance spin–echo modulation: spectroscopic measurement of electron spin pair separations in orientationally disordered solids. *J. Chem. Phys.* **1993,** *98* (7), 5134-5146; (b) Marko, A.; Margraf, D.; Yu, H.; Mu, Y.; Stock, G.; Prisner, T., Molecular orientation studies by pulsed electron-electron double resonance experiments. *J. Chem. Phys.* **2009,** *130* (6), -.
18. (a) Jeschke, G.; Sajid, M.; Schulte, M.; Ramezanian, N.; Volkov, A.; Zimmermann, H.; Godt, A., Flexibility of shape-persistent molecular building blocks composed of *p*-phenylene and ethynylene units. *J. Am. Chem. Soc.* **2010,** *132* (29), 10107-10117; (b) Margraf, D.; Bode, B. E.; Marko, A.; Schiemann, O.; Prisner, T. F., Conformational flexibility of nitroxide biradicals determined by X-band PELDOR experiments. *Mol. Phys.* **2007,** *105* (15-16), 2153-2160; (c) Godt, A.; Schulte, M.; Zimmermann, H.; Jeschke, G., How flexible are poly(para-phenyleneethynylene)s? *Angew. Chem., Int. Ed.* **2006,** *45* (45), 7560-7564.
19. (a) Jeschke, G.; Sajid, M.; Schulte, M.; Godt, A., Three-spin correlations in double electron-electron resonance. *Phys. Chem. Chem. Phys.* **2009,** *11* (31), 6580-6591; (b) Bode, B. E.; Margraf, D.; Plackmeyer, J.; Dürner, G.; Prisner, T. F.; Schiemann, O., Counting the monomers in nanometer-sized oligomers by pulsed electron−electron double resonance. *J. Am. Chem. Soc.* **2007,** *129* (21), 6736-6745; (c) Hilger, D.; Jung, H.; Padan, E.; Wegener, C.; Vogel, K.-P.; Steinhoff, H.-J.; Jeschke, G., Assessing oligomerization of membrane proteins by four-pulse DEER: pH-dependent dimerization of NhaA Na+/H+ antiporter of E. coli. *Biophys. J.* **2005,** *89* (2), 1328-1338; (d) Milov, A. D.; Ponomarev, A. B.; Tsvetkov, Y. D., Electron-electron double resonance in electron spin echo: model biradical systems and the sensitized photolysis of decalin. *Chem. Phys. Lett.* **1984,** *110* (1), 67-72.
20. (a) Margraf, D.; Cekan, P.; Prisner, T. F.; Sigurdsson, S. T.; Schiemann, O., Ferro- and antiferromagnetic exchange coupling constants in PELDOR spectra. *Phys. Chem. Chem. Phys.* **2009,** *11* (31), 6708-6714; (b) Weber, A.; Schiemann, O.; Bode, B.; Prisner, T.

F., PELDOR at S- and X-band frequencies and the separation of exchange coupling from dipolar coupling. *J. Magn. Reson.* **2002,** *157* (2), 277-285.
21. Milov, A. D.; Maryasov, A. G.; Tsvetkov, Y. D., Pulsed electron double resonance (PELDOR) and its applications in free-radicals research. *Appl. Magn. Reson.* **1998,** *15* (1), 107-143.
22. Milov, A. D.; Tsvetkov, Y. D.; Formaggio, F.; Crisma, M.; Toniolo, C.; Raap, J., Self-assembling properties of membrane-modifying peptides studied by PELDOR and CW-ESR spectroscopies. *J. Am. Chem. Soc.* **2000,** *122* (16), 3843-3848.
23. Valera, S.; Bode, B., Strategies for the synthesis of yardsticks and abaci for nanometre distance measurements by pulsed EPR. *Molecules* **2014,** *19* (12), 20227.
24. Milov, A. D.; Ponomarev, A. B.; Tsvetkov, Y. D., Modulation beats of signal of double electron-electron resonance in spin echo for biradical systems. *J. Struct. Chem.* **1984,** *25* (5), 710-713.
25. Reginsson, G. W.; Shelke, S. A.; Rouillon, C.; White, M. F.; Sigurdsson, S. T.; Schiemann, O., Protein-induced changes in DNA structure and dynamics observed with noncovalent site-directed spin labeling and PELDOR. *Nucl. Acids Res.* **2012,** *41*, e11-e21.
26. Schweiger, A.; Jeschke, G., *Principles of pulse electron paramagnetic resonance*. Oxford University Press: 2001.
27. Reginsson, G. W.; Schiemann, O., Pulsed electron–electron double resonance: beyond nanometre distance measurements on biomacromolecules. *Biochem. J.* **2011,** *434* (3), 353-363.
28. Krstic, I., Marko, A., Grytz, C. M., Endeward, B., Prisner, T. F., Structure and conformational dynamics of RNA determined by pulsed EPR. In *RNA structure and folding: biophysical techniques and prediction methods*, Klostermeier, D., Hammann, C., Ed. Walter de Grutyer: Berlin, 2013.
29. Jeschke, G.; Panek, G.; Godt, A.; Bender, A.; Paulsen, H., Data analysis procedures for pulse ELDOR measurements of broad distance distributions. *Appl. Magn. Reson.* **2004,** *26* (1-2), 223-244.
30. Jeschke, G.; Chechik, V.; Ionita, P.; Godt, A.; Zimmermann, H.; Banham, J.; Timmel, C. R.; Hilger, D.; Jung, H., DeerAnalysis2006—a comprehensive software package for analyzing pulsed ELDOR data. *Appl. Magn. Reson.* **2006,** *30* (3-4), 473-498.
31. Schiemann, O.; Piton, N.; Plackmeyer, J.; Bode, B. E.; Prisner, T. F.; Engels, J. W., Spin labeling of oligonucleotides with the nitroxide TPA and use of PELDOR, a pulse EPR method, to measure intramolecular distances. *Nat. Protocols* **2007,** *2* (4), 904-923.
32. Chiang, Y.-W.; Zheng, T.-Y.; Kao, C.-J.; Horng, J.-C., Determination of interspin distance distributions by cw-ESR is a single linear inverse problem. *Biophys. J.* **2009,** *97* (3), 930-936.
33. Schwab, P. F. H.; Levin, M. D.; Michl, J., Molecular rods. 1. Simple axial rods. *Chem. Rev.* **1999,** *99* (7), 1863-1933.
34. Xiao, W.; Shin, Y.-K., EPR spectroscopic ruler: the method and its applications. In *Biological magnetic resonance*, Berliner, L. J.; Eaton, S. S.; Eaton, G. R., Eds. Kluwer Academic/Plenum Publishers: New York, 2000; Vol. 19, pp 249-251.
35. (a) Shelke, S.; Sigurdsson, S., Site-directed nitroxide spin labeling of biopolymers. In *Structural information from spin-labels and intrinsic paramagnetic centres in the biosciences*, Timmel, C. R.; Harmer, J. R., Eds. Springer Berlin Heidelberg: 2013; Vol. 152, pp 121-162; (b) Fielding, A.; Concilio, M.; Heaven, G.; Hollas, M., New Developments in Spin Labels for Pulsed Dipolar EPR. *Molecules* **2014,** *19* (10), 16998-17025.

36. Goldfarb, D., Metal-based spin labeling for distance determination. In *Structural information from spin-labels and intrinsic paramagnetic centres in the biosciences*, Timmel, C. R.; Harmer, J. R., Eds. Springer Berlin Heidelberg: 2013; Vol. 152, pp 163-204.
37. Altenbach, C.; Flitsch, S. L.; Khorana, H. G.; Hubbell, W. L., Structural studies on transmembrane proteins. 2. Spin labeling of bacteriorhodopsin mutants at unique cysteines. *Biochemistry* **1989,** *28* (19), 7806-7812.
38. Tsvetkov, Y. D., Nitroxyls and PELDOR: nitroxyl radicals in pulsed electron-electron double resonance spectroscopy. *J. Struct. Chem.* **2013,** *54* (1), 42-72.
39. (a) Valera, S.; Taylor, J. E.; Daniels, D. S. B.; Dawson, D. M.; Athukorala Arachchige, K. S.; Ashbrook, S. E.; Slawin, A. M. Z.; Bode, B. E., A modular approach for the synthesis of nanometer-sized polynitroxide multi-spin systems. *J. Org. Chem.* **2014,** *79* (17), 8313-8323; (b) Godt, A.; Franzen, C.; Veit, S.; Enkelmann, V.; Pannier, M.; Jeschke, G., EPR probes with well-defined, long distances between two or three unpaired electrons. *J. Org. Chem.* **2000,** *65* (22), 7575-7582.
40. Paletta, J. T.; Pink, M.; Foley, B.; Rajca, S.; Rajca, A., Synthesis and reduction kinetics of sterically shielded pyrrolidine nitroxides. *Org. Lett.* **2012,** *14* (20), 5322-5325.
41. Reginsson, G. W.; Kunjir, N. C.; Sigurdsson, S. T.; Schiemann, O., Trityl radicals: spin labels for nanometer-distance measurements. *Chem. Eur. J.* **2012,** *18* (43), 13580-13584.
42. Martorana, A.; Bellapadrona, G.; Feintuch, A.; Di Gregorio, E.; Aime, S.; Goldfarb, D., Probing protein conformation in cells by EPR distance measurements using Gd3+ spin labeling. *J. Am. Chem. Soc.* **2014,** *136* (38), 13458-13465.
43. Yang, Z., Liu, Y., Borbat, P., Zweier, J. L., Freed, J. H., Hubbell, W. L., Pulsed ESR dipolar spectroscopy for distance measurements in immobilized spin labeled proteins in liquid solution. *J. Am. Chem. Soc.* **2012,** *134*, 9950-9952.
44. Jeschke, G.; Pannier, M.; Godt, A.; Spiess, H. W., Dipolar spectroscopy and spin alignment in electron paramagnetic resonance. *Chem. Phys. Lett.* **2000,** *331* (2–4), 243-252.
45. Borbat, P. P.; Freed, J. H., Measuring distances by pulsed dipolar ESR spectroscopy: spin-labeled histidine kinases. In *Methods Enzymol.*, Melvin I. Simon, B. R. C.; Alexandrine, C., Eds. Academic Press: 2007; Vol. Volume 423, pp 52-116.
46. Pfannebecker, V.; Klos, H.; Hubrich, M.; Volkmer, T.; Heuer, A.; Wiesner, U.; Spiess, H. W., Determination of end-to-end distances in oligomers by pulsed EPR. *J. Phys. Chem.* **1996,** *100* (32), 13428-13432.
47. (a) Pliotas, C.; Ward, R.; Branigan, E.; Rasmussen, A.; Hagelueken, G.; Huang, H.; Black, S. S.; Booth, I. R.; Schiemann, O.; Naismith, J. H., Conformational state of the MscS mechanosensitive channel in solution revealed by pulsed electron–electron double resonance (PELDOR) spectroscopy. *Proc. Natl. Acad. Sci. U.S.A.* **2012,** *109* (40), E2675-E2682; (b) Hagelueken, G.; Ingledew, W. J.; Huang, H.; Petrovic-Stojanovska, B.; Whitfield, C.; ElMkami, H.; Schiemann, O.; Naismith, J. H., PELDOR spectroscopy distance fingerprinting of the octameric outer-membrane protein Wza from Escherichia coli. *Angew. Chem., Int. Ed.* **2009,** *48* (16), 2904-2906; (c) Edwards, D. T.; Huber, T.; Hussain, S.; Stone, K. M.; Kinnebrew, M.; Kaminker, I.; Matalon, E.; Sherwin, M. S.; Goldfarb, D.; Han, S., Determining the oligomeric structure of proteorhodopsin by Gd3+-based pulsed dipolar spectroscopy of multiple distances. *Structure* **2014,** *22* (11), 1677-1686.
48. Junk, M. J. N.; Spiess, H. W.; Hinderberger, D., DEER in biological multispin-systems: A case study on the fatty acid binding to human serum albumin. *J. Magn. Reson.* **2011,** *210* (2), 210-217.

49. (a) Potapov, A.; Song, Y.; Meade, T. J.; Goldfarb, D.; Astashkin, A. V.; Raitsimring, A., Distance measurements in model bis-Gd(III) complexes with flexible "bridge". Emulation of biological molecules having flexible structure with Gd(III) labels attached. *J. Magn. Reson.* **2010,** *205* (1), 38-49; (b) Raitsimring, A. M.; Gunanathan, C.; Potapov, A.; Efremenko, I.; Martin, J. M. L.; Milstein, D.; Goldfarb, D., Gd3+ complexes as potential spin labels for high field pulsed EPR distance measurements. *J. Am. Chem. Soc.* **2007,** *129* (46), 14138-14139.
50. (a) Bode, B. E.; Plackmeyer, J.; Prisner, T. F.; Schiemann, O., PELDOR measurements on a nitroxide-labeled Cu(II) porphyrin: orientation selection, spin-density distribution, and conformational flexibility. *J. Phys. Chem. A* **2008,** *112* (23), 5064-5073; (b) Narr, E.; Godt, A.; Jeschke, G., Selective measurements of a nitroxide–nitroxide separation of 5 nm and a nitroxide–copper separation of 2.5 nm in a terpyridine-based copper(II) complex by pulse EPR spectroscopy. *Angew. Chem., Int. Ed.* **2002,** *114* (20), 4063-4066.
51. Ezhevskaya, M.; Bordignon, E.; Polyhach, Y.; Moens, L.; Dewilde, S.; Jeschke, G.; Van Doorslaer, S., Distance determination between low-spin ferric haem and nitroxide spin label using DEER: the neuroglobin case. *Mol. Phys.* **2013,** *111* (18-19), 2855-2864.
52. Elsässer, C.; Brecht, M.; Bittl, R., Pulsed electron−electron double resonance on multinuclear metal clusters: assignment of spin projection factors based on the dipolar interaction. *J. Am. Chem. Soc.* **2002,** *124* (42), 12606-12611.
53. Pornsuwan, S.; Bird, G.; Schafmeister, C. E.; Saxena, S., Flexibility and lengths of bis-peptide nanostructures by electron spin resonance. *J. Am. Chem. Soc.* **2006,** *128* (12), 3876-3877.
54. (a) Schiemann, O.; Piton, N.; Mu, Y.; Stock, G.; Engels, J. W.; Prisner, T. F., A PELDOR-based nanometer distance ruler for oligonucleotides. *J. Am. Chem. Soc.* **2004,** *126* (18), 5722-5729; (b) Borbat, P. P.; Davis, J. H.; Butcher, S. E.; Freed, J. H., Measurement of large distances in biomolecules using double-quantum filtered refocused electron spin−echoes. *J. Am. Chem. Soc.* **2004,** *126* (25), 7746-7747.
55. Kunjir, N. C.; Reginsson, G. W.; Schiemann, O.; Sigurdsson, S. T., Measurements of short distances between trityl spin labels with CW EPR, DQC and PELDOR. *Phys. Chem. Chem. Phys.* **2013,** *15* (45), 19673-19685.
56. Grigor'ev, I. A.; Dikanov, S. A.; Shchukin, G. I.; Volodarskii, L. B.; Tsvetkov, Y. D., Influence of the N-oxide group in biradicals of the imidazoline series on the intramolecular spin exchange over systems of conjugated bonds. *J. Struct. Chem.* **1983,** *23* (6), 870-875.
57. Kulik, L. V.; Grishin, Y. A.; Dzuba, S. A.; Grigoryev, I. A.; Klyatskaya, S. V.; Vasilevsky, S. F.; Tsvetkov, Y. D., Electron dipole–dipole ESEEM in field-step ELDOR of nitroxide biradicals. *J. Magn. Reson.* **2002,** *157* (1), 61-68.
58. Kulik, L. V.; Dzuba, S. A.; Grigoryev, I. A.; Tsvetkov, Y. D., Electron dipole–dipole interaction in ESEEM of nitroxide biradicals. *Chem. Phys. Lett.* **2001,** *343* (3–4), 315-324.
59. Kulik, L. V.; Paschenko, S. V.; Dzuba, S. A., 130 GHz ESEEM induced by electron–electron interaction in biradical. *J. Magn. Reson.* **2002,** *159* (2), 237-241.
60. Kulik, L. V.; Dzyuba, S. A., Electron spin echo study of molecular structure and dynamics: new approaches based on spontaneous fluctuations of magnetic interactions. *J. Struct. Chem.* **2004,** *45* (2), 298-314.
61. Rosantev, E. G., In *Free Nitroxide Radicals*, 1st ed.; Press, P., Ed. New York, 1970; p 213.

62. Denysenkov, V. P.; Prisner, T. F.; Stubbe, J.; Bennati, M., High-field pulsed electron–electron double resonance spectroscopy to determine the orientation of the tyrosyl radicals in ribonucleotide reductase. *Proc. Natl. Acad. Sci. U.S.A.* **2006,** *103* (36), 13386-13390.
63. Hay, A. S., Oxidative Coupling of Acetylenes. II1. *J. Org. Chem.* **1962,** *27* (9), 3320-3321.
64. Neises, B.; Steglich, W., Simple method for the esterification of carboxylic acids. *Angew. Chem., Int. Ed.* **1978,** *17* (7), 522-524.
65. Jeschke, G.; Zimmermann, H.; Godt, A., Isotope selection in distance measurements between nitroxides. *J. Magn. Reson.* **2006,** *180* (1), 137-146.
66. Jeschke, G.; Koch, A.; Jonas, U.; Godt, A., Direct conversion of EPR dipolar time evolution data to distance distributions. *J. Magn. Reson.* **2002,** *155* (1), 72-82.
67. Jeschke, G.; Bender, A.; Paulsen, H.; Zimmermann, H.; Godt, A., Sensitivity enhancement in pulse EPR distance measurements. *J. Magn. Reson.* **2004,** *169* (1), 1-12.
68. Jeschke, G.; Polyhach, Y., Distance measurements on spin-labelled biomacromolecules by pulsed electron paramagnetic resonance. *Phys. Chem. Chem. Phys.* **2007,** *9* (16), 1895-1910.
69. Sajid, M.; Jeschke, G.; Wiebcke, M.; Godt, A., Conformationally unambiguous spin labeling for distance measurements. *Chem. Eur. J.* **2009,** *15* (47), 12960-12962.
70. Marko, A.; Denysenkov, V.; Margraf, D.; Cekan, P.; Schiemann, O.; Sigurdsson, S. T.; Prisner, T. F., Conformational flexibility of DNA. *J. Am. Chem. Soc.* **2011,** *133* (34), 13375-13379.
71. Marko, A.; Prisner, T. F., An algorithm to analyze PELDOR data of rigid spin label pairs. *Phys. Chem. Chem. Phys.* **2013,** *15* (2), 619-627.
72. Marko, A.; Denysenkov, V.; Prisner, T. F., Out-of-phase PELDOR. *Mol. Phys.* **2013,** *111* (18-19), 2834-2844.
73. Spindler, P. E.; Glaser, S. J.; Skinner, T. E.; Prisner, T. F., Broadband inversion PELDOR spectroscopy with partially adiabatic shaped pulses. *Angew. Chem., Int. Ed.* **2013,** *52* (12), 3425-3429.
74. Schiemann, O.; Cekan, P.; Margraf, D.; Prisner, T. F.; Sigurdsson, S. T., Relative orientation of rigid nitroxides by PELDOR: beyond distance measurements in nucleic acids. *Angew. Chem., Int. Ed.* **2009,** *48* (18), 3292-3295.
75. Reginsson, G. W.; Hunter, R. I.; Cruickshank, P. A. S.; Bolton, D. R.; Sigurdsson, S. T.; Smith, G. M.; Schiemann, O., W-band PELDOR with 1kW microwave power: molecular geometry, flexibility and exchange coupling. *J. Magn. Reson.* **2012,** *216* (0), 175-182.
76. Misra, S. K., Buckmaster, H. A., Reijerse, E., Subramanian, S., Krishna, M. C., Spectrometers. In *Multifrequency electron paramagnetic resonance: theory and applications*, Misra, S. K., Ed. Wiley VCH: Weinheim, 2011.
77. Bonora, M.; Becker, J.; Saxena, S., Suppression of electron spin-echo envelope modulation peaks in double quantum coherence electron spin resonance. *J. Magn. Reson.* **2004,** *170* (2), 278-283.
78. (a) von Hagens, T.; Polyhach, Y.; Sajid, M.; Godt, A.; Jeschke, G., Suppression of ghost distances in multiple-spin double electron-electron resonance. *Phys. Chem. Chem. Phys.* **2013,** *15* (16), 5854-5866; (b) Giannoulis, A.; Ward, R.; Branigan, E.; Naismith, J. H.; Bode, B. E., PELDOR in rotationally symmetric homo-oligomers. *Mol. Phys.* **2013,** *111* (18-19), 2845-2854.

79. Polyhach, Y.; Godt, A.; Bauer, C.; Jeschke, G., Spin pair geometry revealed by high-field DEER in the presence of conformational distributions. *J. Magn. Reson.* **2007,** *185* (1), 118-129.
80. Polyhach, Y.; Bordignon, E.; Tschaggelar, R.; Gandra, S.; Godt, A.; Jeschke, G., High sensitivity and versatility of the DEER experiment on nitroxide radical pairs at Q-band frequencies. *Phys. Chem. Chem. Phys.* **2012,** *14* (30), 10762-10773.
81. (a) Kay, C. W. M.; El Mkami, H.; Cammack, R.; Evans, R. W., Pulsed ELDOR determination of the intramolecular distance between the metal binding sites in dicupric human serum transferrin and lactoferrin. *J. Am. Chem. Soc.* **2007,** *129* (16), 4868-4869; (b) van Amsterdam, I. M. C.; Ubbink, M.; Canters, G. W.; Huber, M., Measurement of a Cu-Cu distance of 26 A by a pulsed EPR method. *Angew. Chem., Int. Ed.* **2003,** *42*, 62-64.
82. van Wonderen, J. H.; Kostrz, D. N.; Dennison, C.; MacMillan, F., Refined distances between paramagnetic centers of a multi-copper nitrite reductase determined by pulsed EPR (iDEER) spectroscopy. *Angew. Chem., Int. Ed.* **2013,** *52* (7), 1990-1993.
83. Razzaghi, S.; Qi, M.; Nalepa, A. I.; Godt, A.; Jeschke, G.; Savitsky, A.; Yulikov, M., RIDME spectroscopy with Gd(III) centers. *J. Phys. Chem. Lett.* **2014,** *5* (22), 3970-3975.
84. Bode, B. E.; Plackmeyer, J.; Bolte, M.; Prisner, T. F.; Schiemann, O., PELDOR on an exchange coupled nitroxide copper(II) spin pair. *J. Organomet. Chem.* **2009,** *694* (7–8), 1172-1179.
85. Ghimire, H.; McCarrick, R. M.; Budil, D. E.; Lorigan, G. A., Significantly improved sensitivity of Q-band PELDOR/DEER experiments relative to X-band is observed in measuring the inter-coil distance of a leucine zipper motif peptide (GCN4-LZ). *Biochemistry* **2009,** *48* (25), 5782-5784.
86. Matalon, E.; Huber, T.; Hagelueken, G.; Graham, B.; Frydman, V.; Feintuch, A.; Otting, G.; Goldfarb, D., Gadolinium(III) spin labels for high-sensitivity distance measurements in transmembrane helices. *Angew. Chem., Int. Ed.* **2013,** *52* (45), 11831-11834.
87. Song, Y.; Meade, T. J.; Astashkin, A. V.; Klein, E. L.; Enemark, J. H.; Raitsimring, A., Pulsed dipolar spectroscopy distance measurements in biomacromolecules labeled with Gd(III) markers. *J. Magn. Reson.* **2011,** *210* (1), 59-68.
88. Lueders, P.; Jeschke, G.; Yulikov, M., Double electron−electron resonance measured between Gd3+ ions and nitroxide radicals. *J. Phys. Chem. Lett* **2011,** *2* (6), 604-609.
89. Ward, R.; Pliotas, C.; Branigan, E.; Hacker, C.; Rasmussen, A.; Hagelueken, G.; Booth, Ian R.; Miller, S.; Lucocq, J.; Naismith, James H.; Schiemann, O., Probing the structure of the mechanosensitive channel of small conductance in lipid bilayers with pulsed electron-electron double resonance. *Biophys. J.* **2014,** *106* (4), 834-842.
90. Endeward, B.; Butterwick, J. A.; MacKinnon, R.; Prisner, T. F., Pulsed electron−electron double-resonance determination of spin-label distances and orientations on the tetrameric potassium ion channel KcsA. *J. Am. Chem. Soc.* **2009,** *131* (42), 15246-15250.
91. Shelke, S. A.; Sigurdsson, S. T., Structural changes of an abasic site in duplex DNA affect noncovalent binding of the spin label ç. *Nucleic Acids Res.* **2012,** *40* (8), 3732-3740.
92. Yu, D. T.; Milov, A. D.; Maryasov, A. G., Pulsed electron–electron double resonance (PELDOR) as EPR spectroscopy in nanometre range. *Russ. Chem. Rev.* **2008,** *77* (6), 487.

93. Ackermann, K.; Giannoulis, A.; Cordes, D. B.; Slawin, A. M. Z.; Bode, B. E., Assessing dimerisation degree and cooperativity in a biomimetic small-molecule model by pulsed EPR. *Chem. Commun.* **2015,** *51* (25), 5257-5260.
94. Milov, A. D.; Samoilova, R. I.; Tsvetkov, Y. D.; De Zotti, M.; Formaggio, F.; Toniolo, C.; Handgraaf, J.-W.; Raap, J., Structure of self-aggregated alamethicin in ePC membranes detected by pulsed electron-electron double resonance and electron spin echo envelope modulation spectroscopies. *Biophys. J.* **2009,** *96* (8), 3197-3209.
95. Junk, M. J. N.; Spiess, H. W.; Hinderberger, D., The distribution of fatty acids reveals the functional structure of human serum albumin. *Angew. Chem., Int. Ed.* **2010,** *49* (46), 8755-8759.
96. (a) Karyagina, I.; Becker, S.; Giller, K.; Riedel, D.; Jovin, Thomas M.; Griesinger, C.; Bennati, M., Electron paramagnetic resonance spectroscopy measures the distance between the external β-strands of folded α-synuclein in amyloid fibrils. *Biophys. J.* **2011,** *101* (1), L1-L3; (b) Pornsuwan, S.; Giller, K.; Riedel, D.; Becker, S.; Griesinger, C.; Bennati, M., Long-range distances in amyloid fibrils of α-synuclein from PELDOR spectroscopy. *Angew. Chem., Int. Ed.* **2013,** *52* (39), 10290-10294; (c) Eaton, S. S.; Eaton, G. R.; Berliner, L., *Biomedical EPR - Part B: methodology, instrumentation, and dynamics*. Kluwer Academic/Plenum Publishers: 2006.
97. Bhatnagar, J.; Sircar, R.; Borbat, P. P.; Freed, J. H.; Crane, B. R., Self-association of the histidine kinase CheA as studied by pulsed dipolar ESR spectroscopy. *Biophys. J.* **2012,** *102* (9), 2192-2201.
98. Valera, S.; Ackermann, K.; Pliotas, C.; Huang, H.; Naismith, J. H.; Bode, B. E., Accurate extraction of nanometer distances in multimers by pulse EPR. *Chem. Eur. J.* **2016,** *22* (14), 4700-4703.
99. Valera, S.; Bode, B., Hexakis{4-[(4′-hydroxybiphenyl-4-yl)ethynyl]phenyl}benzene. *Molbank* **2015,** *2015* (3), M865.
100. Kreilick, R. W., NMR spectra of some nitroxide radicals. *J. Chem. Phys.* **1966,** *45* (6), 1922-1924.
101. X-ray crystallographic data for biradical **88** and triradical **89** have been deposited with the CCDC numbers 1009963 and 1009964 respectively.
102. X-ray crystallographic analysis of biradical **44** is in excellent agreement with the one previously reported, see: Margraf, D.; Schuetz, D.; Prisner, T.F.; Bats, *J. W. Acta Crystallogr.*, **2009**, E65,o1784.
103. (a) Radical-containing molecules cannot be fully characterized via NMR spectroscopy due to the broadening effects induced by the interaction of the paramagnetic center with the nuclei: see: Kreilick; *J. Phys. Chem.* **1966,** 1922; (b) Radical reduction has been reported as alternative method for systems' full characterisation via ^{1}H and ^{13}C NMR. Examples of reducing agents include phenylhydrazine, s.; (a) Lee, T. D.; Keana, J. F. W.; *J. Org. Chem.* **1975,** 3145-3147; and sodium dithionite, see:; (b) Powell, J.; Johnson, E.; Gannett, P.; *Molecules, 5*, 1244-1250.
104. Mohamed Ahmed, M. S.; Mori, A., Sonogashira coupling with aqueous ammonia directed to the synthesis of azotolane derivatives. *Tetrahedron Lett.* **2004,** *60* (44), 9977-9982.
105. Reichert, V. R.; Mathias, L. J., Expanded tetrahedral molecules from 1,3,5,7-tetraphenyladamantane. *Macromolecules* **1994,** *27* (24), 7015-7023.
106. Drew, M. E.; Chworos, A.; Oroudjev, E.; Hansma, H.; Yamakoshi, Y., A tripod molecular tip for single molecule ligand−receptor force spectroscopy by AFM. *Langmuir* **2009,** *26* (10), 7117-7125.

107. Lu, W.; Yuan, D.; Zhao, D.; Schilling, C. I.; Plietzsch, O.; Muller, T.; Bräse, S.; Guenther, J.; Blümel, J.; Krishna, R.; Li, Z.; Zhou, H.-C., Porous polymer networks: synthesis, porosity, and applications in gas storage/separation. *Chem. Mater.* **2010,** *22* (21), 5964-5972.
108. Ho, M.-S.; Hsu, C.-S., Synthesis and hierarchical superstructures of side-chain liquid crystal polyacetylenes containing galactopyranoside end-groups. *J. Polym. Sci., Part A: Polym. Chem.* **2009,** *47* (23), 6596-6611.
109. Riplinger, C.; Kao, J. P. Y.; Rosen, G. M.; Kathirvelu, V.; Eaton, G. R.; Eaton, S. S.; Kutateladze, A.; Neese, F., Interaction of radical pairs through-bond and through-space: scope and limitations of the point−dipole approximation in electron paramagnetic resonance spectroscopy. *J. Am. Chem. Soc.* **2009,** *131* (29), 10092-10106.
110. Domingo Köhler, S.; Spitzbarth, M.; Diederichs, K.; Exner, T. E.; Drescher, M., A short note on the analysis of distance measurements by electron paramagnetic resonance. *J. Magn. Reson.* **2011,** *208* (1), 167-170.
111. Hagelueken, G. W., R.; Naismith, J. H; Schiemann, O. , MtsslWizard: in silico spin-labeling and generation of distance distributions in PyMOL. *Appl Magn Reson* **2012,** *42* (3), 377-391.
112. Cruickshank, P. A. S.; Bolton, D. R.; Robertson, D. A.; Hunter, R. I.; Wylde, R. J.; Smith, G. M., A kilowatt pulsed 94 GHz electron paramagnetic resonance spectrometer with high concentration sensitivity, high instantaneous bandwidth, and low dead time. *Rev. Sci. Instrum.* **2009,** *80* (10).
113. Jeschke, G., Interpretation of dipolar EPR data in terms of protein structure. In *Structural information from spin-labels and intrinsic paramagnetic centres in the biosciences*, Timmel, C. R.; Harmer, J. R., Eds. Springer Berlin Heidelberg: 2013; Vol. 152, pp 83-120.
114. (a) Castellani, F.; van Rossum, B.; Diehl, A.; Schubert, M.; Rehbein, K.; Oschkinat, H., Structure of a protein determined by solid-state magic-angle-spinning NMR spectroscopy. *Nature* **2002,** *420* (6911), 98-102; (b) Lakshmi, K. V.; Brudvig, G. W., Pulsed electron paramagnetic resonance methods for macromolecular structure determination. *Curr. Opin. Struct. Biol.* **2001,** *11* (5), 523-531.
115. Smirnova, T. I.; Smirnov, A. I., Peptide–membrane interactions by spin-labeling EPR. In *Methods in enzymology*, Peter, Z. Q.; Kurt, W., Eds. Academic Press: 2015; Vol. Volume 564, pp 242-249.
116. Chen, M.; Margittai, M.; Chen, J.; Langen, R., Investigation of α-synuclein fibril structure by site-directed spin labeling. *J. Biol. Chem.* **2007,** *282* (34), 24970-24979.
117. de Vera, I. M. S.; Blackburn, M. E.; Galiano, L.; Fanucci, G. E., Pulsed EPR distance measurements in soluble proteins by site-directed spin labeling (SDSL). In *Current protocols in protein science*, John Wiley & Sons, Inc.: 2001.
118. Georgieva, E. R.; Borbat, P. P.; Ginter, C.; Freed, J. H.; Boudker, O., Conformational ensemble of the sodium-coupled aspartate transporter. *Nat Struct Mol Biol* **2013,** *20* (2), 215-221.
119. Dastvan, R.; Bode, B. E.; Karuppiah, M. P. R.; Marko, A.; Lyubenova, S.; Schwalbe, H.; Prisner, T. F., Optimization of transversal relaxation of nitroxides for pulsed electron−electron double resonance spectroscopy in phospholipid membranes. *J. Phys. Chem. B* **2010,** *114* (42), 13507-13516.
120. Prisner, T. F.; Marko, A.; Sigurdsson, S. T., Conformational dynamics of nucleic acid molecules studied by PELDOR spectroscopy with rigid spin labels. *J. Magn. Reson.* **2015,** *252*, 187-198.

121. Chiang, Y.-W.; Borbat, P. P.; Freed, J. H., The determination of pair distance distributions by pulsed ESR using Tikhonov regularization. *J. Magn. Reson.* **2005,** *172* (2), 279-295.
122. Grytz, C. M.; Marko, A.; Cekan, P.; Sigurdsson, S. T.; Prisner, T. F., Flexibility and conformation of the cocaine aptamer studied by PELDOR. *Phys. Chem. Chem. Phys.* **2016,** *18* (4), 2993-3002.
123. El Mkami, H. N., D. G., Relaxation and its impact on the PELDOR experiment. In *Methods in enzymology - electron paramagnetic resonance investigations of biological systems by using spin labels, spin probes, and intrinsic metal ions, Part A*, Quin, P. Z., Warncke, K., Ed. Elsevier - Acam: London, 2015; Vol. 563, pp 135-143.
124. Ward, R.; Bowman, A.; Sozudogru, E.; El-Mkami, H.; Owen-Hughes, T.; Norman, D. G., EPR distance measurements in deuterated proteins. *J. Magn. Reson.* **2010,** *207* (1), 164-167.
125. Kobayashi, K.; Kobayashi, N.; Ikuta, M.; Therrien, B.; Sakamoto, S.; Yamaguchi, K., Syntheses of hexakis(4-functionalized-phenyl)benzenes and hexakis[4-(4‘-functionalized- phenylethynyl)phenyl]benzenes directed to host molecules for guest-inclusion networks. *J. Org. Chem.* **2005,** *70* (2), 749-752.
126. Shinomiya, M.; Higashiguchi, K.; Matsuda, K., Evaluation of the β value of the phenylene ethynylene unit by probing the exchange interaction between two nitronyl nitroxides. *J. Org. Chem.* **2013,** *78* (18), 9282-9290.
127. Branigan, E.; Pliotas, C.; Hagelueken, G.; Naismith, J. H., Quantification of free cysteines in membrane and soluble proteins using a fluorescent dye and thermal unfolding. *Nat. Protoc.* **2013,** *8* (11), 2090-7.
128. Halbmair, K.; Seikowski, J.; Tkach, I.; Hobartner, C.; Sezer, D.; Bennati, M., High-resolution measurement of long-range distances in RNA: pulse EPR spectroscopy with TEMPO-labeled nucleotides. *Chem. Sci.* **2016**.
129. Kerry, P. S.; Turkington, H. L.; Ackermann, K.; Jameison, S. A.; Bode, B. E., Analysis of influenza A virus NS1 dimer interfaces in solution by pulse EPR distance measurements. *J. Phys. Chem. B* **2014,** *118* (37), 10882-10888.

List of figures

Figure 1.1: Interaction between two paramagnetic centres A and B, at a distance r_{AB} and with an angle θ relative to the external magnetic field B_0..... 3
Figure 1.2: Three pulse PELDOR experiment pulse sequence. 5
Figure 1.3: Four pulse PELDOR pulse sequence. 7
Figure 1.4: Pake pattern from the Fourier transformation of a PELDOR simulation of a rigid biradical. 8
Figure 1.5: Processing of dipolar frequency data for extraction of inter-spin distances by DeerAnalysis 2013. In the first panel the green line indicates the zero time of the dipolar time trace and the blue line indicates the starting point for fitting the slope for subtraction of the background signal V_{inter}. The second figure shows the background corrected experimental data (black) V_{intra} and the simulated dipolar trace (red) generate by DeerAnalysis. The third figure shows the distance distribution obtained from the dipolar signal with colour bars indicating the reliability of the distance distribution defined by the length of the measuring time window of choice. 9
Figure 1.6: L-curve obtained from processing of PELDOR data by DeerAnalysis. The effects of choice of regularization parameter α on distance distributions, obtained from distance measurements on a chemical biradical model system, are reported in the three distance distributions in corresponding colours: 0.001 (red – under smoothed), 10 (green – most appropriate) and 1000 (blue – over smoothed). 11
Figure 1.7: Spin labels commonly used for model systems. 14
Figure 1.8: Imidazole-based biradical. 17
Figure 1.9: Esterification of anthraflavic acid to spin label 3. 18
Figure 1.10: Structure of flexible biradical systems. 18
Figure 1.11: Poly(phenyleneethynylene)-based biradical yardsticks. 21
Figure 1.12: Oligo(*para*-phenyleneethynylene)- and oligo(*para*phenylenebutadiynylene)-based biradical yardsticks. 23
Figure 1.13: One linear and one bent biradical. 23
Figure 1.14: Structure of biradical used for calibration of DQC experiments. 26
Figure 1.15: Multi -spin systems with different symmetries. 31
Figure 1.16: Flexible bis-radical based on Gd(III) paramagnetic centres. 37
Figure 1.17: PELDOR background corrected trace from distance measurements on a tetraradical model system at X-band. The trace exceeds the modulation depth of 0.5

usually achieved when performing the same experiment on a biradical. This shows the effects from the behaviour outlined in Equation 1.8. V_λ is defined as 1-Δ..... 39
Figure 2.1: Symmetrical core building blocks for synthesis of polyradical model systems. 48
Figure 2.2: Core building blocks for synthesis of asymmetric tetraradical and hexagonal polyradicals..... 48
Figure 3.1: Crystal structures of membrane channel proteins MscS S196R1 a), sWza Q335R1 b) and corresponding polygons mimicking their geometries and expected distances. 63
Figure 3.2: Background corrected PELDOR data with fit and corresponding distance distributions for 106 a), 107 b), MscS S196R1 c), and sWza Q335R1 d), measured at X-band with MD5 resonator. The * mark the true distances for 106 and 107, the grey distance distributions are modelled from X-ray data of the proteins by the MtsslWizard software.[111] The coloured bars suggest the reliability of distances in relation to the measuring time window. 65
Figure 3.3: Validations for distance distributions PELDOR measurements at X-band using an MD5 resonator with λ_{max} and 20% on 106 a), 107 b), MscS S196R1 c) and sWza Q335R1 d) with MtsslWizard modelling from. The grey areas represent the error bars for each distance; the distance distributions in the white areas delineated by the grey-shaded error bars are stable to changes in background correction parameters, and thus are more reliable. 66
Figure 3.4: Background corrected PELDOR data with fit and distance distributions for tetra-radicals 106 a) and 107 b) measured at X-band (MS3 resonator). The coloured bars suggest the reliability of distances recovered. 67
Figure 3.5: Validations for distance distributions for λ_{max} and 20% on 106 a), and 107 b) from PELDOR measurements at X-band with an MS3 resonator. The grey area, representing the error bar, delineates those distance distributions that are stable to changes in processing parameters. 67
Figure 3.6: Background corrected PELDOR data with fit and corresponding distance distributions for tetra-radical 106 a) and MscS S196R1b) measured at Q-band. The coloured bars suggest the reliability of distances recovered. 68
Figure 3.7: Validations for distance distributions for λ_{max} and 20% PELDOR measurements on 106 a), MscS S196R1 b) at Q-band. The grey area, representing the

error bar, delineates those distance distributions that are stable to changes in processing parameters. 68
Figure 3.8: Simulated λ_{max} and λ reduced PELDOR traces with corresponding distance distributions (coloured) for a tetrahedron a), rectangle b), heptagon c) and octagon d) and expected true distance distributions (black). The coloured bars suggest the reliability of distances recovered. 70
Figure 3.9: Distance distributions without (left) and with (right) power-scaling for tetraradicals 106 a) and 107 b), MscS 196R1 c), and sWza Q335R1 d) obtained from PELDOR measurements performed at X-band using an MD5 resonator. The coloured bars suggest the reliability of distances recovered. 72
Figure 3.10: Triangle - Background corrected PELDOR data with fit (left), distance distributions without (standard, middle) and with power-scaling (right) for 0% (a), 1% (b) and 3% (c) noise. Graphs showing the relationship between λ and sensitivity for 1% (d, left) and 3% (e, left) noise. Tables (d, e, right) with corresponding values for λ, noise and sensitivity with and without normalisation (Norm.). 74
Figure 3.11: Square - Background corrected PELDOR data with fit (left), distance distributions without (standard, middle) and with power-scaling (right) for 0% (a), 1% (b) and 3% (c) noise. Graphs showing the relationship between λ and sensitivity for 1% (d, left) and 3% (e, left) noise. Tables (d, e, right) with corresponding values for λ, noise and sensitivity with and without normalisation (Norm.). 75
Figure 3.12: Pentagon - Background corrected PELDOR data with fit (left), distance distributions without (standard, middle) and with power-scaling (right) for 0% (a), 1% (b) and 3% (c) noise. Graphs showing the relationship between λ and sensitivity for 1% (d, left) and 3% (e, left) noise. Tables (d, e, right) with corresponding values for λ, noise and sensitivity with and without normalisation (Norm.). 76
Figure 3.13: Hexagon – Background corrected PELDOR data with fit (left), distance distributions without (standard, middle) and with power-scaling (right) for 0% (a), 1% (b) and 3% (c) noise. Graphs showing the relationship between λ and sensitivity for 1% (d, left) and 3% (e, left) noise. Tables (d, e, right) with corresponding values for λ, noise and sensitivity with and without normalisation (Norm.). 77
Figure 3.14: Heptagon – Background corrected PELDOR data with fit (left), distance distributions without (standard, middle) and with power-scaling (right) for 0% (a), 1% (b) and 3% (c) noise. Graphs showing the relationship between λ and sensitivity for 1%

(d, left) and 3% (e, left) noise. Tables (d, e, right) with corresponding values for λ, noise and sensitivity with and without normalisation (Norm.). 78
Figure 3.15: Octagon – Background corrected PELDOR data with fit (left), distance distributions without (standard, middle) and with power-scaling (right) for 0% (a), 1% (b) and 3% (c) noise. Graphs showing the relationship between λ and sensitivity for 1% (d, left) and 3% (e, left) noise. Tables (d, e, right) with corresponding values for λ, noise and sensitivity with and without normalisation (Norm.). 79
Figure 3.16: Comparison between background corrected traces and corresponding distance distributions without (solid line) and with power-scaling (dashed line) obtained by performing PELDOR (black) and frequency-interchanged (green) experiments with an MD5 resonator X-band frequencies for tetraradicals 106 a), 107 b) and MscS S196R1 c). The legend reports in the following order: pump pulse length – pulse offset – detection π pulse length. The subscript M indicates the position of the pump pulse on the maximum of the nitroxide field sweep spectrum. The coloured bars suggest the reliability of distances recovered. 81
Figure 3.17: Validation of distance distributions obtained from PELDOR (left) and frequency-interchanged experiments on 106 a), 107 b) and MscS S196R1 at X-band (MD5 resonator). The grey areas represent the error bars for each distance; the distance distributions within the white areas are stable to changes in background correction parameters. The subscript M indicates the position of the pump pulse on the maximum of the nitroxide field sweep spectrum. 82
Figure 3.18: Comparison between background corrected traces and corresponding distance distributions without (solid line) and with power-scaling (dashed line) obtained performing PELDOR distance measurements using PELDOR (black) and frequency-interchanged (green) experiments with an MS3 resonator at X-band frequencies for tetraradicals 106 a), 107 b) and MscS S196R1 c). The legend reports the pump pulse length – pulse offset – detection π pulse length. The subscript M indicates the position of the pump pulse on the maximum of the nitroxide field sweep spectrum. The coloured bars suggest the reliability of distances recovered. The subscript M indicates the position of the pump pulse on the maximum of the nitroxide field sweep spectrum. 83
Figure 3.19: Validation of distance distributions obtained from PELDOR (left) and frequency-interchanged experiments on 106 a), 107 b) and MscS S196R1 at X-band (MS3 resonator). The grey area, representing the error bar, delineates those distance

distributions that are stable to changes in processing parameters. The subscript M indicates the position of the pump pulse. 84
Figure 3.20: Background corrected traces and distance distributions without (solid line) and with power-scaling (dashed line) from PELDOR (black) and frequency-interchanged (green) experiments at Q-band for tetraradical 106 a) and MscS S196R1 b). The legend reports pump pulse length – pulse offset – detection π pulse. The subscript M indicates the pump pulse being on maximum of field sweep. The coloured bars suggest the reliability of distances recovered. 85
Figure 3.21: Validation of distance distributions obtained from PELDOR (left) and frequency-interchanged experiments on 106 a) and MscS S196R1 b) at Q-band. The grey areas represent the error bars for each distance; the distance distributions within the white areas are stable to changes in background correction parameters. The subscript M indicates the position of the pump pulse on the maximum of the nitroxide field sweep spectrum. 86
Figure 3.22: Comparison between background corrected traces and corresponding distance distributions without (solid line) and with power-scaling (dashed line) obtained performing PELDOR (black), frequency-interchanged (green) and λ reduced with similar λ to the frequency-interchanged (red) experiments at X-band frequencies (MD5 resonator) for model system 106 a) and MscS S196R1 b). The legend reports pump pulse length – pulse offset – detection π pulse. The subscript M indicates the pump pulse being on maximum of the field sweep. The coloured bars suggest the reliability of distances recovered. 87
Figure 3.23: Validation of distance distributions for PELDOR with λ_{max} (black), λ reduced (red) and frequency-interchanged (green) experiments performed on 106 a) and MscS S196R1 b) at X-band (MD5 resonator). The coloured areas, representing the error bar, delineate those distance distributions that are stable to changes in processing parameters. 88
Figure 3.24: Comparison between background corrected traces and corresponding distance distributions without (solid line) and with power-scaling (dashed line) obtained performing PELDOR (black) and frequency-interchanged (green) experiments at Q-band frequencies for model system 106 a) and MscS S196R1 b). The legend reports pump pulse length – pulse offset – detection π pulse. The subscript M indicates the

pump pulse being on maximum of field sweep. The coloured bars suggest the reliability of distances recovered. 89
Figure 3.25: Validation of distance distributions for PELDOR with λ_{max} (black), reduced λ (red) and frequency-interchanged (green) experiments performed on 106 a) and MscS S196R1 b) at Q-band. The coloured areas, representing the error bar, delineate those distance distributions that are stable to changes in processing parameters. The subscript M indicates the position of the pump pulse on the maximum of the nitroxide field sweep spectrum. 89
Figure 3.26: 4-pulse DEER (PELDOR) sequence.[7a] 93
Figure 4.1: PELDOR X-band MD5 background corrected traces and with fits (grey) and corresponding distance distributions for 33, 66 and 100% labelled samples of MscS mutants S196R1 a) and D67R1 b). The "expected" grey distance distributions are derived from processing the X-ray data for each protein with the software MtsslWizard.[111] The coloured bars indicate the reliability of distances recovered as a function of the measuring time window..... 100
Figure 4.2: Validation of distance distributions obtained for 33, 66 and 100% labelled samples of MscS S196R1 a) and D67R1 b) mutants at X-band (MD5 resonator). The coloured areas, representing the error bars, delineate those distance distributions that are stable to changes in processing parameters. 101
Figure 4.3: Distance distributions without (left) and with (right) power-scaling from PELDOR measurements performed on sparsely labelled samples of MscS S196R1 a) and MscS D67R1 b) at X-band (MD5 resonator). The coloured bars indicate the reliability of distances recovered as a function of the measuring time window..... 101
Figure 4.4: X-band MS3 background corrected traces with fits and corresponding distance distributions for 33, 66 and 100% labelled samples of MscS mutants S196R1 a) and D67R1 b). The coloured bars indicate the reliability of distances recovered as a function of the measuring time window..... 102
Figure 4.5: Validation of distance distributions obtained for 33, 66 and 100% labelled samples of MscS S196R1 a) and D67R1 b) mutants at X-band (MS3 resonator). The coloured areas, representing the error bars, delineate those distance distributions that are stable to changes in processing parameters. 103
Figure 4.6: Distance distributions without (left) and with (right) power-scaling from PELDOR measurements performed on sparsely labelled samples of MscS S196R1 a)

and MscS D67R1 b) at X-band (MS3 resonator). The coloured bars indicate the reliability of distances recovered as a function of the measuring time window..... 103
Figure 4.7: Q-band background corrected PELDOR traces with fits and corresponding distance distributions for 33, 66 and 100% labelled samples of MscS S196R1 a) and MscS D67R1 b). The coloured bars indicate the reliability of distances as a function of time window. 104
Figure 4.8: Validation of distance distributions obtained for 33, 66 and 100% labelled samples of MscS S196R1 a) and MscS D67R1 b) at Q-band. The coloured areas, representing the error bars, delineate those distance distributions that are stable to changes in processing parameters. 104
Figure 4.9: Distance distributions without (left) and with (right) power-scaling from PELDOR measurements performed on sparsely labelled samples of MscS S196R1 a) and MscS D67R1 b) at Q-band. The coloured bars indicate the reliability of distances recovered as a function of the measuring time window..... 105
Figure 4.10: X-band MD5 background corrected traces with fits and corresponding distance distributions for 100 a), 66 b) and 33% c) labelled samples of MscS S196R1 obtained when performing PELDOR (black) and frequency-interchanged (green) experiments. The legend reports pump pulse length – pulse offset – detection π pulse. The subscript M indicates the pump pulse being on maximum of field sweep. The coloured bars indicate the reliability of distances recovered as a function of the measuring time window. 109
Figure 4.11: Validations of PELDOR (left) and frequency-interchanged (right) experiments on 100 a), 66 b) and 33 c) % labelled samples of MscS S196R1 at X-band (MD5). The grey areas represent the error bars for each distance; the distance distributions within the white areas are stable to changes in background correction parameters, thus more reliable. The subscript M indicates the position of the pump pulse on the maximum of the nitroxide field sweep spectrum. 110
Figure 4.12: X-band MD5 background corrected traces with fits and corresponding distance distributions with (dashed) and without power-scaling (solid) for 100 a), 66 b) and 33% c) labelled samples of MscS D67R1 obtained when performing PELDOR (black) and frequency-interchanged (green) experiments. The legend reports pump pulse length – pulse offset – detection π pulse. The subscript M indicates the pump pulse

being on maximum of field sweep. The coloured bars indicate the reliability of distances recovered as a function of the measuring time window. 111
Figure 4.13: Validations of PELDOR (left) and frequency-interchanged (right) experiments on 100 a), 66 b) and 33 c) % labelled samples of MscS D67R1 at X-band (MD5). The grey area, representing the error bar, delineates those distance distributions that are stable to changes in processing parameters. The subscript M indicates the position of the pump pulse on the maximum of the nitroxide field sweep spectrum. .. 112
Figure 4.14: X-band MS3 background corrected traces with fits and corresponding distance distributions with (dashed) and without power-scaling (solid) for 100 a), 66 b) and 33% c) labelled samples of MscS mutant S196R1 obtained when performing PELDOR (black) and frequency-interchanged (green) experiments. The legend reports pump pulse length – pulse offset – detection π pulse. The subscript M indicates the pump pulse being on maximum of field sweep. The coloured bars indicate the reliability of distances recovered as a function of the measuring time window. 113
Figure 4.15: Validations of PELDOR (left) and frequency-interchanged (right) experiments on 100 a), 66 b) and 33 c) % labelled samples of MscS S196R1 at X-band (MS3). The coloured areas, representing the error bars, delineate those distance distributions that are stable to changes in processing parameters. The subscript M indicates the position of the pump pulse on the maximum of the nitroxide field sweep spectrum. 114
Figure 4.16: X-band MS3 background corrected traces with fits and corresponding distance distributions with (dashed) and without (solid) power-scaling for 100 a), 66 b) and 33% c) labelled samples of MscS mutant D67R1 obtained when performing PELDOR (black) and frequency-interchanged (green) experiments. The legend reports pump pulse length – pulse offset – detection π pulse. The subscript M indicates the pump pulse being on maximum of field sweep. The coloured bars indicate the reliability of distances recovered as a function of the measuring time window. 115
Figure 4.17: Validations of PELDOR (left) and frequency-interchanged (right) experiments on 100 a), 66 b) and 33 c) % labelled samples of MscS D67R1 at X-band (MS3). The coloured areas, representing the error bars, delineate those distance distributions that are stable to changes in processing parameters. The subscript M indicates the position of the pump pulse on the maximum of the nitroxide field sweep spectrum. 116

Figure 4.18: Q-band background corrected traces with fits and corresponding distance distributions with (dashed) and without (solid) power-scaling for 100 a), 66 b) and 33% c) labelled samples of MscS S196R1 obtained when performing PELDOR (black) and frequency-interchanged (green) experiments. The legend reports pump pulse length – pulse offset – detection π pulse. The subscript M indicates the pump pulse being on maximum of field sweep. The coloured bars indicate the reliability of distances recovered as a function of the measuring time window..... 117
Figure 4.19: Validations of PELDOR (left) and frequency-interchanged (right) experiments on 100 a), 66 b) and 33 c) % labelled samples of MscS S196R1 at Q-band. The coloured areas, representing the error bars, delineate those distance distributions that are stable to changes in processing parameters. The subscript M indicates the position of the pump pulse on the maximum of the nitroxide field sweep spectrum... 118
Figure 4.20: Q-band background corrected traces with fits and corresponding distance distributions with (dashed) and without (solid) power-scaling for 100 a), 66 b) and 33% c) labelled samples of MscS D67R1 obtained when performing PELDOR (black) and frequency-interchanged (green) experiments. The legend reports pump pulse length – pulse offset – detection π pulse. The subscript M indicates the pump pulse being on maximum of field sweep. The coloured bars indicate the reliability of distances recovered as a function of the measuring time window..... 119
Figure 4.21: Validations of PELDOR (left) and frequency-interchanged (right) experiments on 100 a), 66 b) and 33 c) % labelled samples of MscS D67R1 at Q-band. The coloured areas, representing the error bars, delineate those distance distributions that are stable to changes in processing parameters. The subscript M indicates the position of the pump pulse on the maximum of the nitroxide field sweep spectrum... 120
Figure 4.22: Comparison between PELDOR measurements performed at Q-band with λ_{max} on 33, 66 and 100% labelled samples together with 33% λ_{max} on the 100% labelled sample. The coloured bars indicate the reliability of distances recovered as a function of the measuring time window..... 126
Figure 4.23: Validation of 100% (measured with λ_{max} and 33% λ_{max}) and 33% labelled (measured with λ_{max}) MscS mutants S196R1 a) and D67R1 b). The coloured areas, representing the error bars, delineate those distance distributions that are stable to changes in processing parameters..... 126

Figure 4.24: Background corrected traces and distance distributions obtained from PELDOR measurements on samples with labelling degree *f* 33% (green), 66% (red) and 100% (black) and for frequency-interchanged experiments (blue) on the fully labelled systems. The legend reports pump pulse length – pulse offset – detection π pulse. The subscript M indicates the pump pulse being on maximum of field sweep. The coloured bars indicate the reliability of distances recovered as a function of the measuring time window. The subscript M indicates the position of the pump pulse on the maximum of the nitroxide spectrum. 129
Figure 5.1: ^{14}N hyperfine tensor in anisotropic nitroxide EPR spectrum at X-band with a cartoon of the bandwidth and spectral position for detection (red) and pump (blue) pulses.[2b] 132
Figure 5.2: The principal molecular axes of the components of the hyperfine tensor in a nitroxide spin-label. 133
Figure 5.3: Background corrected traces PELDOR with fits and corresponding distance distributions obtained when performing distance measurements of samples in d_8 toluene without (black) and with deuterium ESEEM averaging (red), protonated toluene (blue) and *o*-terphenyl (green) measured on model systems 93 a), 105 b) and 106 c). The legend reports: pump pulse length – pulse offset – π pulse length. 137
Figure 5.4: Background corrected PELDOR traces with fits for measurements performed with 40 (red), 60 (blue) and 80 (green) MHz pulse offset and corresponding dipolar spectra on 93 a), 105 b) and 106 c). The legend reports: pump pulse length – pulse offset – π pulse length. 139
Figure 5.5: Distance distributions and corresponding Pake patterns obtained from PELDOR traces for measurements performed with 40 (red), 60 (blue) and 80 (green) MHz pulse offset on 93 a), 105 b) and 106 c). The legend reports: pump pulse length – pulse offset – π pulse length. 140
Figure 5.6: Validation of distance distributions from measurements with 40 (red), 60 (blue) and 80 (green) MHz offset on 93 a), 105 b) and 106 c). The coloured areas, representing the error bars, delineate those distance distributions that are stable to changes in processing parameters. The legend reports: pump pulse length – pulse offset – π pulse length. 141
Figure 5.7: Power-scaled (dashed lines) and non-power-scaled (solid) distance distributions obtained from PELDOR measurements performed on 105 a) and 106 b)

with 40 (red), 60 (blue) and 80 (green) MHz offset. The legend reports: pump pulse length – pulse offset – π pulse length. 142
Figure 5.8: Comparison between experimental dipolar spectra a) and corresponding DeerAnalysis fits b) obtained from PELDOR measurements at 40, 60 and 80 MHz performed on biradical 93. The legend reports: pump pulse length – pulse offset – π pulse length. 143
Figure 5.9: Pake patterns of 93 a) 105 b) and 106 c), from measurements performed at 60 (red lines) and 80 MHz (blue lines) as solid lines with respective DeerAnalysis fits as dashed lines. The legend reports: pump pulse length – pulse offset – π pulse length. . 145
Figure 5.10: Comparison between background corrected traces for orientation averaged (OA) experiments on 93 a), 105 b) and 106 c) (black) and PELDOR together with their corresponding distance distributions (black) with (dashed) and without (solid) power-scaling. The legend reports: pump pulse length – pulse offset – π pulse length. 147
Figure 5.11: Comparison between dipolar spectra from orientation averaged (OA) experiments on 93 and 105 a) and dipolar spectrum from measurements on 106 b) (solid) with corresponding DeerAnalysis fits (dashed). The legend reports: pump pulse length – pulse offset – π pulse length. 148
Figure 5.12: Background corrected traces with fits and corresponding distance distributions from orientation resolved experiments performed with 2 G steps of the magnetic field during performance of the orientation averaged experiment on 93 a), 105 b) and 106 c). 149
Figure A.1: Echo-detected spin nutation experiment pulse train used for calibration of pump pulse flip angle β. 164
Figure A.2: ELDOR nutation experiment showing the occurrence of a 180° inversion of the spin echo after pulses with a flip angle of odd multiples of π (a) and its corresponding time trace (b). 164
Figure A.3: Estimated pulses profiles on nitroxide EPR field spectra at X-band for a PELDOR a) and frequency-interchanged b) and Q-band for a PELDOR c) and frequency-interchanged d) settings.[27, 90, 128] 166